The Thermal Structure of Subduction Zones and Backarcs

by

Claire A. Currie

Ph.D. Dissertation
School of Earth and Ocean Sciences
University of Victoria

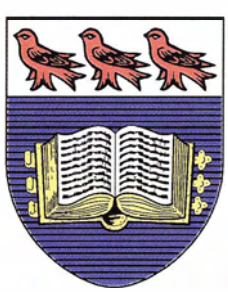

University of
Victoria

2004

The Thermal Structure of Subduction Zones and Backarcs

by

Claire A. Currie
B.Sc., University of Western Ontario, 1999

A Dissertation Submitted in Partial Fulfillment of the
Requirements for the Degree of

DOCTOR OF PHILOSOPHY

in the School of Earth and Ocean Sciences

Supervisor: Dr. Roy D. Hyndman

ABSTRACT

Temperature plays a dominant role in many subduction zone processes, including arc magma generation and the distribution of earthquakes. In this thesis, observational constraints on forearc and backarc thermal structure are integrated with numerical models to better understand the thermal consequences of subduction. Forearc thermal models, applied as an example to the Mexico subduction zone, indicate that the forearc is cool, as expected due to the cool subducting slab. The brittle part of this subduction fault extends to depths >30 km where, even though very weak, the fault may generate small but non-negligible frictional heating. The rupture extent of Mexican megathrust earthquakes is consistent with proposed seismogenic limits of 100 and 350°C. A remarkable feature of subduction zones is that, although the subducting plate cools the over-riding crust and produces low temperatures in the forearc, the arc and backarc regions are consistently extremely hot, as indicated by arc volcanism, surface heat flow, seismic velocities, T_e, and other observations. At the Cascadia subduction zone, backarc temperatures are ~1200°C at 50-60 km depth with little variation for 500 km east to the craton. Thermal constraints from other subduction zone backarcs, including those that have had no recent extension, show that they are similarly hot for 100's-1000's of km behind the arc. Local sources of heat (e.g., radiogenic heat production, frictional heating) appear to be small, and mantle flow is invoked to carry heat into the backarc. Thermal-mechanical numerical models for slab-driven corner flow give flow that is strongly focussed into the wedge corner below the arc but low mantle temperatures further into the backarc, inconsistent with observations. It is concluded that slab-driven flow is insufficient to satisfy the heat budget at a subduction zone. Geodetic and geological constraints indicate extremely low mantle viscosities in several backarcs ($<10^{19}$ Pa s), suggesting that thermal buoyancy may be the primary driving force for flow. High temperatures and hydration of the mantle wedge by the subducting slab may reduce the viscosity, allowing vigourous thermal convection that rapidly carries heat upward from depth into the subduction zone.

TABLE OF CONTENTS

LIST OF TABLES

LIST OF FIGURES

ACKNOWLEDGEMENTS

There are many people who have been invaluable in helping me to achieve my goals, and who have shared the challenges and rewards of scientific research with me. First, I would like to thank my thesis committee:
Roy Hyndman - for being an excellent supervisor, for discussions and ideas that greatly influenced my research, and for always pushing me to do more than I think I can
Kelin Wang - for his energy and guidance, for constantly challenging me and encouraging me, and for always being available to talk about science and more
John Cassidy - for his time, enthusiasm, and ideas, and for carrying my posters all over the world
George Spence - for helpful comments, difficult questions, and encouragement
Henning Struchtrup - for his time on my committee and his interest in my research
Jason Phipps Morgan - for his time and suggestions as my external examiner

Thank you to **everyone at the Pacific Geoscience Centre** for scientific expertise and support, especially:
John He - for developing the finite element computer code, and for his patience with my never-ending questions about numerical modelling
Garry Rogers - for his interest in my research, and for helpful suggestions and questions
Stephane Mazzotti, Herb Dragert, Earl Davis, Trevor Lewis, Bob Thompson, and **Honn Kao** - for discussions and suggestions that have improved my research
Steve Taylor, Bruce Johnson, Richard Baldwin, Robert Kung, Richard Franklin and **Ron Bradley** - for computer support and technical assistance without which this thesis could not have been completed
Ralph Currie and **Sandy Colvine** – for encouragement, and for providing office/computer space at PGC
Pam Olson at the IOS/PGC library - for help with references
Brian Schofield, Suzanne Paradis, Elena Jenner, and **Renee Hetherington** - for friendship and support

At the University of Victoria, I would like to thank **Stan Dosso, Ross Chapman, Terry Russell, Claire Tugwell,** and **Sussi Arason** for support during the EOS 370 class and beyond.

Parts of this thesis research extended off Vancouver Island. Thank you to:
Peter van Keken (Univ. Michigan) - for organizing 2002 MARGINS meeting on subduction zone thermal models and the subduction zone benchmarking exercise
Vladimir Kostoglodov, Shri Singh, and **Vlad Manea** (UNAM) - for discussions about the Mexico subduction zone tectonics and seismicity
Michael Bostock (Univ. British Columbia) - for providing the shear wave splitting analysis code and helpful comments
David Eaton (Univ. Western Ontario) - for discussions about seismic anisotropy, and for encouraging me to pursue geophysical research

During this thesis work, I have been able to participate in fieldwork that did not relate directly to my project. Thank you to **Deb Kelley**, **John Delaney**, and **Will Wilcock** for good times at sea, and to **Nicholas Courtier** for absolute gravity adventures.

One of the best parts about graduate school is the friends who provide encouragement and good memories. I would especially like to thank: **Maiclaire Bolton, Sheri Molnar, Lisa Wolynec, Karen Simon, Ikuko Wada, Ele Willoughby, Ms. Asmaa Anwar, Liesa Lapinski, Tuna Onur, Mark Seemann, Amanda Bustin, Lucinda Leonard, Michael Riedel, Liliane Carle, Ivana Novosel, John Ristau, Yan Hu, Kumar Ramachandran, Mladen Nedimovic,** and **Martin Scherwath.**

This thesis is dedicated to my family (**Mom, Dad, Ian** and **Lynne**) for their endless support and encouragement.

CHAPTER 1
Introduction

1.1 Motivation for Study

Subduction zones are among the most dynamic tectonic settings on Earth. At a subduction zone, cool oceanic lithosphere descends into the warm interior of the Earth. This process results in intensive volcanism and destructive earthquakes that occur within both the subducting and over-riding plates, as well as extremely large earthquakes along the interface between the two (called megathrust earthquakes). Subduction zones are also key sites of material and chemical exchange between the Earth's surface and interior.

The subduction process has a strong effect on the thermal regime of the adjacent continent or arc, and in turn, temperature has an important role in numerous processes associated with subduction. The generation of volcanic magma is controlled by temperature. Temperature also provides one of the main controls on the maximum depth of earthquakes within the subducting and over-riding plates, and on the rupture zone of megathrust earthquakes. Temperature- and pressure-dependent metamorphic reactions within the subducting plate can trigger earthquakes within this plate and also release water to the overlying mantle. The influx of water changes the chemical and rheological properties of the mantle and is an important process in arc magma generation. The thermal structure of the over-riding plate governs how it will deform in response to plate boundary forces. This has implications for orogenesis and the long-term evolution of the plate boundary. This thesis study deals with the thermal structure of subduction zones and the geophysical consequences of the thermal regime.

Figure 1.1 is a schematic cross-section of a subduction zone illustrating the main features. Subduction zones contain a volcanic arc, a narrow band of active volcanoes that are found on the over-riding plate. The volcanic arc divides the subduction zone into two main parts: the forearc (which is cold) and the backarc (which is hot). In this study, the

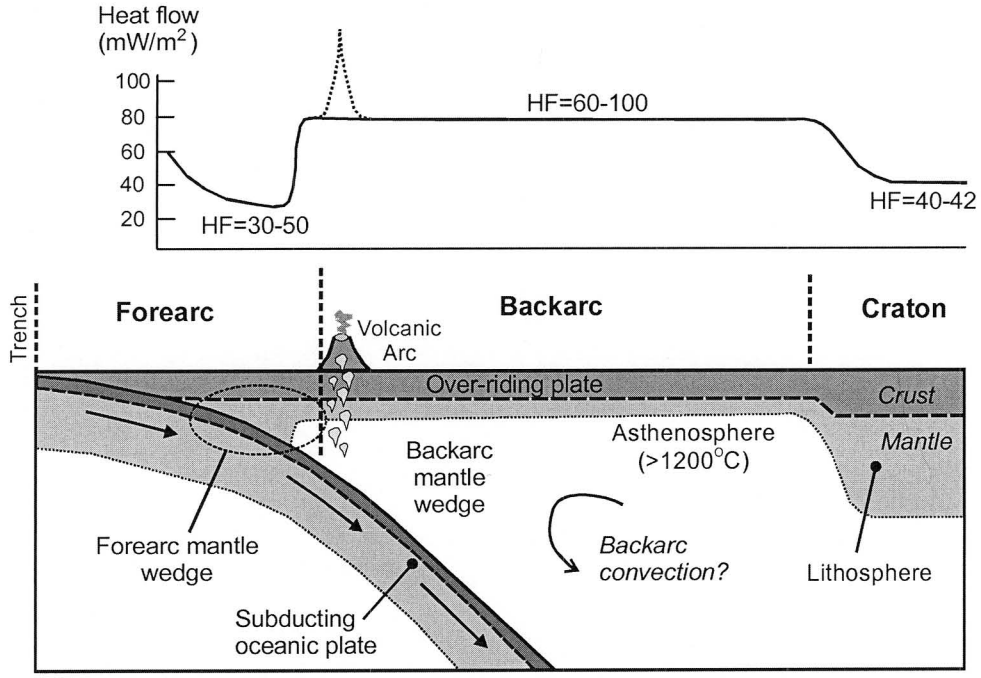

Figure 1.1. Schematic diagram of the key components of a subduction zone (bottom) and the typical surface heat flow profile over a subduction zone (top).

term backarc refers to any part of the subduction zone behind the volcanic arc (away from the trench) that is affected by the subduction process. The mantle wedge is defined as the mantle that overlies the subducting plate; it can be divided into the forearc mantle wedge and the backarc mantle wedge. In some subduction zones, the landward limit of the backarc is a craton, stable continental crust that has not been deformed by tectonic processes since the Archean. In other subduction zones, the limit of the backarc is not as well-defined.

1.2 Thermal Studies of Subduction Zones

The earliest surface heat flow measurements at subduction zones in the western Pacific indicated the forearc and backarc exhibit markedly different heat flow [e.g., *Vacquier et al.*, 1966; *Oxburgh and Turcotte*, 1968, 1970; *McKenzie and Sclater*, 1968]. Whereas values of surface heat flow over the trench and forearc are generally 30-50 mW/m^2, backarc heat flow is 60-100 mW/m^2 for 100's of kilometres behind the volcanic arc (e.g., **Figure 1.1**). For comparison, surface heat flow over cratonic regions is

typically 40-42 mW/m^2 [e.g., *Jaupart and Mareschal*, 1999], and surface heat flow over old (>70 Ma) oceanic crust is ~50 mW/m^2 [e.g., *Stein and Stein*, 1992 and references therein]. Many of the early heat flow measurements are from backarcs that are now known to have undergone recent extension and spreading. However, a number of studies have shown that the heat flow profile for areas with little or no recent backarc extension is similar [e.g., *Ziagos et al.*, 1985; *Lewis et al.*, 1992; *Springer and Forster*, 1998].

The heat flow profile implies a dramatic change in thermal structure between the forearc and backarc. Whereas the forearc regions are inferred to be very cool, the arc and backarc appear to be extremely hot. This is supported by on-going arc volcanism at nearly all subduction zones; the generation of magma requires high temperatures. Other evidence for high backarc temperatures comes from seismic studies that show low velocities and high attenuation in the backarc mantle wedge at many subduction zones [e.g., *Wiens and Smith*, 2003 and references therein].

The occurrence of high heat flow and inferred high mantle wedge temperatures in the arc and backarc regions of subduction zones is extraordinary. Subduction of a cool oceanic plate should result in a cooling of the overlying material, as observed in the low heat flow over the forearc. The paradoxical observation of high heat flow, high temperatures and active volcanism in the backarc in spite of a cool subducting plate has remained an outstanding problem since the inception of plate tectonic theory over 40 years ago.

Early Models

Early ideas about the origin of backarc heat focussed on local sources of heat to generate high backarc temperatures and high surface heat flow. The first studies assumed *a priori* that arc magma was produced by melting of the subducting plate at depths of 100-150 km. Local sources of heat examined were: adiabatic heating of the slab as it descends, radiogenic heating in the subducting crust and mantle wedge, and exothermic metamorphic phase transitions in the subducting plate. All were concluded to increase the temperature of the subducting plate by less than 50°C and could not explain high

backarc heat flow [*Oxburgh and Turcotte*, 1968; *McKenzie and Sclater*, 1968; *Hasabe et al.*, 1970; *Oxburgh and Turcotte*, 1970; *Minear and Toksoz*, 1970; *Toksoz et al.*, 1971].

Most of these studies appealed to shear heating along the top of the subducting plate as the mechanism for generating high temperatures. Heating due to frictional sliding was first considered, where the amount of heat generated depends on the sliding velocity and shear stress. Using a subduction velocity of 5 cm/yr and a shear stress of 10 MPa, compatible with estimates of stress drop in Wadati-Benioff earthquakes (which are now known to occur within the slab, not on top of it), *McKenzie and Sclater* [1968] showed that it was possible to generate enough heat to melt the subducting plate. One problem with this simple model is that it predicts unrealistically high slab temperatures at depths greater than 100 km. In addition, at high temperatures (close to rock melting temperatures), rocks are expected to deform viscously, rather than through brittle sliding so there should be little frictional heating [e.g., *Oxburgh and Turcotte*, 1968].

Viscous dissipation was then investigated as a heat source. Relative motion between the subducting plate and overlying mantle was assumed to be accommodated by viscous deformation in a narrow shear zone above the subducting plate. The amount of heat generated by dissipation in the layer increases with increasing layer viscosity, increasing subduction velocity, and decreasing layer thickness. For a layer that is a few kilometres thick and typical subduction velocities (5-10 cm/y), a viscosity of 10^{20}-10^{21} Pa s is required within the layer to generate enough heat for slab melting [*Oxburgh and Turcotte*, 1968; *Minear and Toksoz*, 1970; *Hasebe et al.*, 1970; *Toksoz et al.*, 1971]. Although high slab temperatures can be obtained, the surface heat flow profile predicted by these models shows a narrow maximum between the trench and volcanic arc and a decrease in heat flow into the backarc [e.g., *McKenzie and Sclater*, 1968]. This is inconsistent with observations. In addition, *Andrews and Sleep* [1974] and *Yuen et al.* [1978] argue the viscosity within the layer should decrease with increasing temperature; with this feedback, a large amount of heat should not be generated.

Local heat sources were soon abandoned as the primary cause of high backarc temperatures. The alternate hypothesis is that the entire mantle wedge is viscous, and flow in the wedge can carry heat into the subduction zone. *McKenzie* [1969] suggested

that flow in the wedge is induced by viscous coupling between the subducting plate and overlying mantle wedge. In this case, the lowermost part of the mantle wedge adjacent to the slab is carried downward with the subducting slab, resulting in the flow of material from the backarc toward the wedge corner at shallow depths. This flow pattern is called "corner flow". *Andrews and Sleep* [1974] developed the first numerical models to study the thermal effects of corner flow. Using a temperature-dependent viscosity for the wedge, they showed that this flow pattern could significantly elevate the temperature of the mantle wedge and subducting slab near the volcanic arc. Modelling studies by *Toksoz and Hsui* [1978], *Bodri and Bodri* [1978], *Hsui and Toksoz* [1979], and *Hsui et al.* [1983] reached similar conclusions.

Recent Models

Slab-induced flow in the mantle wedge is now considered by many to be the dominant mechanism for carrying heat into the mantle wedge. Many recent thermal modelling studies have focussed on the mantle wedge near the volcanic arc (the wedge corner), to reconcile the thermal models with the high temperatures required for arc magma generation and to investigate the effects of induced flow on the thermal structure of the subducting slab [e.g., *Honda*, 1985; *Davies and Stevenson*, 1992; *Furukawa*, 1993a, b; *Peacock*, 1996; *Iwamori*, 1997; *Kincaid and Sacks*, 1997; *Peacock and Wang*, 1999; *Conder et al.*, 2002; *van Keken et al.*, 2002; *Kelemen et al.*, 2003; *Currie et al.*, 2004b]. Contrary to the earliest ideas, geochemical studies of arc magmas have shown that the subducting plate does not melt at most subduction zones [e.g., *Gill*, 1981; see also **Chapter 3**]. Instead, most arc magmas are concluded to be generated by partial melting of the mantle wedge, induced by the infiltration of water and volatiles from the underlying subducting plate as it dehydrates. With the careful choice of model boundary conditions and the use of a realistic temperature- (and stress-) dependent rheology for the mantle wedge, the modelled temperatures in the wedge corner can be brought into good agreement with geochemical constraints on temperature [e.g., *Honda*, 1985; *Furukawa*, 1993a, b; *van Keken et al.*, 2002, *Kelemen et al.*, 2003]. However, as noted by *Iwamori* [1997], most of these studies assume high backarc temperatures as a pre-existing

boundary condition on the models. Induced wedge flow is used as a mechanism to carry the high temperatures from the backarc into the wedge corner, but the source of heat in the backarc is not considered. The latter is one of the problems addressed in this thesis.

1.3 Thesis Objectives

This thesis study focusses on the thermal regime of subduction zones (forearcs and backarcs) and its geological and geophysical consequences (e.g., earthquakes, arc volcanoes). The three major research objectives are:

1. ***An examination of the factors that control forearc thermal structure.*** Numerical models of the Mexico subduction zone are used to investigate the effect of different subduction parameters on the temperature of the shallow (<40 km) part of the thrust fault. The fault temperatures are then compared to the rupture area of recent megathrust earthquakes along the Mexico subduction zone to evaluate the hypothesis that the rupture area (i.e., the seismogenic zone) is limited to temperatures between ~100°C and 350°C, with a transition zone that extends to 450°C. Although not discussed in detail, the results of these models are also important for understanding temperature controls on phase changes within the subducting slab, slab dehydration, slab earthquakes, and plate boundary stress transfer.
2. ***A compilation of observational constraints on the thermal and flow structure of the backarc regions.*** The thermal structure of the mantle wedge beneath the arc and well into the backarc provides important constraints on backarc mantle flow and the source of heat at a subduction zone. Both direct methods (e.g., arc magma petrology, thermobarometry of backarc mantle xenoliths) and indirect methods (e.g., surface heat flow, seismic velocity) are used to constrain backarc mantle temperatures. The thermal structure of the Cascadia subduction zone is examined in detail. Observations for other subduction zones are summarized to show that nearly all backarcs, including those with no recent extension, are anomalously hot for 100's of kilometres behind the volcanic arc.

Flow directions in the backarc mantle can be inferred using seismic anisotropy observations. At the Cascadia subduction zone, the shear wave splitting technique is used to study mantle anisotropy and thus constrain the backarc asthenosphere flow regime. Shear wave splitting data from other subduction zones are also reviewed.

3. ***An investigation of the thermal effects of mantle wedge flow.*** Given the observational constraints on backarc thermal structure, numerical models are used to examine the mantle wedge and backarc advective-convective regime that maintains the inferred high backarc temperatures and to address the source of heat in the backarc. Flow driven by viscous coupling between the subducting plate and wedge (i.e., corner flow) is considered in detail. An initial study of flow driven by thermally-induced density variations is also given.

1.4 Outline of Thesis

Following the objectives given above, this thesis is divided into three main parts. After this introduction, **Chapter 2** presents thermal models of the forearc regions of the Mexico subduction zone to understand the factors that affect forearc temperatures and the consequences of these temperatures for the megathrust earthquake seismogenic zone.

The next three chapters deal with observational constraints on the thermal structure and mantle flow for subduction zone backarcs. The main study region is the Cascadia subduction zone, where the thermal structure is well-constrained and where the backarc has not undergone recent extension. Observations from other subduction zones are also presented to illustrate general characteristics of subduction zone backarcs. **Chapter 3** provides a comprehensive discussion of the thermal structure of the northern Cascadia backarc. The thermal structure for other subduction zones is reviewed in **Chapter 4**, focussing primarily on backarcs that have not undergone extension. In **Chapter 5**, shear wave splitting data for the Cascadia subduction zone is presented to constrain mantle anisotropy and the mantle flow regime. These observations are compared to shear wave splitting studies from other subduction zones.

In the final part of the thesis, numerical models are used to investigate the thermal effects of mantle wedge flow. **Chapter 6** describes the numerical modelling procedure. Models that include mantle wedge flow driven only by the subducting plate are given in **Chapter 7**. For a reasonable range of model parameters and boundary conditions, it is shown that this type of flow cannot satisfy observational constraints on thermal structure, especially the uniform high temperatures in the backarc. An additional component of mantle flow is required. In **Chapter 8**, preliminary models that include thermal buoyancy as a driving force for flow are presented to show that such flow can carry a significant amount of heat into the whole backarc. Given the numerical modelling results, a conceptual model for mantle wedge dynamics is presented. The major conclusions of this research are summarized in **Chapter 9**.

The appendices provide details about numerical tests that were carried out with the numerical code used to model backarc mantle flow. **Appendix A** examines shear flow in a viscous box. **Appendix B** assesses the numerical accuracy of the modelling code for problems with a subduction geometry. **Appendix C** describes the results of tests for the finite element meshes of the Cascadia and NE Japan subduction zones used in **Chapters 7 and 8**.

CHAPTER 2
Thermal Models of the Mexico Subduction Zone

2.1 Introduction

The first part of this thesis focusses on the thermal structure of the forearc regions of subduction zones, using the Mexico subduction zone as the main example. Two-dimensional numerical models are developed to understand the factors that affect the forearc thermal structure. Surface heat flow provides an independent constraint on forearc temperatures. The numerical models can be used to look at thermal controls on processes in the forearc and shallow part of the subducting plate (<40 km depth).

In this study, the primary application of the models is to the study of megathrust earthquakes, which are the largest earthquakes in the world. These earthquakes rupture the subduction thrust fault (the interface between the subducting and over-riding plates). The Mexico subduction zone has experienced numerous megathrust earthquakes over the last century. Some of the largest earthquakes in recent history are the 1985 M_W 8.1 Michoacan earthquake and the 1995 M_W 8.0 earthquake in the Jalisco region. Such earthquakes pose a significant seismic hazard to the coastal regions of Mexico, as well as areas considerably inland, including Mexico City.

Globally, it is observed that only a shallow portion of the subduction fault is seismogenic, i.e., capable of producing earthquakes [e.g., *Zhang and Schwartz*, 1992; *Tichelaar and Ruff*, 1993]. The seismogenic zone is bound at its updip and downdip limits by regions that exhibit stable (aseismic) sliding (**Figure 2.1**). The transition from stable sliding to stick slip marks a change in fault behaviour from velocity strengthening to velocity weakening [e.g. *Scholz*, 1990]. Although a number of factors may control

---

This chapter forms the basis for the paper:

Currie, C.A., R.D. Hyndman, K. Wang, and V. Kostoglodov, Thermal models of the Mexico subduction zone: Implications for the megathrust seismogenic zone, *Journal of Geophysical Research, 107*(B12), 2370, doi: 10.1029/2001JB000886, 2002.

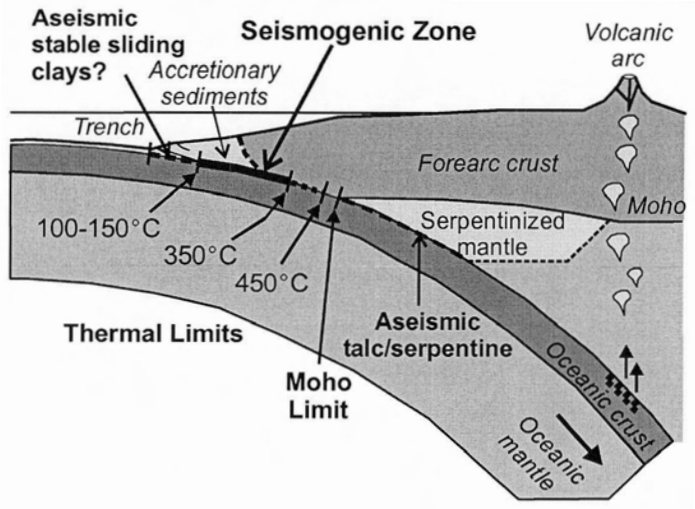

Figure 2.1. The proposed thermal and compositional limits on the seismogenic zone of subduction thrust faults [after *Hyndman et al.*, 1997].

fault behaviour, it is hypothesized that temperature and rock composition provide the primary controls on the width and location of the seismogenic zone [e.g., *Zhang and Schwartz*, 1992; *Tichelaar and Ruff*, 1993; *Hyndman and Wang*, 1993; *Hyndman et al.*, 1997; *Peacock and Hyndman*, 1999]. Thus, the thermal models of the Mexico subduction zone can be used to examine possible temperature controls on the megathrust seismogenic zone.

The location of the seaward (updip) and landward (downdip) limits of the seismogenic zone is critical for studies of seismic hazard. These limits define the maximum earthquake rupture width, which is related to the maximum magnitude that may be expected for the fault. The downdip limit is usually the closest approach of the seismic source zone to near-coastal cities, and thus is important for ground shaking hazard. The location of the updip limit is important for tsunami generation.

2.2 The Megathrust Seismogenic Zone

2.2.1 Temperature limits on the seismogenic zone

The presence of an updip aseismic zone has been attributed to the presence of stable sliding unconsolidated and semi-consolidated sediments [*Byrne et al.*, 1988; *Vrolijk*, 1990]. There are many factors that affect sediment properties, including pore fluid pressure, and physical and chemical changes in the sediments [e.g., *Moore and*

Saffer, 2001]. One change that may be important is the dehydration of smectite clays to illite and chlorite at temperatures between 100 and 150°C [*Vrolijk*, 1990; *Wang*, 1980]. Whether this change marks the updip limit of the seismogenic zone remains a question [*Marone et al.*, 2001; *Saffer et al.*, 2001], and the thermal control on the frictional behaviour of sediments along the updip part of subduction faults is a subject of active research.

The downdip limit of the seismogenic zone is proposed to be limited by a temperature of 350°C for some subduction zones [e.g., *Hyndman and Wang*, 1993]. Laboratory experiments show that quartzo-feldspathic continental rocks exhibit a transition from velocity weakening to velocity strengthening at temperatures of 325-350°C [*Tse and Rice*, 1986; *Blanpied et al.*, 1995]. This temperature agrees well with the maximum depth of earthquakes within continental crust [*Brace and Byerlee*, 1970; *Chen and Molnar*, 1983; *Tse and Rice*, 1986]. There may be a second temperature that limits the maximum rupture depth of megathrust earthquakes, which were initiated at temperatures less than 350°C. This second limit is proposed to be at about 450°C [*Hyndman and Wang*, 1993], corresponding to a rapid increase of instantaneous frictional stress in laboratory data [*Tse and Rice*, 1986].

For SW Japan, *Hyndman et al.* [1995] showed that the proposed thermal limits are consistent with both the coseismic rupture width and the seismogenic zone determined through modelling of coseismic and interseismic crustal deformation. For the Cascadia subduction zone, the proposed downdip thermal limit is consistent with interseismic geodetic observations [*Hyndman and Wang*, 1993; *Dragert et al.*, 1994; *Wang et al.*, 2003]. Both SW Japan and Cascadia have young subducting plates.

2.2.2 Alternative downdip limit: Serpentinized forearc mantle wedge

For subduction zones with older subducting plates, such as Chile and South Alaska, *Oleskevich et al.* [1999] showed that the critical maximum temperatures are reached at depths greater than 90 km, whereas the maximum depth of rupture is limited to depths of 40-50 km [*Tichelaar and Ruff*, 1993]. The intersection of the thrust fault with the continental Moho occurs at a depth of 40-50 km in these subduction zones, and thus it

is suggested that the Moho intersection provides the maximum downdip limit to the seismogenic zone [*Ruff and Tichelaar*, 1996]. One possible mechanism for generating stable sliding behaviour of the fault below the continental Moho intersection is serpentinization of the mantle wedge [*Hyndman et al.*, 1997]. Dehydration reactions within the subducting plate release water into the overlying forearc mantle wedge, resulting in the formation of serpentine minerals and possibly other hydrous minerals, such as talc and brucite [*Peacock and Hyndman*, 1999]. Laboratory studies indicate that serpentinite generally exhibits stable sliding behaviour [e.g., *Reinen*, 2000]. Although there are no laboratory studies of the sliding behaviour of talc and brucite, their layered structure suggests that they are probably weak and aseismic. The existence of serpentine within the mantle wedge is supported by thermal and petrologic models [e.g., *Peacock*, 1993], as well as a number of seismological observations [e.g., *Suyehiro et al.*, 1996; *Kamiya and Kobayashi*, 2000; *Bostock et al.*, 2002; *Hyndman and Peacock*, 2003].

2.3 Modelling the Mexico Subduction Zone Thermal Structure

The proposed controls on the megathrust seismogenic zone are examined through thermal modelling of the Mexico subduction zone, from the northern Rivera Plate (~22°N) to the Tehuantepec Ridge on the Cocos Plate (~15°N) (**Figure 2.2**). Both oceanic plates subduct beneath the North America Plate at the Middle America Trench, located 50-70 km offshore Mexico. Two-dimensional numerical models have been developed for four profiles oriented perpendicular to the Middle America Trench. These are located in the Jalisco, Michoacan, Guerrero, and Oaxaca regions of Mexico.

2.3.1 Modelling approach

The heat equation is used to determine the thermal structure along each profile:

$$\rho c_p \frac{\partial T}{\partial t} = \nabla \cdot (k \nabla T) - \rho c_p (\mathbf{v} \cdot \nabla T) + Q_H \qquad (2.1)$$

where T is the temperature, t is the time, k is the thermal conductivity, ρ is the density, c_p is the heat capacity, and $\mathbf{v}$ is the velocity field. The product ρc_p is the volumetric heat

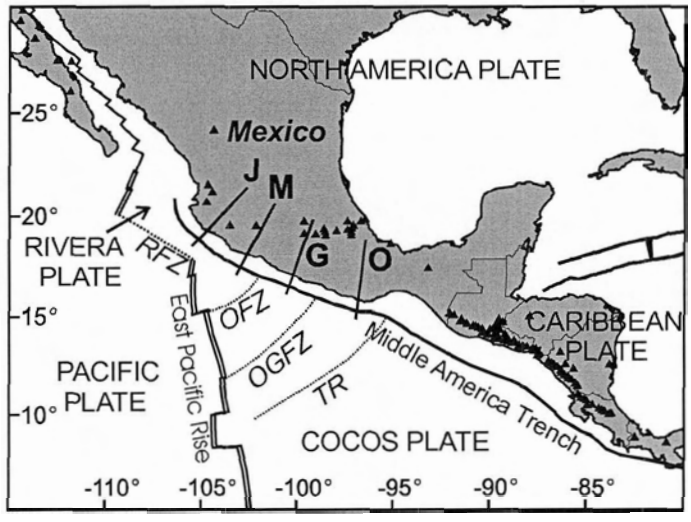

Figure 2.2. Tectonic map of Central America showing the location of the models: J, Jalisco; M, Michoacan; G, Guerrero; O, Oaxaca. Triangles represent active volcanoes. The Trans-Mexico Volcanic Belt is located at ~20°N. Double lines are spreading centres. Dotted lines are fracture zones: RFZ, Rivera Fracture Zone; OFZ, Orozco Fracture Zone; OGFZ, O'Gorman Fracture Zone; TR, Tehuantepec Ridge.

capacity. The term Q_H represents the volumetric heat production and includes local heat sources such as radiogenic heat production and frictional heating.

In the models below, the thermal regime is assumed to be in steady state ($\partial T/\partial t=0$), and the thermal conductivity is assumed to be isotropic. Thus, the two-dimensional temperature field for a horizontal distance (x) and depth (z) is given by:

$$0 = \left[\frac{\partial}{\partial x}\left(k\frac{\partial T}{\partial x}\right)+\frac{\partial}{\partial z}\left(k\frac{\partial T}{\partial z}\right)\right]-\rho c_p\left[v_x\frac{\partial T}{\partial x}+v_z\frac{\partial T}{\partial z}\right]+Q_H \qquad (2.2)$$

The terms on the right-hand side of the equation represent heat conduction, heat advection, and local heat production, respectively.

The above equation is solved numerically using the finite element method, with 8-node isoparametric elements, following the approach described by *Wang et al.* [1995b]. Within each element the thermal properties (thermal conductivity, heat capacity, heat production) are uniform, but the temperature may vary quadratically. For each model profile, the finite element mesh contains 1404 elements and 4363 nodes. Each model extends from 25 km seaward of the trench to 700 km landward of the trench. The upper

boundary of the model is the surface of the Earth. The base of the model is arbitrarily located 100 km below the top of the subducting plate.

Within the entire model, heat is transferred by conduction. In addition, the subducting plate advectively carries heat landward and downward at a fixed subduction rate. Flow within the mantle above the subducting plate was introduced, by prescribing velocities to the wedge using the analytic solution for corner flow in a constant viscosity mantle [*Batchelor*, 1967; see also **Appendix B**]. In this simple model, flow is restricted to the region above the subducting plate and below the continental lithosphere-asthenosphere boundary (taken at 55 km depth). The seaward limit of flow is a vertical boundary located 20 km seaward of the volcanic arc, a limit suggested by a surface heat flow transition [*Ziagos et al.*, 1985]. Such flow transports heat from the backarc region into the wedge. Similar to the model of *Peacock and Wang* [1999], heat is introduced from the backarc through a continental geotherm at the landward boundary (700 km from the trench) that yields a surface heat flow of 90 mW/m^2, consistent with backarc heat flow observations for this region [*Ziagos et al.*, 1985]. As shown below, the thermal effects of mantle wedge flow on the seismogenic part of the thrust fault are very small.

The upper boundary of the model has a fixed temperature of 0°C. The base of the model is assigned a temperature of 1450°C, which approximates the mantle temperature at a depth of ~100 km, following the *Stein and Stein* [1992] model for oceanic plate cooling. Because this boundary is located far from the region of interest (shallow subduction thrust fault), and because the thermal structure of the subducting plate is dominated by advective heat transfer from the seaward boundary, model results are not sensitive to the basal boundary condition.

The critical parameters for the thermal models are the geometry and age of the oceanic plate, the thickness and deposition history of incoming sediments, and the convergence rate. The thickness of the over-riding continental crust and the thermal parameters (thermal conductivity and radioactive heat generation) of each rock unit must also be assigned. Two additional factors of potentially first-order importance are frictional heating along the thrust fault and hydrothermal circulation within the upper incoming oceanic crust (see discussion below).

2.3.2 Oceanic geotherm

The seaward boundary condition for the two-dimensional model is a one-dimensional geotherm for the oceanic plate. There are several factors that control the temperature-depth profile of an oceanic plate: 1) conductive cooling of the plate as it ages away from its spreading ridge origin, 2) deposition of lower conductivity sediments on top of the plate that slow the rate of cooling, 3) an increase in sediment thickness over time, resulting in a transient cooler sediment column, 4) compaction of sediments with increasing sedimentation, resulting in the expulsion of pore water, causing advective upward heat transfer within the sediments, and 5) hydrothermal circulation in the upper oceanic crust. In the following, the effects of hydrothermal circulation are neglected, but will be discussed in **Section 2.3.9**. Following the approach of *Wang and Davis* [1992], the oceanic geotherm is calculated by allowing the plate to cool from zero years to its age at the trench, using the time-dependent sedimentation history and assuming the porosity-depth profile of the sediment column does not change with time [*Hutchison*, 1985].

The Rivera and Cocos Plates are both young oceanic plates. Magnetic anomaly lineations [*Klitgord and Mammerickx*, 1982] indicate a slight increase in plate age to the southeast, from 11.5 Ma at the Jalisco profile to 15.5 Ma at the Oaxaca profile (**Table 2.1**). The age of the Cocos Plate changes discontinuously across fracture zones. Across the Orozco and O'Gorman fracture zones, the change in age is less than 1 Ma [*Kostoglodov and Bandy*, 1995]. However, the oceanic plate age increases by 10-25 Ma

Table 2.1. Oceanic plate parameters.

Profile	Plate age at trench (Ma)	Margin-normal convergence rate (cm/yr)	Plate dip at 15 km depth (degrees)
Jalisco	11.5	3.8	17.0
Michoacan	13.3	5.5	15.3
Guerrero A	13.1	5.8	15.3
Guerrero B	13.1	5.8	13.1
Oaxaca	15.5	6.1	11.3

to the southeast across the Tehuantepec Ridge [*Couch and Woodcock*, 1981]. Such a large discontinuity might become important for the thermal structure in the vicinity of the Tehuantepec Ridge, as heat may be conducted along the margin to the southeast. Since the Oaxaca profile is located ~160 km from the Tehuantepec Ridge, the effects of margin-parallel heat transfer are assumed to be negligible.

Multichannel seismic reflection data shows that the northern Cocos Plate and the Rivera Plate are covered with no more than 200 m of sediments [*Michaud et al.*, 2000]. Seaward of the trench, the Cocos Plate between the Guerrero and Oaxaca profiles is covered with 170-200 m of pelagic and hemipelagic sediments [*Moore et al.*, 1982]. A uniform sediment thickness of 200 m on the incoming oceanic plate was used for all model profiles. Sediment deposition has occurred at a rate of 135 m/my over the last 0.78 my and at a rate of 3-30 m/my before that [*Sheppard and McMillen*, 1981]. Due to the small sediment thickness, uncertainties in the thickness and deposition rate have little effect on the oceanic crust thermal structure.

The calculated oceanic geotherms for each profile are shown on **Figure 2.3**. The Oaxaca geotherm has a slightly shallower thermal gradient, due to the greater plate age.

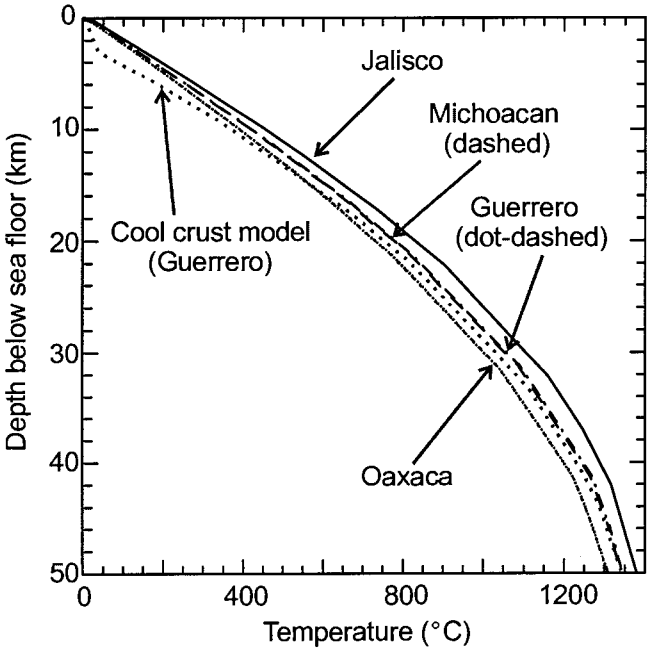

Figure 2.3. Oceanic geotherms for each profile. Also shown is the geotherm for the "cool crust" model for the Guerrero profile to approximate the effects of hydrothermal circulation to a depth of 3 km, using a plate age of 13.1 Ma (see text for discussion).

Despite the young age of the oceanic plates, the Mexico subduction zone is fairly cool relative to the Cascadia and SW Japan subduction zones, which are of similar age [e.g., *Wang et al.*, 1995a, b]. In the latter two regions, the oceanic plates are covered with 1.5 to 3.5 km of sediment, compared to ~200 m for the Mexico margin. The insulating effect of the thicker sediments results in a warmer subducting plate. At the trench, the temperature of the top of the oceanic plate is more than 200°C for the Cascadia subduction zone [e.g., *Hyndman and Wang*, 1993], whereas the temperature is 30 to 50°C for Mexico. The major uncertainty in the oceanic geotherms is the possible cooling of the upper oceanic plate by hydrothermal circulation (see discussion below).

2.3.3 Oceanic plate geometry

For each profile, the geometry of the oceanic plate was defined using: 1) single and multichannel seismic reflection data, 2) seismic refraction data, 3) Wadati-Benioff earthquakes (assumed to occur about 5 km below the top of the oceanic plate), 4) intermediate magnitude thrust earthquakes, and 5) large megathrust earthquakes and their aftershocks. Data within 50 km of each profile was projected onto the cross-section, and a best-fit line was determined using a low-order polynomial for the shallow plate profile (**Figure 2.4**). At depths greater than 55 km, a constant plate dip was used. For all profiles, the geometry is similar to that given by *Pardo and Suarez* [1993, 1995]. The Jalisco profile also agrees well with the crustal structure determined through gravity modelling [*Bandy et al.*, 1999]. Estimated uncertainties in plate depth are 10%.

Between the Orozco and O'Gorman Fracture Zones, it has been proposed that the Cocos Plate flattens for a distance of 125 km at ~50 km depth [e.g., *Suarez et al.*, 1990; *Kostoglodov et al.*, 1996]. A line containing a subhorizontal section was fit to the data (**Figure 2.4**). A second geometry was determined using a smooth downward curvature, more consistent with the plate profiles to the north and south. Both profiles have a similar shape in the upper 30 km. The shallow thermal structure (less than 30-40 km depth) is not affected by the presence or absence of the subhorizontal region, as the thermal structure is most sensitive to the shallow plate geometry (**Figure 2.5**)

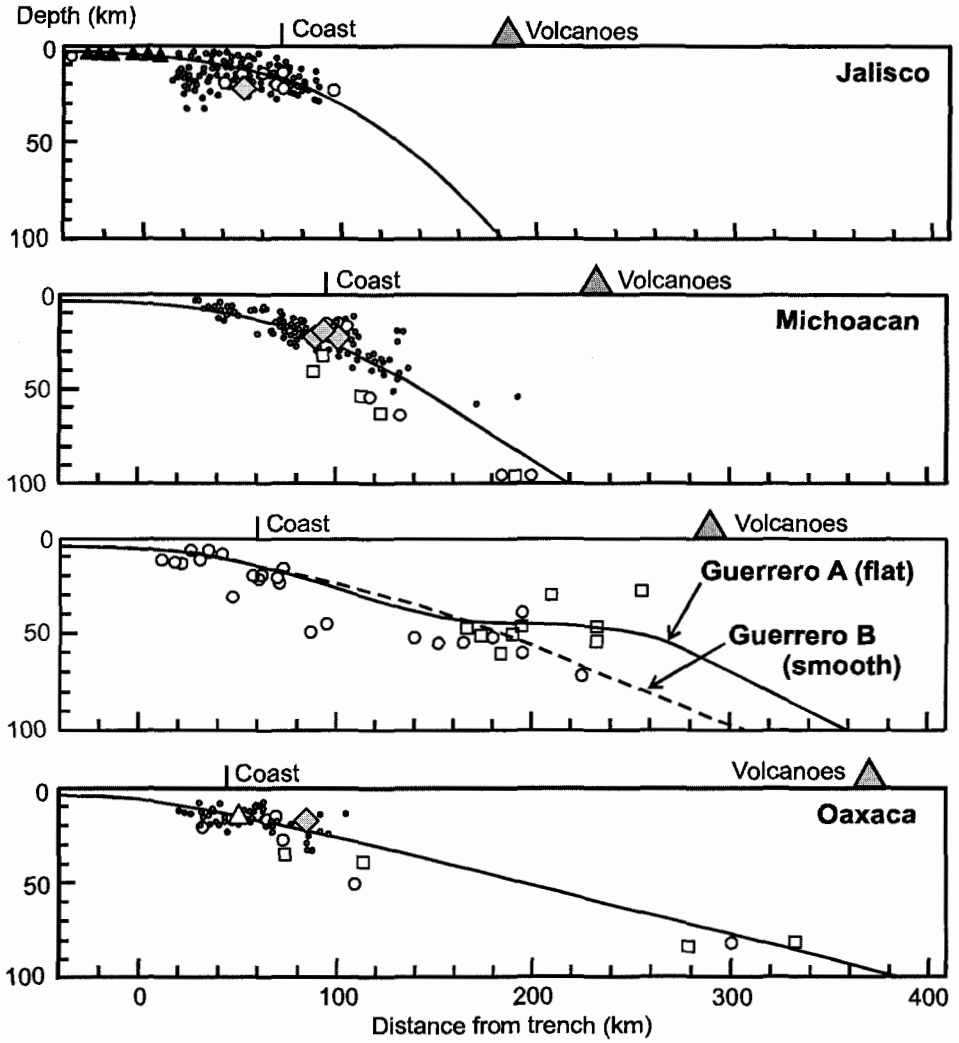

Figure 2.4. Geometry of the subduction thrust fault along each profile. Open squares are in-slab earthquakes [*Singh et al.*, 2000]; open circles are relocated earthquakes [*Pardo and Suarez*, 1995]; solid triangles are seismic reflection data for Jalisco [*Michaud et al.*, 2000]; open triangle is from seismic reflection data for Oaxaca [*Nava et al.*, 1988]. Locations of megathrust main shocks (open diamonds) and their aftershocks (small grey circles) were given by *Pacheco et al.* [1997] for Jalisco, *Stolte et al.* [1986] for Michoacan, and *Singh et al.* [2000] for Oaxaca. Bathymetry data were used to constrain the plate surface seaward of the trench [*Prol-Ledesma et al.*, 1989; *Pardo and Suarez*, 1995].

2.3.4 Continental crust thickness

The thickness of the continental crust defines the approximate location of the Moho intersection with the thrust fault. The crustal thickness beneath Mexico has been inferred from body and surface wave studies, seismic refraction surveys, and modelling of gravity and magnetotelluric data. In the northern part of the study region, *Gomberg et*

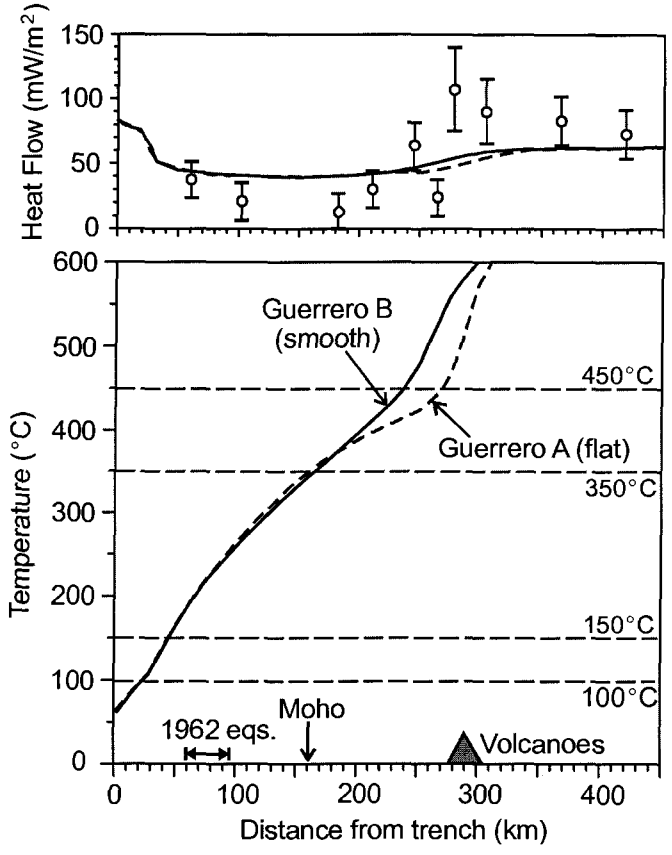

Figure 2.5. Variations in surface heat flow (top) and temperatures along the top of the subducting plate (bottom) for the Guerrero profile for two different plate geometries. There is no shear heating in the models. The heat flow measurements are from *Ziagos et al.* [1985].

al. [1989] and *Bandy et al.* [1999 and references therein] propose a crustal thickness of 36 to 40 km. To the south, crustal thickness studies give values of 33 km [*Couch and Woodcock*, 1981], 44 km [*Arzate et al.*, 1993], 45±4 km [*Valdes et al.*, 1986], and 50 km [*Helsley et al.*, 1975]. In the models, a crustal thickness of 40 km was used for all profiles.

2.3.5 Convergence rate

The convergence rate of the Cocos Plate ranges from 5 cm/yr in the northwest to more than 7 cm/yr in the southeast [*DeMets and Wilson*, 1997]. The margin-normal component of convergence is given in **Table 2.1**. The Rivera-North America convergence rate is much more uncertain, with estimates ranging from 2 to 5 cm/yr [e.g., *Kostoglodov and Bandy*, 1995]. The most recent plate motion studies that use data from

the last 0.78 my give convergence rates between 3.3 and 4.3 cm/yr along the Jalisco profile [*DeMets and Wilson*, 1997; *Bandy et al.*, 1998; *DeMets and Traylen*, 2000]. A steady-state convergence velocity of 3.8 cm/yr is used in the models. Variations of 0.5 cm/yr have little effect on the subduction thrust temperatures, as shown in **Section 2.3.7**.

DeMets and Traylen [2000] suggest that the convergence history of the Rivera Plate is quite complex and variable over the past 10 my. On the basis of magnetic lineations, they propose the cessation or near-cessation of convergence between 2.6 and 1.0 Ma. Time-dependent thermal models containing the convergence history of *DeMets and Traylen* [2000] show that the effect on the present thermal structure is minimal, and therefore the model results are not presented here. If a 1.6 my hiatus in subduction is introduced, the temperature of the top of the subducting plate increases slightly, and the locations of the 350°C and 450°C isotherms are shifted ~7 km seaward of their steady-state positions.

2.3.6 Thermal parameters

Each of the two-dimensional models has four units: oceanic plate, sediments, continental crust, and mantle wedge. The thermal conductivity of the entire continental crust is taken as 2.5 W m^{-1} K^{-1} (**Table 2.2**). This is a reasonable value for continental crust material [e.g., *Peacock and Wang*, 1999] and is consistent with that measured during continental heat flow studies of Mexico [*Smith et al.*, 1979; *Ziagos et al.*, 1985].

Table 2.2. Parameters for thermal model units.

Model unit	Thickness (km)	Thermal conductivity (W m^{-1} K^{-1})	Radiogenic heat production ($\mu W/m^3$)	Heat capacity (MJ m^{-3} K^{-1})
Sediments	0.200	1.0 - 2.0	1.0	--
Upper crust	15	2.5	1.3	--
Lower crust	25	2.5	0.27	--
Mantle wedge	--	3.1	0.02	3.3
Oceanic plate	100	2.9	0.02	3.3

Although there may be localized regions of the crust with varying conductivity, it is only the large-scale crustal conductivity that is of importance in the current study. The upper 15 km of the continental crust is assigned a radioactive heat generation of 1.3 $\mu W/m^3$, while the lower 25 km is 0.27 $\mu W/m^3$. These are typical continental values and reflect the roughly exponential decrease in radioactive heat production with depth [e.g., discussion by *Peacock and Wang*, 1999]. These values are also comparable with measurements by *Ziagos et al.* [1985] which gave values of 1.3±0.6 $\mu W/m^3$ for the upper 4 km.

The accretionary prism and sediments have conductivities that increase landward and with depth from 1.0 W m^{-1} K^{-1} at the seafloor to 2.0 W m^{-1} K^{-1} at 10 km depth, following *Oleskevich et al.* [1999]. The seafloor value is consistent with marine heat flow measurements in this area [e.g., *Vacquier et al.*, 1967; *Prol-Ledesma et al.*, 1989]. A uniform radiogenic heat production of 1.0 $\mu W/m^3$ is assigned to the accretionary prism and sediments, which is similar to the average upper continental source rock for the sediments.

Parameter values for the mantle wedge and oceanic plate are those used in previous modelling studies [e.g., *Hyndman and Wang*, 1993, 1995; *Oleskevich et al.*, 1999]. A conductivity of 2.9 and 3.1 W m^{-1} K^{-1} is assigned to the oceanic plate and mantle, respectively. Both units have a radioactive heat generation of 0.02 $\mu W/m^3$ and a volumetric heat capacity of 3.3 MJ m^{-3} K^{-1}. Reasonable variations in these values have only a small effect on the thermal structure [e.g., *Wang et al.*, 1995a].

2.3.7 Parameter sensitivity analysis

A series of parameter sensitivity tests were carried out to examine the effect of each of the above model parameters on the forearc thermal structure. For the tests, the Michoacan model geometry and parameters are used. Mantle wedge corner flow is not included, except in the first set of tests that examine the effects of flow. The sensitivity of each parameter was assessed by looking at the effect on surface heat flow and temperatures along the subduction thrust fault.

Mantle wedge flow

The effects of isoviscous mantle wedge corner flow were examined by comparing models with no flow to those with varying amounts of flow (**Figure 2.6**). The maximum seaward extent of flow is ~210 km from the trench, well landward of the shallow thrust fault. Mantle wedge flow has only a small effect on the thermal structure of the forearc region. The subduction thrust temperature is increased by a maximum of 6°C at the 40 km depth with the introduction of flow. The temperatures and heat flow in the backarc are significantly increased by even a small amount of flow. See **Chapter 7** for a more detailed examination of the effects of mantle wedge flow on the backarc thermal structure.

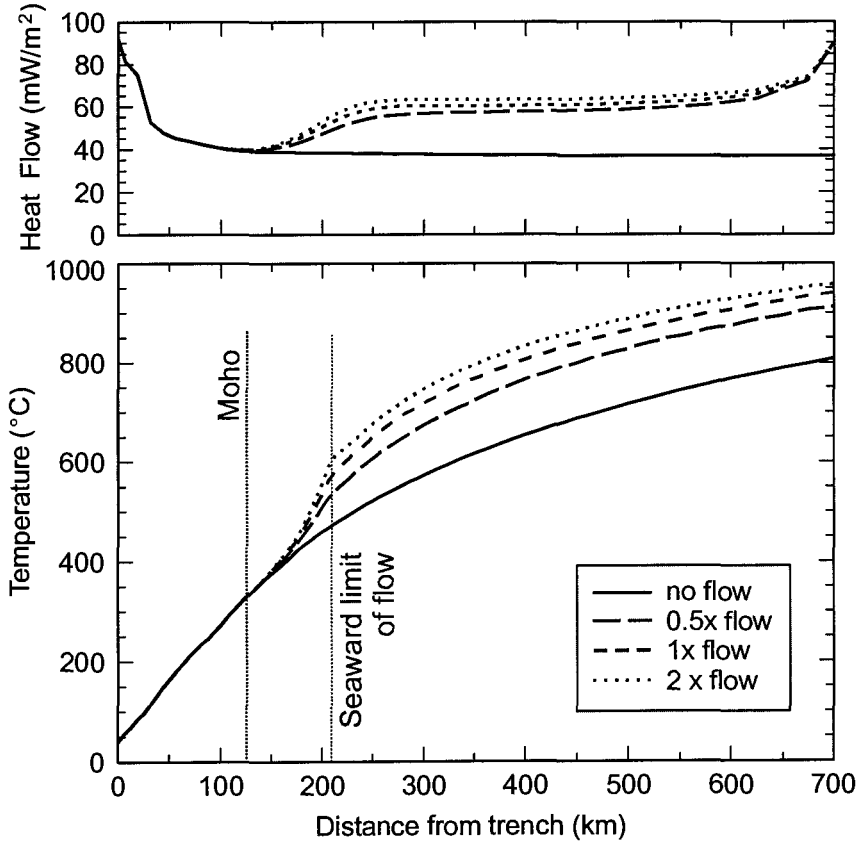

Figure 2.6. The effect of mantle wedge corner flow on the heat flow (top) and temperatures along the top of the subducting plate (bottom). Models with no flow and with flow at 0.5, 1 and 2 times the subducting rate were tested.

Subducting plate age

The age of the subducting plate has a significant effect on the forearc heat flow and subduction fault temperatures, for plates less than 25 my old (**Figure 2.7**). Younger plates are much hotter and produce a higher heat flow over the forearc regions. The effect of plate age decreases as the plate gets older. For plates older than ~50 Ma, variations of 10 Ma in age produce only small variations in the forearc thermal structure (not shown). For the Mexico subduction zone, the plate age is 11.5-15.5 Ma, with an estimated uncertainty of 2-3 Ma. Thus, the uncertainty in thrust fault temperature at the Moho (40 km depth) is ~30°C, with decreasing uncertainty updip.

Sediment thickness

The effects of sediment thickness on the incoming plate were examined for thicknesses between 0 and 3000 m. The sedimentation rate was assumed to be constant

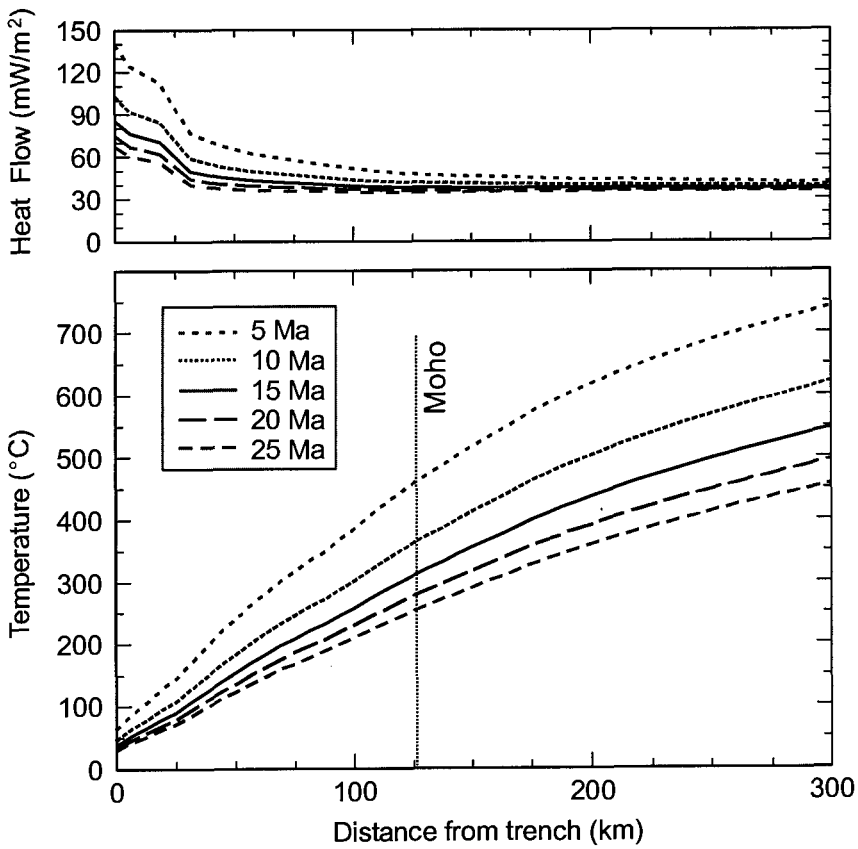

Figure 2.7. Heat flow (top) and temperatures along the top of the subducting plate (bottom) for models with subducting plate ages of 5, 10, 15, 20, and 25 Ma.

over the age of the plate (13.3 Ma). Due to the low thermal conductivity of the sediments, the sediment cover acts to insulate the plate. The temperatures at the top of the subducting plate increase as the sediment thickness increases (**Figure 2.8**). Sediment cover has the largest effect (>50°C) for thicknesses greater than 1 km. The thin 200 m sediment cover offshore Mexico has only a small effect on plate surface temperatures.

Subducting plate geometry

The effects of plate geometry were examined by varying the plate dip by ±20% of the preferred Michoacan geometry (**Figure 2.9**). With the shallower plate dip (-20%), forearc heat flow is slightly (<5 mW/m^2) higher than that for the preferred geometry. At a given distance from the trench, subduction thrust fault temperatures are lower for plates with a shallower dip, as these plates reach this distance in a shorter amount of time and thus experience less heating from the surrounding material. Conversely, at a given depth,

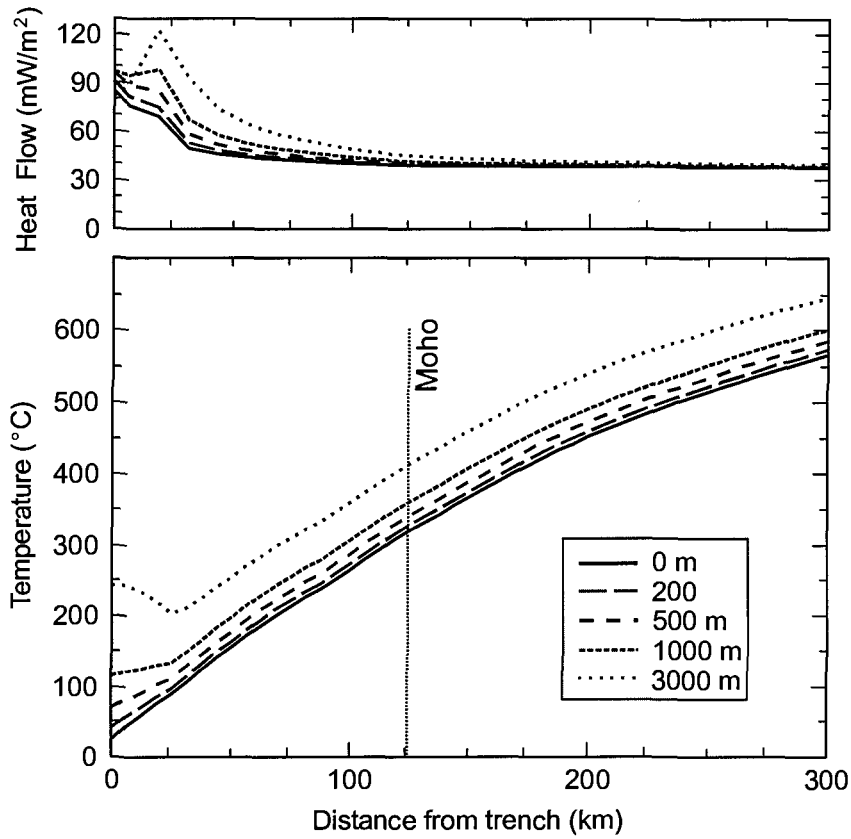

Figure 2.8. Effect of incoming sediment thickness on the heat flow (top) and temperatures along the top of the subducting plate (bottom). Sediment thicknesses of 0, 200, 500, 1000, and 3000 m are used. For each thickness, the sedimentation rate is assumed to be constant over the age of the plate (13.3 Ma).

plates with a shallower plate dip are slightly hotter, due to the longer time taken to reach this depth. For variations in plate dip of 20%, these effects are very small. At the continental Moho intersection (40 km depth), the subduction thrust temperature varies by less than 15°C for the range of plate profiles examined.

Continental crust thickness

The thickness of the continental crust has a direct effect on the location of the intersection of the thrust fault with the continental Moho, but has a negligible effect on the thermal structure of the forearc. For a crustal thickness between 30 and 50 km, the variation in shallow (<40 km) thrust fault temperature is less than 5°C, and forearc heat flow varies by less than 2 mW/m^2. Slightly higher backarc heat flow is observed for a thicker crust, due to the higher radiogenic heat production assumed in the deep crust compared to the upper mantle.

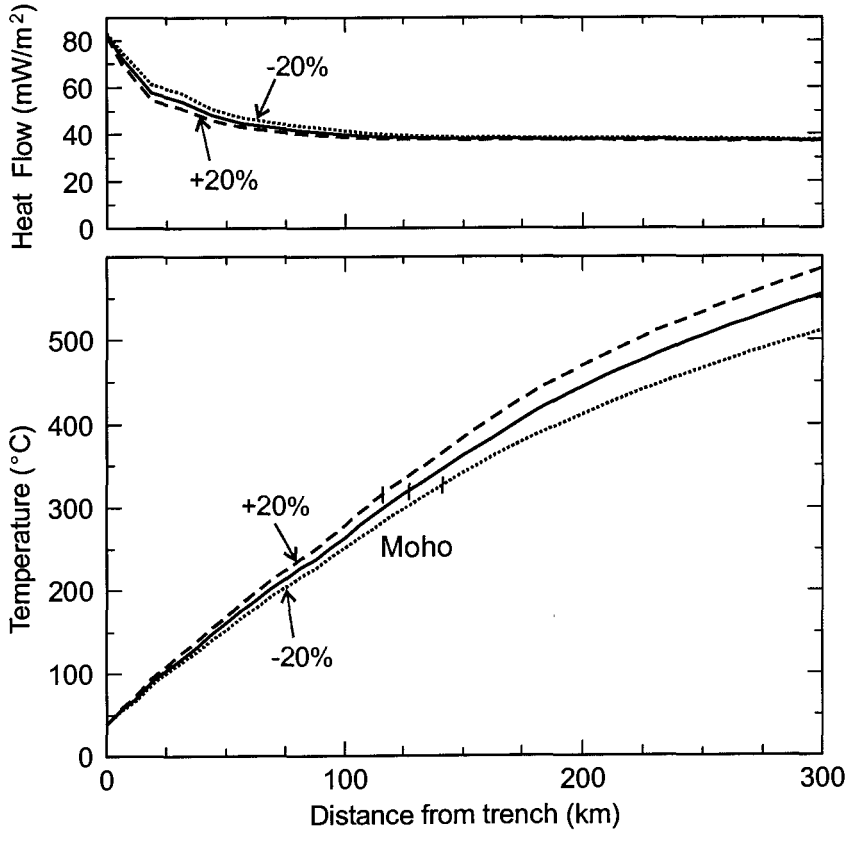

Figure 2.9. Heat flow (top) and temperatures along the top of the subducting plate (bottom) for variations in the dip of the subducting plate between -20% and +20% of the best-fit Michoacan plate geometry. The intersection of the thrust fault with the Moho (40 km depth) for each plate profile is indicated on the lower plot.

Convergence rate

The rate at which the oceanic plate subducts has a significant effect on the forearc thermal structure and the temperature of the subducting plate. Convergence rates between 2 and 8 cm/yr were tested (**Figure 2.10**). A higher convergence rate produces a cooler subducting plate surface and lower forearc heat flow, as cool material from the surface is being injected into the Earth at a greater rate. For Mexico, convergence rates are 3.8-6.1 cm/yr. An uncertainty of 0.5 cm/yr for each profile results in thrust fault temperature variations of ~10°C at the Moho intersection.

Thermal parameters

The thermal conductivity of the continental crust can vary with both composition and temperature [e.g., *Clauser and Huenges*, 1995]. Most crustal rocks exhibit conductivities between 2.0 and 3.0 W m^{-1} K^{-1}. In the models, a constant conductivity of

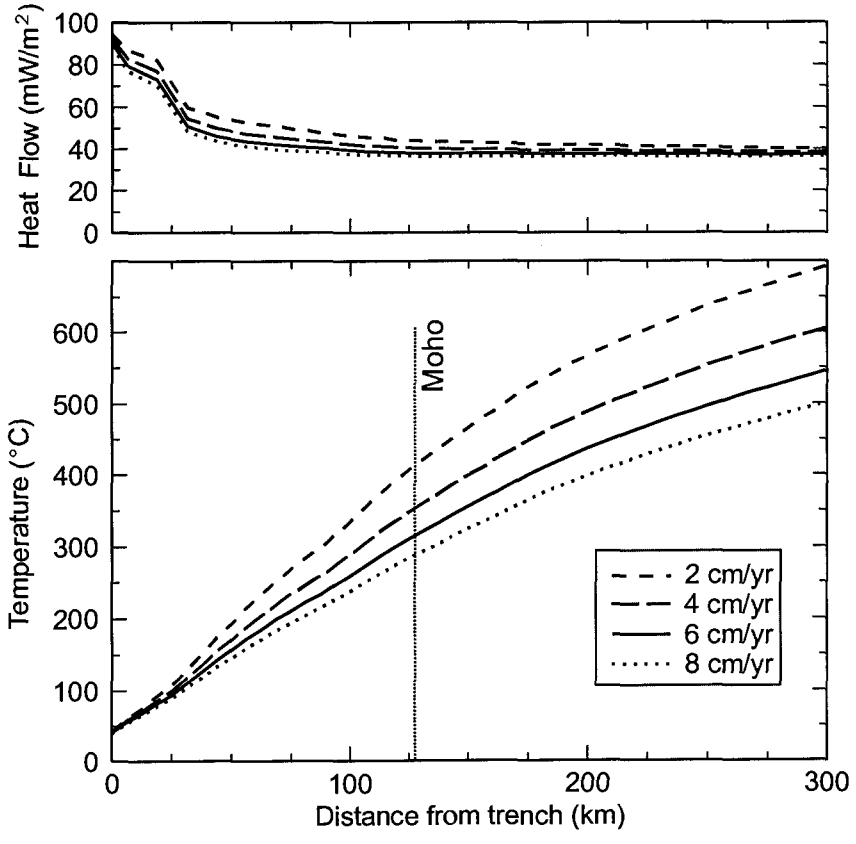

Figure 2.10. The effect of subduction rate on the heat flow (top) and temperatures along the top of the subducting plate (bottom).

2.5 W m^{-1} K^{-1} was assumed. The reasonable variation of 0.5 W m^{-1} K^{-1} in the thermal conductivity results in a change in the thrust fault temperature of less than 15 °C at 40 km depth and heat flow changes of less than 6 mW/m^2 (**Figure 2.11**). Higher crustal conductivities lead to lower thrust fault temperatures but higher surface heat flow. Radiogenic heat production within the continental crust is fairly uncertain, especially at depth, and may vary significantly over short distances. Variations in continental heat generation by a factor of two significantly affect the surface heat flow, but only have a small effect on the underlying thrust fault temperatures (**Figure 2.11**). Variations in the thermal conductivity and radiogenic heat production of the offshore sediments were also examined. Due to the small volume and limited spatial extent of the sediments, the thermal parameters have only a small effect on the forearc temperatures.

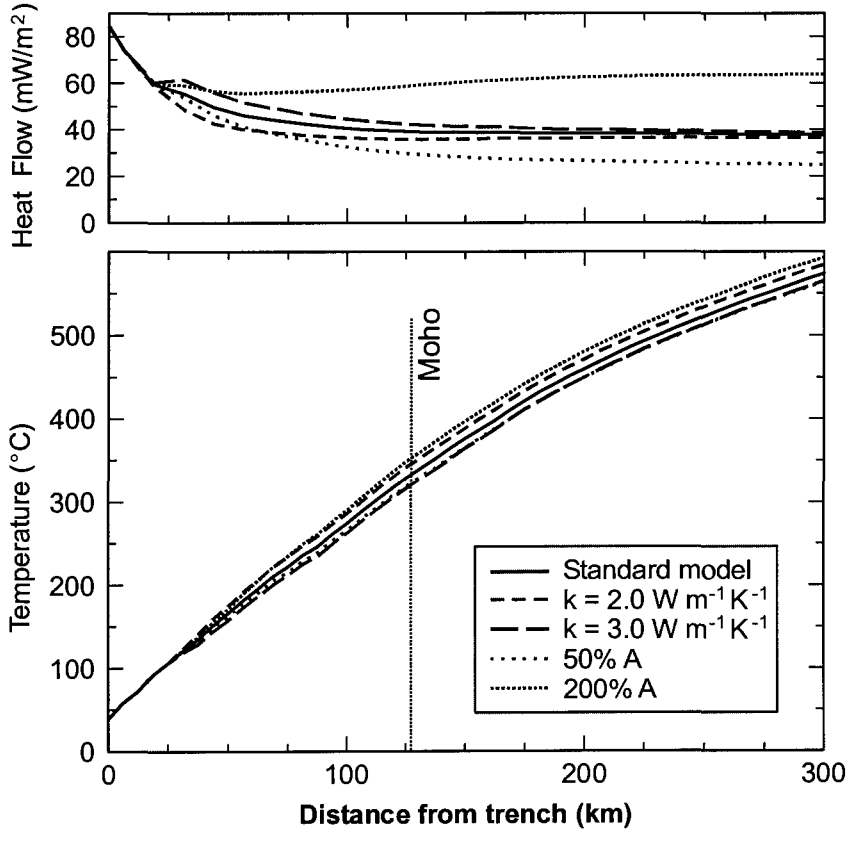

Figure 2.11. The effect of the thermal parameters of the continental crust (thermal conductivity and radiogenic heat production) on the heat flow (top) and temperatures along the top of the subducting plate (bottom). The standard model uses a thermal conductivity of 2.5 W m^{-1} K^{-1} and radiogenic heat production of 1.3 μW/m^3 in the upper 15 km of the crust and 0.27 μW/m^3 in the lower 25 km.

Uncertainties for Mexico thermal models

As shown in the parameter sensitivity tests, the thermal structure of the forearc is most sensitive to the age of the oceanic plate, the incoming sediment thickness, the convergence rate and the plate geometry. For western Mexico, the first three parameters are relatively well-constrained. The subducting plate profile is fairly uncertain, particularly at depths greater than 30-40 km. However, a variation in plate dip of more than 20% is required to produce significant changes in the temperature of the top of the oceanic plate. This is much greater than the estimated uncertainty of 10% in the shallow plate profile. While the values of the thermal parameters (thermal conductivity and radioactive heat production) are relatively uncertain for the continental crust, reasonable variations in these parameters have little effect on the temperature of the plate interface. Uncertainties in mantle wedge flow dynamics and continental crust thickness have a negligible effect on forearc temperatures.

Based on the estimated uncertainties of each of the above parameters for Mexico and their effect on the thrust fault temperatures, the uncertainty in the position of the 100 and 150°C isotherms along the thrust fault is 15 km. The uncertainty in the location of the 350°C and 450°C isotherms is 20 km. Two additional parameters that have a significant effect on thrust fault temperatures are frictional heating and hydrothermal circulation in the incoming oceanic crust. These are discussed in the next two sections.

2.3.8 Frictional heating

The temperature of the thrust fault may be affected by frictional heating [e.g., *van den Beukel and Wortel*, 1987; *Molnar and England*, 1990; *Dimitru*, 1991]. Following the procedure of *van den Beukel and Wortel* [1987] and *Wang et al.* [1995a, b], frictional heating is incorporated into the thermal models by dividing the fault interface into two zones: a shallow region of brittle frictional sliding and a deeper region of ductile shear. In the brittle region, the shear stress along the fault is given by Byerlee's law of friction [*Byerlee*, 1978]. The shear stress (τ) increases with depth, due to the increase in normal stress, approximated by the load of the overlying rock column:

$$\tau = 0.85\,\rho g z(1-\lambda) \tag{2.3}$$

where is the ρ average density of the continental crust (taken to be 2750 kg/m^3), g is the gravitational acceleration, z is the depth along the fault, and λ is the pore pressure ratio, defined as $(p_f-p_d)/(p_l-p_d)$, where p_f, p_l, and p_d are the pore fluid pressure, lithostatic pressure and pressure at the Earth's surface, respectively. The pore pressure ratio is assumed to be constant with depth. A decrease in the pore pressure ratio corresponds to an increase in shear stress (and frictional heating).

In the deeper plastic regime, the magnitude of shear heating is related to the viscous shear stress (τ) along the fault, determined from the strain rate ($\dot{\varepsilon}$) for a power law rheology:

$$\dot{\varepsilon} = A(2\tau)^n \exp(-Q/RT) \tag{2.4}$$

where, A, Q, and n are experimentally-determined parameters for a given rock type, and R is the universal gas constant. In the models, the rheological parameters for diabase are used [*Caristan*, 1982]. In the plastic regime, the heat generated from shear heating is non-linear, due to the dependence of shear stress on the temperature. The magnitude of shear stress decreases with depth, due to increasing temperature. Therefore, the maximum shear stress is found at the transition between brittle and ductile behaviour. This transition is temperature-dependent, and thus, an iterative approach is used in the modelling, following *Wang et al.* [1995b].

In the models, frictional heating is incorporated as a volumetric heat source (Q_H in **Equations 2.1 and 2.2**). For the brittle regime, the amount of heat generated per unit fault area is:

$$Q_f = \tau v \tag{2.5}$$

where v is the sliding velocity. In the ductile regime, the amount of heat generated per unit volume is:

$$Q_d = \tau\dot{\varepsilon} \tag{2.6}$$

In the numerical implementation, the brittle frictional heat is converted into a volumetric heat source by assuming that the shear stress is distributed within a thin, 500 m layer above the subduction thrust fault. The volumetric heat production for this layer can be

calculated using **Equation 2.6**, with $\dot{\varepsilon} = v/w$, where v is the subduction velocity and w is the layer thickness (500 m).

The amount of frictional heating along the thrust fault is controlled by varying the pore pressure ratio. **Figure 2.12** illustrates the effect of frictional heating for pore pressure ratios of 0.9 to 1.0 (no heating). Two different maximum depths for frictional heating were tested: heating to the Moho (40 km depth) or heating to the seaward limit of mantle wedge flow (~90 km depth along plate surface). At depths shallower than 40 km, the temperatures along the thrust fault are similar for each approach. Frictional heating has a significant effect on thrust fault temperatures, with an increase in the deep fault temperatures by over 100°C at 40 km depth for models with a pore pressure ratio of 0.9. Over the reasonable range of frictional heating, surface heat flow varies by only 10 mW/m^2, making it difficult to constrain the magnitude of frictional heating from surface heat flow measurements.

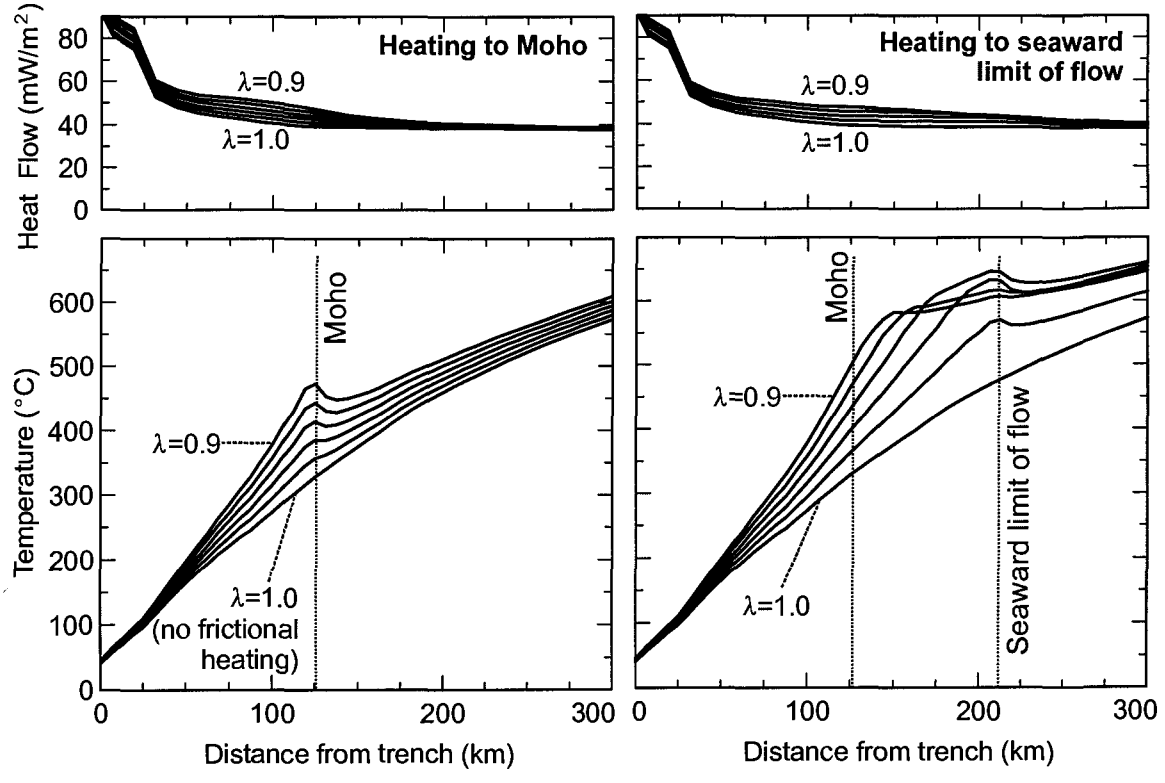

Figure 2.12. The heat flow (top) and temperatures along the top of the subducting plate (bottom) for models that include frictional heating to the Moho (left column) and to the seaward limit of flow (right column). The amount of frictional heating is controlled by the pore pressure ratio (λ). Pore pressure ratios of 0.90, 0.92, 0.94, 0.96, 0.98, and 1.0 (no heating) were tested. Mantle wedge flow was not included in the models.

In the models below, the maximum depth of frictional heating is 40 km (the Moho intersection). Below this, the fault interface is inferred to be in contact with the serpentinized mantle wedge, which is believed to be too weak to allow significant frictional heating. As the incoming oceanic crust at the Mexico subduction zone is cool for all four regions, the brittle-ductile transition along the subduction thrust fault occurs at depths greater than 30 km, and frictional heating may not be negligible. **Figure 2.13** illustrates the effects of frictional heating on the temperatures of the top of the subducting plate for pore pressure ratios of 0.9, 0.94 and 1.0 for each profile. The large peak in the temperature profile near the Moho intersection is a result of the termination of frictional heating at this depth.

Decreasing the pore pressure ratio from 1.0 to 0.9 corresponds to an increase in average shear stress along the fault from 0 to 31 MPa, or an effective coefficient of friction (defined by the ratio of the shear to normal stresses along the fault) from 0 to 0.068. These are within the ranges determined in previous studies of subduction thrust faults [e.g., *van den Beukel and Wortel*, 1987; *Wang et al.*, 1995a, b; *Wang and He*, 1999]. Observations of low heat flow over most forearcs suggest that frictional heating along the thrust fault is relatively low [e.g., *Wang et al.*, 1995b; *Peacock*, 1996; *von Herzen et al.*, 2001]. Low frictional coupling is also implied by stress data from the Cascadia and Nankai (SW Japan) forearcs [*Wang et al.*, 1995b; *Wang and He*, 1999]. For Cascadia, focal mechanisms from crustal earthquakes [*Wang et al.*, 1995b and references therein] indicate that the margin-normal component of stress is similar in magnitude to the lithostatic (vertical) stress, suggesting a very weak, low friction fault.

The effect of frictional heating at shallow depths (< 20 km) is quite small. With a pore pressure ratio of 0.9, the 100°C and 150°C isotherms are shifted a maximum of 10 km seaward from models without frictional heating. The inclusion of the maximum amount of frictional heating results in a seaward shift of the 350°C isotherm of 23 km (Jalisco) to 89 km (Oaxaca) from its position in models with no frictional heating. The position of the 450°C isotherm is shifted seaward by 30 km (Jalisco) to 170 km (Oaxaca).

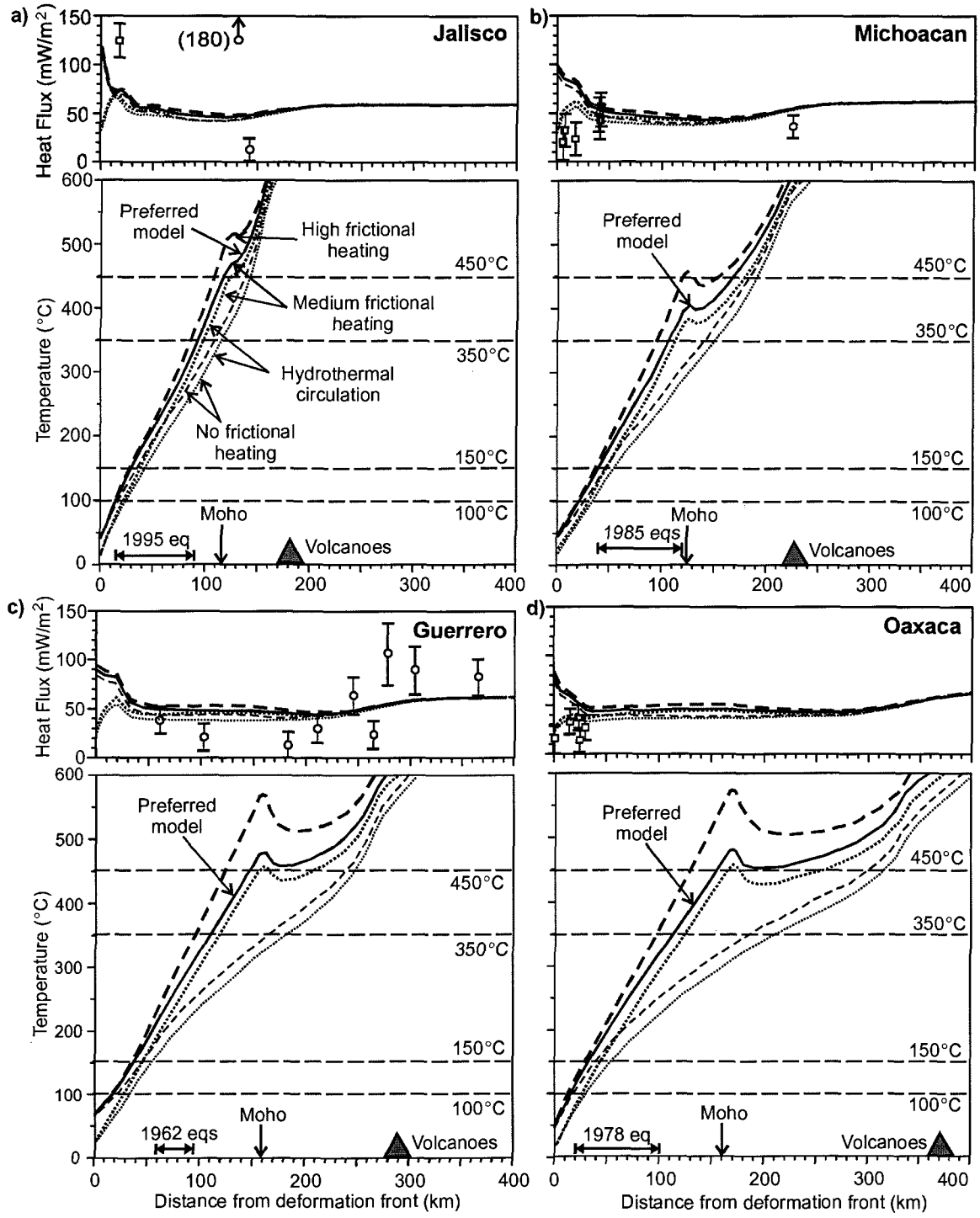

Figure 2.13. Surface heat flow (top) and temperatures along the top of the subducting plate for varying amounts of frictional heating. The dashed line indicates no frictional heating, the solid line is medium frictional heating (λ of 0.94) and the thick dashed line is high frictional heating (λ of 0.90). The peak in the temperature profile near the Moho intersection occurs because frictional heating was only included to this depth. The dotted lines indicate models with hydrothermal circulation within the upper 3 km of the oceanic plate (thin dotted line is a model with no frictional heating; thicker dotted line is a model with medium frictional heating). The rupture widths of past megathrust earthquakes are shown for each profile. The Guerrero profile uses the Guerrero B geometry. Heat flow data are from *Ziagos et al.* [1985] (circles) and *Prol-Ledesma et al.* [1989] (squares).

Frictional heating has the largest effect for profiles with a high convergence rate and shallow plate dip (e.g., the Oaxaca profile). At 40 km depth, the thrust fault along the Oaxaca profile is 200°C warmer with the addition of frictional heating, compared to an increase of ~120°C for Jalisco. The amount of frictional heating provides the major uncertainty in the models, particularly for the deep (> 20 km) temperatures.

2.3.9 Hydrothermal circulation in the incoming oceanic crust

An additional uncertainty in the shallow thrust temperatures comes from possible hydrothermal circulation within the upper oceanic plate. Marine heat flow studies have shown that the heat flow near the trench offshore Mexico is lower than that predicted for a simple conductively cooling oceanic plate overlain by sediments (**Figure 2.13**). This suggests that hydrothermal circulation in the upper oceanic crust may occur in this region. This mechanism has been used to explain the anomalously low heat flow values observed offshore Costa Rica [*Langseth and Silver*, 1996; *Harris and Wang*, 2002].

A "cool crust" thermal model was developed to approximate the effects of hydrothermal circulation, using the method of *Langseth and Silver* [1996] and *Harris and Wang* [2002]. In the model, the oceanic geotherm contains a 3 km thick convectively cooled layer that produces a surface heat flow of 30 mW/m^2, consistent with the observations (**Figure 2.3**). This model examines the maximum thermal effects on the shallow thrust fault and may not accurately model the deep temperatures. The effect on the surface heat flow is confined to the regions near the deformation front (**Figure 2.13**). At distances greater than 100 km, the resulting surface heat flow is indistinguishable from the original models. With hydrothermal cooling to a depth of 3 km, the location of the 100°C and 150°C isotherms are shifted approximately 10 km landward. For hydrothermal cooling to depths less than 3 km, the landward shift is less.

2.4 Surface Heat Flow Observations

As shown above, a major uncertainty in the thermal models is the amount of frictional heating, especially at depths greater than 20 km. Hydrothermal circulation has a large effect on the shallow thrust temperatures. An independent constraint on the

thermal models comes from surface heat flow observations (**Figures 2.13**). Low values of heat flow observed near the trench on the Michoacan and Oaxaca profiles are better fit by models containing the effects of ocean crust hydrothermal circulation. For all models, the forearc has a modelled heat flow of 40-50 mW/m^2, which is slightly larger than most of the borehole heat flow measurements by *Ziagos et al.* [1985]. The surface heat flow is highly dependent on the amount of radioactive heat generation in the continental crust. By reducing the crustal heat generation, the modelled values will better fit the observations, with little impact on the thrust fault temperatures (e.g., **Figure 2.11**).

However, the observed heat flow values have large uncertainties. The boreholes used were very shallow (many were less than 200 m depth). Few thermal conductivity measurements were taken for each hole, and steep topography at many sites required a terrain correction to the data, further increasing the uncertainty. In addition, the complex geological setting of Mexico results in small-scale lateral variations in surface heat flow due to local geological or hydrogeological effects [*Prol-Ledesma*, 1991]. For example, in the forearc near the Jalisco profile, heat flow values of 13 and 180 mW/m^2 were recorded within 200 km of each other [*Ziagos et al.*, 1985]. On the basis of these factors, an average uncertainty of 20% was assigned to each heat flow observation.

The introduction of a reasonable amount of frictional heating results in a surface heat flow increase of less than 10 mW/m^2 (**Figures 2.12, 2.13**). Given the present state of forearc heat flow data and uncertain radioactive heat generation, the existing data cannot constrain the magnitude of frictional heating. The observations suggest that frictional heating must be small but do not exclude it. Future continental heat flow and radioactive heat generation studies in Mexico to constrain thrust temperatures should focus on the continental shelf and coastal areas, as these regions are most sensitive to frictional heating along the fault.

With the simple model of corner flow within the mantle wedge, an increase in heat flow is observed near the volcanic arc (**Figures 2.6, 2.13**). This is consistent with the increase in heat flow documented by *Ziagos et al.* [1985] over the Trans-Mexico Volcanic Belt. However, the observed sharp increase from the forearc to the backarc is not reproduced in the models. This abrupt transition is likely due to near-surface

processes associated with volcanism, such as a magma emplacement, which are not included in the models. The modelled backarc heat flow is consistently lower than the observed values. Heat flow in the backarc is the result of a number of complex processes, including mantle wedge circulation and magma migration, as discussed in later chapters. The effects of such processes on the seismogenic zone (more than 150 km away) are small.

2.5 Past Megathrust Earthquakes

The thermal models can be compared to the rupture widths of past megathrust earthquakes to investigate possible thermal controls on the seismogenic zone. Below, recent well-studied earthquakes near each profile are described. Several types of observations are used to constrain the rupture area. The updip and downdip limits of rupture can be determined through waveform modelling of megathrust earthquake data, as well as the distribution of aftershocks. On-land geodetic measurements (e.g., GPS data) taken before and after the earthquake can be used to delineate the downdip limit of rupture. The updip limit of rupture can be better constrained through modelling of the tsunami wave generated by the earthquake.

2.5.1 Jalisco

On June 3 and 18, 1932, two earthquakes occurred north of the proposed Rivera-Cocos Plate boundary (M_S 8.2 and 7.8, respectively). Aftershocks from these earthquakes have a seaward limit 10-15 km from the trench, and extend to 90-95 km from the trench [*Singh et al.*, 1985]. In 1995, an M_W 8.0 earthquake occurred in the southern part of this region (**Figure 2.14a**). The majority of aftershocks for this earthquake were located between 20 and 100 km from the trench [*Pacheco et al.*, 1997]. As the aftershocks were located using a local station array and a local velocity model, the location uncertainty is estimated to be ±5 km. The aftershock area is in good agreement with the results of waveform modelling that determined a nearly rectangular rupture area, oriented parallel to the Middle America trench, with a margin-normal width of 90 km [*Mendoza and Hartzell*, 1999].

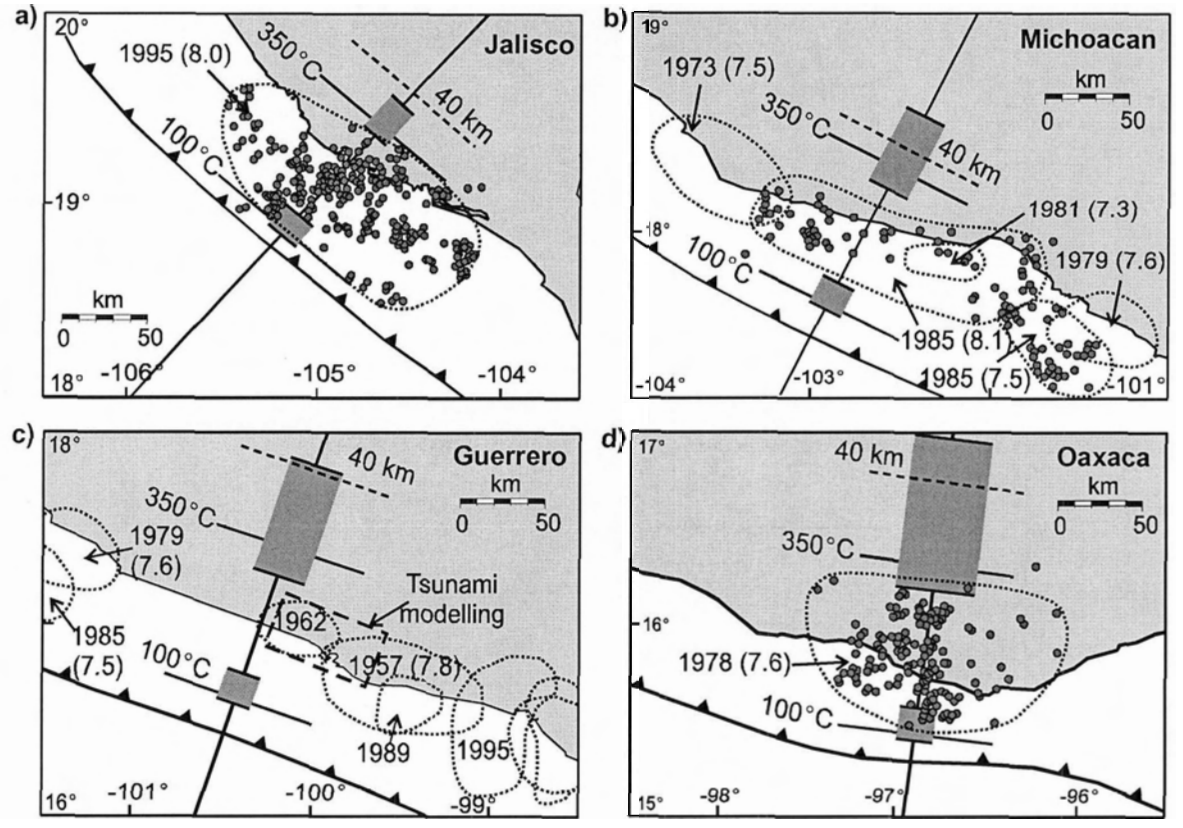

Figure 2.14. Comparison of the aftershock areas of recent megathrust earthquakes with the thermal model results for each region. The year of each earthquake is given (with the magnitude in brackets). (a) The 11-day aftershocks for the 1995 Jalisco earthquake [*Pacheco et al.*, 1997]; (b) 11-day aftershocks for the 1985 Michoacan earthquakes [*UNAM Seismology Group*, 1986], also shown are rupture areas and magnitudes of past earthquakes in this region [after *Kostoglodov and Pacheco*, 1999]; (c) 1962 earthquakes rupture limits from tsunami modelling [*Ortiz et al.*, 2000a] and from the poorly constrained aftershock distribution [*Kostoglodov and Pacheco*, 1999]; and (d) 33-day aftershocks for the 1978 Oaxaca earthquake [*Stewart et al.*, 1981]. The shaded bars represent the range in the position of the 100 and 350° C isotherms, based on the models shown in Figure 2.13. The solid lines indicates the positions of these isotherms for the preferred model. The dashed line shows the Moho intersection at 40 km depth.

Geodetic observations provide additional constraints on the updip and downdip limits of rupture. Modelling of tsunami records from two local tide gauges indicates that the maximum seafloor uplift was located 24 ± 5 km from the trench [*Ortiz et al.*, 2000b]. The downdip limit was constrained through GPS observations from a dense GPS network located directly onshore. Both *Melbourne et al.* [1997] and *Hutton et al.* [2001] were able to fit GPS observations with heterogeneous coseismic slip along the thrust fault to a depth of ~23 km using an elastic model. This corresponds to a downdip limit located 90 km from the trench.

Based primarily on the relocated aftershocks for the 1995 earthquake [*Pacheco et al.*, 1997], the seismic rupture width in the Jalisco region is taken to be 75 km, located between 15 and 90 km from the trench (**Figure 2.14a**). Based on the good agreement among the various types of observations, uncertainties in this width are small (<5 km).

2.5.2 Michoacan

On September 19, 1985, an M_W 8.1 earthquake occurred on the Michoacan segment of the Cocos-North America interface (**Figure 2.14b**). This was followed two days later by an M_W 7.7 earthquake to the southeast. The majority of aftershocks for both events were located between 40 and 120 km from the trench [*UNAM Seismology Group*, 1986; *Stolte et al.*, 1986]. The width of the aftershock area is slightly narrower in the northwest part of the September 19 rupture area, with the landward limit of the aftershocks ~80 km from the trench. Waveform inversion of the September 19 earthquake indicates that slip occurred between depths of 6 and 39 km [*Mendoza and Hartzell*, 1989], in good agreement with the aftershock rupture area. The locations of the updip and downdip limits of rupture from both types of studies are relatively well-constrained due to a close station spacing and the use of a locally-derived velocity model. There are no published tsunami models constraining the updip limit of rupture of the September 19 earthquake. However, distant stations recorded a tsunami with a very low amplitude, which suggests that rupture did not extend all the way to the seafloor [*UNAM Seismology Group*, 1986]. Based on the above studies, seismic rupture in the Michoacan region appears to have occurred between 40 and 120 km from the trench (**Figure 2.14b**).

2.5.3 Guerrero

The region northwest of the Guerrero profile is referred to as the Guerrero Gap as there have been no large megathrust earthquakes for at least 90 years [e.g., *Ortiz et al.*, 2000a]. However, southeast of the profile, there were two intermediate magnitude thrust earthquakes in 1962 within eight days of each other, with magnitudes of 7.1 and 7.0. Southeast of these earthquakes, there was a magnitude 7.8 earthquake in 1957. Although the rupture area of these three earthquakes has been defined using the aftershock

distribution (**Figure 2.14c**), this area has large uncertainties due to a poor regional station distribution [*Ortiz et al.*, 2000a]. Modelling of the tsunamis generated by these earthquakes has provided stronger constraints on the rupture area. The modelled updip limit of all three earthquakes is located at 60 ± 10 from the trench [*Ortiz et al.*, 2000a]. The width of the 1962 rupture area is 35 km, while the width of the 1957 earthquake may be as much as 70 km. Uncertainties in the downdip rupture limit are large, as this limit is not constrained by tsunami observations.

2.5.4 Oaxaca

The Oaxaca profile passes through the rupture area of the 1978 M_w 7.6 earthquake (**Figure 2.14d**). The one-month aftershocks for this earthquake extend from 20 to 100 km from the trench [*Singh et al.*, 1980; *Stewart et al.*, 1981]. As the aftershocks were located relative to the mainshock, the relative positions of each earthquake are very well-constrained. In addition, the aftershocks extend well under the coast and were recorded using a number of local portable seismic stations. Thus, the uncertainties in the absolute lateral location of the group of aftershocks are likely less than ±5 km (J. Cassidy, personal communication, 2002).

2.6 Mexico Seismogenic Zone

2.6.1 Comparison of rupture areas with the Moho intersection

The observed rupture widths for megathrust earthquakes near each profile are shown on **Figure 2.14**. The intersection of the continental Moho with the subduction fault may mark the maximum downdip limit to the seismogenic zone. As discussed above, the continental crustal thickness is not well-resolved for the Mexico margin, with estimates ranging from 33 to 50 km. The Moho intersection with the subduction fault was taken to occur at a depth of 40 km. This corresponds to a lateral distance of 117 km between the Moho intersection and the trench on the Jalisco profile, increasing to 160 km on the Oaxaca profile, due to the shallower plate dip in the southeast. If the crust is as thin as 33 km, the Moho intersection will be shifted seaward by 15 km (Jalisco) to 25 km (Oaxaca). For a Moho at 50 km depth, the intersection with the fault will be shifted

landward by 15 to 35 km. Thus, for all Moho depths, the observed earthquake rupture areas in Jalisco, Guerrero and Oaxaca are updip of the intersection of the continental Moho with the thrust fault. In the middle of the 1985 Michoacan earthquake rupture area, observations suggest that rupture may have extended to the Moho. However, to the northwest and southeast, rupture was much narrower and significantly updip of the Moho intersection.

2.6.2 Comparison of rupture areas with the thermal models

A downdip change in properties along the thrust fault appears to limit the downdip extent of rupture to depths shallower than the Moho intersection for the Mexico subduction zone. The goal of this study is to determine if the observed rupture limits are consistent with the hypothesis that temperature provides the primary control on the sliding behaviour of the subduction thrust fault. As discussed in **Section 2.2**, the 100 and 350°C isotherms are taken to define the thermal limits on the seismogenic zone of the thrust fault. Assuming that the proposed thermal limits are correct, it is necessary to introduce a small amount of frictional heating to the thermal models of Mexico to be consistent with the observed shallow downdip rupture limit. For models with no frictional heating, the location of the 350°C isotherm is landward of the fault intersection with the Moho and deeper than the observed rupture limit (**Figure 2.13**). If the alternative hypothesis that the Moho intersection provides the maximum downdip limit of the seismogenic zone is correct, the seismogenic zone width would be 100 to 145 km along the Mexico margin, significantly wider than the observed rupture widths.

Thermal models that include a small amount of frictional heating, using a pore pressure ratio of 0.94, provide the best agreement with the observed earthquake rupture areas along the entire margin. This corresponds to an average shear stress of about 15 MPa, or an effective coefficient of friction of 0.041, consistent with estimates for other subduction faults [e.g., *van den Beukel and Wortel*, 1987; *Wang et al.*, 1995b; *Wang and He*, 1999]. It is also consistent with a previous thermal model for Mexico that concludes that frictional heating must be fairly small at shallow depths [*Ziagos et al.*, 1985]. Most subduction thrust faults are believed to be weak. *Wang et al.* [1995a, b] assumed

negligible frictional heating in Cascadia and SW Japan thermal models. For these subduction zones, a pore pressure ratio of 0.94 leads to an average shear stress of less than 7 MPa because the brittle part of the fault is confined to depths less than 20 km. The thermal effect of this small shear stress is well within model uncertainties. Frictional heating was not included in the thermal models of the South Alaska and Chile subduction zones [*Oleskevich et al.*, 1999]. For South Alaska and Chile, even with frictional heating, the position of the 350°C isotherm is much deeper than the Moho intersection with the thrust fault, and therefore does not change their conclusion that the downdip limit of megathrust earthquakes in these regions may be limited by the Moho intersection.

Figure 2.15 shows the thermal models for each profile, using a pore pressure ratio of 0.94. The temperature along the top of the oceanic plate at depths less than 20 km is similar for all profiles. The intersection of the 100°C isotherm is 15 to 20 km landward of the trench. The intersection of the 350°C isotherm is 92 km from the trench on the Jalisco profile. It is further landward on the other profiles (~110 km). This is due to the younger age of subducting crust, the slower convergence rate, and the steeper plate dip of the Jalisco profile. The downdip transition zone is inferred to extend to the Moho intersection for all profiles. The Moho intersection coincides with a temperature of ~450°C along the Jalisco, Guerrero, and Oaxaca profiles. The temperature at the Moho intersection is ~380°C along the Michoacan profile, and thus the Moho intersection may provide the downdip limit for the transition zone in this area.

Using the proposed thermal limits on the seismogenic zone, the above thermal models give a seismogenic zone downdip width of 80 to 100 km along the margin (**Figure 2.16**). There is a very good agreement between the well-constrained observed downdip limit of rupture and the proposed downdip temperature limit of 350°C in the Jalisco and Oaxaca regions. The agreement is poorer in the Michoacan and Guerrero regions. The majority of seismic rupture of the 1985 Michoacan earthquakes occurred further updip. The downdip limit of rupture in the Guerrero region is especially poorly constrained, but aftershock observations suggest that it was also significantly updip of the proposed thermal limit. The 1962 and 1957 earthquakes in the Guerrero region were

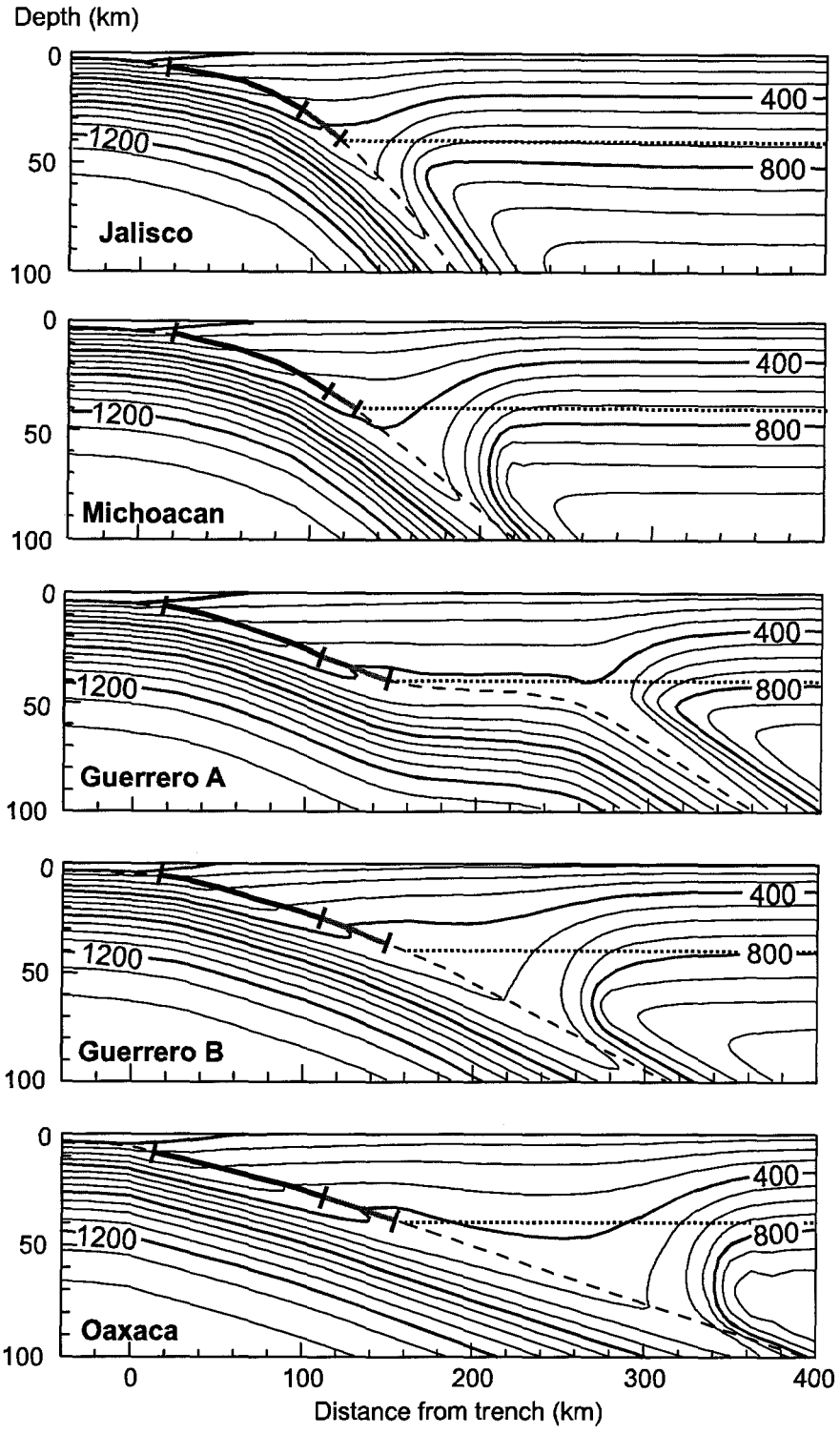

Figure 2.15. Preferred thermal models for each profile (100°C isotherms). These models include frictional heating (λ of 0.94). The dark line indicates the proposed thermally-limited seismogenic zone; the grey line is the transition zone. The dashed line is the top of the subducting oceanic plate, and the dotted line is the continental Moho.

quite small. As there are no large-scale differences in the factors controlling the thermal structure between the four regions, it is possible that these earthquakes did not rupture the entire downdip width of the proposed thermally-limited seismogenic zone.

The shallow fault temperatures are relatively unaffected by frictional heating, and thus, in all models, the proposed updip limit of 100°C is in good agreement with the observed seaward limit of rupture for the 1995 Jalisco and 1978 Oaxaca earthquakes. The updip limit of rupture of the 1985 Michoacan earthquakes corresponds to a temperature of ~150°C. In the Guerrero region, the updip rupture limit of the 1962 earthquakes, as determined through tsunami modelling, is at a temperature of over 200°C. With the inclusion of hydrothermal cooling, the fault temperatures are decreased, and the observed updip rupture limits are more compatible with the proposed thermal

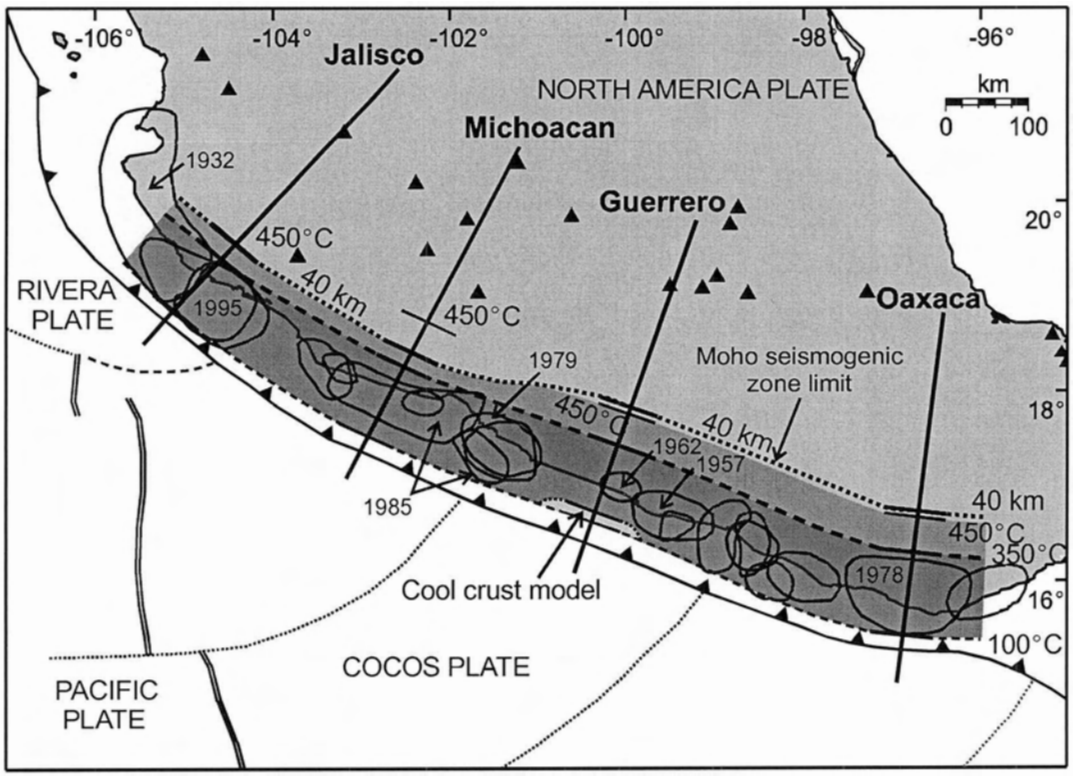

Figure 2.16. Map of the proposed thermally-defined seismogenic zone (darker shading). With no frictional heating, the seismogenic zone may be limited by the intersection of the thrust fault with the continental Moho (40 km depth). Also shown are the rupture areas of past megathrust earthquakes [modified from *Kostoglodov and Pacheco*, 1999]. Earthquakes discussed in the text are labeled. The light region at the seaward end of the Guerrero profile indicates the landward shift in the 100°C isotherm if hydrothermal circulation in the oceanic plate is included.

limit (**Figure 2.16**). The good agreement of the observed updip limit of rupture for most of the megathrust earthquakes with the proposed thermal limit of 100-150°C suggests that hydrothermal cooling is probably a local effect.

2.7 Conclusions

Two-dimensional, steady-state thermal models have been developed for four cross-sections through the Mexico subduction zone. The primary factors controlling forearc temperatures are the convergence rate, the subducting plate geometry, and the thermal structure of the subducting plate, given by its age and sediment cover. Despite the young age of the subducting Rivera and Cocos Plates, they are much cooler than oceanic plates in other warm slab subduction zones, such as Cascadia and SW Japan. This is primarily due to only a thin cover of insulating sediments on the oceanic plates. The thin sediment cover may also allow hydrothermal circulation in the upper oceanic crust, resulting in an even cooler plate surface.

Due to the cool subducting plate, the overall thermal structure of the Mexico subduction zone is intermediate between subduction zones with young, hot oceanic plates (e.g., Cascadia and SW Japan) and those with older oceanic plates (e.g., South Alaska and Chile). The cool subducting plate surface means that the brittle part of the subducting plate surface extends to depths of 30 to 40 km. When brittle friction occurs at depths greater than 20 km, even a very weak fault may produce significant frictional heating. The results of this study show that a small amount of frictional heating can have a large effect on the thrust temperatures. The deep (30-40 km) part of the thrust fault can be increased by over 100°C with the inclusion of only a small amount of frictional heating. The effect of frictional heating is largest for areas that have a shallowly dipping plate and a high convergence rate.

For the Mexico subduction zone, observations indicate that the megathrust earthquake rupture is confined to depths less than 30 km, updip of the intersection of the thrust fault with the continental Moho. If the downdip limit of rupture is controlled by a temperature of 350°C, a small amount of frictional heating must be included in the thermal models. The models that best fit the observed rupture along the entire margin use

an average shear stress of 15 MPa, consistent with the conclusion of past studies of a weak subduction fault and low frictional heating. The observed updip limit of coseismic rupture, although poorly constrained, is in agreement with a thrust temperature of ~100°C for much of the margin. For all models, the proposed downdip thermal limit of the seismogenic zone occurs landward of the coast, with a transition zone that extends up to 100 km inland. This is important for seismic hazard studies for Mexico, as the seismic source zone could underlie populated areas, if there is significant ground shaking produced by slip in the transition zone.

CHAPTER 3

Backarc Thermal Structure I – The Cascadia Subduction Zone

3.1 Introduction

The thermal structure of the forearc region is primarily controlled by the subducting plate (see **Chapter 2**). As a result, forearcs are generally quite cool, as reflected by the low surface heat flow (30 to 50 mW/m^2) observed over nearly all forearcs (e.g., data shown below and in **Chapters 2 and 4**). Heat flow and other thermal indicators suggest a rapid change in the thermal structure that approximately coincides with the location of the volcanic arc. Below the arc and well into the backarc regions, mantle temperatures are inferred to be extremely hot (>1200°C at 50-60 km depth).

The remainder of this thesis study is devoted to the thermal regime of the mantle wedge and backarc. This chapter begins with a summary of geochemical constraints on the temperatures required for arc magmatism. Following this, the thermal structure of the mantle wedge behind the volcanic arc is discussed. The thermal regime in this area is critical for constraining mantle wedge dynamics. With the Cascadia subduction zone as the example, different observations that can be used to constrain temperatures in the backarc mantle are presented. The Cascadia subduction zone was chosen as the focus of this research because the thermal structure is well-constrained, and there has been no significant recent backarc extension.

In the next chapter, an overview of the thermal regime of other subduction zone backarcs is presented. It is shown that high temperatures in the mantle wedge are not localized at the volcanic arc, but extend 100's to 1000's of kilometres into the backarc for nearly all subduction zones. Such high temperatures are contradictory to the expected cooling effects of an underlying subducting plate. In later chapters, numerical models are developed to investigate the backarc mantle flow regime that maintains these high temperatures.

3.2 Constraints from Arc Volcanics

One important indicator of mantle wedge temperatures comes from geochemical and petrological studies of volcanic arc magmas. The existence of an active volcanic arc at nearly all subduction zones requires high temperatures for magma generation. Studies of arc magmas can place constraints on the temperature, pressure and composition in the magma source region.

Geochemical and isotope analyses of magams indicate that limited slab melting occurs in only a few subduction zones, e.g., the Aleutians, Chile, SW Japan, and Cascadia. Magmas produced by slab melting (sometimes called adakites) show distinct geochemical trends, including low Y and Yb concentrations, a very high Sr/Y ratio, and a steep rare earth element (REE) pattern [*Defant and Drummond*, 1990]. Such compositions appear to be restricted to regions with a young subducting plate (<25 Ma) and slow subduction rate [*Defant and Drummond*, 1990; *Peacock et al.*, 1994], or places where a slab window is proposed [e.g., *Johnston and Thorkelson*, 1997]. Friction along the subduction thrust fault may aid in heating the slab, but observations of low heat flow over many forearcs suggest that frictional heating is generally very low [*Peacock*, 1996]. Thus, for most subduction zones, the subducting crust is likely too cold to melt beneath the arc.

The composition of arc magmas can be used to constrain the mechanism for magma generation. Arc magmas are geochemically distinct from mid-ocean ridge basalts (MORB) in that they are predominantely calc-alkaline and have a much higher average water content of 2-6 wt%; MORBs are basaltic and contain <0.4wt% H_2O [*Ulmer*, 2001; *Stern*, 2002]. Relative to MORB, arc magmas are enriched in large ion lithophile elements (LILE, e.g., Rb, K, Cs, Sr, Ba) and light REE (La, Ce, Nd), and are depleted in heavy REE (Yb, Lu) and high field strength elements (HFSE, i.e., Nb, Ta, Zr, Hf). Although widespread slab melting is ruled out, the presence of trace elements B, Be, Th and Pb in arc magma indicates the involvement of subducted material in magma generation [e.g., *Morris et al.*, 1990]. In particular, arc magmas contain ^{10}Be, a cosmogenic isotope that is produced in the atmosphere and has a short half-life (~1.5 my) [e.g., *Morris et al.*, 1990; *Leeman*, 1996]. Such a short half-life argues for very efficient

and rapid magma generation and extrusion to the surface (<10 my from initial subduction to extrusion, as ^{10}Be is difficult to detect after ~6 half-lives). Together, these observations suggest a two-component source for arc magmas: 1) a peridotitic asthenosphere that has been depleted through previous melt extraction, such as at spreading ridges, and 2) a slab-derived hydrous fluid that is enriched in LILE's and light REE's [*McCulloch and Gamble*, 1993; *Ulmer*, 2001].

The current consensus is that arc magma is primarily produced by partial melting of the mantle above the subducting plate, triggered by the infiltration of hydrous fluids from that plate [e.g., *Gill*, 1981; *Tatsumi et al.*, 1983; *Tatsumi*, 1986; *McCulloch and Gamble*, 1993; *Ulmer*, 2001; *Stern*, 2002 and references therein]. With the introduction of even a small amount of water (<1 wt%) into the wedge, the mantle solidus temperature can be lowered significantly (more than 100°C) [*Ulmer*, 2001]. The source of water is likely dehydration metamorphic reactions within the subducting crust and possibly uppermost mantle, as they are subjected to increasing temperatures and pressures.

Early models suggested that magma generation was induced by one or two key pressure-sensitive reactions, based on the apparent near-constant depth of the subducting slab beneath many arcs (100-120 km) [*Gill*, 1981; *Tatsumi*, 1986]. Many studies focused on the breakdown of amphibole, which dehydrates at pressures of 3.0 GPa (~95 km depth) and temperatures of 1000-1100°C [*Tatsumi*, 1986; *Davies and Stevenson*, 1992; *Schmidt and Poli*, 1998]. However, these models require a complicated series of dehydration and hydration reactions to transport water to the sub-arc regions [e.g., *Davies and Stevenson*, 1991] and do not adequately explain the observed geochemical composition or water content in magmas [*Schmidt and Poli*, 1998]. More recent studies have shown that dehydration of the slab does not occur as discrete pressure-sensitive events, but instead occurs fairly continuously to great depths (>300 km for cold slabs), with decreasing amounts of dehydration at greater depths [*Peacock*, 1990; *Schmidt and Poli*, 1998]. In these models, it is the thermal structure of the mantle wedge that controls the location of arc magma generation. Note that there is ongoing debate about how water transported from the slab into the magma source region.

Constraints on the mantle temperatures required for arc magmatism come from experimental studies of magma/mantle equilibrium, i.e., the pressure-temperature-composition conditions at which magma last equilibrated with mantle peridotite prior to eruption. As more water is added to the mantle wedge, its solidus temperature will decrease, but the composition of the melt will also change [*Ulmer*, 2001]. Although there is some variation in water content and magma composition among different arcs, in general, magma composition indicates the mantle below the arc is not completely water-saturated (< 1 wt% H_2O). With this amount of water, temperatures greater than 1200°C are required in the uppermost mantle below the arc (35-50 km depth) for partial melting [*Ulmer*, 2001]. There is some indication for temperatures above 1300°C at depths greater than 50 km [*Tatsumi et al.*, 1983; *Ulmer*, 2001; *Kelemen et al.*, 2003 and references therein]. These temperatures are in fair agreement with temperatures at the base of arc crust from petrologic studies on sections of exposed lower crust. For exposed sections in Pakistan and Alaska, metamorphic closure temperatures indicate temperatures of 980-1030°C at ~1 GPa (~30 km depth) [*Kelemen et al.*, 2003]. One important caveat is that studies of magma equilibrium and crustal metamorphism may give temperatures associated with transient movement of magma. However, *Kelemen et al.* [2003] argue that regional high temperatures at shallow depths are required to explain the low seismic velocities and high seismic attenuation observed below most arcs. In addition, the longevity of arc magmatism at subduction zones requires an ongoing source of heat to maintain high wedge temperatures.

Based on the above studies, the generation of arc magmas requires temperatures of at least 1000°C at the base of the arc crust, and greater than 1200°C in the mantle wedge below the arc. Most models assume that magma is generated in the wedge directly below the volcanic arc, although lateral transport of magma from the source region to the arc may occur.

3.3 Observational Techniques for Constraining Backarc Temperatures

Of greatest importance to this thesis study is the thermal structure of the backarc

mantle, away from the volcanic arc. The thermal structure of the backarc can be constrained using indirect methods and direct methods. These are summarized below.

3.3.1 Indirect methods

The primary indirect constraint on the backarc thermal structure is surface heat flow; high heat flow generally indicates a high thermal gradient and high temperatures at depth. However, near-surface radiogenic heat production has a significant effect on surface heat flow and must be considered. Using measurements of surface heat flow and near-surface radiogenic heat production, the deep thermal structure can be calculated through downward extrapolation, assuming values for the thermal properties of the crust and mantle at depth (see **Section 3.6.3**).

Other indirect methods for constraining the deep thermal structure use measurements of temperature-sensitive properties of the crust and mantle. One key measurement is seismic velocity. Seismic velocity is affected by both composition and temperature. In the crust, composition provides the primary control on velocity. In the mantle, the temperature effect dominates; velocity decreases with increasing temperature [*Goes et al., 2000* and references therein; *Wiens and Smith*, 2003]. Composition and seismic anisotropy can be important second-order effects. P-wave and S-wave velocities (V_P and V_S, respectively) in the backarc mantle can be constrained with regional and global tomographic studies. The velocity of the uppermost mantle can also be constrained using P_n waves, i.e, P-waves that refract along the Moho. In addition, observations of the V_P/V_S ratio and seismic attenuation (e.g., measurements of the seismic quality factor, Q) can be used to constrain the presence of partial melt, and hence high temperatures. Fluid/melt has a much larger effect on S-waves than on P-waves.

Surface heat flow and seismic velocity studies are the most common observations, with data available for most regions. Other indirect methods that can be used to constrain backarc temperatures are:

- the effective elastic thickness (T_e) from studies of surface flexure using gravity and topography; hotter regions will have a smaller elastic thickness, i.e., approximately the depth to the thermally-controlled brittle-ductile transition

- the depth to the base of the rigid lithosphere, as inferred from seismic and electrical data; the base of the lithosphere is controlled by a critical temperature, close to the solidus temperature of upper mantle minerals (usually taken as 1200-1300°C)
- the electrical conductivity in the lower crust and mantle; high conductivity may indicate the presence of partial melt (and therefore high temperatures), although this interpretation is non-unique because some crustal compositions and the presence of water will also produce high conductivity
- the maximum depth of earthquakes within the subducting and over-riding plates, under the assumption that this is controlled by a critical temperature (typically ~350°C for continental crust)
- the depth to the Curie temperature in the backarc crust from magnetic studies; hotter regions have a shallower Curie temperature
- studies of isostasy, using surface elevation, crustal thickness, and gravity measurements. For a region in isostatic equilibrium, the elevation of the Earth's surface is determined by the crustal thickness, crustal density, and density of the underlying mantle. If it can be shown that the surface elevation is too high for the crustal thickness and crustal density, then a low-density mantle is required. Such low densities may be related to the thermal expansion of the mantle due to high temperatures.
- estimates of the viscosity of the mantle from post-seismic relaxation, post-glacial rebound and other observations; high temperatures result in a low mantle viscosity. A discussion of backarc mantle viscosity is given in **Chapter 8**.

3.3.2 Direct methods

The main method to directly constrain the backarc thermal structure is through thermobarometry measurements on xenoliths (samples of lower crustal or upper mantle material that have been rapidly extruded to the surface). The mineral assemblages and mineral compositions at the xenolith source region are "frozen" into the sample, due to

the rapid transport to the surface. Estimates of the P-T conditions in the source region can be obtained by looking at temperature- and pressure-sensitive chemical equilibria among different minerals in the samples. Unfortunately, for regions with high temperatures, the indicators used to determine pressure (e.g., garnet) are often not present in the samples, and thus there are large uncertainties in the pressure determinations. For cratons and other cool regions, the pressure is better constrained. Note that the xenoliths provide only point measurements and may be biased by only providing information for areas/conditions where xenoliths occur. Thus, they may not represent the present-day regional thermal conditions.

Another direct indication of high mantle temperatures is the presence of basaltic (i.e., mantle-derived) volcanics in the backarc, which suggest an upper mantle that is close to its solidus temperature.

3.4 Cascadia Subduction Zone

The main study area for investigating the backarc thermal structure is the Cascadia subduction zone (42-50°N), where the oceanic Juan de Fuca Plate subducts beneath the continental North America Plate (**Figure 3.1**). The main Juan de Fuca Plate is bounded on its north and south ends by two small, internally-deforming micro-plates, the Explorer and Gorda Plates, respectively. The entire subduction system is limited by the San Andreas fault system at the south and the Queen Charlotte fault at the north. Both are large-scale mainly dextral, strike-slip faults that accommodate relative motion between the North America and Pacific Plates.

The North America Plate is made up of the Cordillera mobile belt in the west and the ancestral North America craton further east. The Cordillera is a mountainous belt that extends from Alaska to Mexico. In western Canada, the Cordillera is divided into five morphological belts [e.g., *Gabrielse and Yorath*, 1992]. From west to east, these are: 1) the Insular Belt, 2) the Coast Plutonic Belt, 3) the Intermontane Belt, 4) the Omineca Belt and 5) the Foreland Belt. The first four are primarily arc-related volcanic, plutonic and sedimentary terranes that have been accreted to the western edge of the North America craton since the Mesozoic. The Foreland Belt is composed of deformed shallow marine

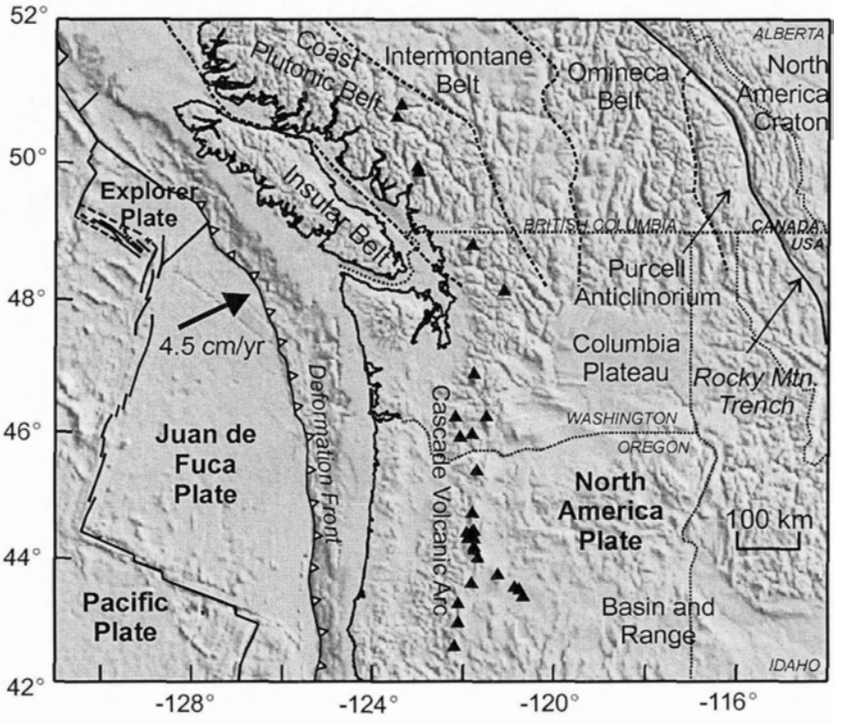

Figure 3.1. Map of the Cascadia subduction zone showing the main tectonic features. Solid triangles are active volcanoes in the Cascade volcanic arc. Dashed lines show the terrane boundaries for the northern part of the study area; dotted lines are international/provincial/state borders.

sedimentary rocks that overlie the relatively undeformed crystalline basement rock of the ancestral North America craton. The eastern boundary of the Foreland Belt represents the limit of Phanerozoic orogenic activity. East of this is the Western Canada Sedimentary Basin, a region of nearly flat-lying sediments overlying the North America craton. This ~5 km deep basin was created by the westward downwarping of the North America craton as it was over-ridden by the Cordillera crust, followed by infilling with sediments eroded from the adjacent Cordillera. The North America craton is exposed at the Earth's surface ~600 km northeast of the deformation front.

Subduction along the Cascadia margin has been continuous for nearly 200 my, with tectonic activity extending back even further [e.g., *Engebretson et al.*, 1985; *Monger and Price*, 2002]. The western margin of the North America craton was formed by rifting of the Rodinia supercontinent at ~750 Ma [e.g., *Atwater*, 1989; *Gabrielse and Yorath*, 1992; *Monger and Price*, 2002]. For the next 400 my, this remained a passive margin, likely similar to present-day eastern North America. At ~390 Ma, passive

tectonics were replaced by convergence, and by 185 Ma, a single subduction margin was established along the entire western margin of North America [*Atwater*, 1989]. Since then, the offshore spreading centres have gradually approached the margin, resulting in the fragmentation of the subducting plate into a number of smaller plates. Along some parts of the margin, subduction has ceased altogether, being replaced by strike-slip faults (e.g., the San Andreas and Queen Charlotte fault systems).

This study focuses primarily on the northern part of the Cascadia subduction zone (48-51 °N), where there are numerous observations to constrain the thermal structure, and where the backarc is tectonically quiescent. There are several major margin-parallel strike-slip faults in the backarc, but geologic evidence suggests that the last motion along these faults was in the early Cenozoic [*Gabrielse*, 1992]. The most recent significant deformation was a short-lived (<10 my) extension event in the eastern Omineca Belt in the Eocene (~50 Ma) (see **Section 3.9**). This region was also chosen because there is a clear eastern limit to the backarc. This limit is concluded to coincide with the Rocky Mountain Trench, the boundary between the Omineca Belt and Foreland Belt, based on rapid changes lithosphere properties, thermal regime, and deformation styles across this boundary [*Lowe and Ranalli*, 1993; *Hyndman and Lewis*, 1999; see also **Section 3.8**].

There are large differences in geological structure and Cenozoic tectonics in the backarc south of ~48 °N. However, heat flow and other temperature indicators suggest that the thermal structure is similar to that in the north [e.g., *Blackwell et al.*, 1990a, b; *Lowry and Smith*, 1994]. The thermal regime of the southernmost Cascadia backarc is complicated by both the proximity of the Yellowstone hotspot (44 °N, 111 °W) and present-day extension in the Basin and Range Province. The eastern limit of the hot backarc in this region also appears to be the stable North America craton, but this boundary is not as well-defined as in the north.

3.5 General Observations

The Cascadia volcanic arc extends the length of the present subduction zone. Recent volcanism includes the 1980 eruption of Mt. St. Helens and pyroclastic flows at Lassen Peak between 1914 and 1917, illustrating that this arc is currently active.

Petrological studies from the southernmost part of the arc (~42°N) give temperatures of 1300-1450°C between 36 and 66 km depth in the mantle [*Elkins Tanton et al.*, 2001], consistent with the estimates given above for arc volcanism at other subduction zones.

Numerous observations indicate that northern Cascadia backarc is extremely hot for nearly 500 km east of the volcanic arc. Backarc seismicity is generally confined to shallow depths (<15 km) [J. Ristau, personal communication, 2004]. The effective elastic thickness is <20 km throughout the entire region [*Flück et al.*, 2003]. Electrical conductivity is very high throughout the lower crust and upper mantle of the southern Canadian Cordillera [*Majorowicz et al.*, 1993 and references therein]. Another indication for a high temperature upper mantle is the presence of sporadic Cretaceous to Tertiary basaltic volcanic centres throughout Cordillera, from Mexico to northern Canada (e.g., the Chilcotin basalt field) [*Wheeler and McFeely*, 1991].

Below, five key observations are discussed in detail: 1) surface heat flow and near-surface radiogenic heat production, 2) upper mantle seismic velocity, 3) temperature-pressure data from upper mantle xenoliths, 4) thermal isostasy, and 5) depth to the base of the lithosphere from seismic, xenolith and electrical data.

3.6 Surface Heat Flow and Heat Generation Observations

3.6.1 Surface heat flow

The Cascadia subduction zone is one of the most densely sampled regions for surface heat flow (**Figure 3.2**). There are a total of 1675 heat flow values in this area; 203 in Canada and 1472 in the US (west of 114°W, north of 40°N). Data for southwestern Canada are from compilations by *Davis and Lewis* [1984], *Lewis et al.* [1988; 1992], *Hyndman and Lewis* [1999], and *Flück* [2003]. The US data is from the Global Heat Flow Data Base [*Pollack et al.*, 1993; *Global Heat Flow Database*, 2004]. Note that some data for the offshore regions are not shown on **Figure 3.2**.

Heat flow data for Cascadia is generally of high quality, with estimated uncertainties of 10-20% [*Blackwell et al.*, 1990a, b; *Hyndman and Lewis*, 1995; *Hyndman and Lewis*, 1999]. Perturbations in heat flow come from possible groundwater flow, thermal refraction due to lateral variations in thermal conductivity, and uncorrected

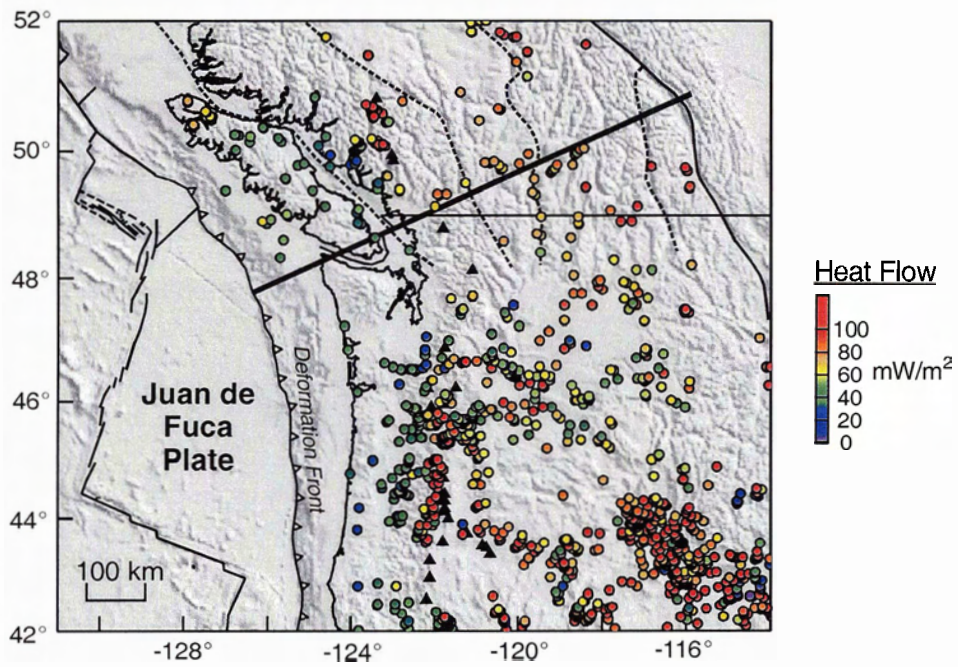

Figure 3.2. Location of surface heat flow measurements for the Cascadia subduction zone. The dark line shows the profile location. Solid triangles are active volcanoes.

variations in surface temperature history. The heat flow measurement accuracy is affected by the borehole depth, and the number and quality of thermal conductivity measurements at each site [*Hyndman and Lewis*, 1995].

Statistics of the heat flow values for the entire southwestern Canada heat flow data set are given in **Table 3.1** for each of the terranes. The high heat flow values (> 60 mW/m^2) in the northern part of Vancouver Island were not included in the calculations for the Insular Belt. These lie north of the projected edge of the subducting slab and may be related to an underlying slab window [*Lewis et al.*, 1997]. The present-day Cascade volcanic arc passes through the centre of the Coast Plutonic Belt. Thus, this terrane was divided into three regions: forearc, arc, and backarc. The arc region is defined as a 30 km wide band, centred on the line of Tertiary volcanoes; the forearc is the region to the west; the backarc is to the east. In addition, the easternmost Omineca Belt is considered as a separate region (the Purcell Anticlinorium), as high thermal conductivity and high heat flow in this area make it distinct from the rest of the Omineca Belt [*Hyndman and Lewis*, 1999].

Table 3.1. Heat flow and heat generation for SW Canada.

Region	Heat Flow (mW/m^2)				Near surface heat generation ($\mu W/m^3$)				Corrected heat flow[1]	
	# data	mean	st. dev.	st. err.	# data	mean	st. dev.	st. err.	0	1.3
Offshore	6	50.0	9.5	4.2	0	--	--	--	--	--
Insular	36	39.8	7.1	1.2	20	0.9	0.6	0.1	--	--
North Van. Is.	12	74.3	26.6	7.1	9	0.8	0.4	0.1	--	--
CPB[2] forearc	27	47.7	19.3	3.8	26	0.9	0.4	0.1	--	--
CPB[2] arc	14	63.2	12.3	3.4	14	0.9	0.2	0.1	54.7	67.7
CPB[2] backarc	11	70.5	15.7	5.0	8	0.8	0.5	0.2	62.9	75.9
Garibaldi	28	375.7	533.4	105.7	5	0.7	0.3	0.2	--	--
Intermontane	35	70.4	12.6	2.2	31	1.2	0.9	0.2	58.7	71.7
Omineca	29	87.2	22.3	4.2	23	3.2	1.5	0.3	55.3	68.3
Purcell	5	100.4	13.0	6.5	3	3.1	0.8	0.6	69.1	82.1

[1]surface heat flow was corrected for differences in near-surface heat generation between the observed value and two arbitrary values (0 $\mu W/m^3$ and 1.3 $\mu W/m^3$), assuming constant heat production in a 10 km thick upper crustal layer.
[2]Coast Plutonic Belt

Figure 3.3a shows the surface heat flow within 200 km of a profile line through the northern Cascadia subduction zone. Over the forearc, heat flow decreases from >50 mW/m^2 at the deformation front to a minimum of 20-30 mW/m^2 approximately 50 km seaward of the volcanic arc. Similar forearc heat flow is observed to the south in Washington and Oregon [*Blackwell et al.*, 1990a, b]. Previous thermal modelling studies have shown that low and eastward-decreasing forearc heat flow values are consistent with subduction of the Juan de Fuca Plate [e.g. *Hyndman and Wang*, 1993; 1995; *Wang et al.*, 1995b]. The observed heat flow values suggest negligible frictional heating along the top of the subducting plate [*Wang et al.*, 1995b]. Numerical models, constrained by heat flow data, indicate temperatures of 400-600°C in the forearc mantle wedge. Hydration of the wedge by fluids released from the subducting plate can result in serpentinization of the forearc mantle if temperatures are less than 700°C [*Hyndman and Peacock*, 2003]. Evidence of extensive serpentinization of the forearc mantle comes from seismic studies [*Bostock et al.*, 2002; *Brocher et al.*, 2003] and other geophysical observations [*Hyndman and Peacock*, 2003], confirming the presence of a cool forearc mantle wedge.

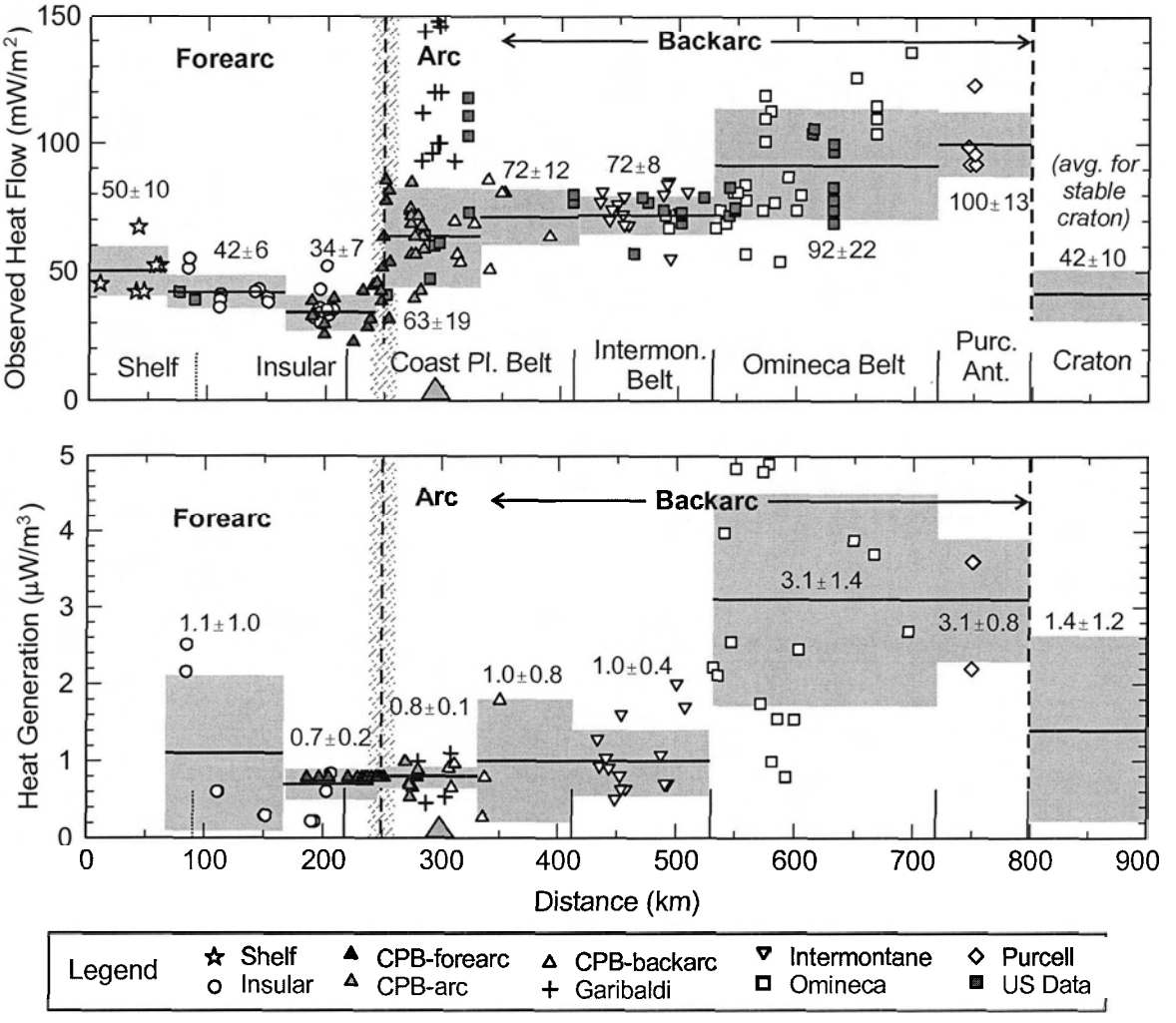

Figure 3.3. a) Surface heat flow data and b) near-surface heat production data within 200 km of the profile shown in Figure 3.2. The mean and standard deviation for each data block are also given. Symbols indicate the terrane for each data point (see legend). The craton values are for the Superior province [*Jaupart and Mareschal*, 1999].

Approximately 30 km seaward of the volcanic belt, an abrupt increase in surface heat flow by a factor of two or more is observed. Detailed local heat flow studies show that this increase occurs over a distance of 20 km in British Columbia, southern Washington and Oregon [*Lewis et al.*, 1988; *Blackwell et al.*, 1990a, b]. In northern Washington, the transition appears to be more gradual, due to either sparse data or local geological/hydrological effects [*Blackwell et al.*, 1990b]. On the profile shown in **Figure 3.3a**, this increase is smeared out due to the 400 km swath width and the oblique orientation of the volcanic arc relative to the profile.

Along the axis of the volcanic arc, heat flow exhibits considerable scatter, which likely reflects local effects such as magma emplacement and groundwater flow driven by steep topography [*Lewis et al.*, 1992]. The local extrema appear to be super-imposed on a regionally high heat flow. Away from the volcanic centres, the heat flow is 80 mW/m^2 in British Columbia [*Lewis et al.*, 1992], and 75-90 mW/m^2 in Washington and Oregon [*Blackwell et al.*, 1990a; b]. A regional heat flow of ~80 mW/m^2 is consistent with the high temperatures (>1300°C at >35 km depth) inferred from arc magma petrological studies in southern Oregon [*Elkins Tanton et al.*, 2001]. Along the profile, the average arc heat flow is 63 mW/m^2, excluding all data from the Garibaldi volcanic belt.

Surface heat flow remains high well into the backarc regions for the entire Cascadia subduction zone. For northern Cascadia, the backarc surface heat flow shows an eastward increase from ~72 mW/m^2 in the eastern Coast Plutonic Belt to ~100 mW/m^2 in the Omineca Belt and Purcell Anticlinorium. As shown below, this increase appears to be correlated with an eastward increase in the near-surface radiogenic heat production, suggesting that there is little variation in deep heat flow across the region. In the Washington and Oregon backarc, surface heat flow is generally 75-90 mW/m^2, with fluctuations attributed to variations in near-surface radiogenic heat production [*Blackwell et al.*, 1990a, b]. Over the Columbia Plateau, the average surface heat flow is 62 mW/m^2 [*Blackwell et al.*, 1990a, b]. This region is characterized by an unusually mafic crust. Both low crustal radiogenic heat production associated with mafic rocks, as well as evidence for groundwater flow, may contribute to the low heat flow values observed here. The surface heat flow in southwest Oregon is generally high (~100 mW/m^2). The thermal regime in this region may be perturbed by the proximity of the currently extending Basin and Range province.

3.6.2 Near-surface radiogenic heat production

Heat flow at the surface depends on 1) radiogenic heat production in the uppermost crust, 2) radiogenic heat production in the deep crust and mantle, and 3) heat flow from the deep mantle. For the northern Cascadia subduction zone, there are numerous high quality measurements of near-surface heat production. These data are

obtained from unweathered surface samples and borehole samples of representative plutonic upper crustal rock types [e.g., *Lewis et al.*, 1992]. **Figure 3.3b** shows values of near-surface heat generation within 200 km of the profile line. Over the forearc and arc region, heat production is ~1 $\mu W/m^3$. Radiogenic heat production in the northern Cascadia backarc increases eastward, from ~1 $\mu W/m^3$ over the western Coast Plutonic Belt and Intermontane Belt to over 3 $\mu W/m^3$ in the Omineca Belt.

There are 58 co-located heat flow and heat generation data points for the northern backarc. A plot of heat flow and surface heat flow shows that sites with higher heat flow are generally associated with higher heat generation (**Figure 3.4**). The near-linear relationship between these parameters suggests that the backarc forms a single heat flow province [e.g., *Lachenbruch*, 1968; *Roy et al.*, 1968]. In this case, the observed heat flow (q_0) and near-surface heat generation (A_0) can be related by the linear equation:

$$q_0 = q_r + DA_0 \qquad (3.1)$$

where q_r (the intercept) is the reduced heat flow and D (the slope) is the depth parameter. A simple interpretation of this relation is that the observed heat flow within a heat flow province can be decomposed into a constant heat flow (q_r) from the deep crust and mantle, and an uppermost crustal component that arises from lateral variations in the concentration of radiogenic elements. The depth parameter (D) is related to the depth scale for the upper crustal component.

For the Cascadia backarc data, the linear regression yields a depth parameter of 10.4±1.5 km and a reduced heat flow of 60.1±3.3 mW/m^2. These values agree well with those obtained in previous studies for this region [*Lewis et al.*, 1992; *Hyndman and Lewis*, 1999; *Flück*, 2003]. Note that the mean values for the heat flow and heat generation from the northern Cascadia forearc regions (38±9 mW/m^2 and 0.8±0.6 $\mu W/m^3$, respectively) are well below the best-fit backarc line, indicating that the forearc lies within a different heat flow province.

For the backarc in Washington and Oregon (excluding the Basin and Range region), the heat flow-heat production relation gives a reduced heat flow of 55-65 mW/m^2 and a depth parameter of 10 km [*Blackwell et al.*, 1990b]. An early analysis of heat flow

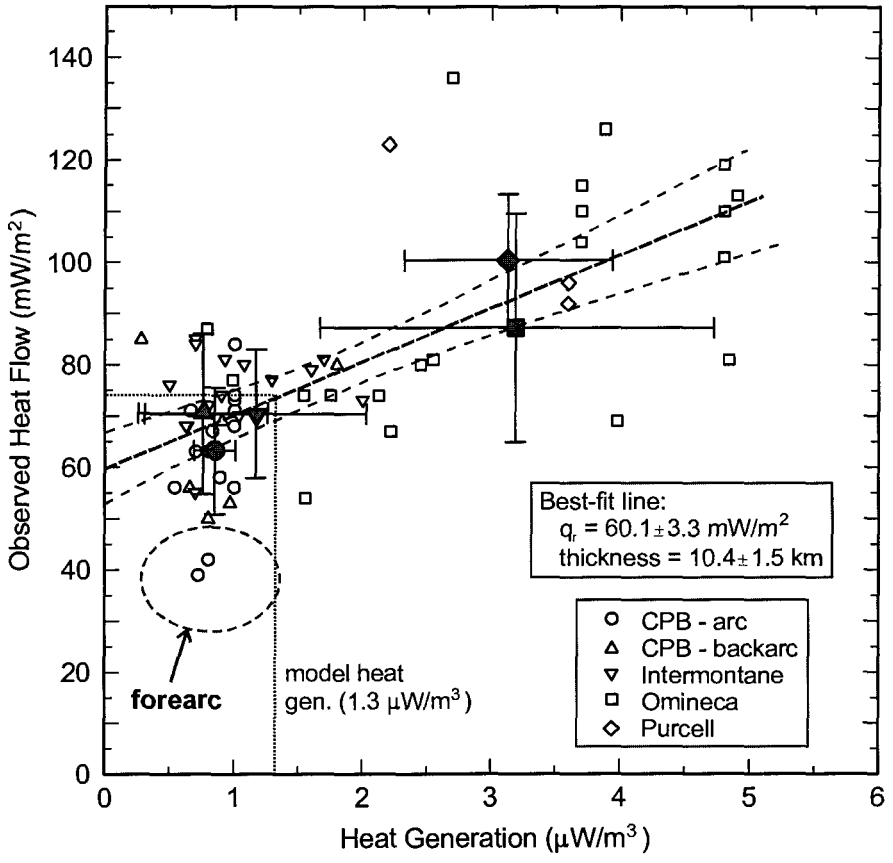

Figure 3.4. Heat flow-heat generation plot for the northern Cascadia backarc. Solid symbols indicate the mean values (with standard devation) for each region. The solid line is the best-fit line, with 95% confidence limits. Also shown are the range of heat production and heat flow for Cascadia forearc sites.

and heat generation data from the Basin and Range region also yields a reduced heat flow of 59 mW/m^2 and a depth parameter of 9.4 km [*Roy et al.*, 1968]. This suggests that the entire backarc region of the Cascadia subduction zone (including the Basin and Range) forms a single heat flow province.

In the numerical models in **Chapter 7**, the model upper crust for the Cascadia backarc has a uniform heat production of 1.3 μW/m^3, over a 10 km thickness. This thickness is similar to the depth parameter from the heat flow-heat generation relationship. To facilitate comparison with the models, the observed heat flow has been corrected to the model crustal heat generation, by correcting for heat flow differences resulting from differences between the observed and model heat generation values. This variation in upper crustal heat production has only a small effect on deep temperatures

[e.g., *Hyndman and* Lewis, 1999]. For heat flow sites without an associated heat generation value, the average heat generation for that region (e.g., **Figure 3.3**) was used. The corrected heat flow for the profile line is shown in **Figure 3.5**. After this correction, the surface heat flow for the northern Cascadia backarc is quite constant, 75±15 mW/m^2, with a reduced heat flow of ~60 mW/m^2.

3.6.3 Calculation of geotherms

Surface heat flow can be used to determine the temperature (T) as a function of depth (z) for the northern Cascadia backarc. To calculate the geotherm, the one-dimensional, steady-state, conductive heat equation is used (see *Lowe and Ranalli* [1993] for a discussion of 2-D models):

$$\frac{d}{dz}\left(k\frac{dT}{dz}\right)+\frac{A}{k}=0 \qquad (3.2)$$

where A and k are the radiogenic heat production and thermal conductivity, repectively. Integration of this equation, with the boundary conditions of surface heat flow (q_s) and surface temperature (T_0), gives:

$$T(z)=T_0+\frac{q_s}{k(z)}z-\frac{A(z)}{2k(z)}z^2 \qquad (3.3)$$

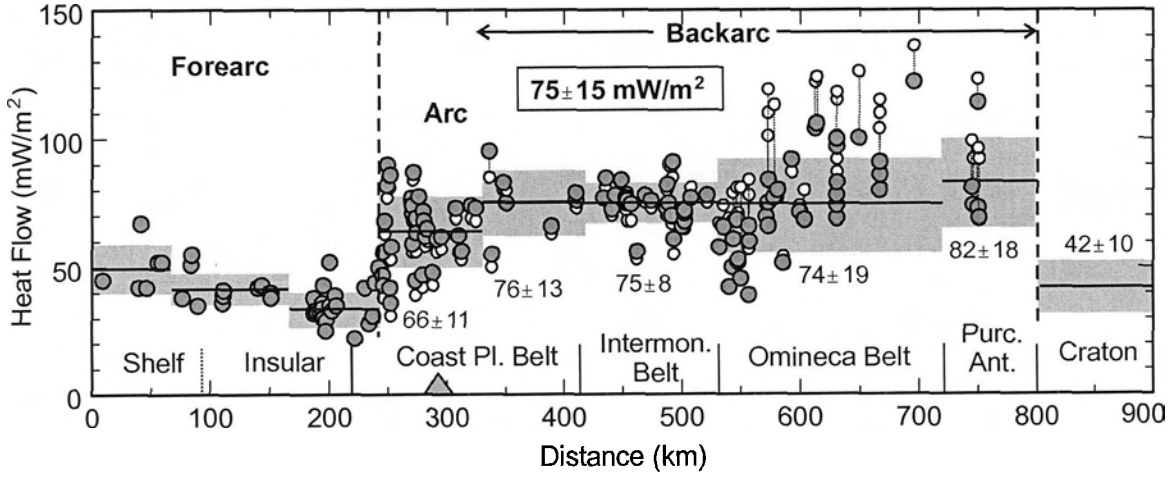

Figure 3.5. Corrected surface heat for the northern Cascadia backarc. The measured heat flow values (open circles) have been corrected for variations in near-surface heat generation to give the corrected values that use an upper crustal heat generation of 1.3μW/m (solid circles). The correction was only applied to the backarc measurements.

[e.g., *Chapman*, 1986]. Both heat production and thermal conductivity vary with depth in the Earth. This equation is applied by dividing the earth into layers of thickness Δz, and downward continuing the surface heat flow and surface temperature (taken to be 0°C). Given the heat flow (q_T) and temperature (T_T) at the top of each layer, the temperature (T_B) and heat flow (q_B) at the base of the layer are:

$$T_B = T_T + \frac{q_T}{k_L}\Delta z - \frac{A_L}{2k_L}(\Delta z)^2 \qquad (3.4a)$$

and

$$q_B = q_T - A_L \Delta z \qquad (3.4b)$$

where A_L and k_L are the average heat production and average thermal conductivity, respectively, in the layer.

The base of the lithosphere is approximated by the intersection of the conductive gradient in **Equation 3.3** with the mantle adiabat. Below this, an adiabatic gradient of 0.3°C/km is used [*Turcotte and Schubert*, 2002]. In this study, the mantle adiabat corresponds to a potential (zero pressure) temperature of 1295°C, consistent with experimental constraints on the temperature of the 660 km phase transition [*Ito and Katsura*, 1989]. This is similar to the average current mantle adiabat proposed by *McKenzie and Bickle* [1988].

For the calculation of the Cascadia backarc geotherm, a three-layer model is used, consisting of a two-layer crust and an underlying mantle layer. The upper crust has a thickness of 10 km. The lower crust extends to the Moho, which is taken to be at 35 km depth. This is consistent with seismic studies that indicate a Moho depth of 32-37 km within the northern Cascadia backarc [*Clowes et al.*, 1995; *Burianyk et al.*, 1997]. The Moho depth has little effect on the temperature-depth profile (<20°C at each depth). However, the temperature at the Moho will be larger for a deeper Moho due to the thermal gradient of 10-20°C/km in the lower crust.

The other required model parameters are the surface heat flow, the thermal conductivity (and its temperature-dependence) of each model unit, and the distribution of radiogenic heat production with depth. The calculations use the average (model) backarc surface heat flow of 75 mW/m^2. The crust and mantle have a constant thermal

conductivity of 2.5 W m^{-1} K^{-1} and 3.1 W m^{-1} K^{-1}, respectively. A constant radiogenic heat production of 1.3 $\mu W/m^3$, 0.4 $\mu W/m^3$, and 0.02 $\mu W/m^3$ are used for the upper crust, lower crust, and mantle, respectively. The thermal conductivities and heat production values represent the average values for the crust and mantle and are similar to those used in other studies [e.g., *Chapman*, 1986; *Rudnick and Fountain*, 1995; *Rudnick et al.*, 1998; *Hyndman and Lewis*, 1999; *Flück*, 2003] and in the numerical models in **Chapter 7**. Parameter sensitivity tests were carried out to determine the effects of each parameter.

Surface heat flow

Surface heat flow was varied by 10% and 20% from the standard value of 75 mW/m^2. The surface heat flow has a large effect on geotherm calculations; higher heat flow results in higher temperatures at depth, if the upper crustal heat generation remains constant (**Figure 3.6a**). At the Moho, a 10% increase in surface heat flow results in an increase in temperature of ~12%. Note that if surface heat flow variations are coupled with variations in near-surface heat generation (i.e., as suggested by **Figure 3.4**), the deep thermal structure is not significantly affected [e.g., *Hyndman and Lewis*, 1999].

Thermal conductivity

The geothermal gradient is inversely related to the thermal conductivity within the crust; as the conductivity decreases, the gradient increases resulting in higher temperatures. The standard models use a constant thermal conductivity for each model unit. Laboratory observations indicate that thermal conductivity decreases with temperature [*Zoth and Haenel*, 1988; *Sass et al.*, 1992; *Clauser and Huenges*, 1995]. On the basis of a compilation of laboratory data, *Zoth and Haenel* [1988] propose that the thermal conductivity (k) decrease with temperature (T, in °C) may be approximated by:

$$k(T) = A + \frac{B}{350 + T} \tag{3.5}$$

where A and B are constants that depend on rock type. Two end-member cases were examined: felsic rocks (A=0.64; B=807) and mafic rocks (A=1.18; B=474).

Sass et al. [1992] suggest an alternate temperature correction of the form:

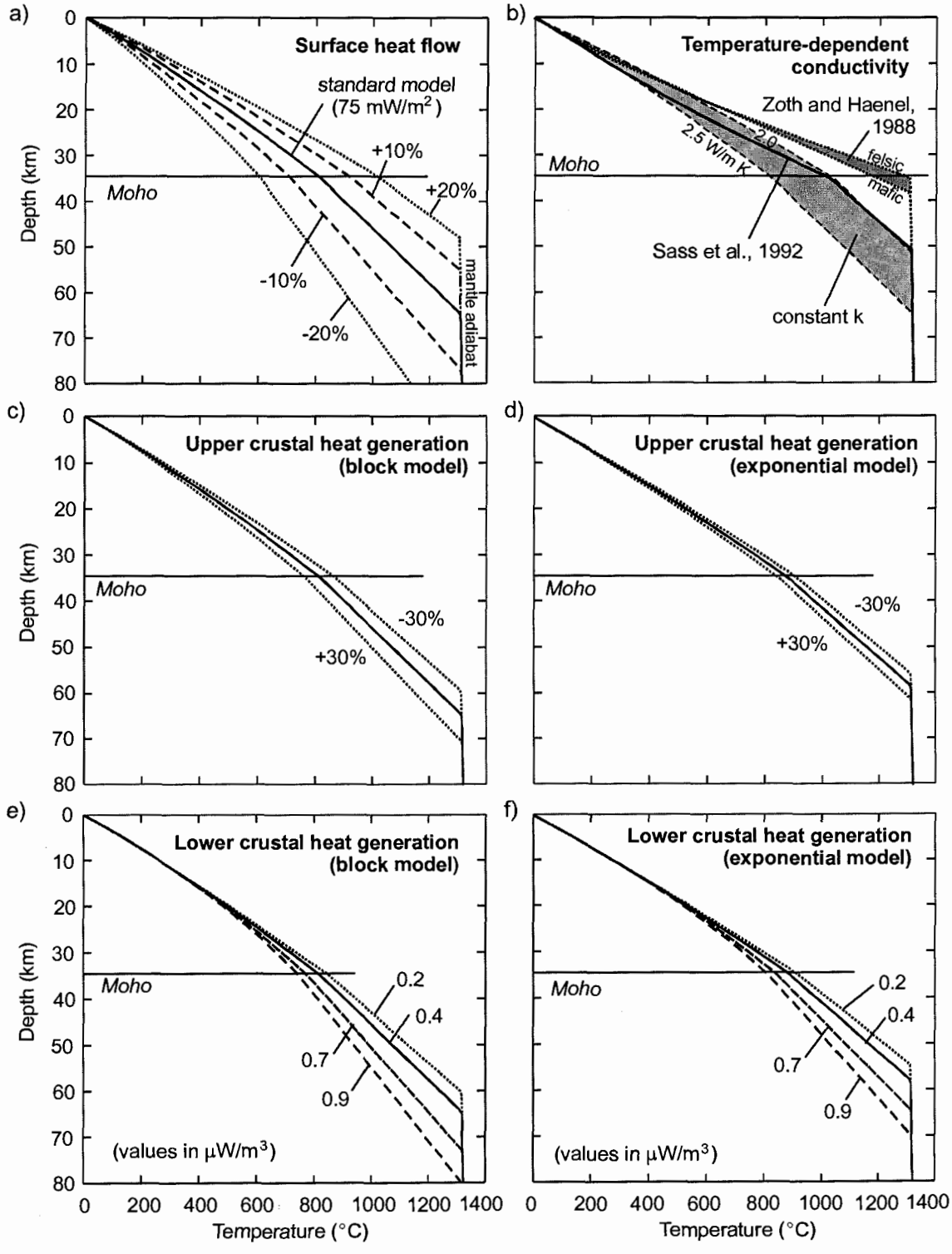

Figure 3.6. Parameter sensitivity tests for geotherm calculations (see text for details). a) Effect of surface heat flow. b) Constant vs. temperature-dependent conductivity. Effect of near-surface heat generation for c) a block model and d) an exponential model. The lower crust has a constant heat generation. Effect of variations in lower crustal heat generation for models that use e) a block model and f) an exponential model for heat generation in the upper crust.

$$k(T) = \frac{k(0)}{1 + cT} \tag{3.6}$$

where k(0) is the conductivity at 0°C, and c is the temperature coefficient. Following the *Sass et al.* study, as well as those by *Lewis et al.* [2003] and *Flück* [2003], the 0°C conductivity is taken to be 3.0 W m^{-1} K^{-1} for the crust and 3.5 W m^{-1} K^{-1} for the mantle, and the temperature coefficient is 0.001/°C for the crust and 0.0002/°C for the mantle.

With the introduction of a temperature-dependent conductivity, **Equation 3.4a** becomes non-linear, and thus an iterative approach is used in the geotherm calculations [*Flück*, 2003]. With either formulation, the thermal conductivity decreases rapidly with depth, due to the high temperatures at shallow depths. This results in a significant (>180°C) increase in deep crustal/mantle temperatures, relative to the constant conductivity model (**Figure 3.6b**). The *Zoth and Haenel* [1988] relation produces much higher temperatures, as the thermal conductivity decrease is much more rapid between 0-400°C, and the high temperature (>700°C) conductivity is slightly lower, especially for a felsic composition. Also shown on **Figure 3.6b** is a model that uses a constant conductivity of 2 W m^{-1} K^{-1}, further illustrating that lower thermal conductivities result in higher temperatures at depth.

There is considerable uncertainty in the thermal conductivity at high temperatures. *Lee and Deming* [1998] note that the *Sass et al.* relation should only be applied up to 300°C, the maximum temperature of the laboratory data used in that study. *Zoth and Haenel* [1988] used a larger database, with measurements up to at least 800°C. However, with their relation, the calculated temperature at the Moho is extremely high (>1200°C). As shown below, constraints on Moho/uppermost mantle temperatures from seismic velocities and xenoliths predict temperatures of 800-1000°C, suggesting that this geotherm is unrealistically hot. At high temperatures (>900°C), the effects of radiative heat transfer may become significant, especially for mantle rocks (i.e., peridotite) and crustal rocks with a diabase or dolerite composition [*Clauser and Huenges*, 1995], but these effects are not well-constrained. If there is radiative heat transfer at high temperatures, the thermal conductivity will increase with increasing temperature. This produces lower model temperatures at depth than predicted for geotherms with the *Zoth*

and Haenel [1988] parameters. The net effect may be to produce a geotherm similar to that with the *Sass et al.* [1992] parameters.

Radiogenic heat production

Crustal radiogenic heat production is another critical model parameter. Heat production in the uppermost crust can be constrained by measurements of representative rock samples at each site, but its depth distribution remains an important uncertainty. Most studies conclude that radiogenic heat production must decrease with depth, but the nature of this decrease is not well-known [e.g., *Rudnick and Fountain*, 1995; *Rudnick et al.*, 1998]. Two possible simple models for the upper crust that fit the linear heat flow-heat generation relationship (**Equation 3.1**) are: 1) constant heat production within the upper crust to a depth D (the block model), and 2) an exponential decrease in heat production with depth over length scale D (the exponential model) [*Lachenbruch*, 1970]. For the exponential model, the distribution of heat production (A) as a function of depth (z) is:

$$A(z) = A_0 \exp(-z/D) \tag{3.7}$$

where A_0 is the measured near-surface value.

These two models were examined, using a surface heat production (A_0) of 1.3 $\mu W/m^3$ and a depth scale (D) of 10 km (**Figure 3.6c, d**). The lower crust has a constant heat production of 0.4 $\mu W/m^3$. The exponential model predicts slightly higher temperatures at depth (~65°C higher at the Moho). Because there is less total heat production in the crust with this model, the mantle heat flow must be higher, resulting in an increase in deep temperatures. For each model, a variation of 30% in A_0 changes the deep temperatures by ~5%.

Heat production in the lower crust is also quite uncertain. *Rudnick and Fountain* [1995 and references therein] suggest an average lower crustal heat production of 0.4 $\mu W/m^3$, consistent with that measured in Archean granulite facies terranes. If the lower crust is more fertile (i.e., amphibolite facies), heat production may be higher. Due to the large uncertainty in composition of the lower crust for the northern Cascadia backarc, a

range of lower crustal values were tested, from 0.2-0.9 $\mu W/m^3$ (**Figures 3.6e, f**). This represents the expected range of crustal values for a reasonable range of compositions [*Rudnick and Fountain*, 1995; *Rudnick et al.*, 1998]. This also encompasses the range of values used in previous geotherm calculations for this region [e.g., *Lewis et al.*, 1992, *Hyndman and Lewis*, 1999; *Flück*, 2003]. Heat production in the lower crust was assumed to be constant. For the upper crust, both the constant and exponential decay models were examined, using a near-surface value of 1.3 $\mu W/m^3$. For either upper crustal model, variations in lower crustal heat production have a similar effect on deep crustal temperatures, with higher temperatures at depth for models with lower heat production in the lower crust.

3.6.4 Cascadia backarc geotherm

As shown in **Figure 3.6**, the downward continuation of surface heat flow and near-surface heat generation data to obtain a regional geotherm is subject to considerable uncertainty, especially at depths greater than 10 km. The main uncertainties for the northern Cascadia backarc are the thermal conductivity at high temperatures and heat production in the lower crust.

With the observed high heat flow across the Cascadia backarc, the above tests show that it is difficult to get temperatures at the Moho that are less than 800°C, especially if the crustal thermal conductivity decreases to <2 $W\ m^{-1}\ K^{-1}$ at high temperatures. For the remainder of the discussion, the geotherm that uses the *Sass et al.* [1992] thermal conductivity is taken as the reference geotherm for the Cascadia backarc (**Figure 3.7**). This geotherm includes the effect of temperature on thermal conductivity, but the effects are not as dramatic as those observed using the *Zoth and Haenel* [1988] relation. The *Sass et al.* [1992] relation may be a better approximation for the thermal conductivity at depth, especially if radiative heat transfer occurs. The estimated uncertainty for the geotherm is 20%, based on the parameter tests above, as well as those by *Flück* [2003]. With the reference geotherm, the temperature at the Moho (35 km

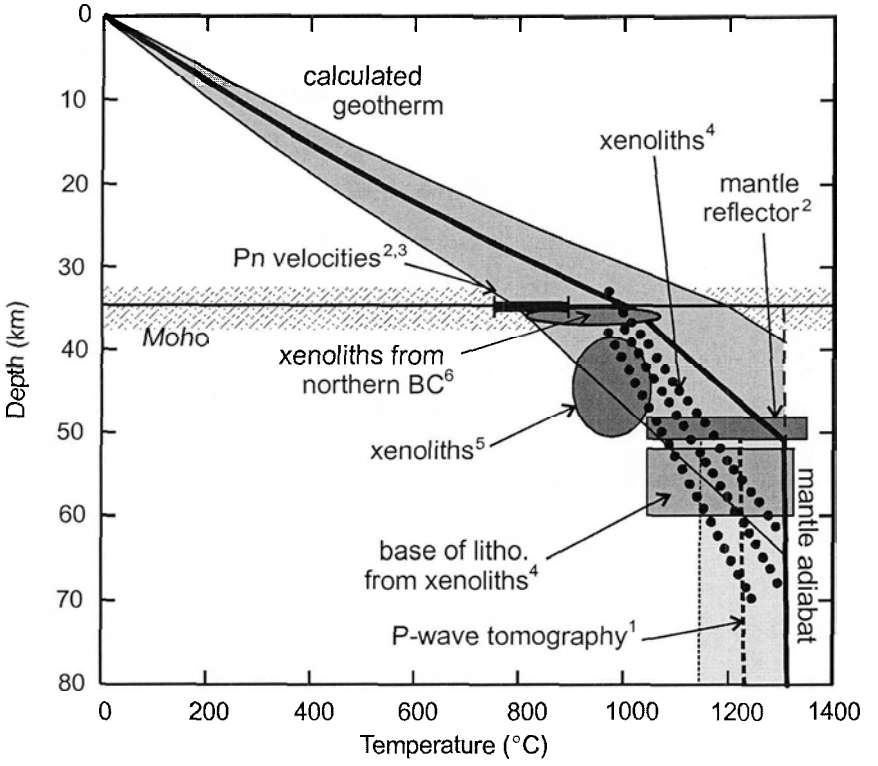

Figure 3.7. Comparison of the calculated geotherm with additional constraints on the thermal structure of the northern Cascadia backarc. References are: [1]*Goes and van der Lee*, 2002; [2] *Clowes et al.*, 1995; [3] *Burianyk and Kanasewish*, 1995; [6] *Ross*, 1983; [5] *Saruwatari et al.*, 2001; [6] *Harder and Russell*, submitted manuscript, 2004.

depth) is 1020±200°C. The intersection between the conductive geotherm and the mantle adiabat (approximately the base of the lithosphere) occurs at a depth of 50±12 km.

3.7 Additional Thermal Constraints

Given the large uncertainties in calculating lower crust/upper mantle temperatures from surface heat flow/heat generation data, it is desirable to use other observations to better constrain temperatures at depth and to substantiate the very high temperatures in the Cascadia backarc. In this section, constraints from seismic velocities, upper mantle xenoliths, and thermal isostasy are considered. Constraints on the depth to the base of the rigid lithosphere are also discussed.

3.7.1 Upper mantle seismic velocities

Seismic tomography studies clearly show that the upper mantle throughout the

Cascadia backarc is characterized by low P-wave and S-wave seismic velocities to depths greater than 200 km [e.g., *Grand*, 1994; *van der Lee and Nolet*, 1997; *Frederiksen et al.*, 2001; *Goes and van der Lee*, 2002]. These seismic velocities are anomalously low relative to global average 1-D velocity models, e.g., model ak135 [*Kennett et al.*, 1995]. Using a velocity-temperature relation for P-waves, *Goes and van der Lee* [2002] derived temperatures of 1220±80°C between 50 and 100 km depth (**Figure 3.7**). The observed S-wave velocity anomalies are somewhat larger than P-wave anomalies. These are attributed to the combined effects of high temperatures in the upper mantle, as well as the presence of a small amount (<2%) of water (or other volatiles) and/or melt [*Goes and van der Lee,* 2002].

The temperature of the uppermost mantle can be better constrained by looking at P_n velocities. *Black and Braile* [1982] proposed a relation between P_n velocity and Moho temperature (T_m) for North America:

$$P_n = 8.456 - 0.000729T_m \qquad (3.8)$$

This relation was developed based on Moho temperatures estimated from heat flow data. This leads to uncertainties because variations in crustal heat generation were not considered, and because there is a large uncertainty in determining Moho temperature from heat flow (as shown above). The temperature coefficient (-0.000729 km s^{-1} $°C^{-1}$) is in good agreement with that obtained in laboratory data [e.g., *Christensen*, 1979], but the constant (8.456 km/s) has significant uncertainty. The estimated uncertainties in Moho temperature from this relation are 150°C [*Hyndman and Lewis*, 1999].

Seismic refraction data for the southern Canadian Cordillera indicate consistently low P_n velocities of 7.8-7.9 km/s [*Zelt and White*, 1995; *Clowes et al.*, 1995; *Burianyk and Kanasewish*, 1995]. P_n velocities may be slightly (~0.1 km/s) higher beneath the eastern Intermontane Belt, but this variation is well within the uncertainties of this method. Given a P_n velocity of 7.8-7.9 km/s, the estimated Moho temperature is 760-900°C for the northern Cascadia backarc (**Figure 3.7**). This is slightly lower that that determined from heat flow, but within the uncertainties of the methods.

3.7.2 Upper mantle xenoliths

There are several localities in the northern Cascadia backarc (and Cordillera regions further north) where upper mantle xenoliths have been recovered. The equilibrium in-situ temperatures are well-constrained but there are considerable uncertainties in pressure (depth). Three suites of xenoliths from the Intermontane and Omineca Belts give temperatures of 900-1300°C at depths between 30-60 km, suggesting a geothermal gradient of ~15°C/km [*Ross*, 1983] (**Figure 3.7**). These agree well with measurements on xenoliths from the western Omineca Belt, which indicate temperatures of 900-1040°C at 1.2-1.6 GPa (37-50 km depth) [*Saruwatari et al.*, 2001]. Also included in this compilation are xenoliths from northern British Columbia (~59°N), where heat flow and other indicators suggest similar a thermal structure to that in the south [e.g., *Lewis et al.*, 2003]. A recent study of northern BC xenoliths gives temperatures between 805 and 1100°C, with a mean of ~925°C for 44 measurements [*Harder and Russell*, submitted manuscript, 2004]. Although no pressure/depth was determined for these samples, a pressure of 1 GPa was assumed based on the observed phase assemblages. This places the xenoliths in the uppermost mantle, and thus the xenoliths constrain the mantle just below the Moho to have a minimum temperature 805°C.

3.7.3 Thermal isostasy

Another indication for high temperatures at depth in the northern Cascadia backarc comes from studies of isostasy. Gravity measurements indicate that the region is generally in isostatic equilibrium, such that variations in surface elevation are compensated by variations in subsurface density [*Flück*, 2003]. In the northern Cascadia backarc, the surface elevation is 1500-2000 m, whereas the crustal thickness from seismic studies is 32-37 km [e.g., *Clowes et al.*, 1995; *Burianyk et al.*, 1997]. For such a thin crust, the expected elevation is close to, or below, sea level. In contrast, there are low elevations and a ~40 km thick crust for the adjacent North America craton [e.g., discussion by *Hyndman and Lewis*, 1999, see also **Section 3.8**]. The high elevations in the Cordillera can not be explained by an anomalously low density crust [*Hyndman and*

Wang, 1999; *Flück*, 2003]. Instead, the high elevations appear to be related to a low density upper mantle [*Lowe and Ranalli*, 1993; *Hyndman and Lewis*, 1999]. The low density is attributed to high temperatures in the mantle. *Hyndman and Lewis* [1999] show that high upper mantle temperatures, similar to those estimated above, result in a reduction of the average upper mantle density by 40 kg/m^3 relative to stable craton regions and can explain the observed 1.5-2 km surface elevation.

3.7.4 Base of the lithosphere

There are several observations that constrain the base of the lithosphere for the Cascadia backarc to shallow depths. *Clowes et al.* [1995] report an upper mantle reflector at a depth of ~50 km in seismic data from the Intermontane and Omineca Belts, which they interpret as the base of the lithosphere. This is in good agreement with an earlier surface wave study, which shows a low-velocity layer, with its upper boundary 15-20 km below the Moho [*Wickens*, 1977]. Additional constraints on the base of the lithosphere come from estimates of strain rate in upper mantle xenoliths from this region [*Ross*, 1983]. These samples show a sharp downward increase in strain rate at depths of 50-60 km, which may indicate a transition from lithosphere to convecting asthenosphere.

3.7.5 Summary of backarc thermal structure

The above observations indicate extremely high temperatures at depth below the northern Cascadia backarc. Taken together, the temperature at the Moho (~35 km depth) appears to be 800-1000°C, with no indication of significant lateral variations for ~500 km eastward of the Cascade volcanic arc. These high temperatures are consistent with a relatively thin lithosphere (50-60 km).

The good agreement between the different observations suggests that the thermal structure of this region has not changed significantly within the last few 10's of millions of years. Seismic velocities and electrical conductivity measurements reflect the present thermal regime. On the other hand, surface heat flow represents the thermal structure over the last 10-80 my, due to the large time constant for heat diffusion. Xenolith data and backarc volcanics represent the thermal conditions at the time of extrusion.

All of the above observations indicate that temperatures in the lowermost crust are greater than 800°C, which is much higher than the solidus temperature for wet lower crustal rocks. For example, phase diagrams for gabbro show that the wet (water-saturated) solidus is ~700°C at 35 km depth; the dry solidus is ~1100°C [e.g., *Peacock and Wang*, 1999]. There is no obvious geological or geophysical evidence for significant melting of the lower crust in the Canadian Cordillera, which may indicate that the lower crust is dry. This is difficult to explain, as this region is underlain by a subducting slab that is dehydrating and releasing water upward. The apparent discrepancy between the inferred high temperatures and lack of evidence for significant crustal melting remains an important unresolved question.

Both high surface heat flow and high temperatures at depth suggest that the heat flow from the mantle is fairly high. As shown above, the reduced heat flow for the Cascadia backarc is ~60 mW/m^2. This is the heat flow resulting from the sum of deep crustal heat generation (below ~10 km), and heat flow from the mantle. Radiogenic heat production in the mid-to-lower crust is relatively uncertain, but it is unlikely to be more than 1.0 $\mu W/m^3$ [*Rudnick and Fountain*, 1995]. The amount of heat production decreases as the metamorphic grade increases. For the Cascadia backarc, *Hyndman and Lewis* [1999] prefer high heat generation in the crust below 10 km depth (0.9 $\mu W/m^3$), consistent with an amphibolite composition. The other end-member is a granulite facies lower crust, with a heat production of 0.4 $\mu W/m^3$ [*Rudnick and Fountain*, 1995 and references therein]. *Lewis et al.* [2003] and *Flück* [2003] suggest an intermediate model where the heat production is 0.9 $\mu W/m^3$ in mid-crust (10-20 km), and 0.5 $\mu W/m^3$ at greater depths.

For the 35 km thick crust in the Cascadia backarc, the contribution to surface heat flow from radiogenic heat production below 10 km depth is 10, 17 and 23 mW/m^2, for the low, intermediate, and high heat production models, respectively. Thus, for a reduced heat flow of 60 mW/m^2, these models predict a mantle heat flow of 37-50 mW/m^2. In contrast, the mantle heat flow below cratons is estimated to be 10-15 mW/m^2 [e.g., *Jaupart et al.*, 1998].

3.8 Eastern Limit of the Cascadia Backarc

At the northern Cascadia subduction zone, the eastern limit of the hot backarc is concluded to coincide with the Rocky Mountain Trench (RMT), 500 km east of the subduction deformation front ("trench") [*Lowe and Ranalli*, 1993; *Hyndman and Lewis*, 1999]. There is a pronounced change in lithospheric properties from the west to east of the RMT, including: 1) a decrease in surface heat flow from 80-100 mW/m^2 to <60 mW/m^2 [*Hyndman and Lewis*, 1999 and references therein], 2) an increase in P_n velocities from 7.8-7.9 km/s to >8.0 km/s [*Clowes et al.*, 1995; *Burianyk and Kanasewich*, 1995], 3) an increase in continental crust thickness from ~35 km to ~50 km, with little change in elevation or gravity, suggesting a higher density (and cooler) mantle east of the RMT [*Hyndman and Lewis*, 1999], 4) an increase in effective elastic thickness from <25 km to >40 km [*Flück et al.*, 2003], and 5) a decrease in electrical conductivity in the lower crust and upper mantle [*Majorowicz and Gough*, 1991]. The RMT correlates well with the western edge of a high velocity region observed in seismic tomography studies to depths greater than 250 km [e.g., *Grand*, 1994; *van der Lee and Nolet*, 1997; *Fredericksen et al.*, 2001; *Goes and van der Lee*, 2002]. This boundary also marks the eastern extent of the Cenozoic basaltic volcanic centres that are scattered throughout the backarc [*Wheeler and McFeely*, 1991].

These observations suggest that temperatures at depth are much cooler east of the RMT, relative to the hot Cascadia backarc. Surface heat flow, P_n velocities, and xenolith data provide the main constraints on deep temperatures for this area. Unfortunately, it is difficult to obtain accurate heat flow measurements within the Foreland Belt due to fluid flow. In the adjacent Western Canada Sedimentary Basin (WCSB), surface heat flow values of 50-70 mW/m^2 are observed, although there is evidence of significant fluid flow within the sediments [*Majorowicz and Jessop*, 1981]. Once possible high heat generation in the 3-5 km thick sediment section is considered, the heat flow for the basement rocks is suggested to be 50-56 mW/m^2 [*Hyndman and Lewis*, 1999]. Surface heat flow for the exposed Archean craton, located further to the east and to the north is slightly lower, 42±10 mW/m^2 [*Jaupart et al.*, 1998; *Jaupart and Mareschal*, 1999].

Using the observed surface heat flow, geotherms were constructed for the WCSB and exposed North America craton. Following *Hyndman and Lewis* [1999], temperatures for the WCSB were calculated starting at a depth of 5 km, corresponding to the base of the sediment section. At this depth, the assumed temperature is 80°C, and the basement heat flow is taken to be 56 mW/m^2. The depth of the Moho for the WCSB is 45 km. For the exposed craton, a Moho depth of 40 km is used. In each model, the upper crustal thickness is 10 km and the lower crustal thickness is 30 km. As before, the *Sass et al.* [1992] formulation for thermal conductivity is used for both the crust and mantle (**Equation 3.6**). There is considerable uncertainty in the amount and distribution of radiogenic heat production in the crust. For the WCSB, *Hyndman and Lewis* [1999] suggest heat production of 2.3 $\mu W/m^3$ in the upper crust and an average of 0.6 $\mu W/m^3$ in the lower crust. For the craton in the Superior province, the average upper crustal heat production is 1.4±1.2 $\mu W/m^3$ [*Jaupart and Mareschal*, 1999], but there is some indication that the craton east of the WCSB may have lower heat production, 0.75±0.65 $\mu W/m^3$ [*Flück*, 2003]. At depth, the heat production is also uncertain and may range from 0.4-0.9 $\mu W/m^3$ [*Hyndman and Lewis*, 1999]. In the models, the upper crustal heat production is 1.4 $\mu W/m^3$ for the craton and 2.3 $\mu W/m^3$ for the WCSB. The lower crust is taken to have a heat production of 0.4 $\mu W/m^3$.

Figure 3.8 shows the calculated geotherm for each region. The estimated uncertainty in each geotherm is 20%. The higher heat flow and higher heat generation for the WCSB results in higher temperatures at depth relative to the exposed craton. These geotherms give Moho temperatures of 500-750°C for the WCSB and 320-480°C for the exposed craton. The WCSB temperatures are slightly higher than those calculated in previous studies (~565°C) [*Hyndman and Lewis*, 1999; *Flück*, 2003]. A better agreement would be obtained if the lower crustal heat generation was increased to 0.6 $\mu W/m^3$, similar to those studies.

P_n velocities provide further constraint on the temperature of the uppermost mantle. For the WCSB, the P_n velocities are ~8.1 km/s [*Zelt and White*, 1995]. P_n velocities are slightly higher below the exposed craton, ~8.2 km/s [*Mooney and Brocher*,

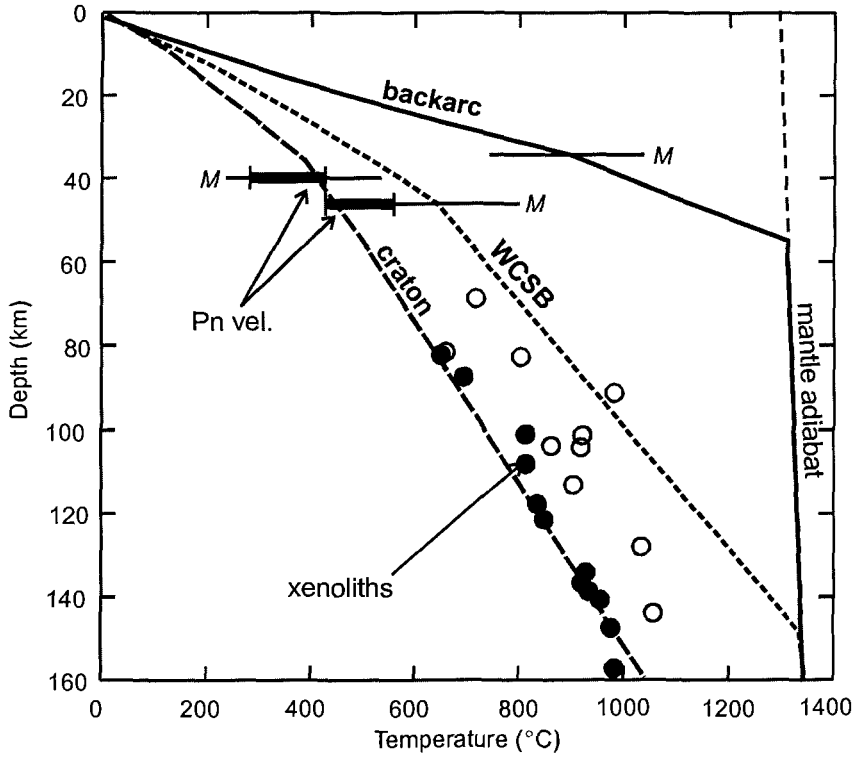

Figure 3.8. Calculated geotherms for the Western Canada Sedimentary Basin (WCSB) and exposed North America craton from surface heat flow. Note that each geotherm has an uncertainty of 20%. Low temperatures at depth are supported by P_n velocities for both regions and mantle xenoliths for the Slave craton [*MacKenzie and Canil*, 1999 (open circles); *Russell and Kopylova*, 1999 (solid circles)]. For comparison, the average geotherm for the northern Cascadia backarc is also shown (based on Figure 3.7).

1987]. Using **Equation 3.8** and assuming an uncertainty of 0.05 km/s, calculated Moho temperatures are 420-555°C and 285-420°C, for the WCBS and exposed craton, respectively. For the craton, the upper mantle temperature is also constrained using thermobarometry measurements on upper mantle xenoliths from kimberlite pipes in the Slave craton (**Figure 3.8**) [*MacKenzie and Canil*, 1999; *Russell and Kopylova*, 1999]. For the craton, temperatures from P_n velocities and xenoliths are in fair agreement with the calculated geotherms. For the WCSB, Moho temperatures from P_n velocities are slightly lower than those calculated from heat flow. With an increased lower crustal heat production, the calculated geotherm would be slightly cooler, and the two observations would be in better agreement.

Based on these observations, the Moho temperature below the WCSB appears to be 450-600°C, and the Moho temperature below the exposed craton is 350-450°C.

These are both much less than the Cascadia backarc Moho temperature (800-1000°C). For the craton, heat flow and heat generation data suggest a reduced heat flow of 30-35 mW/m^2, with a mantle heat flow of 10-15 mW/m^2 [*Jaupart et al.*, 1998; *Jaupart and Mareschal*, 1999; *Russell and Kopylova*, 1999], which is about one-third of that estimated for the backarc (see above). Such low temperatures result in a much thicker lithosphere below WCSB and craton. For the craton, thermal arguments suggest a conductive lithosphere thickness of 200-250 km [*Jaupart et al.*, 1998]. This is consistent with the inferred lithosphere thickness from seismic studies [*van der Lee and Nolet*, 1997; *Frederiksen et al.*, 2001; *Goes and van der Lee*, 2002].

The thermal difference between the hot backarc and terranes to the east is reflected in the contrasting deformation styles on either side of the RMT [*Lowe and Ranalli*, 1993; *Hyndman and Lewis*, 1999]. Whereas deformation in the Cordillera generally involves the entire crust (i.e., thick-skinned deformation), deformation in the Foreland Belt is confined to the uppermost part of the sedimentary sheets; the underlying crystalline crust and mantle are relatively undeformed (i.e., thin-skinned deformation).

The RMT is proposed to mark the western margin of the unextended part of the North America craton [*Hyndman and Lewis*, 1999]. The original rifted margin of Rodinia was located further west than the RMT, as illustrated by the presence of craton material in the Cordillera. However, it is suggested that crustal extension and lithosphere thinning associated with rifting did not extend further east than the RMT. The unextended part of the North America craton has existed as a stable region since the Archean. The observed cool temperatures at depth, in addition to the long-term stability of cratons, suggest that cratonic mantle is isolated from the global mantle convection system. *Jordan* [1975] argues that the stability is the result of both an increase in mantle viscosity associated with lower temperatures and chemical depletion of basaltic minerals through the removal of Fe and other heavy elements. Chemical depletion will lower the mantle density, compensating for the thermally-induced density increase, as well as increasing the mantle viscosity [*Jordan*, 1975; *Forte and Perry*, 2000]. The cratonic mantle may also contain significantly less water than the adjacent oceanic/backarc mantle, further increasing its viscosity and lithosphere strength [*Hirth et al.*, 2000].

3.9 Discussion

The thermal structure of the mantle wedge and backarc regions of a subduction zone provides important constraints for geodynamic models of subduction zones. One characteristic of nearly all subduction zones is the presence of an active volcanic arc. Petrologic studies indicate that the generation of arc magmas at subduction zones requires temperatures greater than 1200°C in the mantle wedge below the arc. To understand how heat is transported to the magma source region, it is important to constrain the temperatures in the backarc mantle.

For the northern Cascadia subduction zone, surface heat flow, seismic velocities, xenoliths, and numerous other observations indicate extremely high temperatures at shallow depths. Temperatures at the Moho (35 km depth) are inferred to be 800-1000°C, and temperatures at the base of the lithosphere (50-60 km depth) are ~1200°C. The high temperatures appear to be related to an enhanced mantle heat flow (37-50 mW/m^2) below this area. The high temperatures extend for 500 km east of the arc, with no significant lateral variation. The eastern limit of the hot backarc coincides with the Rocky Mountain Trench, which marks the western edge of the unextended North America craton. A variety of observational constraints (e.g., surface heat flow, seismic velocity, effective elastic thickness) indicate that the deep temperatures east of this boundary are significantly less than those in the backarc. The occurrence of such high temperatures in the backarc is contradictory to the expected cooling due to the underlying subducting plate. Although the Juan de Fuca Plate is fairly young (<10 Ma), seismic studies indicate the presence of the slab as a high velocity anomaly to at least 300 km depth [*Bostock and van Decar,* 1995]. The high backarc temperatures are even more surprising, due to the cool craton on the eastern edge of the backarc.

Observations of high backarc temperatures and high heat flow in many western Pacific subduction zones have often been attributed to recent or on-going extension/spreading of the backarc [e.g., *Watanabe et al.*, 1977]. For the Cascadia backarc, there is no evidence of current extension. There was a short-lived (<10 my) extension event in the Eocene that affected only a small area in the easternmost Omineca Belt (49-50°N). It has been suggested that extension may be the cause of the present

high temperatures and heat flow [e.g., *Bardoux and Mareschal*, 1994]. However, *Liu and Furlong* [1993] document abundant evidence that indicates high temperatures prior to extension in the Omineca Belt. For example, thermochronologic studies on exposed metamorphic core complexes give temperatures of 700°C at 25 km depth immediately before extension. Although the crust was in the process of shortening and thickening before the Eocene extension, *Liu and Furlong* [1993] show that an additional heat source is required to explain the high temperatures, because the time scale of shortening is insufficient to generate high temperatures by radioactive heating and shear heating. High temperatures at depth prior to extension are further supported by geologic observations that suggest that the Eocene extension was the result of gravitational collapse of a thermally-weakened 60 km thick crust [*Liu and Furlong*, 1993; R. Thompson, personal communication, 2003].

Although Eocene extension may have affected the thermal regime in the easternmost Omineca Belt, the widespread high backarc temperatures and inferred high mantle heat flow require an ongoing process, where large amounts of heat are carried into the backarc by mantle flow [*Hyndman and Lewis*, 1999]. It has been suggested that the Cascadia backarc, as well as regions to the north and south, overlie a region of upwelling of anomalously hot mantle [e.g., *Gough*, 1986]. The current study supports an explanation of convective upwelling in the mantle, but suggests that it is not unique to this region. As shown in the next chapter, nearly all backarcs appear to be extremely hot (relative to cratons). This implies that a hot backarc is a characteristic feature of subduction zones and may be a direct result of backarc mantle dynamics associated with the subduction process [e.g., *Davis and Lewis*, 1984]. Numerical models that explore the mantle flow regime that maintains the observed high temperatures are presented in **Chapters 7 and 8.**

CHAPTER 4
Backarc Thermal Structure II – A Global Survey

4.1 Introduction

In the previous chapter, it was shown that the backarc regions of the Cascadia subduction zone are anomalously hot for over 500 km behind the volcanic arc. The high temperatures appear to be related to backarc mantle flow, but whether this reflects mantle flow associated with subduction or mantle flow unique to Cascadia is unclear. A critical question is whether all subduction zone backarcs are hot.

A characteristic of nearly all subduction zones is the presence of an active volcanic arc, which implies high temperatures (>1200°C) in the mantle wedge below the arc (see **Chapter 3**). Of most importance to this thesis study is the thermal structure of the uppermost mantle in the backarc regions behind the arc. Temperatures here can be constrained using the observational techniques outlined in **Chapter 3**. Three important indicators of high temperatures (>800°C) at shallow depths (~40 km) in the backarc are:

- surface heat flow greater than 70 mW/m^2 for backarcs with continental crust of average thickness (35-40 km) and average radiogenic heat production (1-1.3 $\mu W/m^3$ in the upper 10 km, and 0.4-0.9 $\mu W/m^3$ in the lower 25-30 km). For a backarc with oceanic crust, similar high mantle temperatures are implied by a surface heat flow of 60 mW/m^2 or greater, as there is less crustal radiogenic heat production in oceanic crust.
- P_n velocity of 7.85 km/s or less. From the *Black and Braile* [1982] relation (**Equation 3.8**), these velocites correspond to temperatures of 800°C or more in the mantle immediately below the Moho.
- seismic velocities slower than global average mantle velocities. A 100°C increase in mantle temperature causes a decrease in seismic velocity of ~1% for P-waves and ~2% for S-waves [*Goes et al.*, 2000; *Wiens and Smith*, 2003]. By assuming

an average mantle temperature profile, seismic velocity can be used as a proxy for mantle temperature [e.g., *Goes et al.*, 2000]. Note that low velocities generally indicate high temperatures, but that the presence of partial melt and/or volatiles (e.g., water) may also affect velocites, especially the S-wave velocities.

Other important constraints on backarc mantle temperatures come from P-T estimates from mantle xenoliths, effective elastic thickness, lithosphere thickness, electrical and magnetic studies, and isostasy studies to infer the density (and thus temperature) of the backarc mantle. It should be noted that there are large uncertainties associated with each of the above methods. However, a fairly good constraint on mantle temperatures can be obtained using two or more independent observational techniques that give consistent temperatures.

In this chapter, the thermal structure of the backarcs of a number of subduction zones is examined (**Figure 4.1**). The discussion first focusses on subduction zones that have had no recent backarc extension. The thermal structure of these backarcs is inferred

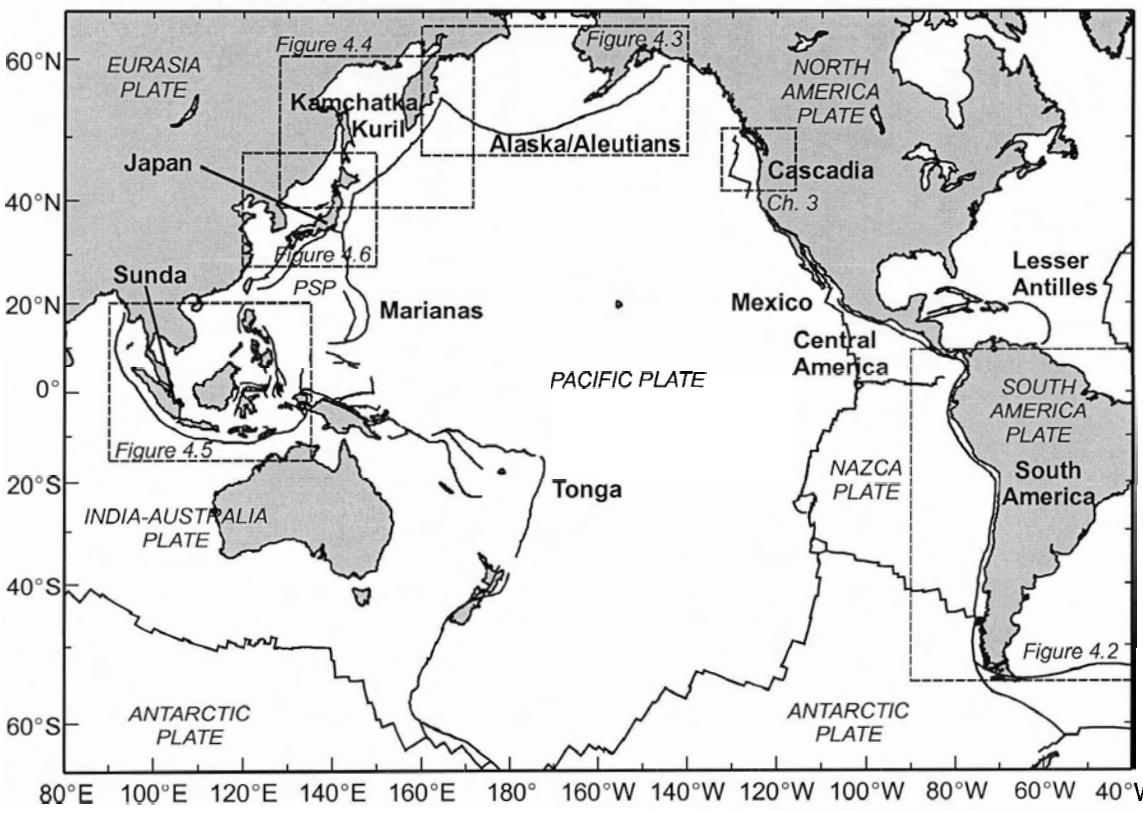

Figure 4.1. Location of subduction zones discussed in text. Names of main tectonic plates are also shown. PSP is the Philippine Sea Plate.

to be primarily controlled by subduction-related processes. This is followed by a brief overview of the thermal structure along the convergent margins of southern Europe and Asia. A discussion of backarcs with recent or on-going extensional backarcs is then given. The thermal structure of these regions is complicated by extension and spreading, making it difficult to determine the thermal effects of subduction alone. Next, the thermal structure of two regions that are in the backarc of former subduction zones is summarized. Temperatures of these areas provide valuable information about the thermal effects of the termination of subduction. In nearly all cases, the observations indicate high temperatures in the mantle of both present-day and recent backarcs. The important exception is that several regions with a flat subducting slab do not appear to be hot. The chapter ends with a discussion of the implications of the observed high backarc temperatures.

4.2 Non-extensional Backarcs

There are six subduction zones where there has been no significant backarc extension over the last 50 my: 1) northern Cascadia (see **Chapter 3**), 2) Mexico/Central America, 3) South America, 4) Alaska/eastern Aleutians, 5) Kamchatka, and 6) Sunda. For each of the latter five regions, a literature review was undertaken to establish constraints on the backarc thermal structure, following the observational techniques given above. **Table 4.1** gives the available observations for each backarc.

4.2.1 Mexico/Central America

Northern Mexico and the backarc regions of the Mexico subduction zone appear to be hot. Heat flow over northwestern Mexico is generally high, 70-100 mW/m^2, with a reduced heat flow of ~60 mW/m^2 [*Smith et al.*, 1979], similar to that in the Canadian and US Cordillera. Subduction in northern Mexico terminated at ~12.5 Ma [*Klitgord and Mammerickx*, 1982]. The thermal regime in northwestern Mexico may be affected by the proximity of active extension in the Gulf of California, but the high heat flow appears to extend well east of this extension area. Further south, few thermal data are available for

Table 4.1. Observational constraints on thermal structure of non-extensional backarcs.

	North. Cascadia	Mexico/ Central America	Central Andes	South Chile	Alaska/ Aleutian	Kam-chatka	Sunda
surface heat flow	x	x	x	x	x	x	x
P_n velocity	x	x	x		x	x	
seismic tomography	x	x	x	x	x	x	x
seismic attenuation			x				
earthquake depths	x						
eff. elastic thickness	x						
isostasy/ gravity	x	x				x	
electricity/ magnetics	x		x				
xenoliths	x		x	x	x		
backarc volcanism	x		x	x	x		

the backarc regions of the present Mexico subduction zone. Six heat flow measurements in the backarc of the present-day subduction zone yield an average of 89±27 mW/m^2 [*Ziagos et al.*, 1985].

Further support for high temperatures at depth is suggested by seismic tomography studies that show that Mexico is underlain by a low velocity mantle [*Grand*, 1994; *van der Lee and Nolet*, 1997; *Goes and van der Lee*, 2002]. Shear wave velocities are 3-4% lower than reference earth models to depths of at least 200 km. There is some indication that the velocity anomaly below Guererro has a lower amplitude than regions to the north and south, which may be related to the proposed flat slab in this area and hence the absence of a thick mantle wedge [*van der Lee and Nolet*, 1997] (see the flat slab discussion below). A regional seismic study of northern and central Mexico gives P_n velocities of 7.8±0.2 km/s [*Gomberg et al.*, 1988], characteristic of upper mantle

temperatures greater than 800-1000°C. High mantle temperatures are also suggested by the high elevation of this region (1.5-3 km), although the crust has a normal thickness of ~40 km [*Gomberg et al.*, 1988 and references therein].

Seismic tomography shows that the low mantle seismic velocities below Mexico extend south through Central America to depths of at least 200 km [*Grand*, 1994; *van der Lee and Nolet*, 1997; *Goes and van der Lee*, 2002]. Shear-wave velocity anomalies up to 4% slower than global average velocities occur in a ~1500 km wide band that underlies Central America and adjacent regions in the Caribbean Sea. Heat flow for the Caribbean Sea is 50-60 mW/m^2 [*Epp et al.*, 1970; *Global Heat Flow Data Base*, 2004]. The basement of the Caribbean Sea is an oceanic plateau, which is thought to have been created at ~90 Ma during the Cretaceous superplume event [*Meschede and Frisch*, 1998]. The observed heat flow is slightly higher than expected for oceanic crust of this age. This region is unusual in that it forms the backarc of two subduction zones, the Central America subduction zone on the west and the Lesser Antilles on the east. Simultaneous subduction has been ongoing for at least 85 my [*Meschede and Frisch*, 1998]. In addition to a complicated history of subduction, the thermal regime may also be affected by a proposed slab window associated with subduction of the Cocos-Nazca spreading ridge near 10°N [*Johnston and Thorkelson*, 1997]. With the absence of a slab below this region, high temperature mantle from below the slab may enter the mantle wedge through the window, increasing the wedge temperatures near the window.

4.2.2 South America

The South America subduction zone follows a similar tectonic history to that of North America, with over 200 my of continuous subduction [*Atwater*, 1989]. Along most of the margin, the Nazca Plate subducts below the continental South America Plate (**Figure 4.2**). South of the intersection of the Chile Rise spreading centre with the trench (~46°S), the subducting plate is the Antarctic Plate. Like North America, South America can be divided into a western orogenic belt (the Andes) and a cratonic region further east. Crustal thickness is 30-40 km for most of the Andes [e.g., *Meissnar et al.*, 1976; *Robertson Maurice et al.*, 2003], except in the Altiplano/Puna area (15-30°S) where

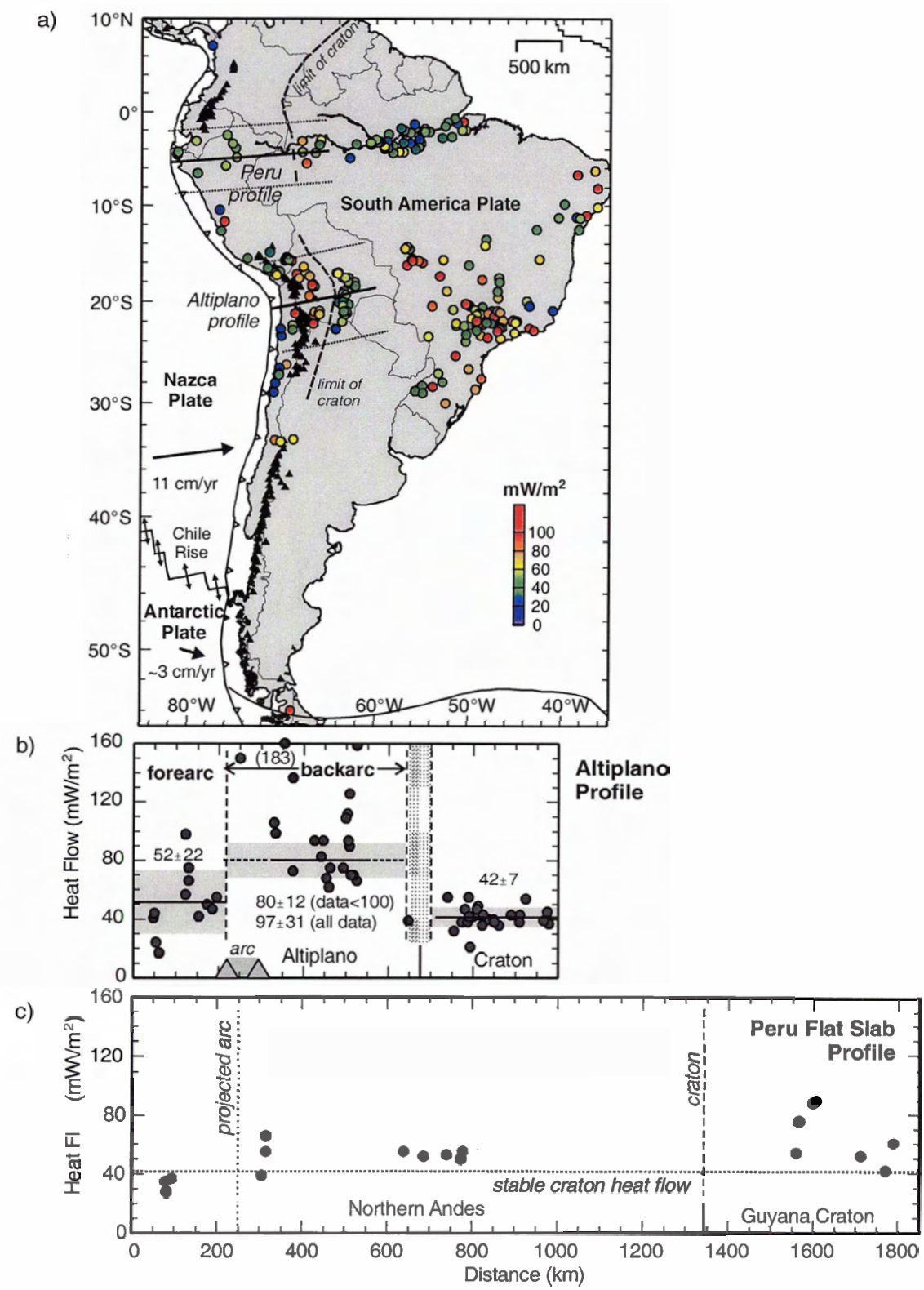

Figure 4.2. Map of heat flow measurements for South America (see legend). Dashed lines are the western limit of the stable craton [after *Hamza and Munoz*, 1996]. Solid lines are profile locations (dotted lines show swath width for profiles). b) Heat flow profile for the Altiplano/Puna area. c) Heat flow profile for the Peru flat slab area, with the projected location of the arc (based on the volcanoes to the north).

crustal thickness reaches 70 km [e.g., *Beck et al.*, 1996; *Allmendinger et al.*, 1997]. Volcanism along western South America occurs in three distinct segments along the margin. The gaps in the volcanic arc (2-15°S and 28-34°S) coincide with regions where the subducting plate flattens to near-horizontal at a depth of ~100 km [*Cahill and Isacks*, 1992].

Seismic tomography studies show that the subducting plate below South America is imaged as a high velocity region [e.g., *van der Lee et al.*, 2001]. In the mantle wedge below areas with an active volcanic arc, anomalously low velocities are observed (up to 10% less than average mantle velocities). The entire width Andes orogenic belt is characterized by low seismic velocities to depths of at least 150 km. The eastern limit of low velocities coincides with the western extent of the cratons that make up eastern South America. Below the cratonic regions, high seismic velocities are imaged to depths greater than 100 km, suggesting the presence of thick, cool lithosphere.

Hamza and Munoz [1996] summarize surface heat flow data for South America. Data from this compilation, as well as 14 additional observations for the Altiplano region [*Springer and Forster*, 1998] are shown on **Figure 4.2a**. Note that the complete data set is plotted for the western part of South America; some values east of 50°W have been omitted.

Below, observations constraining the thermal structure in southernmost South America and the central Andes are discussed in greater detail. These two regions have been the focus of numerous studies. Later in the chapter (**Section 4.6**), observations for the Peru flat slab region will be presented.

Southern Chile/Argentina (south of 30°S)

There is only one recorded surface heat flow measurement for southernmost South America (**Figure 4.2a**). However, high geothermal gradients (>30°C/km) have been measured in oil exploration wells in the backarc of this region, suggesting high surface heat flow and high temperatures at depth [*Hamza and Munoz*, 1996]. Seismic studies show that S-wave velocities in the upper mantle are 4.3-4.4 km/s (~5% slower

than global average velocities) and that the lithosphere in this area is relatively thin (~60 km) [*Robertson Maurice et al.*, 2003].

The backarc is also characterized by sporadic Plio-Quaternary basaltic volcanism, particularly south of 39°S [*Stern et al.*, 1990]. Geochemical studies on these magmas suggest that they were generated by a relatively small amount of partial melt in the upper mantle, induced by minor thermal and mechanical perturbations in a mantle that is close to its solidus temperature [*Stern et al.*, 1990]. Upper mantle xenoliths have been recovered from the Pali-Aike basalt field (~52°S, 70°W). Geothermobarometry measurements on these samples yield temperatures of 970°C at 1.9 GPa (~60 km depth), increasing to 1160°C at 2.4 GPa (~75 km depth) [*Stern et al.*, 1999]. Such high temperatures suggest a thin lithosphere (< 100 km) below southern Chile. The thermal structure in this area may be affected by the subduction of the Chile Rise spreading centre at ~46°S, which may have produced a slab window. However, it is difficult to explain the inferred regionally extensive high temperatures by the slab window model.

Central Andes (15-30°S)

The central Andes region is the best-studied part of the South America margin. In this region, the Andes orogenic belt is divided into the Altiplano plateau in the north and Puna plateau in the south. Both are characterized by high elevations (3.5-4 km) and thick crust (60-75 km) [e.g., *Allmendinger et al.*, 1997]. Geological evidence shows that these are relatively young plateaus, formed primarily by tectonic shortening and thickening of western South America [*Allmendinger et al.*, 1997]. Thickening in the Altiplano region began about 25 Ma and continued to 6-12 Ma. In the Puna region, thickening started at 15-20 Ma and ceased at 1-2 Ma. The shortening/thickening mechanism appears to be complex, with evidence for both underthrusting, as well as more uniformly distributed crustal thickening (i.e., pure shear) [*Allmendinger and Gubbels*, 1996].

The active volcanic arc associated with the subduction zone lies near the western edge of the Altiplano/Puna. There is a noticeable contrast in surface heat flow on either side of the arc (**Figure 4.2b**). Over the forearc, heat flow is ~50 mW/m^2, consistent with

Nazca Plate subduction and with little friction along the subduction thrust fault (shear stress of ~15 Ma) [*Springer*, 1999]. In the backarc, heat flow is ~80 mW/m^2 over a distance of over 400 km east of the arc. There have been few radiogenic heat production studies for South America [*Hamza and Munoz*, 1996]. The measured K, Th, and K content in exposed basement sections in the central Andes (21-27°S) indicate a near-surface radiogenic heat production of 1.3 $\mu W/m^3$ [*Lucassen et al.*, 2001]. The depth distribution is not constrained. The eastern limit of high heat flow appears to be the edge of the Brazilian Shield craton. Heat flow east of this averages 42 mW/m^2, a typical value for Archean cratons [e.g., *Jaupart and Mareschal*, 1999]. This heat flow profile is very similar to that of northern Cascadia, suggesting a hot backarc sandwiched between a cool forearc and cool craton.

In addition to surface heat flow, there are numerous observations to suggest that the Altiplano/Puna crust is extremely hot. At depths greater than 20 km, the crust is characterized by low P-wave velocities (V_P), extremely low S-wave velocities (V_S), a high V_P/V_S ratio, and low density [*Schmitz et al.*, 1997; *Baumont et al.*, 2002; *Yuan et al.*, 2002; *ANCORP Working Group*, 2003]. Note that crustal seismic velocities are more sensitive to composition than temperature. The observed velocities are consistent with a felsic crust to depths of 50-55 km [e.g., *Yuan et al.*, 2002]. This is supported by the abundance of granitoid lower crustal xenoliths from the backarc in this region [*Lucassen et al.*, 1999]. Low S-wave velocities and the high V_P/V_S ratio indicate the presence of a small amount of melt in the lower crust [*Yuan et al.*, 2002], which is consistent with observations of high lower crustal electrical conductivity [*ANCORP Working Group*, 2003 and references therein]. In seismic reflection studies, a region of high reflectivity has been identified at ~20 km depth [*ANCORP Working Group*, 2003]. As the reflectors occur near the top of the low velocity/high conductivity region, it has been suggested that they represent the top of a partially molten region in the crust. The presence of partial melt in the lower crust requires high temperatures in the mid-to-lower crust. Further constraints on crustal temperature are provided by widespread Late Miocene-Early Pliocene ignimbrites throughout the backarc [*Allmendinger et al.*, 1997]. These magmas appear to have resulted from large amounts of melting of a thickened felsic crust.

Petrologic data indicates pre-eruptive temperatures of 700-800°C at mid-crustal depths [*Babeyko et al.*, 2002 and references therein]. Taken together, the above observations suggest a temperature of ~800°C at 20-25 km depth in the Altiplano/Puna backarc crust.

High heat flow and high crustal temperatures in the central Andes backarc have often been attributed to increased radiogenic heat production associated with the thick continental crust. However, as noted by *Babeyko et al.* [2002], crustal thickening only occurred within the last 25 my. For crustal thickening by pure shear (vertical stretching of the crust), the surface heat flow will first decrease, followed by an increase as the crust is heated from below and by radiogenic heating. *Babyeko et al.* [2002] showed that the effects of thickening should still dominate the present-day surface heat flow, due to the short time since thickening.

In addition, to produce high temperature in the mid-lower crust by radiogenic heating, it is not sufficient to simply double the thickness of the near-surface radiogenic layer; this layer must be thrust to great depths. *Liu and Furlong* [1993] developed numerical models for the thermal evolution of crustal thickening by the thrusting of one crustal sheet over another. Although they focussed on the southeastern Canadian Cordillera, their results illustrate that the crustal heating after thickening is a slow process. Even after 100 my (which is much longer than the time scale for Altiplano thickening), the effects of thermal relaxation, radiogenic heating, and shear heating due to thrusting are insufficient to generate high temperatures in the mid-crust.

The numerical models suggest that the high crustal temperatures cannot be adequately explained by processes associated with crustal thickening. In addition, it is unlikely that the crust will deform and thicken unless it is hot and weak first. This is supported by lower crustal xenoliths from the Altiplano backarc that suggest that the crust in this region was anomalously hot *before* crustal thickening occurred. Thermobarometry studies of mafic granulite xenoliths from the Salta Rift (~24°S, 66°W) give temperatures of 850-900°C at 0.95-1.05 GPa (~30 km depth) [*Lucassen et al.*, 1999]. Dating of the samples showed that these conditions were recorded at 90 Ma. There are also samples of upper mantle xenoliths from this location, which record temperatures of

1000-1200°C at 1.3-1.5 GPa (~45 km depth) [*Lucassen et al.*, 1999]. Based on this data, the thickness of the Altiplano crust at 90 Ma is inferred to have been ~35 km, with Moho temperatures of ~900°C.

High crustal temperatures before thickening and 10-20 my after thickening suggest a deep, long-lived heat source. Indeed, both *Babeyko et al.* [2002] and *Liu and Furlong* [1993] note that enhanced mantle heat flow may be required to explain the high temperatures in thickened crust. This is consistent with observations of present-day high temperatures in the mantle below the crust. Shear wave tomography images show that backarc mantle velocities are up to 7% slower than global mantle velocities to depths of 150 km [*van der Lee et al.*, 2001]. The low seismic velocities are attributed to the combined effects of increased volatiles in the mantle, due to dehydration of the subducting slab, as well as temperatures of ~1200°C in the mantle. Surface wave dispersion studies also indicate a low velocity upper mantle below the Altiplano backarc [*Baumont et al.*, 2002]. From a seismic refraction study, P_n velocities are moderately low (8-8.1 km/s) below the Altiplano, and increase abruptly to 8.2 km/s at the boundary between the backarc and craton [*Baumont et al.*, 2001]. Using the *Black and Braile* [1982] relation (**Equation 3.8**), the Altiplano P_n velocities suggest Moho temperatures of 490-630°C. However, the crustal thickness in this region is ~70 km, and thus, the higher velocity (relative to the Cascadia backarc) may be partially due to the greater depth [e.g., *Christensen*, 1979], not lower temperatures. It should also be noted that the data are from an unreversed seismic profile, which leads to large uncertainties in the velocities.

Low seismic velocities in the backarc upper mantle are coupled with high seismic attenuation to a depth of 100 km [*Haberland and Rietbrock*, 2001], further supporting high temperatures and/or the presence of partial melt or fluids. Finally, there are several Oligocene to Recent basaltic (i.e., mantle-derived) volcanic centres and fissure flows scattered in the backarc of the Altiplano/Puna region [*Allmendinger et al.*, 1997]. Taken together, the above observations suggest that the backarc crust and upper mantle of the central Andes are extremely hot over the ~400 km width of the backarc.

4.2.3 Alaska and the eastern Aleutians

At the Alaska/Aleutian subduction zone, the Pacific Plate subducts beneath the North America Plate at a rate of 6-7 cm/yr (**Figure 4.3**). Below Alaska and the Bering Sea shelf, the over-riding plate is continental crust, consisting of terranes accreted to North America during the Jurassic [*Fliedner and Klemperer*, 2000]. West of the shelf edge, the basement of the Aleutian Basin is oceanic crust, overlain by up to 4 km of sediments. This part of the backarc was formed in the early Eocene (50-55 Ma), when subduction along the then-active Beringian margin (near the Bering Sea Shelf edge) jumped southwest to its present location, trapping a fragment of oceanic crust. The trapped crust is generally thought to be early Cretaceous in age (117-132 Ma), although this is still under debate [*Cooper et al.*, 1992]. Subduction along the Alaska/Aleutian margin has been stationary for the last 50 my. There is evidence of recent (<20 Ma) backarc spreading in the Komandorsky (or Kamchatka) basin, the most western part of the backarc [*Cooper et al.*, 1992 and references therein]. This is consistent with very high heat flow (>100 mW/m^2) observed in this area.

The rest of the backarc is considered to be inactive, with no significant extension. In the Aleutian basin, the main constraint on thermal structure comes from surface heat flow observations [*Langseth et al.*, 1980; *Global Heat Flow Database*, 2004]. **Figure 4.3** shows the heat flow as a function of latitude for the Aleutian Basin. Most values are 40-80 mW/m^2, with no clear decrease with distance from the arc. If the three values greater than 100 mW/m^2 are excluded, the mean heat flow for the Aleutian basin is 61±17 mW/m^2. *Langseth et al.* [1980] note that rapid sedimentation rates in the Aleutian Basin, especially over the last 10 my, may have a significant effect on surface heat flow and suggest that the observed heat flow should be increased by 16-22% to correct for sedimentation. With this correction, the mean heat flow for the Aleutian basin becomes 71-74 mW/m^2. The Aleutian Basin heat flow is significantly higher than the expected heat flow for ~120 my old oceanic crust (44-50 mW/m^2) [*Parsons and Sclater*, 1977; *Stein and Stein*, 1992]. This discrepancy could indicate that the Aleutian Basin crust is younger than previously thought [*Langseth et al.*, 1980; *Cooper et al.*, 1992], although the observed heat flow requires a crustal age that is similar to the time that the crust was

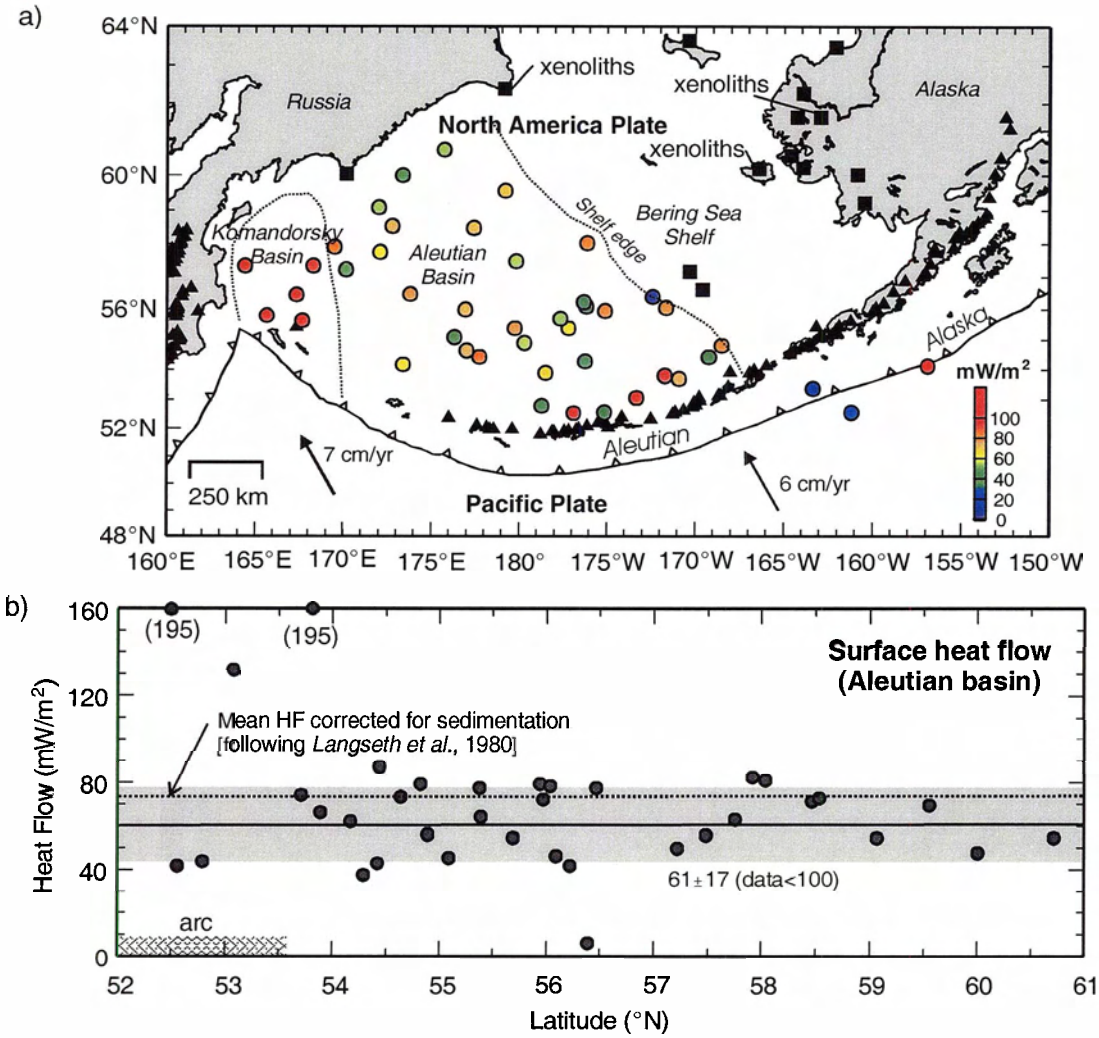

Figure 4.3. a) Map of the Alaska/Aleutian subduction zone. Triangles are active arc volcanoes; squares are volcanic fields of the Bering Sea basalt province [after *Akinin et al.*, 1997]; circles are heat flow measurements (see legend). The xenolith locations are also shown. b) Surface heat flow as a function of latitude for the Aleutian basin.

trapped in the backarc (~50 Ma), rather than the inferred ~120 Ma age. There is also some evidence for recent faulting and possible minor extension in the basin, which would perturb the heat flow [*Cooper et al.*, 1992]. Alternatively, the high heat flow may represent enhanced temperatures in the mantle wedge and backarc of the Aleutian subduction zone. This model is supported by seismic studies that show P_n velocities of 7.8-8 km/s throughout the Aleutian basin [*Levshin et al.*, 2001].

There are no heat flow data for the backarc in the Bering Shelf nor continental Alaska regions. However, there are at least 15 distinct basaltic volcanic fields scattered

in the backarc (**Figure 4.3**). These volcanic fields, which form the Bering Sea basalt province, are all younger than 10 Ma [*Akinin et al.*, 1997]. In three fields, upper mantle xenoliths have been recovered. Calculated equilibrium temperatures for the xenoliths are 850-1030°C at an assumed pressure of 1.5 GPa (~45 km) based on mineral phase assemblages [*Akinin et al.*, 1997]. There have also been numerous seismic studies across the eastern part of the backarc, which indicate low velocities in the uppermost mantle. P_n velocities are ~7.8 km/s beneath the Bering Sea shelf [*Fliedner and Klemperer*, 2000; *Levshin et al.*, 2001]. Below continental Alaska, P_n velocities are 7.8-8 km/s [*Stone et al.*, 1987; *McNamara and Pasyanos*, 2002; *Levshin et al.*, 2001]. A seismic tomography study of Alaska gives similar low upper mantle P-wave velocities and shows that these low velocities extend to at least 150 km depth in the mantle [*Zhao et al.*, 1995].

Heat flow over the Aleutian Basin, as well as backarc volcanics, xenoliths and seismic velocities studies over the Bering Sea Shelf and continental Alaska, suggest high backarc mantle temperatures for more than 700 km north of the Alaska/Aleutian arc. As noted by *Cooper et al.* [1992], the tectonics of the Aleutian backarc may be more complex than previously thought. Although some backarc extension cannot be ruled out, the spatial extent and apparent uniformity of the high temperatures seems to require a more widespread process.

4.2.4 Kamchatka

The Kamchatka subduction zone lies southwest of the Aleutian subduction zone and is the most northern part of the ~5500 km long subduction system that includes the Mariana, Izu-Bonin, NE Japan and Kuril subduction zones (**Figure 4.4**). The Kamchatka backarc crust is composed of arc terranes and oceanic plateaus that have been accreted to northeast Asia [*Konstantinovskaia*, 2001]. The Kamchatka-Kuril backarc is generally considered to be part of the North America Plate. However, recent plate models suggest that the Kamchatka Peninsula and Sea of Okhotsk may form the Okhotsk microplate [*Seno et al.*, 1996]. The present subduction margin was established by at least 50 Ma [*Konstantinovskaia*, 2001]. Prior to this, the tectonic history is fairly complex, with possible evidence for a short period of southeast-directed subduction from 65-55 Ma.

Despite these complexities, there is no evidence for recent extension in the Kamchatka backarc. It is well-established that the Kuril backarc basin (southernmost Sea of Okhotsk) was formed by spreading between 32 and 15 Ma [*Baranov et al.*, 2002]. The region of extension is southeast of the study area, and thus the thermal structure in the

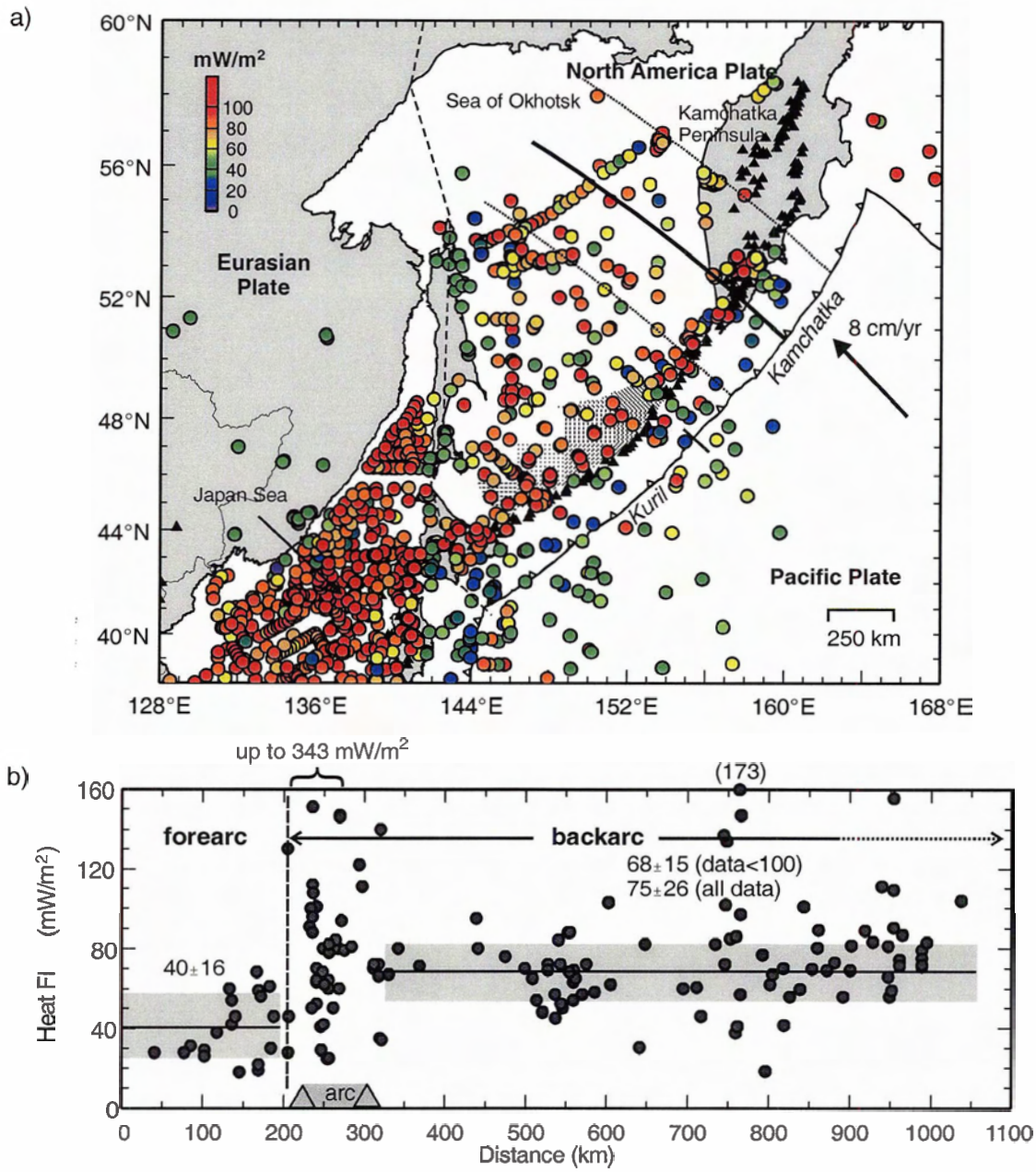

Figure 4.4. a) Map of the Kuril-Kamchatka subduction zone with observed surface heat flow (see legend). Solid line shows the heat flow profile; dotted lines are the width of data used in the profile. The dashed line shows the inferred boundary between the North America and Eurasian Plates. The hatched area is the region of extension for the Kuril backarc [after *Mantovani et al.*, 2001]. b) Surface heat flow data as a function of distance from the trench. Measurements within 300 km of the profile line in (a) are shown.

Kamchatka backarc is inferred to be relatively unaffected by extension.

For the Kuril-Kamchatka subduction zone, surface heat flow is generally low over the forearc and high over the arc. The Sea of Okhotsk is characterized by relatively high heat flow, although there is some scatter in the data (**Figure 4.4a**) [*Watanabe et al.*, 1977 and references therein; *Sugrobov and Yanovsky*, 1993; *Global Heat Flow Database*, 2004]. Along a profile through the Kamchatka backarc, the mean heat flow is 75±26 mW/m^2 for all data and 68±15 mW/m^2 if data greater than 100 mW/m^2 are excluded. As the crust in this region is mostly oceanic, radiogenic heat production is expected to be fairly low. Thus, these heat flow values suggest high mantle heat flow and high mantle temperatures, consistent with other non-extensional backarcs.

Additional constraints on the backarc mantle thermal structure come from seismic and gravity studies. Most studies have concluded that the upper mantle below the Kamchatka Peninsula and Sea of Okhotsk is characterized by low seismic velocities. Mantle P-wave velocities (from tomography and refraction studies) are up to 6% slower than global velocity models [e.g., *Gorbatov et al.*, 1999, *Levshin et al.*, 2001]. This is in agreement with seismic studies that show that the upper mantle (~35 km depth) below the Kamchatka peninsula has S-wave velocities that are ~7% less than global velocity models [*Shapiro et al.*, 2000]. Low mantle velocities are also observed in surface wave studies in this region [e.g., *Kaila and Krishna*, 1984; *Ritzwoller and Levshin*, 1998]. An early gravity study showed that the Kamchatka forearc and arc regions are characterized by high gravity values, consistent with the presence of a cool, dense subducting slab [*Kogan*, 1975]. In contrast, the backarc has relatively low gravity values, which were modelled using a hot, low density backarc mantle.

The heat flow, seismic and gravity observations all point to a hot backarc mantle for the Kamchatka subduction zone. The thermal structure of the northernmost Kamchatka backarc may be affected by the proximity of the edge of the subducted Pacific Plate, which could represent a region of complex mantle flow and unusual thermal conditions. However, mantle temperatures appear to be high well away from this boundary, and far from the inferred region of Oligocene-Miocene extension in the Kuril

backarc, suggesting that another mechanism, such as backarc mantle flow, is required to maintain the hot conditions.

4.2.5 Sunda

The Sunda subduction zone (Sumatra/Java region of Indonesia) marks the northward subduction of the Indian-Australian Plate beneath the continental Eurasian Plate (**Figure 4.5a**). Tectonic reconstructions suggest that the Sunda backarc immediately behind the arc has been relatively stable for at least 50 my [*Lee and Lawver*, 1995]. Surface heat flow values were obtained from the *Southeast Asia Heat Flow Database* [2004]. Most of the measurements in the region are oil company data, and thus are confined to sedimentary basins and are of relatively low accuracy.

Figure 4.5 shows two heat flow profiles through this region. For both profiles, heat flow is generally low over the forearc and high in the backarc for over 1000 km behind the arc. The eastern profile has the best heat flow coverage, with backarc values of 70-80 mW/m^2. Heat flow appears to be slightly higher (~100 mW/m^2) along the western profile. *Puspito and Shimazaki* [1995] suggest that variations in heat flow between the two areas are due to variations in crustal composition and thickness; the higher heat flow in the west may be associated with higher crustal radiogenic heat production.

Along the western profile, the heat flow measurements are distributed in two distinct clusters. In the cluster immediately north of the volcanic arc, heat flow is extremely high (>100 mW/m^2), with significant scatter. *Thamrin* [1985] attributes the high heat flow to shallow magmatic diapirism associated with the nearby active volcanic arc and to perturbations associated with Tertiary faulting and folding of the basin sediments. In addition, the granitoid rocks that form the basement of the basin may be enriched in radiogenic elements U, Th, K [*Gasparon and Varne*, 1995]. Heat production in the uppermost basement may be as high as 5 $\mu W/m^3$. Thus, upper basement heat generation may account for up to 50 mW/m^2 of surface heat flow, assuming a standard 10 km thickness for the enriched layer. Even with the enhanced crustal heat production, the

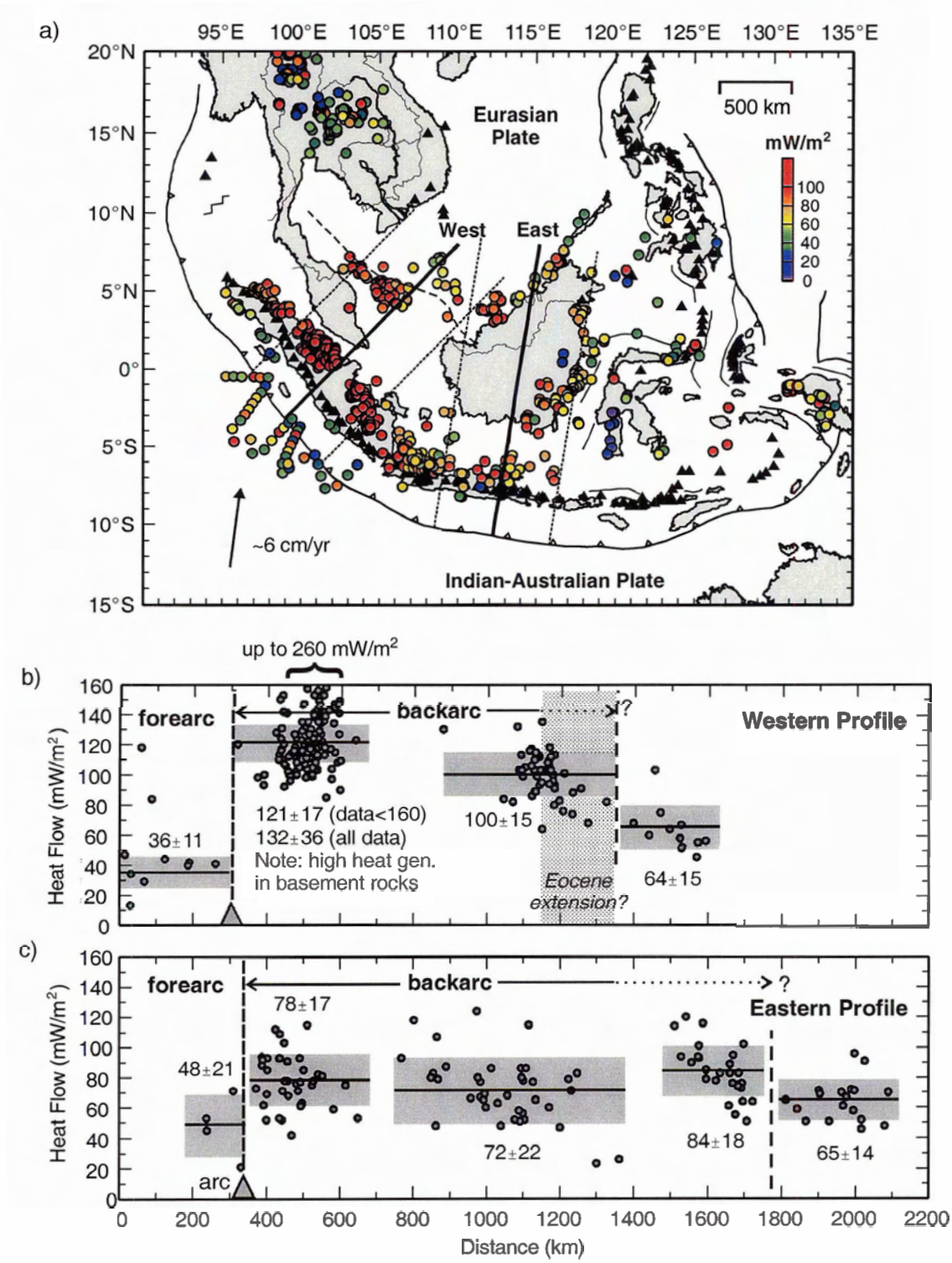

Figure 4.5. a) Map of the Sunda subduction zone with observed heat flow (see legend). Solid lines show the heat flow profiles; dotted lines show the width of data used for each profile. The inferred region that underwent extension in the Eocene is shown with a dashed line [after *Lee and Lawver*, 1995]. Surface heat flow profiles for the b) western and c) eastern profiles. Each profiles uses data within 400 km of the profile line. The mean heat flow (with standard deviation) is given for each data block.

average reduced surface heat flow is still above 70 mW/m^2, indicative of high temperatures at depth.

Heat flow remains high (80-90 mW/m^2) well into the backarc for the western profile, although there is a large gap in the data. Some of the high heat flow between 1000 and 1300 km from the trench may be associated with possible minor extension in this region between 30 and 40 my [*Lee and Lawver, 1995*]. North of the inferred extensional region, heat flow decreases to ~64 mW/m^2. This may mark the northern limit of the hot backarc, but there are no additional observations to support this.

Further evidence for high mantle temperatures in the Sunda backarc is provided by P-wave tomography studies that indicate upper mantle velocities that are ~2% slower than global mantle velocity models [*Puspito and Shimazake*, 1995; *Widiyantoro and van der Hilst*, 1997]. Unfortunately, no other observations could be found to further constrain the thermal structure.

4.2.6 Summary

The above discussion has focussed on five subduction zone backarcs where there has been no significant extension in the last 50 my. In all backarcs, surface heat flow is generally high and seismic velocities are several percent lower than global average mantle velocities, suggesting an anomalously hot backarc mantle. Additional observations (e.g., backarc volcanism, P-T estimates for xenoliths, isostasy studies) also indicate high temperatures at depth. These observations are similar to those for the northern Cascadia backarc (see **Chapter 3**).

4.3 Southern Europe and Asia

Another area where the thermal effects of subduction can be examined is southern Europe and Asia. This region is dominated by plate convergence. In southern Europe, convergence between the Eurasia and Africa Plates has produced a series of subduction zones (e.g., Aegean, Tyrrhenian), many with present-day backarc spreading, as well as numerous orogenic belts (e.g., Alps, Apennines). Convergence between the Arabia and Eurasia Plates in western Asia has resulted in the development of the Iran-Turkey plateau

orogenic belt. Further east, convergence between the India-Australia and Eurasia Plates has produced the Makran subduction zone (east of India) and the Himalaya mountains (north of India).

The tectonics of this region are highly complex, particularly in southeastern Europe. A detailed examination of the individual subduction/collision zones along the southern Eurasia margin is deferred to a future study. It is useful to point out some general characteristics. Surface heat flow in southern Europe is high (>60 mW/m^2), with heat flow >100 mW/m^2 in some regions [*Cermak and Rybach*, 1979; *Cermak*, 1993; *Global Heat Flow Database*, 2004]. The mantle heat flow is inferred to be >30 mW/m^2 [*Cermak*, 1993; *Artemieva and Mooney*, 2001]. Although there are fewer heat flow measurements in southern Asia, the backarc regions of the subduction/collision margin are characterized by high heat flow and high mantle heat flow [*Artemieva and Mooney*, 2001]. For this region, inferred temperatures at 50 km depth are >1000°C [*Artemieva and Mooney*, 2001].

Several studies have looked at seismic velocities below southern Europe and Asia. Both regions are characterized by low upper mantle seismic velocities from surface wave tomography and P_n velocity studies [*Ritzwoller and Levshin*, 1998; *Ritzwoller et al.*, 2002]. The lowest seismic velocities appear to coincide with regions of thickened crust in the areas of continental collision (Himalayas/Tibet and the Turkish-Iranian plateau). Tomography images using P- and S- waves for southern Europe show low velocities to depths of more than 100 km, with velocities more than 5% slower than global mantle velocities [*Goes et al.*, 2000]. Using a velocity-temperature relation, *Goes et al.* [2000] suggested that these velocities correspond to temperatures of 1000°C or more at 50 km depth. Overall, surface heat flow and upper mantle seismic velocities point to high mantle temperatures in the backarcs regions of the southern Europe and Asia convergent system, but a more detailed study is required to better constrain the thermal regime of individual backarcs.

4.4 Backarcs with Recent or On-going Extension

4.4.1 General observations

More than half of present-day subduction zones either have present-day backarc spreading (e.g., Marianas), or have experienced spreading and extension in the recent (<50 Ma) past (e.g., NE Japan). The process of spreading causes substantial crustal extension, as well as the creation of new oceanic crust in the backarc. The driving mechanism for backarc extension/spreading remains a topic of debate. One issue is whether there is a causal relationship between subduction and backarc extension, as implied by the observation that these types of ocean basins are only associated with subduction zones [e.g., discussion by *Mantovani et al.*, 2001].

Regardless of the mechanism, extension and spreading have a significant effect on the thermal structure of the backarc. The processes of thinning the lithosphere through extension increases lithosphere temperatures, resulting in higher heat flow. At the backarc spreading centre, the upwelling of hot mantle also leads to increased temperatures and heat flow, similar to a spreading ridge. These processes are super-imposed on the thermal effects of subduction. Extensional backarcs exhibit extremely high heat flow [e.g., *McKenzie and Sclater*, 1968; *Oxburgh and Turcotte*, 1968; *Sclater*, 1972; *Watanabe et al.*, 1977], as well as low seismic velocities and high seismic attenuation [e.g., *Zhao*, 2001; *Wiens and Smith*, 2003], indicative of high temperatures in the backarc mantle. The question is whether these backarcs are hotter than expected, both in the areas where the oceanic crust that has undergone extension and for the newly-formed oceanic crust at the backarc spreading centre.

Early studies by *Sclater* [1972] and *Watanabe et al.* [1977] concluded that the heat flow for many western Pacific backarcs is much greater than expected for the age of oceanic crust. For backarcs with crust older than 30-40 Ma, *Watanabe et al.* [1977] argue that the surface heat flow is 80-90 mW/m^2, regardless of basin age, which they attribute to enhanced convection in the backarc asthenosphere. For oceanic crust created at a mid-ocean ridge, the cooling plate models predict a surface heat flow of 40-60 mW/m^2 for crustal ages greater than 30 Ma [e.g., *Parsons and Sclater*, 1977; *Stein and Stein*, 1992]. However, other studies of backarc heat flow have suggested that with a re-analysis of the

heat flow data and more accurate basin ages, the heat flow may not be significantly higher than that of "normal" oceanic crust [e.g., *Sclater et al.*, 1976; *Anderson*, 1980].

The depth of the backarc can also be used as an indicator of its thermal structure; seafloor depth increases as the crust ages and cools. It has been noted that many western Pacific extensional backarcs have depths that are up to 1 km *larger* than expected for their age, although there is scatter in the data [e.g., *Sclater*, 1972; *Sclater et al.*, 1976; *Watanabe et al.*, 1977; *Park et al.*, 1990]. For regions with an anomalously hot mantle, the seafloor should be shallower than expected. One possible explanation for the observed large depths is that the backarc crust is thinner than normal oceanic crust [*Sclater*, 1972], although there is no clear evidence that this is the case [*Anderson*, 1980; *Wheeler and White*, 2002]. Alternatively, the backarc bathymetry may be dynamically controlled by the subducting plate [*Sclater*, 1972]. This is supported by the observation that deeper basins are associated with more steeply dipping slabs [*Park et al.*, 1990]. On the other hand, early gravity studies suggested that the majority of backarcs are in isostatic equilibrium [*Slater et al.*, 1976; *Watanabe et al.*, 1977], which would rule out dynamic effects. In addition, there is no evidence for significant dynamically-controlled subsidence over many western Pacific backarcs from analyses of bathymetry, geoid and gravity data [*Billen and Gurnis*, 2001; *Wheeler and White*, 2002].

A full analysis of the thermal structure of extensional backarcs is beyond the scope of this thesis study, due to the complexity in separating the extension-related and subduction-related thermal effects. However, it is worthwhile to point out several key observations, using the Japan Sea as an example.

4.4.2 Extension in the Japan Sea

The Japan Sea forms the backarc of the present-day SW and NE Japan subduction zones (**Figure 4.6**). The Japan Sea opened between 30 and 12 Ma, as the Japanese Islands were separated from mainland Asia by dextral shear and counterclockwise rotation [*Jolivet et al.*, 1994]. The basement of the Japan Sea is composed of highly extended continental crust and oceanic crust intruded during the opening of the Japan

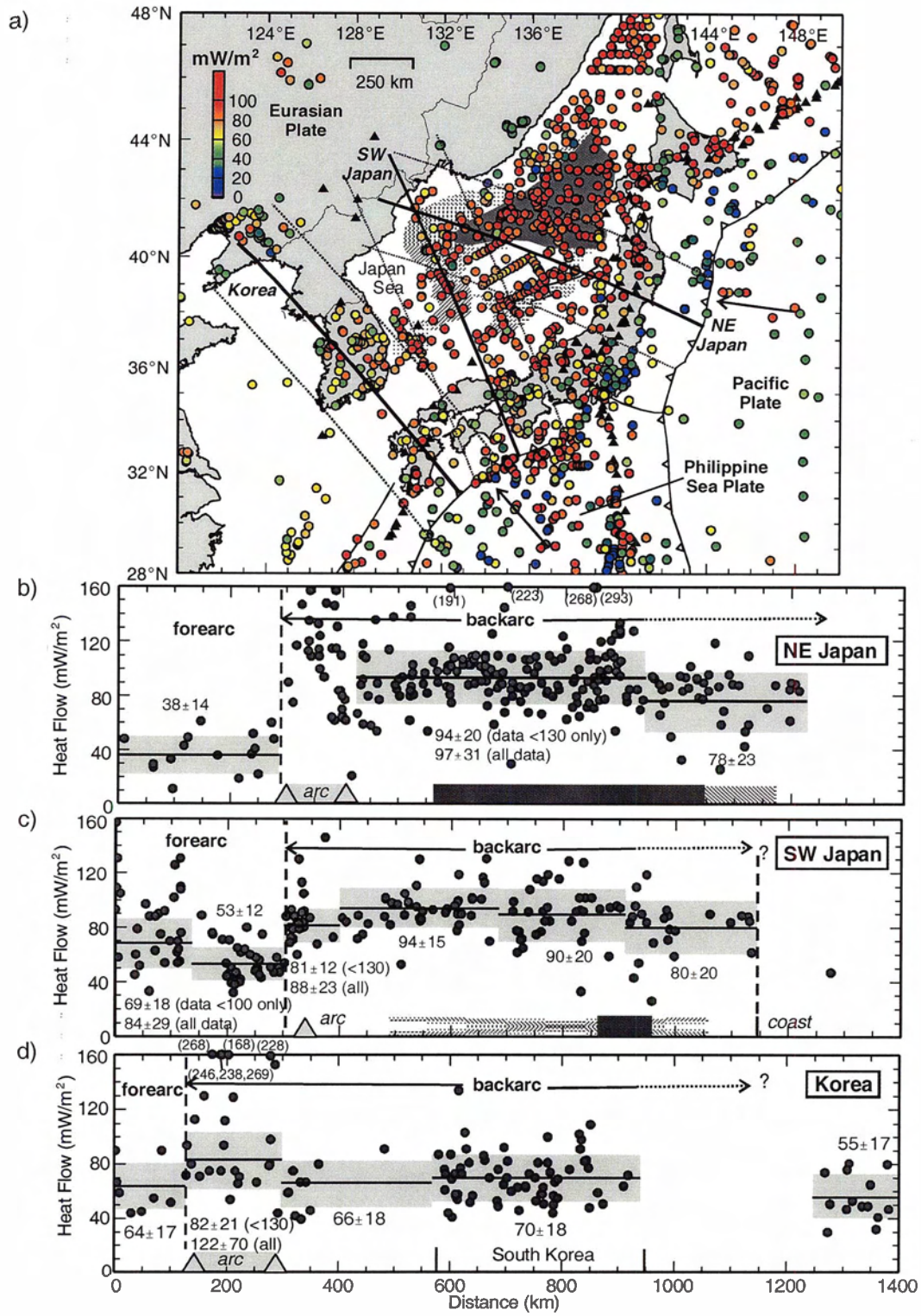

Figure 4.6. a) Heat flow for the Japan region. In the Japan Sea, the hatched region shows the area with significant stretching/extension, and the dark shading shows the area of new oceanic crust created during Japan Sea opening (~12-30 Ma) [after *Jolivet et al.*, 1994]. Solid lines show profile locations; dashed lines show profile width (400 km total). b) NE Japan heat flow profile, with mean and standard deviation of heat flow for each segment. Hatched bar shows area with significant extension; dark area shows region with new oceanic crust. c) SW Japan heat flow profile. d) Korea heat flow profile.

Sea. **Figure 4.6a** shows the region where new oceanic crust was formed, as well as the regions with greatest extension. Opening of the Japan Sea was completed by 12 Ma, and was replaced by E-W compression, which continues to the present.

The heat flow data in **Figure 4.6** are from a compilation by *Yamano* [1995]. Profiles taken through the NE and SW Japan subduction zones illustrate the contrast in heat flow between the forearc and backarc regions (**Figure 4.6 b, c**). Forearc heat flow is higher for SW Japan, due to the younger age of the subducting plate and slower subduction rate [e.g., *Peacock and Wang*, 1999]. At the volcanic arc, the heat flow exhibits a fair amount of scatter. In the backarc, heat flow is extremely high and fairly constant throughout the Japan Sea, where the average heat flow is ~95 mW/m^2. The remarkable uniformity of the heat flow has been noted by previous authors [e.g., *Watanabe et al.*, 1977]. High heat flow is also found on the Korean Peninsula, which is composed of continental crust that has not experienced extension. Here, the average heat flow is 70 mW/m^2, which is similar to regions of the northern Cascadia backarc where surface heat generation is ~1 $\mu W/m^3$.

Additional observations also indicate high crust and mantle temperatures throughout the Japan Sea and adjacent regions. Upper mantle xenoliths from the eastern coast of Honshu (NE Japan) suggest temperatures of ~1000°C at 40 km depth, which are consistent with upper mantle temperatures inferred from heat flow [*Nakajima and Hasegawa*, 2003 and references therein]. High temperatures at depth well behind the arc are indicated by the presence of Neogene to Quaternary basalt fields on the northeastern China coast, west of the region of Japan Sea extension. Seismic tomography studies show low velocities beneath the entire Japan Sea, with velocities up to 6% slower than global mantle models [*Ritzwoller and Levshin*, 1998; *Zhao*, 2001 and references therein]. For NE Japan, the lowest velocities are found in a dipping layer ~50 km above the top of the subducting slab, extending from below the volcanic arc to depths > 150 km. A similar dipping low velocity zone is imaged below Tonga-Lau [*Zhao*, 2001; *Wiens and Smith*, 2003]. For both regions, the ratio of the P to S velocity anomalies suggests that there is less than 1% partial melt in the wedge (at the 25-50 km resolution of the studies) [*Wiens and Smith*, 2003]. It is interpreted that the low velocities represent a combination

of high temperature and increased volatile content. In particular, the dipping layer of low velocities is attributed to a region of hydrated mantle, caused by fluid flux from the subducting slab.

In addition to low seismic velocities, high seismic attenuation is observed in the mantle to depths of at least 200 km throughout the Japan Sea [*Flanagan and Wiens*, 1994; *Nakajima and Hasegawa*, 2003]. Using a theoretical relation between attenuation and temperature, *Nakajima and Hasegawa* [2003] determined the thermal structure of the mantle wedge for NE Japan to a distance of ~100 km behind the arc. With the uppermost mantle temperatures from xenoliths as a reference, they showed that the mantle wedge temperature increases from ~1000°C at 40 km depth to ~1200°C at 100 km depth. This is 200°C cooler than suggested by *Tatsumi et al.* [1983] on the basis of petrologic studies of arc magmas for this area.

It is unclear if extension and backarc spreading are sufficient to explain the high temperatures for the Japan Sea. In the region of new oceanic crust, the average crustal age is ~20 Ma and the average heat flow is 100±10 mW/m^2. Note that the observed heat flow has not been corrected for the effects of sedimentation. The expected heat flow for crust of this age is 105-115 mW/m^2 [*Parsons and Sclater*, 1977; *Stein and Stein*, 1992], in good agreement with that observed. However, the crust is fairly young, and thus, may not have reached the "backarc steady-state heat flow" proposed by *Watanabe et al.* [1977]. In addition, high heat flow is not confined to the region of backarc spreading. There is no significant variation in heat flow for the Japan Sea, despite heterogeneities in the amount of extension and the creation of oceanic crust within a concentrated region. These two observations appear to require an anomalously hot mantle throughout the Japan Sea and adjacent regions.

4.4.3 Are extensional backarcs anomalously hot?

Heat flow measurements, seismic velocity, seismic attenuation, and other observations indicate high temperatures in the upper mantle for the Japan Sea and other extensional backarcs [e.g., *Flanagan and Wiens*, 1994; *Zhao*, 2001; *Wiens and Smith*, 2003]. It remains uncertain whether these extensional backarcs are hotter than expected

for their age and amount of extension. Since the initial publications in the 1970's, there have been no further detailed studies that have examined the thermal structure of extensional backarcs in general. An updated study is certainly warranted. Such a study should examine:

- observational constraints on the thermal structure, including surface heat flow, seismic velocities and attenuation, xenoliths, and petrological constraints from arc and backarc magmas. Of particular importance is the lateral variation in the thermal structure, relative to the location of the backarc spreading centre(s) and regions of greatest backarc extension.
- depth of the basement and the crustal thickness
- sediment cover and sedimentation history of the basin; sediments will affect the rate of cooling of the basin, the observed surface heat flow, and the subsidence of the basin
- opening history of the basin, including accurate dating of the oceanic crust created during basin opening and estimates of the amount of extension

The thermal structure of the basins can be compared to that expected for extended crust and for oceanic crust created at mid-ocean ridge [e.g., *Parsons and Sclater*, 1977; *Stein and Stein*, 1992] to determine if extension/spreading is sufficient to explain the observations, or if an additional heat source is required.

4.5 Former backarcs

From the above discussion, it appears that nearly all present-day backarcs are hot. This may reflect a characteristic feature of subduction zones, which may be associated with subduction–related backarc mantle flow (see discussion below). If this is true, it is important to examine areas that are located in the backarcs of former subduction zones. The thermal structure of these areas provides constraints on how mantle temperatures evolve once subduction stops. The critical range for this evolution appears to be approximately 300 my after the termination of subduction [*Hyndman et al.*, submitted manuscript, 2004]. Two examples that span this age range are the central/northern Canadian Cordillera (~42 Ma) and the Appalachians (~260 Ma).

4.5.1 Central and Northern Canadian Cordillera

Present-day subduction at the Cascadia subduction zone terminates at ~51°N. However, heat flow and other temperature-sensitive indicators suggest that the high temperatures observed in the northern Cascadia backarc extend to the north through the central Canadian Cordillera (51-59°N) and northern Canadian Cordillera (59-64°N). These regions once formed the backarc regions for subduction of the Farallon and Kula Plates below North America. Plate reconstructions suggest that subduction in this area stopped at ~42 Ma [*Engebretson et al.*, 1985]. Presently, both regions are bounded on the west by the Queen Charlotte-Fairweather transform fault system. The eastern limit of each is the stable North America craton.

The central and northern Cordillera are characterized by high surface heat flow of 78 and >100 mW/m^2, respectively [*Lewis et al.*, 2003, and additional measurements by T. Lewis, as reported by *Flück*, 2003]. The higher heat flow for the northern Cordillera is attributed to a greater radiogenic heat production in the upper crust (>4 μW/m^3), such that the reduced heat flow for both regions is ~60 mW/m^2 [*Lewis et al.*, 2003]. High temperatures at depth are supported by: 1) low P_n velocities (7.8-7.9 km/s) [*Lewis et al.*, 2003 and references therein], 2) low upper mantle velocities from seismic tomography [*Grand*, 1994; *Frederiksen et al.*, 1998, 2001], 3) a small effective elastic thickness (<30 km) [*Flück et al.*, 2003], 4) P-T estimates from xenoliths [*Harder and Russell*, submitted manuscript, 2004], 5) observations of high elevations although the crust is only 32-35 km thick [*Lewis et al.*, 2003], and 6) deformation styles that suggest a thin, weak lithosphere [*Lewis et al.*, 2003]. All observations indicate that the thermal structure of the central and northern Canadian Cordillera is similar to that of the northern Cascadia backarc.

The origin of a hot crust and mantle in the central and northern Cordillera is enigmatic. One possibility is that the high temperatures result from backarc mantle flow associated with past subduction in this region [*Lewis et al.*, 2003]. This implies that subduction-related mantle flow persists for over 40 my after subduction ceases.

4.5.2 Appalachians

The Appalachian mountains in eastern North America represent an orogenic belt developed by the accretion and subsequent deformation of arcs and micro-continents to the eastern margin of the North America craton [e.g., *Hatcher*, 1989; *Keller and Hatcher*, 1999]. The Appalachians are part of the former backarc regions of primarily westward-directed subduction associated with closing of the Iapetos/Theic/Rheic Oceans between 500 and 260 Ma. The last major period of deformation was the Alleghanian Orogeny (325-260 Ma), which resulted in the final closure of the Rheic Ocean, as the North America and Africa cratons collided.

The present-day surface heat flow over the Appalachians is 50-60 mW/m^2 [*Jaupart et al.*, 1982; *Jaupart and Mareschal*, 1999], which is slightly higher than that of the adjacent North America craton, 42 ± 10 mW/m^2. However, it appears that much of the difference in heat flow can be explained by higher radiogenic heat production in the Appalachian crust, such that the reduced heat flow of both regions is similar, 30-40 mW/m^2 [*Jaupart et al.*, 1982; *Jaupart and Mareschal*, 1999]. *Artemieva and Mooney* [2001] suggest that there may be higher temperatures at depth and a thinner thermal lithosphere below the Appalachians, due to a slightly higher mantle heat flow. From their study, they determined a temperature of 700-800°C at 50 km depth for the Appalachians, compared to 500-600°C for the craton.

In seismic tomography images, the Appalachian mantle is characterized by only a small S-wave velocity anomaly (generally <1%), relative to average mantle velocities [*Grand*, 1994; *van der Lee and Nolet*, 1997; *Goes and van der Lee*, 2002]. In contrast, mantle velocities below the craton are 2-4% faster than average velocities to depths >250 km. This velocity contrast may reflect 100-300°C higher temperatures in the upper mantle below the Appalachians (relative to the craton), although variations in composition and volatile content also affect velocities [*Goes and van der Lee*, 2002]. This temperature difference is consistent with that inferred from heat flow data [*Artemieva and Mooney*, 2001].

Overall, it appears that the thermal structure of the Appalachians is only slightly hotter than the adjacent craton. If the excess heat comes from backarc processes

associated with past subduction in this area, this suggests that much of the thermal anomaly decays within 300 my after subduction ceases.

4.6 Flat slab subduction

Nearly all of backarcs discussed above have characteristics indicative of high temperatures in the uppermost mantle well behind the volcanic arc, such as high surface heat flow and low upper mantle seismic velocities. The only evidence that any backarc is cool comes from regions where the subducting slab flattens to near-horizontal in the shallow mantle (depths of 100 km or less).

The most clear example of this is the Peru flat slab region of South America (2-15°S). Heat flow data from the northern part of this region shows that there is little variation in heat flow across the margin [*Hamza and Munoz*, 1996] (**Figure 4.2c**). Values closest to the coast are 30-40 mW/m^2. Further inland, heat flow remains fairly low (~50 mW/m^2) across the northern Andes and into the eastern Guyana craton. There is no active volcanic arc in this region. Seismic tomography shows that the mantle below this part of the Andes has low velocities (relative to average mantle), but that the amplitude of the anomaly is reduced relative to regions to the north and south [*van der Lee* et al., 2001]. These observations suggest that the mantle overlying the Peru flat slab is cooler than other parts of the South America subduction zone backarc.

A flat slab has also been proposed for the Guererro region of the Mexico subduction zone [e.g., *Suarez et al.*, 1990; see also **Chapter 2**]. Here, the flat slab is at a depth of 50 km. There is some indication that the seismic velocities in mantle above the subducting slab in this region have slightly higher velocities than regions to the north and south [e.g., *van der Lee and Nolet*, 1997].

4.7 Discussion

For nearly all the present-day subduction zones examined in this study, surface heat flow, seismic velocities, and other thermal indicators suggest high temperatures in the backarc mantle. For these subduction zones, high temperatures are observed over

backarc widths of 400 km to over 1000 km. The only clear evidence for a cool backarc is in the Peru region of South America where a flat subducting slab is inferred.

Many subduction zones have active backarc extension/spreading. In these areas, the observed high temperatures may, in part, be due to these processes; further study is necessary to determine if an additional heat source from backarc convection is required. However, at six subduction zones with no recent backarc extension, all the thermal constraints examined indicate anomalously high backarc mantle temperatures (i.e., 800-1000°C at 40 km depth). For each subduction zone, the presence of a hot backarc is often interpreted using site-specific explanations. The most common are:

1. ***Thickened backarc crust.*** High surface heat flow in the Central Andes of South America is often attributed to increased radiogenic heat production in the thick (>60 km) over-riding crust. However, crustal thickening only occurred over the last 25 my and in a restricted area. Numerical modelling indicates that over this time, it is not possible to elevate crustal temperatures to the observed values through either crustal radiogenic heating or shear heating associated with thickening. Also, xenolith data suggests that the high temperatures existed well before crustal thickening, and present-day observations indicate high temperatures in the mantle wedge below the thickened crust.
2. ***Backarc extension.*** For backarcs with recent spreading, it is unclear whether the observed high temperatures can be completely explained by extension. Extension has also been used as an explanation for the high temperatures in the eastern Omineca Belt for the northern Cascadia backarc. However, this extension was confined to only a small geographic area and so does not explain the regionally high temperatures. In addition, geologic evidence indicates extremely high temperatures in the deep crust prior to extension.
3. ***The proximity of a slab window or slab edge.*** There is evidence for a slab window below southern Chile and parts of central America, as well as the presence of a slab edge at the northern Kamchatka subduction zone. Although mantle temperatures may be higher in the vicinity of the slab window/edge, it is difficult to explain observations of high temperatures throughout the entire backarc.

4. ***Trapped piece of young oceanic crust.*** Some backarcs are underlain by a fragment of oceanic crust trapped when the subduction zone location changed. It is suggested that the crust in these areas may be fairly young and therefore hot. However, for the Aleutian subduction zone, the surface heat flow suggest an age that is similar to the time when the crust was trapped (~50 Ma), rather than the inferred age of ~120 Ma.
5. ***Region of anomalous mantle upwelling.*** For the northern Cascadia subduction zone, as well as areas to the north and south, the high temperatures have been attributed to a mantle upwelling unique to this area, which carries high temperatures from depth to the uppermost mantle.

Although one or more of these factors may explain the high temperatures at one or several subduction zones, observations of similar high temperatures for nearly all backarcs (except those with a flat slab) suggests that a hot backarc is a characteristic feature of a subduction zone. Indeed, active volcanism at all subduction zones requires high temperatures (>1200°C) in the upper mantle above the subducting plate. The observations described above suggest that the high temperatures extend 100's to 1000's of kilometres into the backarc, with no indication for a significant increase in temperature near the arc.

Given that all subduction zones appear to be similarly hot, there may be a common subduction-related mechanism to produce the high temperatures. The current consensus is that flow within the mantle wedge advectively carries heat from outside the subduction zone into the backarc and mantle wedge (see **Chapter 1**). This model provides a mechanism to heat the backarc both during subduction and for some time after subduction has stopped. Observations of low temperatures over regions with a flat slab provide support for this model; the flat slab displaces the mantle wedge, and thus there is little material to undergo convection.

In subsequent chapters, possible flow geometries will be examined to investigate the thermal effects of mantle wedge flow. High backarc temperatures, particularly in areas that have not undergone recent extension, provide an important constraint for these

models. The two key constraints that must be matched are: 1) temperatures greater than 1200°C in the mantle wedge near the arc for magma generation, and 2) high and constant heat flow and upper mantle temperatures across backarc widths of 400 km or more.

CHAPTER 5
Seismic Anisotropy and Backarc Mantle Flow

5.1 Introduction

Observational constraints on mantle wedge flow patterns are critical for understanding the dynamics of the backarc mantle. In recent years, seismic anisotropy has become a powerful tool for constraining mantle flow, based on the assumption that there is a direct relationship between mantle strain and the development of seismic anisotropy. This chapter describes observations of seismic anisotropy in the mantle at subduction zones, primarily using the shear wave splitting technique. The chapter begins with the theoretical background for the observation and interpretation of seismic anisotropy. This is followed by a summary of shear wave splitting observations at the Cascadia subduction zone and a review of seismic anisotropy at subduction zones worldwide. Most of the Cascadia observations are part of a seismic anisotropy study that was carried out during this thesis research. Details of the study are given in *Currie et al.* [2004a]. The chapter ends with a discussion of the implications of anisotropy observations for mantle dynamics at a subduction zone.

5.2 Theoretical Background

5.2.1 Observational techniques

Seismic anisotropy occurs when the elastic properties of a material exhibit a directional-dependence. This results in a variation in seismic wave velocity with direction of propagation (azimuthal anisotropy) or with the polarization direction of the seismic wave (polarization anisotropy) [e.g., *Savage*, 1999]. Shear wave splitting is an example of polarization anisotropy. When a shear wave travels through an anisotropic material, it will split into two components, one that is polarized parallel to the fast direction of the material and one with an orthogonal polarization. The two components

travel at different velocities and thus become separated in time, producing the phenomenon called shear wave splitting. Shear wave splitting is characterized by two parameters: the polarization direction, or fast direction, of the first-arriving shear wave (which is related to the orientation of the anisotropy) and the delay time between the two shear waves (which is related to the amount of anisotropy).

Most shear wave splitting observations use recordings of shear waves that are at near-vertical incidence at the Earth's surface. The use of (near) vertically-propagating shear waves restricts observations to anisotropy that is in a near-horizontal plane. A high lateral resolution (~50 km) of the subsurface horizontal anisotropic structure can be obtained. The depth resolution is much poorer, as there is an exact trade-off between the thickness of the anisotropic layer and the amount of anisotropy within the layer.

For many regions, shear wave splitting is primarily observed using SKS waves, which are shear waves generated by conversion of P-waves at the core-mantle boundary. Therefore, any observed splitting is due to anisotropy along the travel path from that boundary to the station at the Earth's surface. A second source of shear wave splitting data comes from shear waves generated by local earthquakes. At some subduction zones, earthquakes within the subducting plate occur to great depths (up to 700 km). Shear waves from these earthquakes can be used to constrain anisotropy from the earthquake hypocenter to the Earth's surface. These observations are invaluable for constraining anisotropy within the mantle wedge [e.g., *Fouch and Fischer*, 1996].

5.2.2 Physical interpretation of anisotropy

Anisotropy has been observed in both the Earth's crust and mantle (see *Savage* [1999] for a review). Anisotropy can result from: 1) thin layering of otherwise isotropic material (e.g., lithologic layering, aligned dyke intrusions), 2) aligned, fluid-filled fractures or cracks, or 3) aligned anisotropic minerals. Within the mantle, the dominant source of anisotropy appears to be the strain-induced alignment of anisotropic mantle minerals, primarily olivine (i.e., mechanism 3) [e.g. *Silver and Chan*, 1991; *Savage*, 1999].

Laboratory studies on water-poor samples of olivine show that under moderate to large strains, olivine will deform by dislocation creep, resulting in a lattice preferred orientation (LPO) of the olivine crystal [e.g., *Karato*, 1987; *Nicolas and Christensen*, 1987; *Karato and Wu*, 1993; *Zhang and Karato*, 1995]. These studies indicate that the a-axis of olivine (the axis of fastest seismic velocity) tends to align with the direction of maximum extension for pure shear [e.g., *Nicolas and Christensen*, 1987; *Ribe*, 1992] and with the flow direction for progressive simple shear [*Zhang and Karato*, 1995]. Thus, for simple shear deformation of the mantle, as is the case for mantle flow, the direction of fast seismic velocity will indicate the flow direction. This is true for regions that do not contain much water. Recent studies show that the behaviour of olivine under water-rich conditions is more complicated. At high stresses, the fast axis of wet olivine may align *perpendicular* to the flow direction [*Jung and Karato*, 2001].

One key factor controlling the development of mantle anisotropy through LPO is temperature. At temperatures greater than 900°C, the grains are sufficiently mobile to develop LPO [*Karato and Wu*, 1993; *Savage*, 1999]. Thus, anisotropy may be actively produced by present-day mantle deformation. At lower temperatures, LPO cannot be produced by present-day deformation, but may be "frozen in" from a past episode of high-temperature deformation. Temperature also controls the maximum depth of mantle anisotropy. The maximum depth is determined by the rheological transition from dislocation creep to diffusion creep, which depends on both temperature and pressure [*Karato*, 1992]. For regions that are hot, the maximum depth of anisotropy is expected to be less than 250 km, corresponding to a shallow dislocation-diffusion creep transition. For cooler regions, anisotropy may extend to greater depths. Most mantle seismic anisotropy originates in the upper mantle; the transition zone and lower mantle are inferred to be largely isotropic [e.g., *Fouch and Fischer*, 1996; *Savage*, 1999]. Seismic studies and analyses of mantle xenoliths suggest that the amount of anisotropy in the upper mantle ranges from 0 to 5% [*Savage*, 1999 and references therein].

Seismic anisotropy at subduction zones is complex, with numerous sources for anisotropy, including the over-riding crust, mantle wedge, subducting lithosphere, and mantle below the subducting lithosphere. Anisotropy in the over-riding crust usually

appears to be small compared to that in the mantle [e.g., *Savage*, 1999]. It is difficult to separate the effects of anisotropy within the subducting lithosphere from that in the asthenosphere below. Many studies have argued that fossil anisotropy in the subducting lithosphere is fairly small, based on the expected fast directions based on plate motions [e.g., *Kaneshima and Silver*, 1995; *Fouch and Fischer*, 1996; *Polet et al.*, 2000], although up to 5% anisotropy has been observed for regions with old and thick subducting lithosphere [*Hiramatsu et al.*, 1997; *Matcham et al.*, 2000]. For studies that use teleseismic shear waves (like the Cascadia study below), the observed shear wave splitting may be due to anisotropy in the mantle above the subducting plate, or anisotropy in the subducting lithosphere and underlying asthenosphere. Studies that use local shear waves from intermediate to deep earthquakes in the subducting plate can isolate anisotropy within the mantle wedge.

5.3 Shear wave splitting at the Cascadia subduction zone and adjacent regions

As part of this thesis research, a study of anisotropy at the Cascadia subduction zone was undertaken. SKS arrivals were analyzed at 26 three-component broadband seismic stations that cover the Cascadia forearc and backarc, as well as the western North America craton. This work builds on two previous studies that have noted SKS anisotropy at six stations in this region [*Silver and Chan*, 1991; *Bostock and Cassidy*, 1995]. A detailed description of the analysis procedure and interpretation can be found in *Currie et al.* [2004a]. Only a brief summary is given here.

For each SKS waveform, the *Silver and Chan* [1991] method was used to find the shear wave splitting parameters (fast direction and delay time). Clear shear wave splitting was observed at 23 of the 26 stations. Only three stations (BBB, LLLB, SLEB) did not have resolvable splitting for most waveforms, suggesting that there is either only weak horizontal anisotropy or highly complex anisotropy beneath these stations (see discussion below).

Figure 5.1 shows lower hemisphere projections of the fast directions and delay times at ten stations (see **Figure 5.2** for station locations). Azimuthal variations in the splitting parameters are indicative of complex anisotropy beneath the station, such as

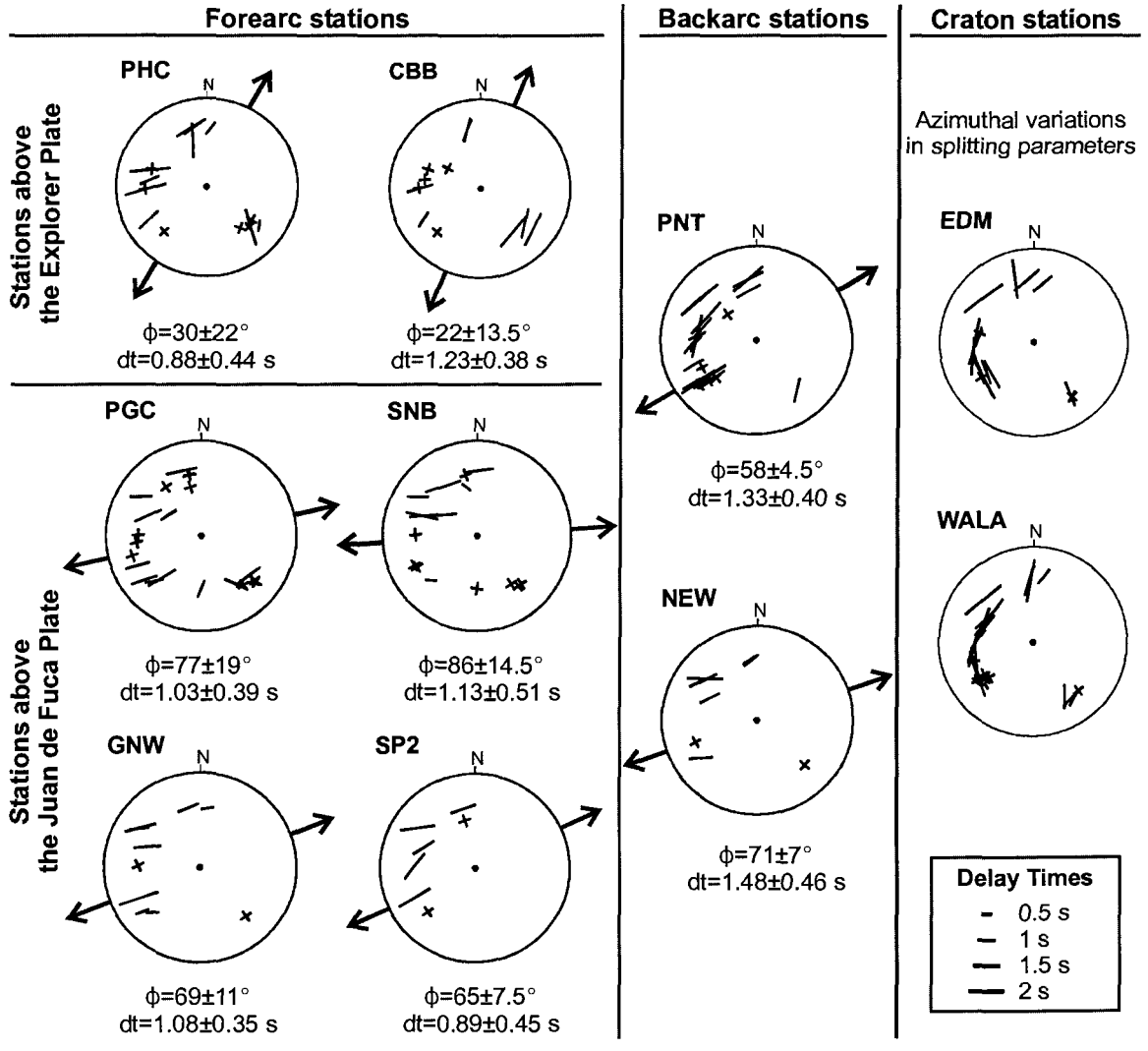

Figure 5.1. Lower hemisphere, equal area projections of SKS splitting parameters at ten stations (see Figure 5.2 for locations). The outer circle corresponds to an incidence angle of 15°. The orientation of each bar indicates the fast direction; bar length is proportional to the delay time (see legend). A cross indicates a null measurement (no clear splitting), with one arm of the cross parallel to the fast direction given by the splitting analysis (in nearly all cases, this direction is the backazimuth of the energy). The large arrows show the mean fast direction at each station (obtained from stacking all non-null data). The average fast directions (ϕ) and delay times (dt) are given below each plot, with 95% confidence intervals. Average values were not calculated at EDM and WALA as the splitting parameters show an azimuthal dependence.

small-scale lateral variations in anisotropy, dipping anisotropic layers, or multiple anisotropic layers. The only stations for which a clear azimuthal variation in the splitting parameters could be identified are stations EDM and WALA, located on the North America craton. At all other stations with a good azimuthal distribution of high quality data, there are no significant azimuthal variations in the splitting parameters. For all

stations except EDM and WALA, the splitting results were stacked to obtain a single set of splitting parameters, following *Wolfe and Silver* [1998]. **Figure 5.2** shows the results for the entire study region. The stations can be divided into three groups based on their location: 1) forearc stations (west of the Cascade volcanic arc), 2) backarc stations (east of the arc), and 3) stations on the North America craton.

The majority of stations are located in the forearc above the subducting Juan de Fuca Plate. In this region, fast directions are parallel to the direction of absolute plate motion of the Juan de Fuca Plate (~N70°E), with delay times of 0.7-1.5 s. The large delay times require a mantle source for the anisotropy [*Savage*, 1999; *Currie et al.*, 2004a]. In addition, the fast directions are approximately perpendicular to fast directions observed from shear wave splitting within the crust of the over-riding North America Plate [*Cassidy and Bostock*, 1996; *Currie et al.*, 2001], indicating that the anisotropy originates below the North America crust. There is some evidence for a small amount of anisotropy in the forearc mantle wedge of this region, but this is not well-constrained using either SKS waves or local shear waves from slab earthquakes at depths of 50-100 km [discussion in *Currie et al.*, 2004a]. The majority of SKS anisotropy is inferred to originate within the subducting Juan de Fuca lithosphere and in the asthenosphere below. The fast directions are parallel to the absolute plate motion direction of the Juan de Fuca Plate, suggesting that the anisotropy may be due to strain-induced lattice preferred orientation of mantle minerals within or below the plate, associated with present-day plate motion.

At stations overlying the Explorer Plate, the fast directions are oriented approximately N25°E, i.e., more northerly than the Juan de Fuca forearc stations. This 45° counterclockwise rotation in fast direction may reflect the combination of the more northerly direction of Explorer Plate motion [e.g., *Mazzotti et al.*, 2003] and a change in mantle deformation related to the transition from subduction to along-margin flow parallel to the Queen Charlotte Fault north of the study area. At station BBB, north of the subduction system, no clear shear wave splitting was identified, suggesting that there is no strong horizontal flow in the mantle in this region.

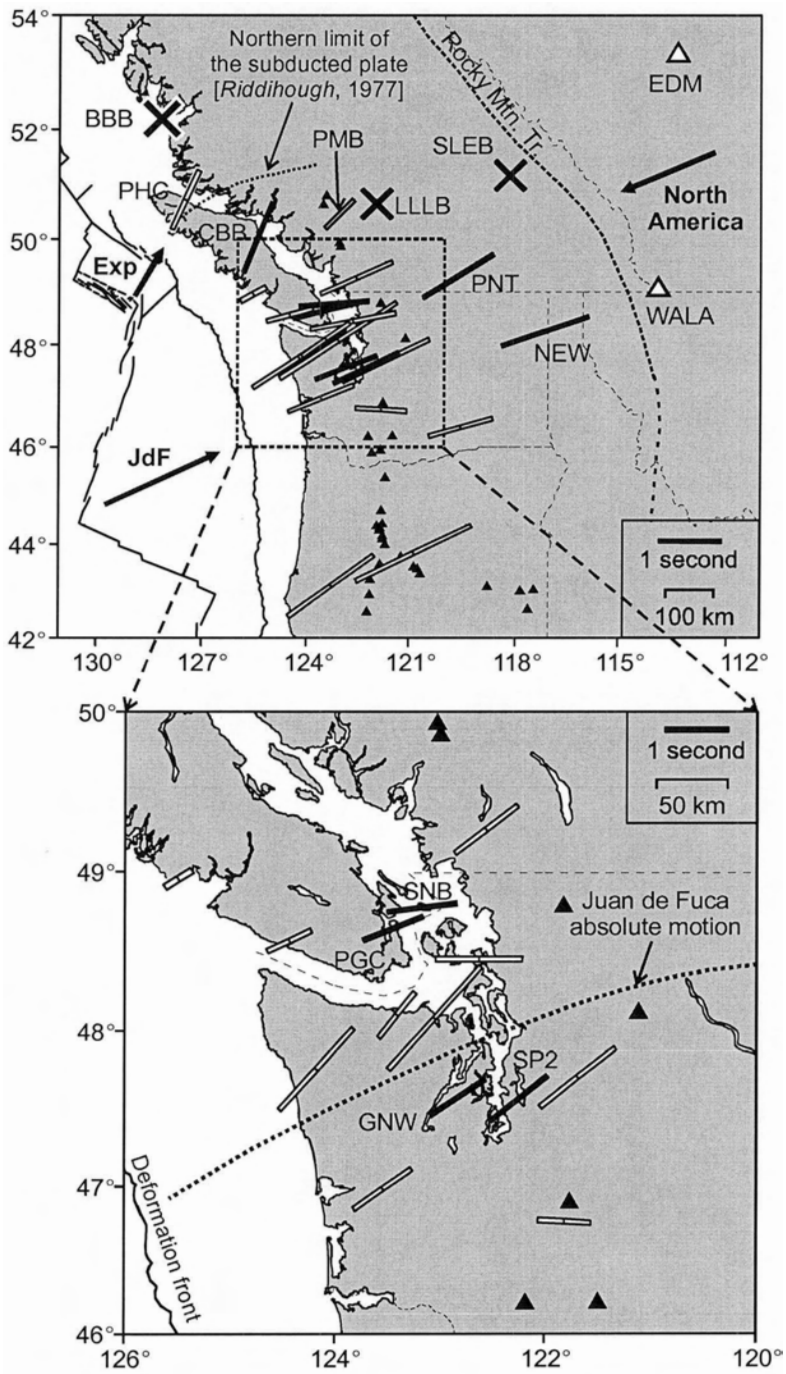

Figure 5.2. Average shear wave splitting parameters at each station across the Cascadia subduction zone. Orientation of the bar indicates the fast direction; bar length is proportional to delay time. Solid bars indicate well-constrainted results; open bars indicate more poorly constrained results; a cross indicates a null result (no clear splitting). Results for PMB are from *Bostock and Cassidy* [1995]. An azimuthal dependence of the splitting parameters was observed at WALA and EDM. Arrows in the upper figure indicate the absolute plate motion of the Explorer [*Ristau et al*, 2002], Juan de Fuca and North America plates [*Gripp and Gordon*, 2002]. The dotted line in the lower figure shows the variations in the direction of absolute plate motion of the Juan de Fuca plate [*Gripp and Gordon*, 2002].

Clear shear wave splitting was observed at five of seven stations in the Cascadia backarc (including results from station PMB, as reported by [*Bostock and Cassidy*, 1995]). The fast directions at these five stations are parallel to the Juan de Fuca-North America convergence direction (~N70°E), with delay times of ~1.3 s. Heat flow and other thermal indicators show that the backarc regions are hot, with estimated temperatures of 800-1000°C at 35 km depth (see **Chapter 3**), suggesting that the anisotropy is likely produced by present-day deformation of the asthenospheric mantle. Due to the poor depth resolution of the measurements, it is difficult to isolate where anisotropy occurs in the backarc mantle. Because the Cascadia backarc is extremely hot, it is expected that anisotropy is confined to the uppermost mantle (i.e., above the subducting plate), although anisotropy below the subducting plate is not ruled out. The subducting plate has been imaged in seismic studies as far east as station PNT, where it is at a depth of 300 km [*Bostock and van Decar*, 1995]. Assuming that most of the anisotropy is in the mantle above the subducting plate, the overall consistency of the fast directions and the relatively large delay times suggest that there may be an organized flow pattern in the mantle wedge, with flow in the direction of plate convergence, if the fast directions are parallel to the flow direction. At the two most northern backarc stations (LLLB, SLEB) no clear splitting was observed. These stations are near the inferred edge of the subducting slab. The absence of anisotropy at these stations may indicate that mantle flow becomes more complex at the slab edge.

At the two stations located on the North America craton (WALA and EDM), the splitting parameters show significant azimuthal variations, which appear to have a 90° periodicity. Such periodicity is characteristic of multiple layers of anisotropy [e.g., *Silver and Savage*, 1994], although dipping anisotropy and lateral variations in anisotropy may also be present. A two-layer anisotropy model that best fits the observations has an upper layer with a fast direction of N12°E and delay time of 1.4 s, and a lower layer with a fast direction of N81°E and delay time of 2.0 s. The North America craton is underlain by a thick (>150 km) lithosphere, and thus, the two anisotropic layers may reflect an upper

layer of "fossil" anisotropy within the cool (<900°C) lithosphere and a lower layer within the asthenospheric mantle produced by present-day deformation.

5.4 Global Comparison of Backarc Anisotropy

Anisotropy in the mantle wedge behind the volcanic arc and in the backarc is of greatest importance to this thesis study, due to its potential for mapping mantle flow and thus constraining models of mantle wedge dynamics. For Cascadia, SKS splitting observations indicate a convergence-parallel fast direction. As noted above, it is difficult to constrain the depth distribution of the anisotropy using teleseismic data. Unfortunately, the maximum depth of in-slab earthquake for this region is ~100 km and thus local shear waves can not be used to better localize backarc seismic anisotropy.

Numerous studies have examined shear wave splitting at subduction zones. **Table 5.1** summarizes results for studies that have examined data recorded at seismic stations in the backarc regions of several subduction zones. These studies have been divided into two groups, those that use local shear waves from intermediate and deep focus earthquakes in the subducting slab, and those that use teleseismic shear waves. In backarcs where both types of data are available, the fast directions and delay times from local shear waves are similar to those obtained using teleseismic shear waves. Some notable exceptions are: the fast directions for NE and SW Japan and Kamchatka, and the delay times for Alaska and Hikurangi. These differences may result from anisotropy below the subducting plate that affects the teleseismic energy.

The best constraints on the amount of anisotropy in the mantle wedge come from splitting of local shear waves. In general, delay times tend to be small, with many values less than 1 s. In several studies, an increase in delay time with increasing earthquake depth has been observed [e.g., *Fischer and Wiens*, 1996; *Fouch and Fischer*, 1996; *Wiemer et al.*, 1999; *Audoine et al.*, 2000]. From these studies, the amount of anisotropy in the mantle wedge is estimated to be 1-2%. This is less than that observed in other tectonic environments, suggesting that anisotropy in the mantle wedge may be poorly developed [e.g., *Kaneshima and Silver*, 1995; *Silver*, 1996; *Peyton et al.*, 2001].

Table 5.1. Anisotropy in the backarc mantle wedge from shear wave splitting.

Subduction Zone	Shear Wave Phases Used (and earthquake depths for local shear waves)	Fast Direction	Delay Time (s)	% Anis.	Refs.
South America	local S (100 km to 250 km)	Margin-parallel	< 0.5	< 0.5	1, 2, 3, 4
	local S, SKS	Margin-normal, eastern backarc (~20°S)	0.7-1.5		4
Cascadia	SKS	Parallel to convergence direction	1-1.5		5, 6
Alaska/ Aleutians	local S (< 230 km)	Margin-parallel	< 0.4	1-2	7, 8
	SKS (station may be NE of backarc)	Margin-parallel	1-1.6		5, 9
Kamchatka	sS-S differencing technique to isolate wedge anisotropy	Margin-normal	1-2		10
	SKS	Variable, generally margin-parallel	< 1		11, 12
Kuriles	local S (300-600 km)	N-S (35° to margin)	0.4-1.4	0.5	13
	SKS	N-S (35° to margin)	1		13
NE and SW Japan	local S (200-450 km)	Highly variable	0.6-1.5	0.7-1.1	13, 14, 15, 16
	SKS	Margin-normal	1		11
Izu-Bonin	local S (420-480 km)	WNW-ESE, Sub-parallel to conv. dir.	0.3-1	0.35-0.8	13
Mariana	local S (< 200 km)	NW-SE (20°N of APM of Pacific Plate)	0.1-0.4	0.65-2.25	17
	local S (< 150 km)	E-W	< 0.35		18
Tonga	local S (< 400 km)	Parallel to APM of Pacific Plate	0.8-1.5	0.8-3	19, 20
Hikurangi	local S (< 250 km)	Margin-parallel	< 1 s	1.2	21
	SKS	Margin-parallel	1.5-2 s		21

1 *Shih et al.*, 1991; 2 *Russo and Silver*, 1994; 3 *Kaneshima and Silver*, 1995; 4 *Polet et al.*, 2000; 5 *Bostock and Cassidy*, 1995; 6 *Currie et al.*, 2004a; 7 *Yang et al.*, 1995; 8 *Wiemer et al.*, 1999; 9 *Silver and Chan*, 1991; 10 *Fischer and Yang*, 1994; 11 *Vinnik et al.*, 1992; 12 *Peyton et al.*, 2001; 13 *Fouch and Fischer*, 1996; 14 *Ando et al.*, 1983; 15 *Iidaka and Obara*, 1995; 16 *Okada et al.*, 1995; 17 *Fouch and Fischer*, 1998; 18 *Xie*, 1992; 19 *Bowman and Ando*, 1987; 20 *Fischer and Wiens*, 1996; 21 *Audoine et al.*, 2000

The orientation of the fast direction shows considerable variation among subduction zones, as well as within a single subduction zone (**Figure 5.3**). At the Mariana subduction zone, the fast directions are sub-parallel to the convergence direction from local shear wave studies [*Xie*, 1992; *Fouch and Fischer*, 1998]. In contrast, the fast direction is nearly parallel to the margin in the Hikurangi and Alaska/Aleutian regions for both local and teleseismic shear waves [*Audoine et al.*, 2000; *Yang et al.*, 1995; *Wiemer et al.*, 1999]. In the Tonga backarc, the fast direction of local shear waves at stations more than 300 km from the trench are parallel to the subduction direction [*Bowman and*

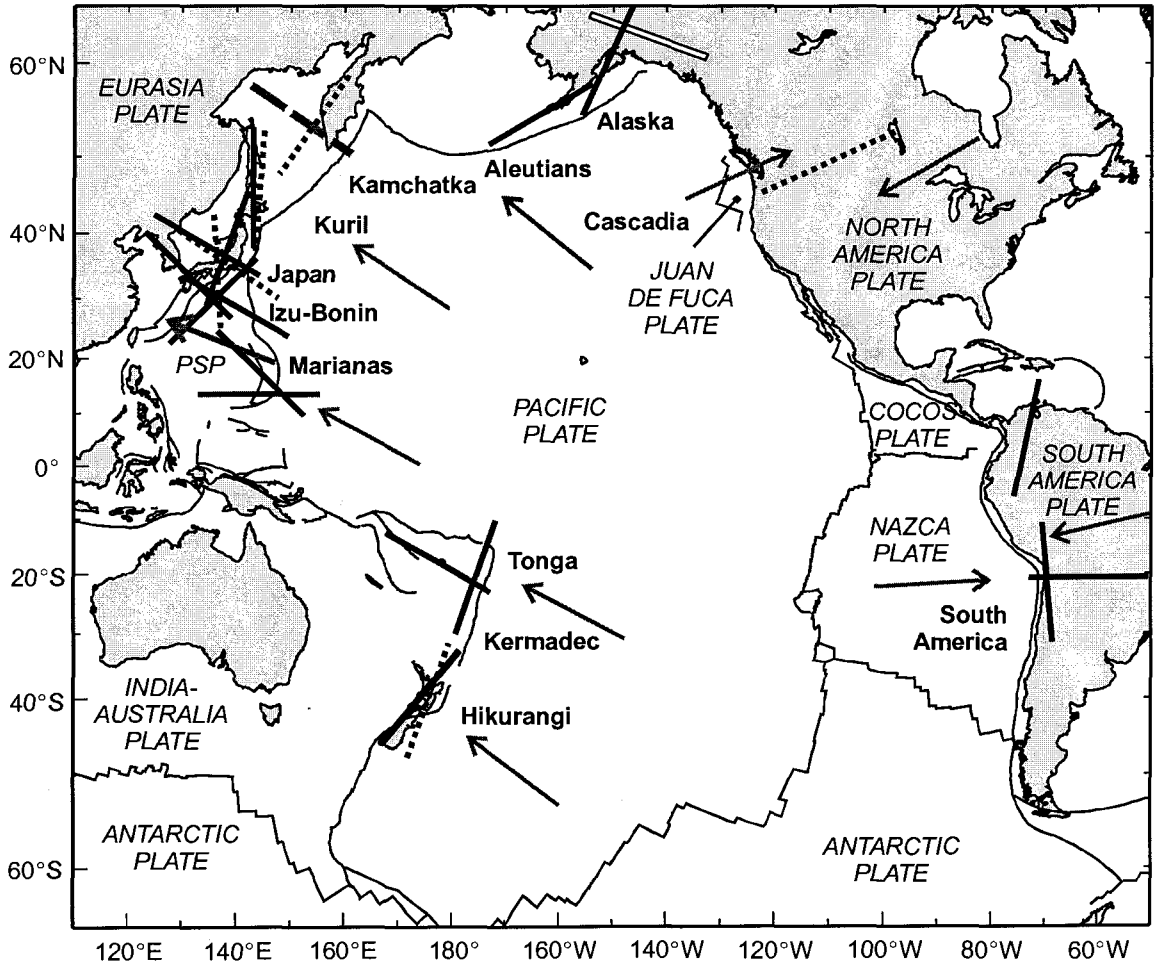

Figure 5.3. Compilation of fast polarization directions for subduction zone backarcs (see Tables 5.1 for references). Solid lines are the fast directions in the backarc mantle above the subducting slab from local shear waves; dotted lines are measurements from teleseismic shear waves; grey dashed line is the fast direction in the Kamchatka mantle wedge obtained using a Ss-S differencing technique. The open symbol is from SKS measurements that may be NE of the present-day Alaska backarc [*Silver and Chan*, 1991; *Bostock and Cassidy*, 1995]. Grey arrows indicate the absolute plate motion directions [*Gripp and Gordon*, 2002]. PSP is the Philippine Sea Plate.

Ando, 1987; *Fischer and Wiens*, 1996]. Closer to the trench, *Smith et al.* [2001] observed a rotation to a more margin-parallel orientation below the Lau Basin and Tonga volcanic arc, where the subducting plate is at a depth of 100-150 km. In this region, geochemical studies indicate that there may be significant along-margin flow above the subducting plate [*Turner and Hawkesworth*, 1998].

Fast directions of local and teleseismic shear waves are highly variable through the Izu-Japan-Kamchatka subduction system. Over most of the Izu-Bonin backarc, local shear waves yield a fast direction that is parallel to the subduction direction (WNW-ESE) [*Fouch and Fischer*, 1996], but may rotate to NE-SW near the northeast limit of the backarc [*Oda and Shimizu*, 1997]. For both SW and NE Japan, the fast directions are scattered. In the Kamchatka backarc, many fast directions are margin-normal, but large scatter in the observations and small delay times in teleseismic data suggest that this is poorly constrained [e.g., *Fisher and Yang*, 1994, *Peyton et al.*, 2001].

Along most of the South America subduction zone, local shear waves indicate that the fast direction in the wedge is parallel to the margin [*Shih et al.*, 1991; *Russo and Silver*, 1994; *Kaneshima and Silver*; *Polet et al.*, 2000]. In the eastern part of the central Andes, *Polet et al.* [2000] observed a rotation in the fast direction from N-S to E-W, as well as a slight increase in delay times, which may mark a transition from the actively deforming Andean mantle to the stable Brazilian craton. This transition lies ~100 km west of the surface backarc-craton boundary, which may indicate that the craton has been over-ridden by the Cordillera backarc crust.

5.5 Implications for Backarc Mantle Dynamics

At the Cascadia subduction zone, the observed fast directions in the backarc are oriented sub-parallel to the convergence direction [*Silver and Chan*, 1991; *Bostock and Cassidy*, 1995; *Currie et al.*, 2004a]. If this reflects anisotropy in the wedge, these observations are consistent with subduction-induced corner flow within the mantle wedge, where a flow cell is generated by the entrainment of lowermost mantle wedge material by the subducting plate. In this model, LPO develops from progressive simple shear of the mantle, with a fast direction aligned with the subduction direction

[*McKenzie*, 1979; *Ribe*, 1989]. Numerical modelling by *Fischer et al.* [2000] for a constant viscosity mantle wedge shows that this simple two-dimensional flow pattern can explain the observed fast directions and delay times for the Tonga backarc.

However, only the backarc regions of the Cascadia, Tonga and Mariana subduction zones clearly exhibit the expected fast directions for simple corner flow; other regions exhibit much different fast directions, including many that are margin-parallel. Some of the variation in fast direction orientation may be attributed to slab rollback, or the effects of water or melt in the mantle. Laboratory experiments indicate that slab rollback can produce an along-trench alignment of olivine fast axes [*Buttles and Olson*, 1998]. The presence of water may affect the lattice preferred orientation of olivine [*Karato and Wu*, 1993; *Jung and Karato*, 2001] and may also act to suppress anisotropy [e.g., *Silver*, 1996]. Anisotropy may also be produced by the alignment of thin melt pockets in the wedge by the stress field [*Kendall*, 1994]. For two-dimensional corner-flow in the wedge, this model predicts the alignment of cracks parallel to the margin, resulting in trench-parallel fast directions [e.g., *Fischer et al.*, 2000]. None of these three mechanisms can satisfactorily explain all the observations [e.g., discussion by *Wiens and Smith*, 2003]. For example, if rollback, water or melt is responsible for the trench-parallel fast direction in the Hikurangi or Alaska subduction zones, the same effect should be observed in the Mariana subduction zone, which is characterized by a similar old subducting plate. Instead, a margin-normal fast direction is observed.

One hypothesis to explain the variation in fast directions is that strain in the backarc mantle is dominated by present-day deformation of the over-riding plate, and not subducting plate motion [e.g., *Silver*, 1996, *Fouch and Fischer*, 1996; *Fischer et al.*, 1998]. Numerical models by *Fischer et al.* [2000] and *Hall et al.* [2000] indicate that although backarc mantle flow may be partially induced by the subducting plate, motion of the over-riding plate can strongly affect flow in the mantle wedge. This is supported by the observation that subduction zones with trench-parallel fast directions are characterized by significant along-margin shearing or strong compression of the over-riding plate. Trench-parallel fast directions at the Hikurangi, southern Kuriles and Alaska all align with the orientation of major crustal transcurrent faults and shear zones [e.g.,

Bostock and Cassidy, 1995; *Yang et al.*, 1995; *Fouch and Fischer*, 1996; *Audoine et al.*, 2000]. In South America, the margin-parallel fast directions agree with the predicted along-margin extension resulting from E-W shortening of the over-riding plate [*Polet et al.*, 2000]. In contrast, the Izu-Bonin, Mariana and Tonga (west of the Lau Basin) backarcs exhibit backarc extension. Fast directions in these regions are nearly margin-normal and sub-parallel to the direction of extension [*Fouch and Fischer*, 1996; *Fischer et al.*, 1998]. At the Cascadia subduction zone, there is presently no significant along-margin deformation of the over-riding plate in the backarc [e.g., *Gabrielse*, 1992], although there is evidence of along-margin compressive stress in the forearc. Present-day motion of the backarc appears to be to the southwest, with the North America craton. Thus, the Cascadia observations are also consistent with the model of mantle deformation induced by the over-riding plate.

The interpretation of seismic anisotropy in terms of mantle dynamics is not straightforward for subduction zone backarcs. The large variability in fast directions, combined with observations of relatively weak anisotropy (1-2%) for many mantle wedges using local shear wave data, may indicate that there is not a strong, homogeneous flow pattern in the mantle overlying the subducting plate. Most regions do not fit the simple two-dimensional corner flow model, suggesting that there may only be weak coupling between the mantle wedge and subducting plate [see also discussion by *Wiens and Smith*, 2003]. Instead, mantle anisotropy in many regions may be determined by either deformation of the over-riding plate, or by local factors such as slab rollback or the presence of water/melt.

CHAPTER 6
Numerical Modelling of Viscous Mantle Flow

6.1 Introduction

At nearly all subduction zones, surface heat flow, seismic velocities and other temperature indicators suggest high temperatures (>1200°C) in the mantle wedge below the arc and for 100's to 1000's of kilometres into the backarc, even in areas that have not undergone recent extension (see **Chapters 3 and 4**). The observed high temperatures are contradictory to the expected cooling effects of the underlying subducting plate, which represents a substantial heat sink. In addition, the backarcs of some subduction zones are located next to cratons, which are noted for their low surface heat flow, low mantle heat flow, and cool temperatures to great depths. The presence of the adjacent thick, cool craton lithosphere makes the high backarc temperatures even more surprising.

As described in **Chapter 1**, early models used frictional or shear dissipation along the top of the subducting plate as a heat source for arc volcanism. However, observations of low forearc temperatures (where frictional heating should be greatest), as well as difficulties in sustaining the required high shear stresses at high temperatures make this an unsatisfactory mechanism [e.g., *Yuen et al.*, 1978; *Peacock,* 1996]. Similarly, other local sources of heat, such as radiogenic heat production and heat associated with metamorphism in both the subducting plate and mantle wedge, have been discarded as significant heat sources [e.g., *McKenzie and Sclater*, 1968; *Minear and Toksoz*, 1970; *Oxburgh and Turcotte*, 1970; *Andrews and Sleep*, 1974; Yuen *et al.*, 1978; *Peacock*, 1987; *Wang et al.*, 1995b, *Peacock*, 1996]. Thus, mantle flow is invoked as a mechanism for transporting heat into the mantle wedge from below.

There are three main driving forces for mantle flow: 1) viscous coupling between the downgoing plate and overlying mantle (forced convection), 2) increased density of the material immediately above the slab, due to cooling from the slab, and 3) positive

buoyancy of hot material at depth in the backarc, due to heating from below (**Figure 6.1**). The latter two are forms of free convection, arising from thermally-induced density variations in the mantle wedge. A more detailed discussion of free convection is given in **Chapter 8**.

In the case of forced convection, viscous coupling occurs because the subducting slab will cool the mantle material immediately above it, resulting in the accretion of mantle wedge material to the top of the subducting plate, due to the inverse dependence of mantle viscosity on temperature [e.g., *Kincaid and Sacks*, 1997]. Thus, mantle wedge material immediately above the slab is entrained and carried downward with the slab. The material is then replaced by hot material from the backarc. This has been modelled using a simple corner flow model for the mantle wedge [e.g., *McKenzie*, 1969].

Two other factors that may affect mantle wedge flow are: 1) compositional buoyancy, due to density variations associated with compositional changes, and 2) the migration of arc magmas from their mantle wedge source region to the arc. If there is a corner flow-type pattern, with the downwelling limb near the wedge corner, the magma must have to oppose this flow to reach the arc. This remains a topic of debate [e.g., *Iwamori*, 1998]. It has been suggested that the generation and migration of magma may trigger secondary convection cells, with possible flow reversal below the arc [*Davies and*

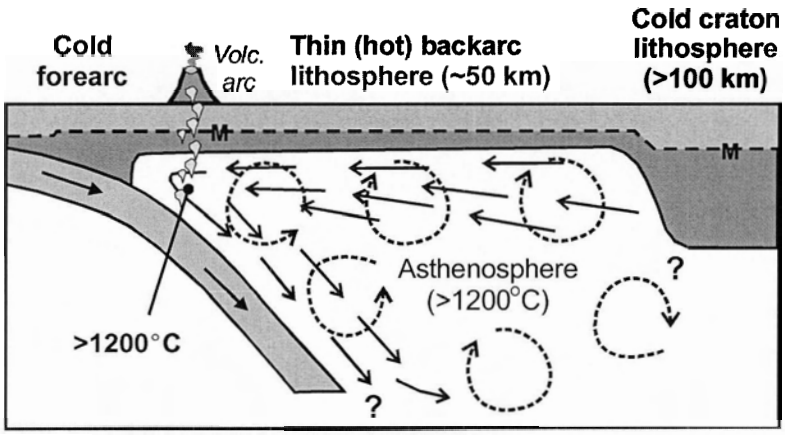

Figure 6.1. Schematic diagram of possible flow patterns in the mantle wedge. With forced convection (solid arrows), flow is driven by viscous coupling between the subducting plate and mantle wedge. With free convection (dashed arrows), flow is driven by thermally-induced density variations in the wedge. Both cooling of the mantle immediately above the subducting slab and heating of the deep backarc mantle from below can drive free convection. Some subduction zones (e.g., Cascadia, South America) are located adjacent to thick, cool craton lithosphere.

Stevenson, 1992]. Both compositional buoyancy and magma migration are expected to have a second-order effect on mantle wedge flow. The main focus of this study is the large-scale convection pattern in the wedge, which is believed to be primarily driven by slab-wedge coupling and thermal buoyancy.

The remainder of this thesis research focusses on the backarc advective-convective regime that maintains high temperatures in the mantle wedge below the arc and throughout the backarc regions. Numerical thermal-mechanical models are used to better understand the thermal effects of mantle wedge flow. The approach used here follows that of recent modelling studies of mantle wedge flow [e.g., *Honda*, 1985; *Furukawa*, 1993a, b; *van Keken et al.*, 2002]. A subducting plate with a fixed geometry and prescribed velocity subducts under a rigid over-riding plate. Flow within the viscous mantle wedge is determined by the driving forces for flow and the rheology of the mantle. This approach is partly kinematic in that the geometry and velocity of the subducting and over-riding plate are prescribed. This type of model is effective for investigating the effect of the subducting slab on the deformation and thermal structure of the overlying mantle wedge. Note that there is another class of subduction zone thermal models where the dynamics of the subduction slab are computed as part of the modelling procedure [e.g., *Kincaid and Sacks*, 1997].

In this study, the models are two-dimensional, oriented perpendicular to the subduction margin. In this study, the "landward" or "backarc" end of the model refers to the model boundary furthest from the trench. The "seaward" end coincides with the trench. The models are in the reference frame of the over-riding plate, which is assumed to be stationary relative to the trench. In addition, the geometry and velocity of the subducting plate are assumed to be constant, such that there is no slab-normal motion of the subducting plate (e.g., slab rollback where the plate dip increases with time). These models are designed to examine the first-order thermal effects of one plate under-thrusting another. Although three-dimensional flow and temporal changes in the subducting slab geometry may occur, they are not considered here.

In this chapter, the numerical modelling approach used in this study is described. The chapter begins with a discussion of the rheology of the upper mantle. This is

followed by the equations that describe mechanical flow and the thermal structure. As will be shown, the flow and thermal fields are strongly coupled through the temperature-dependence of mantle rheology. The chapter ends with a description of the numerical techniques used in the models. The modelling approach presented in this chapter is used in the development of subduction zone models in **Chapter 7 and 8**.

6.2 Rock Rheology

The rheology of upper mantle minerals determines how they will deform in response to imposed forces. *Kirby* [1983], *Karato and Wu* [1993], *Ranalli* [1995], *Blenkinsop* [2000] and *Turcotte and Schubert* [2002] provide comprehensive discussions of rock deformation and rheology. Only a brief review of conclusions relevant to the current study is given here.

6.2.1 Viscous flow law

At high temperatures and stresses, mantle minerals deform plastically through sub-solidus creep, due to the movement of atoms, vacancies, and dislocations within the crystalline lattice structure. Diffusion creep results from the migration of atoms either along grain boundaries (Coble creep) or through the interiors of crystal grains (Nabarro-Herring creep). On the other hand, dislocation creep is the result of the movement of dislocations (imperfections in the crystalline lattice structure).

Sub-solidus creep produces viscous flow of the mantle on macroscopic distance scales and geologic time scales. The viscous behaviour of mantle minerals has been studied in laboratory deformation experiments. The majority of experiments are performed under uniaxial/triaxial stress conditions. Mineral samples are subjected to a differential stress $(\sigma_1 - \sigma_3)$, taken as the difference between the applied axial stress (σ_1) and the confining stress (σ_3). Note that a uniaxial experiment is a special case of a triaxial set-up with $\sigma_3 = 0$. These experiments have shown that the uniaxial strain rate $(\dot{\varepsilon}_1)$ and the differential stress can be related by the constitutive equation [e.g., *Kirby*, 1983]:

$$\dot{\varepsilon}_1 = A(\sigma_1 - \sigma_3)^n \exp\left(\frac{-(Q+PV)}{RT}\right) \quad (6.1)$$

where P is the confining pressure, R is the universal gas constant (8.3145 J mol^{-1} K^{-1}), and T is the absolute temperature. A, n, Q, and V are rheological parameters that depend on the material and are assumed to be independent of temperature and stress. A is the pre-exponential factor, n is the stress exponent, Q is the activation energy, and V is the activation volume. In this formulation, the pre-exponential factor (A) is a constant that includes the effects of grain size, water, and structural characteristics of the mineral grains [e.g., *Karato and Wu*, 1993; *Mei et al.*, 2002].

Diffusion and dislocation creep can both be described with **Equation 6.1**. In each case, the strain rate increases as the differential stress increases. For diffusion creep, the strain rate and stress are linearly related (n=1), and the material behaves as a Newtonian viscous fluid. For dislocation creep, an increase in stress results in a non-linear increase in strain rate (n>1). This type of deformation is also known as power law creep. Although both diffusion and dislocation creep can occur at the same time, the one that gives the larger strain rate is the dominant mechanism. In general, dislocation creep dominates for high differential stress, large grain size, and high temperatures. At high stresses (> 200 MPa), deformation of the mantle may be better described by the Dorn (exponential) creep law [e.g., *Tsenn and Carter*, 1987]. The stresses associated with mantle flow are generally small, and thus, the Dorn law is not used in this study.

Table 6.1 gives a compilation of rheological parameters from various laboratory studies of upper mantle minerals. Most experiments have focused on olivine deformation, as olivine is the most abundant mineral in the upper mantle and is likely the weakest. Thus, olivine deformation should dominate upper mantle rheology. Also included in **Table 6.1** are parameters for six hypothetical rheologies, three Newtonian and three power law creep. These are used to examine the effects of the rheological parameters on viscous flow (**Section 6.2.3, Section 7.3.4** and **Appendix A**).

It should be noted that there are large uncertainties associated with the extrapolation of laboratory results to nature [e.g., *Karato and Wu*, 1993; *Blenkinsop*,

Table 6.1. Rheological parameters for the upper mantle for uniaxial deformation.

Mineral/ Rock	Wet/ Dry	A ($Pa^{-n} s^{-1}$)	n	Q (J/mol)	V (m^3/mol)	B ($Pa\ s^{1/n}$)	Ref.
Hypothetical Temperature-Dependent (Newtonian) Rheology[a]							
--	--	4.85×10^{-15}	1.0	200000	--	6.67×10^{13}	--
--	--	1.02×10^{-11}	1.0	300000	--	3.28×10^{10}	--
--	--	2.13×10^{-8}	1.0	400000	--	1.57×10^{7}	--
Hypothetical Temperature- and Stress-Dependent (Power Law) Rheology[b]							
--	--	6.97×10^{-19}	1.0	100000	--	4.78×10^{17}	--
--	--	2.08×10^{-28}	3.0	300000	--	4.64×10^{9}	--
--	--	5.22×10^{-40}	5.0	500000	--	1.90×10^{7}	--
Dislocation Creep							
Dunite A	Dry	7.20×10^{-18}	3.6	535000	--	15625.3	1
Dunite B	Dry	4.85×10^{-17}	3.5	535000	--	12440.9	2
Lherzolite	Dry	4.50×10^{-23}	4	523000	--	103722.2	3
Olivine A	Dry	6.31×10^{-17}	3.5	533000	1.70×10^{-5}	11539.8	4
Olivine B[c]	Dry	2.85×10^{-17}	3.5	540000	2.00×10^{-5}	14484.3	5
Olivine-Basalt[d]	Dry[e]	3.90×10^{-19}	3.5	470000	2.00×10^{-5}	49355.2	6
Anita Bay Dunite	Wet	7.59×10^{-17}	3.4	535000	--	15007.7	7
Aheim Dunite	Wet	4.17×10^{-25}	4.5	498000	--	65574.5	7
Dunite C	Wet[f]	4.89×10^{-15}	3.5	515000	--	3329.7	2
Lherzolite	Wet	4.50×10^{-23}	4	523000	--	184447.0	3
Olivine[c]	Wet	6.51×10^{-16}	3	430000	1.50×10^{-5}	31748.0	5
Olivine-Basalt[d]	Wet[g]	1.17×10^{-16}	3.5	470000	2.00×10^{-5}	9673.5	6
Diffusion Creep							
Olivine[c, d]	Dry	8.22×10^{-13}	1	300000	6.00×10^{-6}	4.05×10^{11}	5
Olivine-Basalt[d]	Dry[e]	2.52×10^{-12}	1	300000	2.00×10^{-5}	1.32×10^{11}	6
Olivine[c, d]	Wet	5.01×10^{-13}	1	240000	5.00×10^{-6}	6.66×10^{11}	5
Olivine-Basalt[d]	Wet[g]	7.56×10^{-10}	1	300000	2.00×10^{-5}	4.41×10^{8}	6

1 *Chopra and Paterson*, 1984; 2 *Hirth and Kohlstedt*, 1996; 3 *Ji and Xia*, 2002; 4 *Kirby*, 1983; 5 *Karato and Wu*, 1993; 6 *Mei et al.*, 2002; 7 *Chopra and Paterson*, 1981

[a]Arbitrary parameters to give an effective viscosity of 3×10^{20} Pa s at T=1300°C

[b]Arbitrary parameters to give an effective viscosity of 10^{21} Pa s at T=1300°C and $\dot{\varepsilon}=10^{-13}$ s^{-1}

[c]Parameters were reported for simple shear deformation [*Karato and Wu*, 1993] and have been converted to uniaxial stress by multiplying the pre-exponential factor by $2^{2-n}/3$ [*Ranalli*, 1995]

[d]A grain size of 3 mm was used for the calculation of the pre-exponential factor

[e]Assumed a water fugacity of 1 MPa (dry conditions)

[f]Sample was not completely water-saturated

[g]Assumed a water fugacity of 300 MPa (water-saturated conditions)

2000]. The most serious limitation is that laboratory experiments are performed at high strain rates (10^{-7} to 10^{-5} s^{-1}), which are several orders of magnitude greater than tectonic strain rates (10^{-15} to 10^{-12} s^{-1}). Secondly, the experiments are generally performed at low

confining pressures (< 3 GPa), corresponding to depths less than 100 km. Also, the laboratory samples are small, and thus, the effects of centimetre to metre scale heterogeneities are not included. Nevertheless, the results of laboratory experiments have been widely used in geodynamical studies.

6.2.2 Effective viscosity

The stress-strain rate relation in **Equation 6.1** can be expressed using the effective viscosity (η), a scalar quantity that relates the maximum shear stress (σ_s) and maximum shear strain rate ($\dot{\varepsilon}_{max}$) in viscous flow:

$$\eta = \frac{\sigma_s}{2\dot{\varepsilon}_{max}} \tag{6.2}$$

For uniaxial/triaxial deformation of an incompressible material (i.e., $\dot{\varepsilon}_3 = -\frac{1}{2}\dot{\varepsilon}_1$), the maximum shear stress and strain rate are:

$$\sigma_s = \frac{(\sigma_1 - \sigma_3)}{2} \tag{6.3a}$$

and

$$\dot{\varepsilon}_{max} = \frac{(\dot{\varepsilon}_1 - \dot{\varepsilon}_3)}{2} = \frac{3}{4}\dot{\varepsilon}_1 \tag{6.3b}$$

Thus, the effective viscosity is equal to:

$$\eta = \frac{\sigma_s}{2\dot{\varepsilon}_{max}} = \frac{1}{3}\frac{(\sigma_1 - \sigma_3)}{\dot{\varepsilon}_1} \tag{6.4}$$

Following *Chen and Morgan* [1990], **Equations 6.1 and 6.4** can be matched to give the effective viscosity in terms of the maximum shear stress ($\dot{\varepsilon}_{max}$):

$$\eta = B\dot{\varepsilon}_{max}^{\frac{1-n}{n}} \exp\left(\frac{Q+PV}{nRT}\right) \tag{6.5}$$

where

$$B = \frac{1}{4}\left(\frac{4}{3A}\right)^{\frac{1}{n}} \tag{6.6}$$

The effective viscosity governs how shear stresses are transmitted through a material. For a Newtonian material (n=1), the effective viscosity is constant for a given

set of conditions (pressure, temperature, etc.) and is independent of the strain rate. Thus, it is often simply called the viscosity. For power law creep (n>1), the effective viscosity also depends on stress (or strain rate), and thus the effective viscosity reflects the deformational behaviour of the material at a given strain rate.

6.2.3 Factors affecting upper mantle rheology

For both Newtonian and power law creep, the strain rate and effective viscosity are strongly sensitive to temperature. A small increase in temperature may produce a dramatic decrease in effective viscosity. This is illustrated in **Figure 6.2a**, which shows the effective viscosity as a function of temperature for the hypothetical Newtonian rheologies given in **Table 6.1**. In this case, as the activation energy (Q) increases, the effective viscosity is more sensitive to temperature.

Figure 6.2b shows effect of the stress-dependence (n) on the effective viscosity for the hypothetical power law rheologies. The temperature-dependence is primarily given by the ratio Q/n. As this ratio increases, temperature-dependence becomes much stronger. The three hypothetical power law rheologies have a similar weak temperature-dependence (Q/n=100000 J/mol), as shown by the identical effective viscosity of each at a strain rate of 10^{-13} s^{-1}. The stress-dependence is determined by n. With n>1, higher strain rates lead to a smaller effective viscosity; the effect is slightly larger for a stronger stress-dependence.

The strain rate and effective viscosity also depend on the confining pressure (or depth). The activation volume (V) is poorly constrained in laboratory experiments [*Karato and Wu*, 1993]. Most studies give values of V less than 2×10^{-5} m^3/mol (**Table 6.1**). For these values, the effective viscosity increases by about an order of magnitude for a 100 km increase in depth (assuming that all other parameters are constant), i.e., it is more difficult for deformation to occur at greater depths. As this parameter is not well-constrained and because temperature is the dominant effect on strain rate for the subduction zone models, the effect of pressure has been ignored in this study (i.e., V is assumed to be 0 m^3/mol).

For diffusion creep, deformation is sensitive to the grain size; strain rates are greater for smaller grain sizes. The grain size effect is included in the pre-exponential factor (A) for diffusion creep, as the grain size dependence is approximately constant over the range of conditions in the mantle [e.g., *Karato and Wu*, 1993]. In this study, a

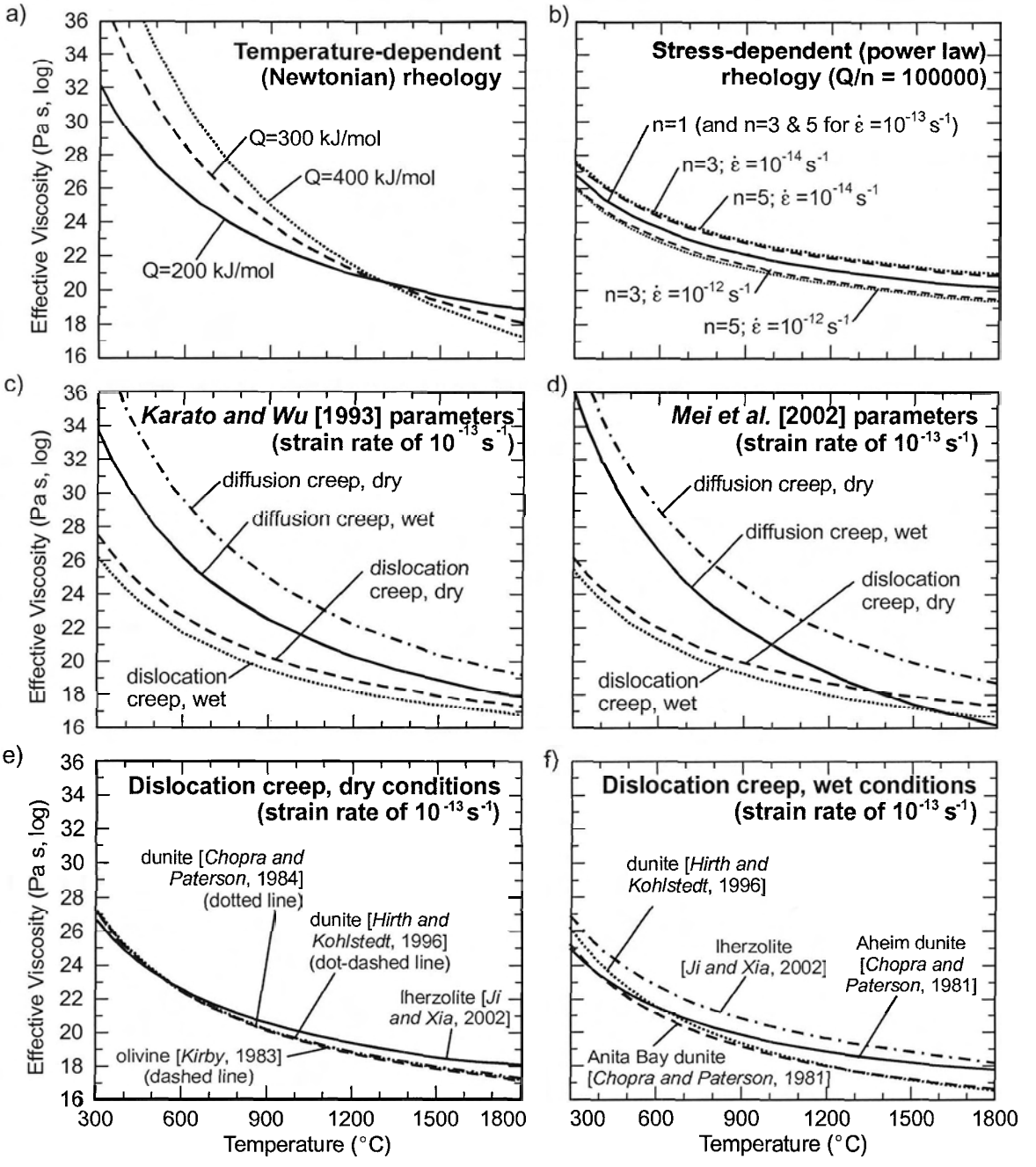

Figure 6.2. Effective viscosity as a function of temperature for a) hypothetical Newtonian rheologies, b) hypothetical power law rheologies with only a weak temperature-dependence (solid line for n=1, dashed line for n=3; dotted line for n=5), and c-f) upper mantle rheologies from laboratory experiments (see Table 6.1).

grain size of 3 mm is assumed for diffusion creep deformation (**Table 6.1**), comparable to estimates of grain size in the upper mantle [e.g., *Turcotte and Schubert*, 2002]. If instead a grain size of 1 mm were used, the effective viscosity would decrease by a factor of 15-30 for both dry and wet conditions. Dislocation creep is insensitive to grain size [e.g., *Karato and Wu*, 1993].

Figures 6.2c-f show the effective viscosity as a function of temperature for each of the upper mantle rheologies given in **Table 6.1**. A common plate boundary strain rate of 10^{-13} s^{-1} is used in all dislocation creep calculations. The rheology parameters given by *Karato and Wu* [1993] and *Mei et al.* [2002] have been plotted on separate plots, as these studies report parameters for dislocation and diffusion creep of olivine (or olivine-basalt), under both dry and water-saturated (wet) conditions. The remaining rheological parameters are for dislocation creep and have been separated into those determined under dry conditions and those under water-saturated conditions. These plots illustrate the strong effect of temperature on the effective viscosity of upper mantle compositions. Rheologies with a high Q/n ratio have the strongest temperature-dependence. Diffusion creep generally has the largest effective viscosity. Overall, the flow laws for dislocation creep of different upper mantle compositions give a similar effective viscosity.

Upper mantle deformation is also sensitive to the presence of water and partial melt. The strength of upper mantle minerals decreases with increasing water fugacity (or water content) [*Kirby*, 1983; *Karato et al.*, 1986; *Karato and Wu*, 1993; *Hirth and Kohlstedt*, 1996; *Mei et al.*, 2002]. Recent studies provide detailed discussions of the effect of water on the stress-strain rate relation for upper mantle minerals [e.g., *Mei and Kohlstedt*, 2000a, b; *Mei et al.*, 2002]. In the current study, two end-member cases are considered: dry minerals and those that are water-saturated (e.g., **Table 6.1**). As shown in **Figure 6.2**, the effective viscosity of water-saturated minerals is, on average, one order of magnitude less than that of dry minerals under dislocation creep. For diffusion creep, the effect is slightly larger.

The presence of partial melt will weaken upper mantle minerals, particularly at melt fractions greater than 0.04 [*Hirth and Kohlstedt*, 1995a, b; *Kohlstedt and Zimmerman*, 1996; *Mei et al.*, 2002, *Xu et al.*, 2004]. For olivine-basalt aggregates and

lherzolite with melt fractions less than 0.15, triaxial laboratory experiments have shown that the strain rate depends exponentially on the melt fraction (φ):

$$\dot{\varepsilon}(\varphi) = \dot{\varepsilon}(0) \times \exp(\alpha\varphi) \tag{6.7}$$

where $\dot{\varepsilon}(0)$ is the strain rate for a melt-free sample and α is a constant (26 for diffusion creep and 31 for dislocation creep of olivine-basalt aggregates) [e.g., *Mei et al.*, 2002]. The amount of partial melt increases with increasing temperature, at temperatures greater than the mantle solidus temperature. There have been several laboratory studies that have attempted to parameterize the melt fraction as a function of temperature, i.e., $\varphi(T)$ [e.g., *Zimmerman and Kohlstedt*, 2004]. By combining the results of these studies with **Equations 6.5 and 6.7**, it is possible to derive an expression for the effective viscosity as a function of temperature that includes the effects of melt. As an example, **Figure 6.3** shows the effect of melt on the effective viscosity for dislocation creep of dry lherzolite, using the temperature-melt fraction relation and the α value from *Zimmerman and Kohlstedt* [2004], and the rheological parameters of *Ji and Xia* [2002, see also **Table 6.1**]. As the melt fraction increases, the strain rate become larger, resulting in lower effective

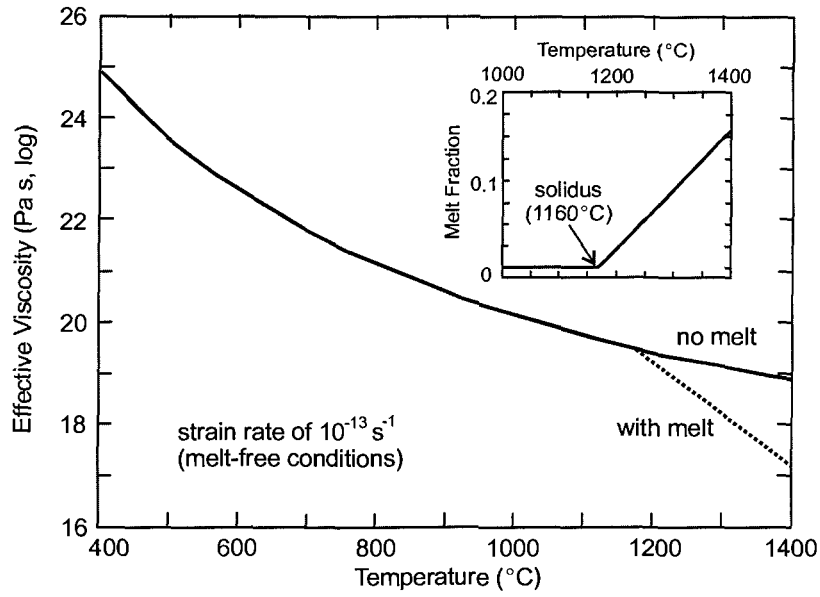

Figure 6.3. The effective viscosity as a function of temperature for dislocation creep of dry lherzolite. The solid line assumes no melt; the dotted line incorporates the effects of melt, using Equation 6.7 with α=27 (as determined by *Zimmerman and Kohlstedt* [2004] for lherzolite). The inset shows the melt fraction as a function of temperature [*Zimmerman and Kohlstedt*, 2004].

viscosities. As a result, the effective viscosity becomes more strongly temperature-dependent at temperatures above the solidus temperature.

The effect of partial melting under hydrous conditions may be complex when the amount of water in the system is limited. *Karato* [1986] suggests that partial melting under these conditions may result in a *hardening* of the mantle, based on the observation that water will partition into the melt phase, dehydrating the mineral grains and thus increasing their strength. However, *Mei et al.* [2002] argue that for a water-saturated system or where there is a constant source of water (e.g., continual hydration of the mantle wedge by the subducting plate), the net effect of partial melt is to reduce the strength, according to **Equation 6.7**. In this study, melt weakening is not included in the rheological formulation, but a discussion of the effects of melt on model results is given in **Section 7.3.4**.

6.3 Governing Equations for Thermal-Mechanical Models

6.3.1 Flow equations

In the numerical models, the mantle wedge is assumed to be a Boussinesq, incompressible viscous fluid. In the Boussinesq approximation, density variations are assumed to be sufficiently small that they can be neglected in all terms except the gravitational body force term. Viscous flow in the mantle is governed by the conservation of mass and momentum equations:

$$\nabla \cdot \mathbf{v} = 0 \tag{6.8}$$

$$\nabla \cdot \boldsymbol{\sigma}' - \nabla P + \rho' \mathbf{g} = \mathbf{0} \tag{6.9}$$

where $\mathbf{v}$ is velocity, $\boldsymbol{\sigma}'$ is the deviatoric stress tensor, P is the dynamic pressure (i.e., the pressure generated by flow), and $\mathbf{g}$ is the gravitational acceleration (9.81 m/s^2). The incremental density variations caused by temperature changes (ρ') are given by:

$$\rho' = -\rho_0 \alpha_V (T - T_0) \tag{6.10}$$

where ρ_0 is the reference density at a reference temperature T_0, T is the temperature, and α_V is the thermal expansion coefficient. The first set of models in this study (**Chapter 7**) examines wedge flow driven by viscous coupling with the subducting plate only; thermal

buoyancy is neglected (i.e., α_V=0), so there is no gravitational body force. The effects of thermal buoyancy are discussed in **Chapter 8**.

Viscous flow depends only on the deviatoric stress tensor, as flow is driven by pressure gradients and shear stress. The deviatoric stress tensor is defined as:

$$\sigma_{ij}' = \sigma_{ij} - \frac{1}{3}\sigma_{kk}\delta_{ij} \tag{6.11}$$

where σ_{ij} is the full stress tensor and δ_{ij} is the Kronecker delta (δ_{ij}=1 for i=j; δ_{ij}=0 for i≠j). In index notation, σ_{kk} is the sum of the diagonal components of the stress rate tensor $(\sigma_{11} + \sigma_{22} + \sigma_{33})$. The second term on the right-hand side of the equation is the mean normal stress (or total pressure).

The strain rate tensor is defined as:

$$\dot{\varepsilon}_{ij} = \frac{1}{2}\left(\frac{\partial v_i}{\partial x_j} + \frac{\partial v_j}{\partial x_i}\right) \tag{6.12}$$

For an incompressible fluid, the deviatoric strain rate is equal to the strain rate tensor. The deviatoric stress and (deviatoric) strain rate are related by the effective viscosity:

$$\sigma'_{ij} = 2\eta\dot{\varepsilon}_{ij} \tag{6.13}$$

Thus, the equation for conservation of momentum (**Equation 6.9,** with no gravitational body force) can be written in terms of the strain rate tensor:

$$\nabla \cdot (2\eta\dot{\varepsilon}) - \nabla P = \mathbf{0} \tag{6.14}$$

Note that for an incompressible, constant viscosity fluid, the conservation of momentum equation can be simplified to:

$$\eta\nabla^2 \mathbf{v} - \nabla P = \mathbf{0} \tag{6.15}$$

In the numerical implementation, **Equations 6.8 and 6.14** are used to calculate the flow field within the mantle wedge.

6.3.2 Heat equation

The steady-state energy (heat transfer) equation is used to calculate the temperatures (T) for the entire model space:

$$0 = \nabla \cdot (k\nabla T) - \rho c_p (\mathbf{v} \cdot \nabla T) + Q_H \tag{6.16}$$

where k is the thermal conductivity, ρ is the density, c_p is the specific heat, and Q_H is the volumetric heat production from various sources (in W/m^3), including radiogenic heat production, frictional heating, and viscous dissipation. The energy equation is coupled to the flow equations through the velocity term; heat is transported advectively by viscous flow. In addition, the rheology of the mantle wedge may depend on both stress and temperature. In this case, the thermal and flow fields are even more strongly coupled, making the problem highly non-linear.

In this study, real temperatures are used throughout the model calculations. Some previous modelling studies have performed calculations using potential temperatures (i.e., the temperature at a pressure of 0 GPa) and have converted the results to real temperatures by adding an adiabatic gradient [e.g., *van Keken et al.*, 2002]. For the subduction zone models, both methods yield similar results in the upper 300 km of the model (**Appendix C**).

6.3.3 Viscous dissipation

The dissipation of heat energy by viscous flow is the product of the deviatoric stress and strain rate:

$$Q_{sh} = \sigma'_{ij} \dot{\varepsilon}_{ij} = 2\eta \dot{\varepsilon}_{ij} \dot{\varepsilon}_{ij} \tag{6.17}$$

Thus, viscous dissipation depends on both the effective viscosity and strain rate of the mantle. For Newtonian and power law rheologies, the amount of viscous dissipation is buffered by the non-linear dependence of the viscosity on temperature. Cool regions will have a high viscosity and will not readily deform, leading to low strain rates and therefore little heat dissipation. On the other hand, hot regions with a low viscosity can have significantly higher strain rates, but the low viscosity leads to only a small amount of heat dissipation. Viscous dissipation is studied in detail in **Appendix A**.

6.3.4 Plane strain assumption

The numerical models in this study are two-dimensional, whereas the above equations use the full three-dimensional strain rate and stress tensors. Thus, the plane strain assumption is introduced, such that there is no strain in the direction normal to the model plane. This assumption implies that there is a stress acting normal to the model to prohibit strain in this direction. The model-perpendicular stress will increase the local mean normal stress (pressure) at each point in the wedge. It can be shown that this does not affect the pressure gradient, as there is no deviatoric stress in this direction, and flow everywhere will be parallel to the model plane [*Ranalli*, 1995].

Note that the rheological formulation (**Equation 6.1**) was developed for uniaxial/triaxial deformation. For application to the models, it is necessary to transform these parameters to a plane strain state of stress, using the second invariants of the strain rate and deviatoric stress tensors [e.g., *Ranalli*, 1995]. This transformation results in a multiplication of the pre-exponential factor by $3^{(n+1)/2}/2$; the other rheological parameters (Q and n) are not affected. In the PGC modelling code (see below), the input data file specifies the rheological parameters for uniaxial (or triaxial) conditions, and the program converts these parameters to plane strain internally.

6.4 Numerical Methods

The finite element method is used to numerically solve the system of equations given by **Equations 6.5, 6.8, 6.14 and 6.16**. The computer modelling code in this study was developed by Dr. Jiangheng He at the Pacific Geoscience Centre, Geological Survey of Canada. The code uses 9-node isoparametric finite elements for the temperature and velocity fields and compatible 4-node elements for the pressure field. The quadratic elements allow high spatial resolution with relatively large elements.

The modelling approach uses the conventional penalty function formulation to stabilize pressure solutions and the Galerkin-Least-Squares method [*Hughes et al.*, 1989] to alleviate instabilities in advection-dominated temperature solutions. In cases that use a temperature- and stress-dependent viscosity, the flow and temperature fields are strongly coupled, and the resulting nonlinear system is efficiently solved using a multi-corrector

fixed-point algorithm [J. He, manuscript in preparation, 2004]. The resultant linear algebra equation is solved with the commonly-used direct LU decomposition method after an optimal node-reordering. At each iteration, the flow and temperature fields are solved simultaneously, instead of sequentially.

For constant viscosity models, only one iteration is needed to solve for the flow and thermal fields. For models with a temperature- (and stress-) dependent rheology, several iterations are required, due to the non-linear relationship between temperature, effective viscosity and the flow fields. At each iteration, the residuals of the velocity and temperature are calculated. These are defined as the maximum difference (the L_∞-norm) in the nodal values of temperature and velocity between consecutive iterations. The velocity differences are normalized by the maximum velocity value in the flow field; there is no normalization for the temperature differences. Convergence is achieved with residuals for both velocity and temperature of less than 10^{-6}. Little improvement in the velocity or temperature fields is observed for models that are allowed to converge to a residual of 10^{-8} (see **Appendices B and C**).

6.5 Benchmarking the Modelling Code

Extensive tests were performed to establish the numerical accuracy of the modelling technique and to better understand the dynamics of viscous flow. Two different types of models were examined: a sheared box and mantle wedge flow at a subduction zone. The benchmarking exercises are described in **Appendix A** and **Appendix B**, respectively. The key observations are summarized below.

6.5.1 Sheared box models

The first benchmarks examine shear flow in a viscous box, where flow is induced by horizontal movement (10 cm/yr) of the upper boundary. The temperature at the top and bottom of the box are fixed at 300°C and 1300°C, respectively. These tests illustrate the effects of wedge rheology and viscous dissipation on the flow field and thermal structure of the box. With an isoviscous (constant viscosity) rheology, the box undergoes a uniform strain rate ($1.58\ 10^{-14}\ s^{-1}$), and the flow velocities decrease linearly from the top

of the box (10 cm/yr) to the bottom (0 cm/yr). The inclusion of viscous dissipation does not affect the flow field, as the viscosity has no temperature dependence. The amount of heat generated is directly proportional to the viscosity of the box. For viscosities larger than 10^{21} Pa s, the temperatures within the box are increased significantly (>500°C).

For Newtonian and power law rheologies, regions of high temperature will have a low viscosity. As a result, shear deformation becomes concentrated in low viscosity regions, resulting in a localization of strain near the base of the viscous box, due to the high temperatures in this region. For a Newtonian rheology, the amount of localization increases as the temperature-dependence increases (given by a higher activation energy, Q in **Equations 6.1 and 6.5**). For a power law rheology, strain localization will increase as the stress-dependence increases (n in **Equations 6.1 and 6.5**), and as the temperature-dependence increases (given by the ratio Q/n).

For Newtonian and power law rheologies, the inclusion of viscous dissipation slightly enhances strain localization, due to the feedback between high strain rates, temperature, and effective viscosity. However, viscous dissipation becomes a self-defeating mechanism for generating heat, due to the strong temperature-dependence of the viscosity. For strain rates of 10^{-13} s^{-1} or less (i.e. typical tectonic strain rates), viscous dissipation does not have a strong effect on the thermal field, if the effective viscosity is less than 10^{20} Pa s. For most upper mantle rheologies in **Table 6.1**, the effective viscosity is less than 10^{20} Pa s at temperatures greater than 1000°C, and a strain rate of 10^{-13} s^{-1} (**Figure 6.2**).

6.5.2 Subduction zone benchmarks

The second set of benchmarks examine a subduction zone geometry, consisting of a slab with a 45° dip subducting at 5 cm/yr below a 50 km thick lithosphere. Flow in the mantle wedge is driven only by the subducting plate (i.e., corner flow). The primary goal of this exercise is to verify the numerical accuracy of the modelling code, especially in the wedge tip, which represents a theoretical singularity for pressure and velocity. As shown in **Appendix B**, by using a high node density in this region and quadratic elements, the PGC modelling code is able to accurately model the near-singularity

behaviour. For an isoviscous wedge, the numerical modelling results can be compared to an analytic solution for corner flow [*Batchelor*, 1967]. Numerical tests show that the PGC modelling code can reproduce the analytic pressure and velocity solutions to within 1.2% and 3×10^{-3} cm/yr, respectively, for all parts of the wedge.

Subduction zone models were also developed using Newtonian and power law rheologies for the wedge. As there is no analytic solution with which to compare the numerical results, the models have been compared with those generated using different numerical modelling codes. So far, the main comparisons have been between the PGC modelling code and a modelling code used by Dr. Peter van Keken at the University of Michigan. Although this work is still in progress, the comparison to date has been exceptionally good. Overall, the PGC modelling code has proved to be extremely stable in obtaining accurate numerical solutions with the subduction zone geometry, particularly near the singularity at the tip of the wedge.

CHAPTER 7

The Thermal Effects of Slab-Driven Mantle Wedge Flow

7.1 Introduction

The corner flow model of mantle wedge dynamics pervades through much of earth sciences literature. In this model, flow in the mantle wedge consists of one large cell, where flow is induced by viscous coupling between the wedge and subducting plate. This model has been used in the interpretation of variations in arc and backarc magma geochemistry [e.g., *Turner and Hawkesworth*, 1998; *Hochstaedter et al.*, 2000; *Elkins Tanton et al.*, 2001], seismic tomography images of the mantle wedge [e.g., *van der Lee et al.*, 2001; *Wiens and Smith*, 2003 and references therein], and seismic anisotropy in the backarc mantle [e.g., *Fischer et al.*, 2000]. As well, corner flow has been invoked as a mechanism for triggering backarc spreading, as this flow pattern is expected to exert a margin-normal extensional stress on the base of the over-riding lithosphere [e.g., *Sleep and Toksoz*, 1971; *Toksoz and Hsui*, 1978]. Corner flow has also been proposed as the main way to transport heat into the mantle wedge.

To date, the majority of numerical modelling studies of subduction zone thermal structure have focused on slab-driven corner flow [e.g., *Andrews and Sleep*, 1974; *Honda*, 1985; *Davies and Stevenson*, 1992; *Furukawa*, 1993a, b; *Iwamori*, 1997; *Peacock and Wang*, 1999; *Conder et al.*, 2002; *van Keken et al.*, 2002; *Kelemen et al.*, 2003]. All of these studies use numerical models in which flow within the mantle wedge is driven by a kinematically prescribed subducting plate, i.e., wedge dynamical models. Thermal buoyancy forces are not included in most models, primarily due to the assumption of high viscosities in the mantle wedge. These studies have shown that that slab-driven flow can

---

This chapter forms the basis for the paper:

Currie, C.A., K. Wang, R.D. Hyndman and J. He, The thermal effects of steady-state slab-driven mantle flow above a subducting plate: The Cascadia subduction zone and backarc, *Earth and Planetary Science Letters*, 223, 35-48, 2004b.

significantly elevate temperatures in the mantle wedge below the volcanic arc [e.g., *Furukawa*, 1993a, b; *Kelemen et al.*, 2003]. Temperatures in the upper part of the subducting slab are also strongly affected by wedge flow [e.g., *van Keken et al., 2002*].

Using the numerical modelling code described in the previous chapter, thermal-mechanical models are developed to evaluate the corner flow model as a mechanism for carrying heat into the arc and backarc mantle. Most previous studies have concentrated on the thermal structure of the mantle wedge below the volcanic arc, as the main focus was on obtaining temperatures high enough for arc magma generation. In the current study, the thermal effects of corner flow are examined for both the arc and backarc regions. As shown in **Chapters 3 and 4**, the backarc regions of nearly all subduction zones are extremely hot (relative to cratons), with near-uniform high temperatures for 100's of kilometres behind the arc. This appears to be a characteristic feature of subduction zones, and thus, is a critical constraint that must be matched by any thermal model. This chapter provides an assessment of the distribution of heat within the wedge by corner flow, using first an isoviscous mantle wedge and then a more realistic power law (non-linear) rheology for the wedge.

The interpretation of numerical models requires an understanding of the influence of boundary conditions and model parameters. It is clear that the thermal structure of the incoming oceanic plate strongly affects temperatures in the forearc regions, as well as temperatures in the interior of the slab. One objective is to assess the importance of the backarc (landward) boundary condition to the model results. In the models presented here, as in most previous studies, asthenosphere material enters the wedge through this boundary. As shown below, the thermal structure of the wedge is strongly affected by the boundary location, as well as the prescribed temperature and velocity conditions along this boundary.

The models in this chapter are developed primarily for the northern Cascadia subduction zone. Models are also developed for the contrasting NE Japan subduction zone to examine the effects of key subduction parameters. The NE Japan subduction zone has a greater subducting plate age, shallower subducting plate dip and larger subduction rate. The thermal models may be compared with surface heat flow and other

observational constraints on mantle wedge temperatures. For northern Cascadia, temperatures in the mantle wedge below the arc are inferred to be over 1200°C at 50-60 km depth. The high temperatures extend for nearly 500 km into the backarc, with little lateral variation. As shown in **Chapter 4**, nearly all subduction zones have similar high backarc temperatures.

7.2 Subduction Zone Model Set-up: Cascadia and NE Japan

7.2.1 Model geometry and finite element meshes

The finite element meshes for the Cascadia and NE Japan subduction zones are shown in **Figure 7.1**. The location of the two-dimensional models approximately coincides with the heat flow profiles for Cascadia (**Figure 3.2**) and NE Japan (**Figure 4.6**). In the Cascadia models, the geometry of the subducting Juan de Fuca Plate to 60 km depth has been constrained by seismic reflection and refraction data and Wadati-Benioff seismicity [*Flück et al.*, 1997]. At greater depths, teleseismic studies suggest that the plate dip increases to ~60° [*Bostock and van Decar*, 1995]. The thickness of the over-riding crust is 35 km throughout the forearc and backarc regions, similar to that inferred from seismic studies [*Clowes et al.*, 1995; *Burianyk et al.*, 1997]. The base of the rigid lithosphere is at 50 km depth, consistent with the depth of the lithosphere-asthenosphere boundary inferred from shear structures in mantle xenoliths from this region [*Ross*, 1983] and from thermal estimates [*Hyndman and Lewis*, 1999; see also **Chapter 3**]. The landward (backarc) boundary of the model is 800 km from the trench, in agreement with the inferred eastern limit of the hot backarc and western limit of the North America craton [*Hyndman and Lewis*, 1999].

The observed forearc heat flow is consistent with cooling of the forearc by the subducting plate [*Lewis et al.*, 1988, 1992; *Hyndman and Wang*, 1993; *Wang et al*, 1995b], suggesting that wedge flow does not extend into the tip of the wedge (see **Section 7.3.7**). In the models, wedge flow is prohibited from entering the wedge tip by placing a vertical boundary in the wedge where the subducting plate is at a depth of 70 km (x=240 km), coinciding with the location of the abrupt landward increase in surface heat flow. Seaward of this boundary, the wedge is assumed to be rigid (non-flowing).

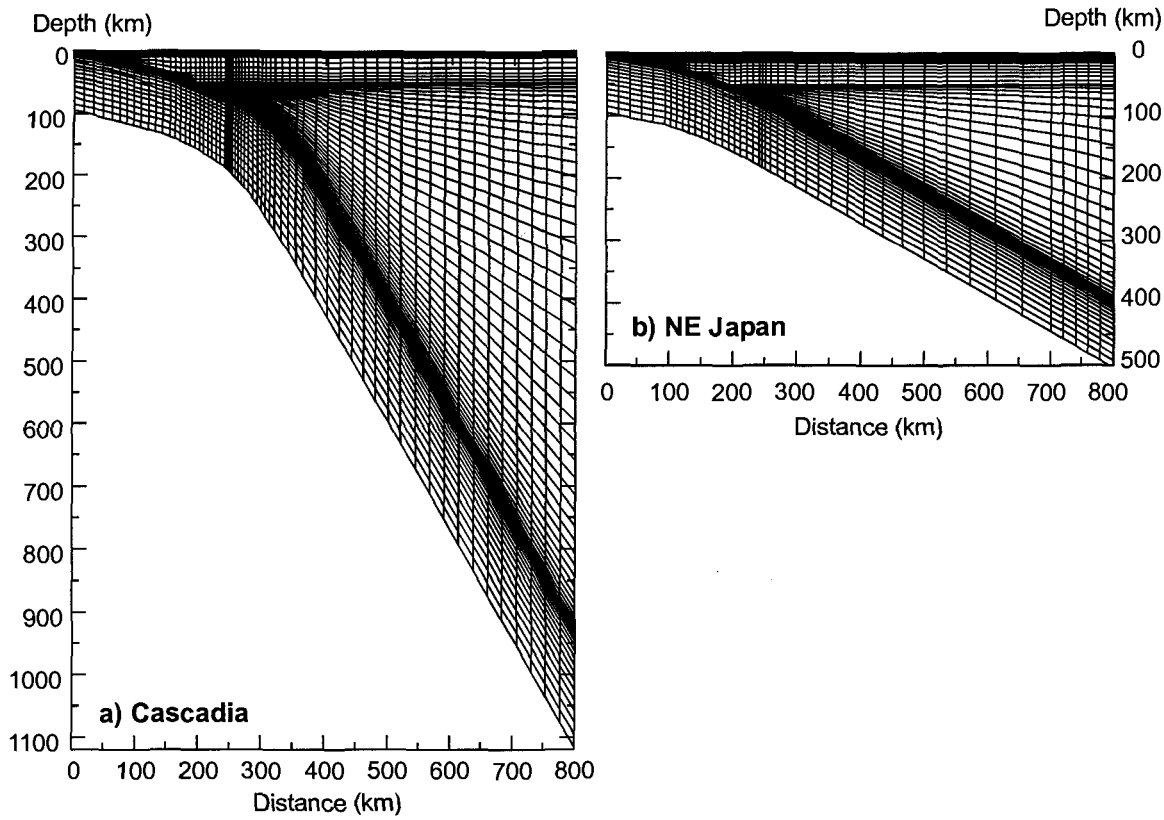

Figure 7.1. Finite element meshes for a) Cascadia and b) NE Japan subduction zone models.

For the NE Japan subduction zone, the subducting plate geometry assumed by *Peacock and Wang* [1999] is used. At depths less than 70 km, the geometry of the subducting Pacific Plate interface is similar to Cascadia. At greater depths, the plate has a dip of 30°. The thickness of the over-riding crust is 30 km and the thickness of the lithosphere-asthenosphere boundary is 50 km. As in the Cascadia models, the wedge tip is assumed to be rigid. The seaward limit of wedge flow is taken to be 240 km from the trench, consistent with the heat flow transition for NE Japan [e.g., *Furukawa*, 1993b].

The Cascadia finite element mesh has 4563 elements (1800 in the viscous wedge), and the NE Japan mesh has 2360 elements (600 in the viscous wedge). Element sizes range from 0.3 km to 50 km, with an average of 9 km. Extensive tests were carried out using these meshes to verify that numerically accurate results for the thermal and flow fields can be obtained with the PGC modelling code (**Appendix C**). The tests focus on

the numerical instability that arises near the seaward end of the viscous mantle wedge (at x=240 km), where the sharp transition from no flow to flow at the full subduction rate introduces mathematical difficulties. In this region, a very dense node spacing is used in order to reduce instabilities. As shown in **Appendix C**, the analytic pressure and velocity solutions for an isoviscous wedge [*Batchelor*, 1967] can be closely reproduced using these meshes. Satisfactory results are also obtained for slab-driven flow with a non-linear temperature- and stress-dependent wedge rheology, with convergence to a residual of 10^{-6} for both velocity and temperature. Additional tests were carried out using NE Japan and Cascadia meshes with a landward boundary 500 km from the trench, similar to that used by *Peacock and Wang* [1999] and *van Keken et al.* [2002]. Using their backarc boundary conditions, the results obtained with the PGC modelling code are in good agreement with the results of these studies for both an isoviscous and power law wedge rheology.

In the models, the base of the mantle wedge is the top of the subducting plate, which exits the model domain at the backarc boundary (x=800 km). For NE Japan, the top of the plate is at ~400 km depth at this boundary. For Cascadia, the depth is ~900 km, due to the steeper plate dip. This means that the viscous mantle wedge in the model extends through the mantle transition zone (410-660 km depth) and into the lower mantle. The transition zone represents a region where mantle minerals undergo phase changes, resulting in density changes that may affect mantle flow patterns [e.g., *Turcotte and Schubert*, 2002]. In order to ensure that the model geometry, with the extremely deep mantle wedge, does not affect the shallow wedge temperatures, Cascadia models were tested with a horizontal basal boundary at a depth of 600 km, such that the subducting plate exits the model through this boundary. Two different boundary conditions were tested: a flow-through basal boundary and a boundary with no vertical flow. The results of these models are shown in **Appendix C**. For all cases, the thermal structure in the upper 250 km of the model is relatively insensitive to the lower boundary of the models.

7.2.2 Model parameters and boundary conditions

Figure 7.2a shows the model parameters and boundary conditions used for the subduction zone models. The subducting plate drives flow within the wedge, assuming full coupling (no slip) along the slab-wedge interface at depths greater than 70 km. For the Cascadia subduction zone, estimates of the rate of subduction of the Juan de Fuca Plate at northern Cascadia range from 3.9 to 4.5 cm/yr [*Mazzotti et al.*, 2003 and references therein]. Following *van Keken et al.* [2002], a subduction rate of 4.5 cm/yr is used. The upper boundary of the wedge is assumed to be fully coupled to the stationary over-riding plate. Flow passes through the landward boundary of the model, using a boundary condition which requires that there be no velocity gradient across the boundary (see **Appendix A** for discussion). The inflow/outflow point along the boundary marks a transition from material entering the wedge at shallow depths to material leaving the wedge at greater depths. The position of this point depends on wedge rheology and subducting plate geometry. This point is iteratively determined within the modelling code.

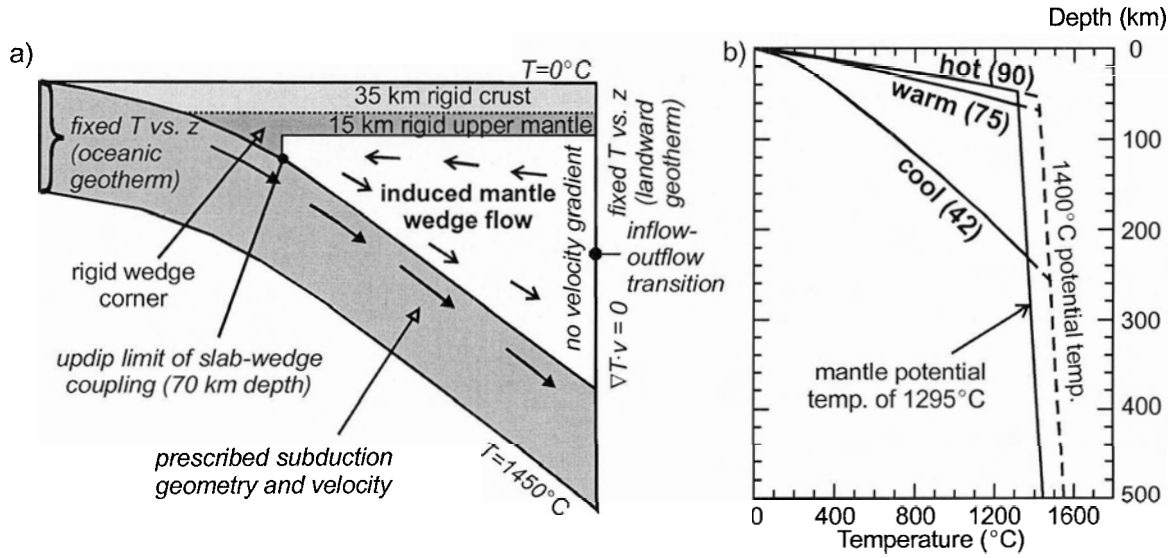

Figure 7.2. a) Schematic model geometry and boundary conditions for the 2D models. Flow in the wedge is driven by full coupling between the subducting slab and overlying mantle below 70 km depth. Flow is only calculated in the white region of the wedge. b) Geotherms prescribed to the inflow part of the landward (backarc) boundary of the models. The numbers in brackets indicate the surface heat flow for each geotherm (in mW/m^2). The transition from a conductive gradient to an adiabatic gradient (0.3 °C/ km) is determined by the mantle potential temperature of 1295° C (solid lines) or 1400° C (dashed lines).

Viscous flow is driven by deviatoric stress induced by pressure gradients. The absolute value of the pressure does not affect the flow field. However, to obtain a solution, it is necessary to specify the absolute value of pressure at one point in the viscous model domain. In the models, a pressure of 0 GPa was prescribed at the intersection of the base of the lithosphere with the landward boundary of the model (x = 800km, z = 50 km).

Previous studies have shown that the rheology of the wedge exerts a strong control on the flow field [e.g., *Furukawa*, 1993b; *van Keken et al.*, 2002]. The models below use either a constant wedge viscosity or a temperature- and stress-dependent (non-linear) viscosity. For the non-linear models, the power law rheology for dislocation creep of wet olivine is used [*Karato and Wu*, 1993; **Table 6.1**], based on the assumption that there is substantial input of water to the wedge from dehydration of the underlying subducting slab. The effects of other rheologies are considered in **Section 7.3.4**.

The four main model units are the subducting plate, the upper and lower crust of the over-riding plate, and the mantle wedge. Both the rigid wedge (lithosphere) and viscous wedge (asthenosphere) are assumed to have the same thermal properties. The thermal parameters of each model unit are similar to those used by *Peacock and Wang* [1999] and *van Keken et al.* [2002] (**Table 7.1**). The only local heat source included in the models is radiogenic heat production. Other local heat sources are assumed to be negligible (see **Section 7.5**). Reasonable variations in the thermal parameters have only a minor effect on model results. Variations in upper crustal heat production, including an eastward increase consistent with Cascadia backarc observations, have a direct effect on the surface heat flow but only a negligible effect on wedge temperatures (<15°C). A temperature-dependent thermal conductivity for all model units was also tested [e.g., *Sass et al.*, 1992; *Clauser and Huenges*, 1995]. For both an isoviscous and non-linear rheology, the temperature-dependent thermal conductivity leads to temperatures that are within ~30°C of those for models with a constant thermal conductivity for each unit (**Appendix C**).

Table 7.1. Thermal parameters for slab-driven flow models

Model Unit	**Thermal Conductivity** ($W\ m^{-1}\ K^{-1}$)	**Radiogenic Heat Production** ($\mu W/m^3$)	**Heat Capacity** ($MJ\ m^{-3}\ K^{-1}$)
Upper crust (0-15 km depth)	2.5	1.3	--
Lower crust (15 km to Moho)	2.5	0.4	--
Mantle wedge	3.1	0.02	4.1
Subducting plate	3.1	0.02	4.1

The upper boundary of the model has a constant temperature of 0°C. The base of the model is the inclined bottom of the subducting slab, taken to be 95 km below the slab surface. A constant temperature of 1450°C is assigned to this boundary. Uncertainties in this temperature have a negligible effect on the upper part of the subducting slab and mantle wedge due to the efficient advective heat transfer from the seaward boundary by the subducting slab. For the Cascadia models, a geotherm is prescribed to the oceanic boundary consistent with an 8 Ma subducting plate overlain by 3 km of sediments [*Stein and Stein*, 1992; *Wang and Davis*, 1992].

7.2.3 Backarc thermal boundary conditions

One objective of this chapter is to examine the effect of the backarc boundary on the thermal structure of the wedge. Because flow passes through this boundary, the prescribed thermal boundary conditions determine the temperature of material entering the mantle wedge. Three different geotherms for the landward boundary are tested (**Figure 7.2b**): 1) a "cool" geotherm that gives a surface heat flow of 42 mW/m^2, typical of cratons [*Rudnick et al.*, 1998; *Jaupart and Mareschal*, 1999]; 2) a "warm" geotherm with a surface heat flow of 75 mW/m^2, consistent with the inferred thermal structure of the Cascadia backarc [*Hyndman and Lewis*, 1999; **Chapter 3**]; and 3) a "hot" geotherm producing a surface flow of 90 mW/m^2, representative of an extremely hot backarc. Each geotherm is calculated assuming a conductive gradient, based on the surface heat flow and the thermal properties of the model crust and mantle (i.e., **Equation 3.3**). At depths

greater than the intersection of the conductive geotherm with the mantle adiabat, an adiabatic gradient of 0.3°C/km is used. The mantle adiabat corresponds to a mantle potential (zero pressure) temperature of 1295°C, consistent with experimental constraints on the temperature of the 660 km phase transition [*Ito and Katsura*, 1989].

Along the backarc boundary of the model, temperatures are prescribed for the over-riding plate and the inflow part of the viscous wedge. For the outflow part of the boundary, the thermal boundary condition is:

$$\nabla T \cdot \mathbf{v} = 0 \qquad (7.1)$$

where T is the temperature and **v** is the velocity field. This boundary condition requires that there be no conductive heat flow parallel to flow lines across the boundary.

7.3 Cascadia Modelling Results

7.3.1 Isoviscous wedge rheology

The most simple rheology for the mantle wedge is a constant viscosity. In the models, a viscosity of 10^{21} Pa s is used, but the results are independent of the absolute value of the viscosity. An isoviscous wedge results in subhorizontal flow in the shallow asthenospheric mantle from the backarc boundary of the model toward the wedge corner [*Batchelor*, 1967; *McKenzie*, 1969; see also **Appendix B**]. **Figure 7.3a** shows the modelled thermal structure and heat flow for each of the backarc geotherms. The thermal structure is highly sensitive to the prescribed temperatures on the landward boundary. For the Cascadia subduction zone, the most realistic geotherm for the boundary of the model is the "cool" geotherm, representative of the adjacent North America craton. With this geotherm, the low temperatures prescribed to the shallow part of the boundary are advected into the wedge, leading to an extremely cold mantle wedge and a nearly constant low heat flow of ~40 mW/m^2 across the backarc and at the volcanic arc. For an isoviscous mantle, the flow field is independent of temperature and thus, flow will occur even when temperatures are extremely low.

The "warm" and "hot" landward geotherms produce a hotter wedge, although temperatures are 200-400°C lower than those inferred from observations. In the backarc,

a seaward decrease in surface heat flow occurs from the prescribed value at the landward boundary to ~60 mW/m^2. This decrease indicates that the flow velocities in the upper part of the mantle wedge are insufficient to maintain the prescribed initial high geothermal gradient, leading to a conductive cooling of the upper part of the wedge. The "equilibrium" value of ~60 mW/m^2 reflects a balance between horizontal advective heat

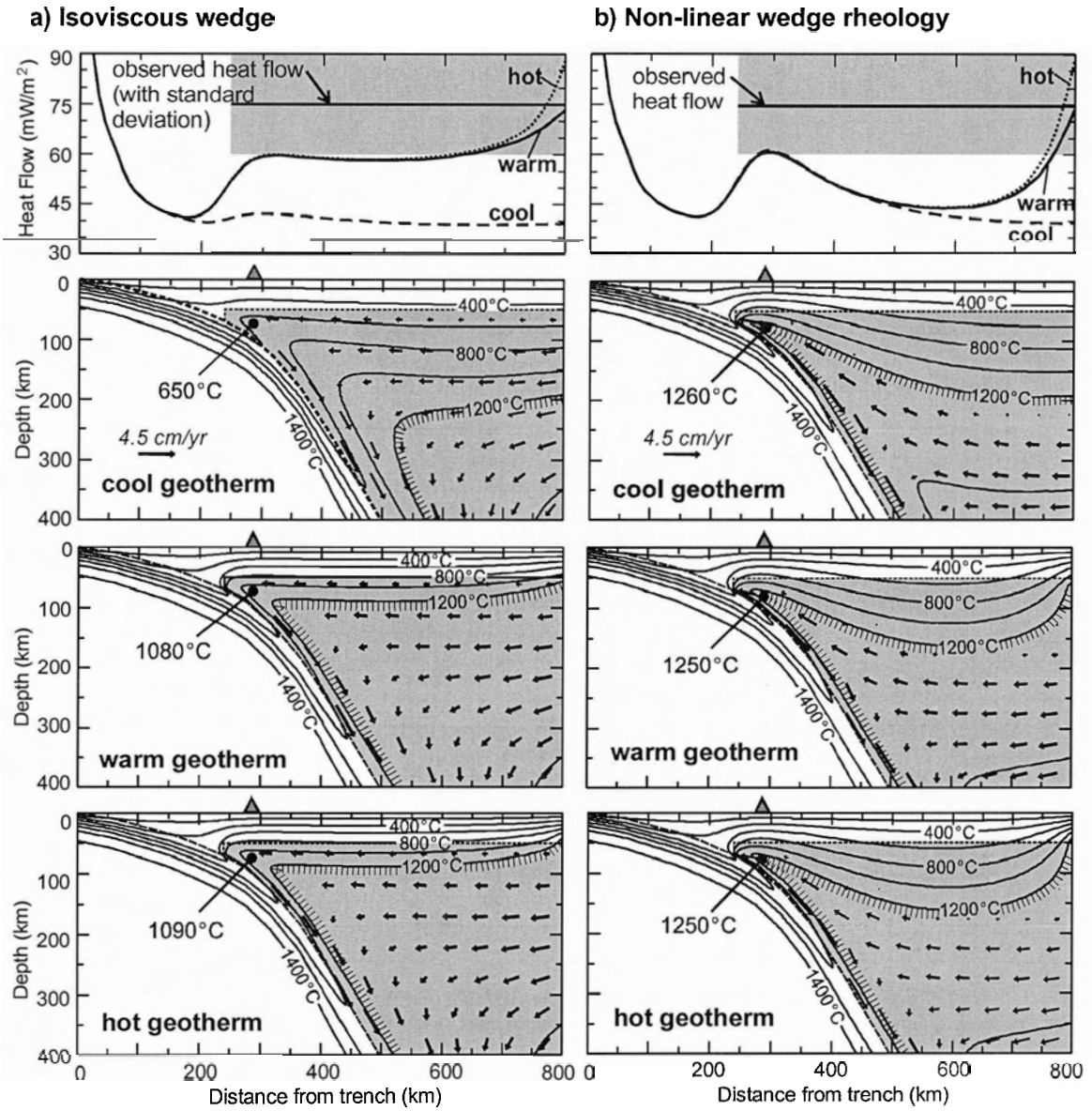

Figure 7.3. Surface heat flow (top) and thermal structure (lower three plots) for Cascadia subduction zone models that use a) an isoviscous mantle wedge and b) a non-linear mantle wedge rheology. For each contour plot, the prescribed geotherm on the landward boundary is indicated. The shaded region shows the viscous part of the wedge (where flow was calculated); arrows indicate the calculated flow direction. Temperatures contours are 200°C.

transfer from the backarc boundary toward the wedge corner, heat loss to the surface, and the very small upward component of wedge flow.

7.3.2 Non-linear wedge rheology

A more realistic stress- and temperature- dependent rheology for the wedge gives a much different flow pattern (**Figure 7.3b**). With this rheology, regions with a high temperature and high strain rate have a low effective viscosity. Due to the non-linear feedback between the temperature and flow fields, a thin low viscosity channel develops sub-parallel to the subducting slab. High velocity flow is concentrated within this channel, resulting in a strong focussing of flow from depth into the wedge corner, as observed in previous studies that use a non-linear wedge rheology [e.g., *Andrews and Sleep*, 1974; *Honda*, 1985; *Furukawa*, 1993a, b; *van Keken et al.*, 2002; *Kelemen et al.*, 2003]. Flow originates from great depths (>150 km) along the backarc boundary, corresponding to the high temperature part of the prescribed geotherm. At these depths, the three geotherms described above have similar temperatures. The similar high temperatures from depth are rapidly advected upward toward the wedge corner. Therefore, all three geotherms produce similar maximum wedge temperatures below the arc of 1250-1260°C, in fair agreement with the inferred temperature for arc magma generation.

As a direct consequence of the strong flow focussing caused by the non-linear rheology, a thick, nearly stagnant "lid" develops in the shallow backarc mantle, where feedback between low stresses and low temperatures produces a high viscosity region. Heat is transferred primarily by conduction within this lid. For models with "warm" and "hot" landward geotherms, this leads to a significant cooling of the shallow backarc mantle seaward of the landward model boundary, as reflected by the rapid seaward decrease in surface heat flow (**Figure 7.3b**). Away from the landward model boundary, all three geotherms produce similar wedge temperatures and a backarc heat flow of 40-45 mW/m^2, much lower than observed. Near the volcanic arc, heat flow increases by 15-20 mW/m^2, as flow is focussed upward into the wedge corner. Although the observed heat flow is high near volcanic centres, the regional heat flow does not increase significantly

approaching the volcanic arc from the backarc [*Blackwell et al.* 1990a, b; *Lewis et al.*, 1992].

7.3.3 Mantle potential temperature

Due to the large depth of inflow for the non-linear viscosity models, the sub-arc mantle temperatures are most sensitive to the deep (>150 km) temperatures prescribed to the vertical landward boundary, given by the assumed mantle potential (zero pressure) temperature and adiabatic gradient. In the above models, an adiabatic geotherm representing a potential temperature of 1295°C was used. If instead a potential temperature of 1400°C is used (**Figure 7.2b**), the maximum mantle temperatures below the volcanic arc are increased by ~95°C (**Figure 7.4**), and surface heat flow at the arc is ~8 mW/m^2 higher. There is little change in the shallow backarc temperatures or heat flow; these regions are still cool with a surface heat flow of 40-45 mW/m^2. For an isoviscous wedge, sub-arc mantle temperatures are increased by ~80°C for models that use a 1400°C mantle potential temperature (**Figure 7.4**).

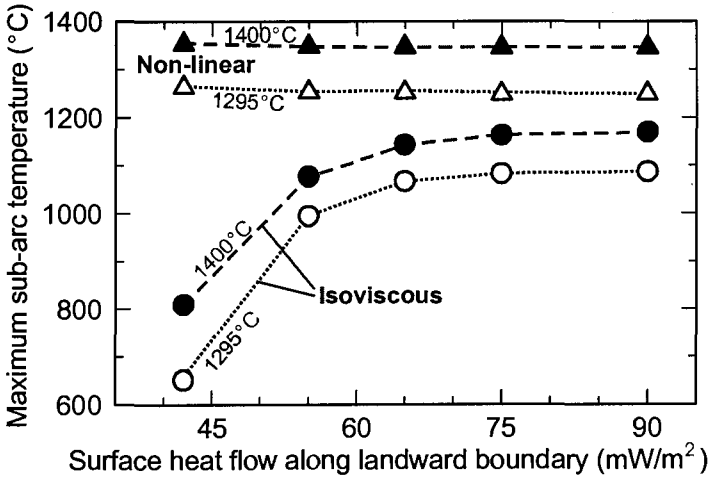

Figure 7.4. The effect of the mantle potential temperature on the maximum mantle temperature below the volcanic arc. Sub-arc temperature is plotted as a function of the prescribed landward geotherm (given by the surface heat flow). Open symbols represent a potential temperature of 1295°C; solid symbols are a potential temperature of 1400°C. Circles are isoviscous models; triangles are models with a non-linear wedge rheology.

7.3.4 Rheological parameters

Different Newtonian and power law rheologies for the mantle wedge are examined, using parameters from **Table 6.1**. In these tests, the warm (75 mW/m^2) geotherm is prescribed to the backarc boundary. Because the flow field is dominated by the kinematic velocity boundary conditions in the subduction zone models, the absolute value of viscosity does not affect the flow structure; it is only the temperature-dependence and, to a lesser degree, the stress-dependence, that affect the results.

For the hypothetical Newtonian rheologies in **Table 6.1**, the viscosity only depends on temperature. As the temperature-dependence increases (given by the activation energy, Q), the maximum mantle temperature below the arc increases (**Figure 7.5a**). With a stronger temperature-dependence, the feedback between temperature, effective viscosity and flow produces a slightly stronger focussing of flow into the wedge corner, resulting in higher temperatures in this region and a somewhat cooler backarc.

For the hypothetical power law rheologies, a greater stress-dependence (given by the stress exponent, n) results in somewhat higher wedge temperatures below the arc (**Figure 7.5b**), reflecting a slightly stronger focusing of flow. Note that this rheology has a very weak temperature-dependence with Q/n = 100000 J/mol. This is less than that of the hypothetical Newtonian rheologies, and thus, the amount of flow focusing is reduced relative to the above models, leading to lower mantle temperatures below the arc.

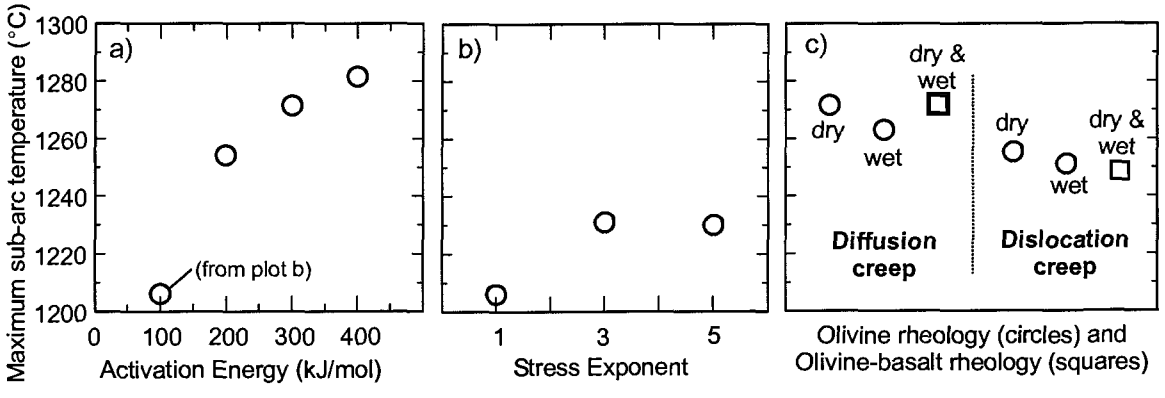

Figure 7.5. Sensitivity of the maximum wedge temperature below the volcanic arc for variations in rheological parameters. a) Effect of temperature-dependence for a Newtonian rheology (given by variations in activation energy, Q). b) Effect of stress-dependence (parameter n) for a rheology that has only a small temperature-dependence (Q/n = 100000). c) Diffusion and dislocation creep parameters for olivine [*Karato and Wu*, 1993] and olivine-basalt [*Mei et al.*, 2002]. Both wet and dry conditions are considered.

Variations in the rheological parameters were examined using the laboratory studies of *Karato and Wu* [1993] and *Mei et al.* [2002]. These flow laws describe diffusion and dislocation creep of both wet and dry mantle minerals. The effects of the different flow laws on the wedge thermal structure are small, with temperature changes less than 30°C and heat flow variations less than 3 mW/m^2. Slightly higher temperatures below the arc are observed for flow laws that have a stronger temperature-dependence (given by the ratio Q/n) (**Figure 7.5c**). For example, diffusion creep (with n=1) tends to have a stronger temperature-dependence, resulting in slightly higher sub-arc temperatures. Other dislocation creep rheologies given in **Table 6.1** give similar results, as the values of Q and n show little variation over the range of mantle compositions examined in the laboratory studies.

Overall, reasonable variations in the rheological parameters have only a small effect on the flow and thermal fields in the wedge. The critical factor is whether the rheology is isoviscous or temperature- (and stress-) dependent. The isoviscous model gives a maximum sub-arc temperature of 1080°C (with the warm landward geotherm), whereas more realistic non-linear mantle rheologies give temperatures of 1240-1280°C.

The effects of partial melt are not included in the models. It is likely that there is a small amount of melt in the mantle wedge, due to the high temperatures and hydrous conditions. As noted in **Chapter 6**, melt will weaken upper mantle minerals [e.g., *Mei et al.*, 2002]. At temperatures above the solidus temperature for the upper mantle (~1300°C for a dry mantle and ~1000°C for a water-saturated mantle at 50 km depth [*Hirth and Kohlstedt*, 1996]), the amount of melt increases with increasing temperature, resulting in a decrease in effective viscosity (e.g., **Figure 6.3**). It is expected that the inclusion of melt in the rheological formulation would result in an even stronger flow focussing into the wedge corner, as the effective viscosity is highly dependent on temperature.

7.3.5 Location of backarc boundary

In addition to the rheology and prescribed wedge inflow boundary temperatures, the location of the backarc boundary is also a critical model parameter. This boundary is

placed 800 km from the trench for the Cascadia models. Distances of 500 and 1000 km were also examined. For isoviscous flow, the location of the boundary has little effect on the thermal structure when the cool geotherm is prescribed to the boundary (**Figure 7.6**). Wider models have slightly higher heat flow and mantle temperatures at the volcanic arc,

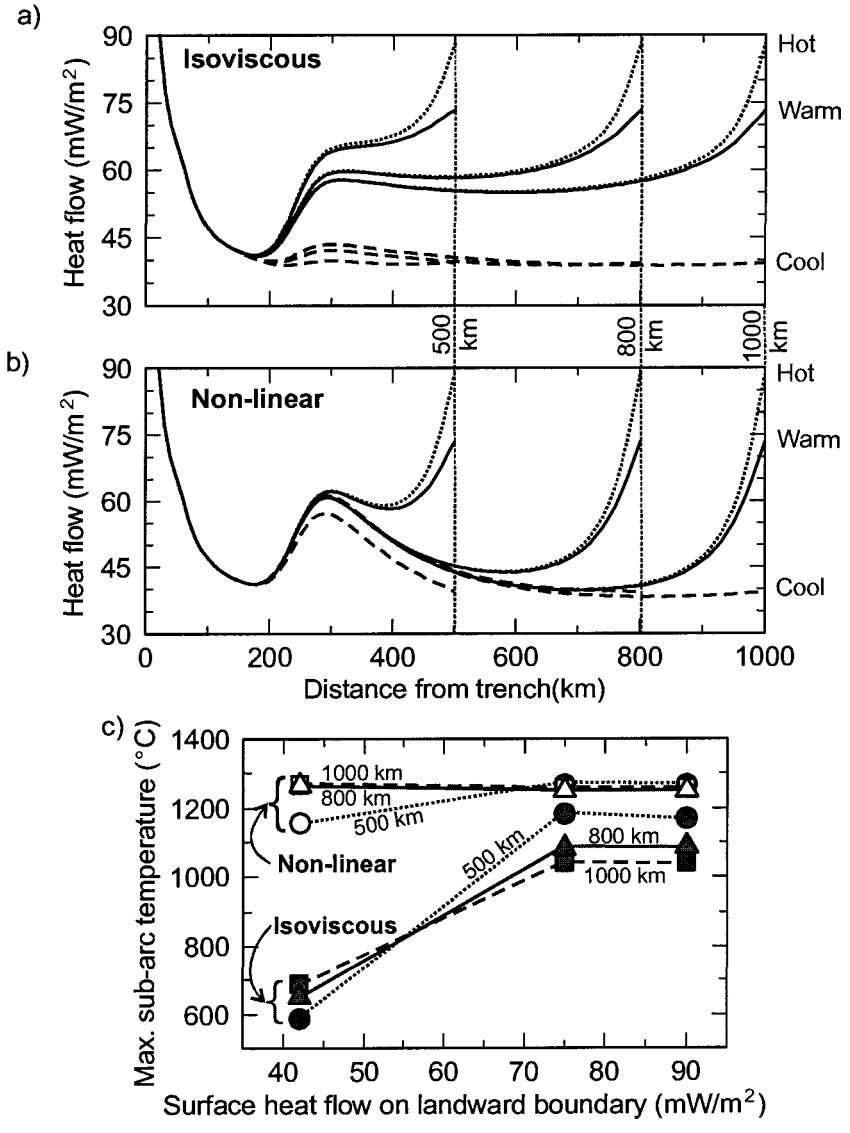

Figure 7.6. Effect of finite element mesh width on thermal structure. Three widths are tested: 500 km, 800 km (standard model) and 1000 km. Surface heat flow for a) an isoviscous wedge and b) a non-linear wedge rheology. The model width is indicated by the landward extent of heat flow line; the prescribed landward geotherm is indicated by the line style (cool geotherm = dashed line; warm = solid; hot = dotted). c) Maximum mantle wedge temperature below the volcanic arc as a function of the prescribed landward geotherm used (given by surface heat flow). Circles are a model width of 500 km; triangles are 800 km; squares are 1000 km. Solid symbols are an isoviscous rheology; open symbols are a non-linear rheology.

due to the small upward component of wedge flow. For the warm and hot geotherms, the location of the boundary strongly affects surface heat flow; a greater decrease in heat flow away from the boundary is observed as the model width increases. For these geotherms, wider models produce lower surface heat flow and lower temperatures at the volcanic arc, due to the greater loss of heat to the surface over the wider backarc.

For models with a non-linear rheology, the location of the boundary has only a small effect on the temperatures below the arc, regardless of the prescribed landward geotherm. However, the development of the cool backarc lid is sensitive to the distance between the boundary and the arc. With a wider model domain, the cool backarc lid becomes more pronounced. For a model width of 500 km, only a slight cooling is observed in the shallow backarc mantle for the warm and hot geotherms, due to the proximity of the hot boundary to the arc. Many previous studies that use a non-linear rheology have placed the backarc boundary relatively close (200-300 km) to the volcanic arc [e.g., *Furukawa*, 1993a; *van Keken et al.*, 2002]. In studies that use a wide (>400 km) backarc model domain, a cool backarc lid is observed, similar to that in the models above [e.g., *Keleman et al.*, 2003].

For both an isoviscous and a non-linear wedge rheology, these tests suggest that the location of the boundary has little effect on the temperatures below the volcanic arc, if this boundary is located more than 500 km from the arc. However, the backarc surface heat flow is fairly sensitive to the boundary location.

7.3.6 Thick craton lithosphere at the backarc boundary

In the above models, flow was allowed to enter the backarc from anywhere along the backarc boundary shallower than the inflow-outflow transition point. For the next set of tests, a thick, rigid lithosphere is introduced to this boundary, which prohibits flow from entering the wedge at shallow depths. This thick lithosphere simulates the presence of a craton adjacent to the backarc.

Many subduction zones are located next to cratons or stable platforms, including the Cascadia and South America subduction zones. The lithosphere beneath cratons may be 200-400 km thick, based on seismic evidence, surface heat flow and xenolith

thermobarometry [e.g., *Jordan*, 1975; *Rudnick et al.*, 1998; *Jaupart and Mareschal*, 1999; *Russell and Kopylova*, 1999; *Forte and Perry*, 2000; *Artemieva and Mooney*, 2001]. These observations suggest cool temperatures to great depths. The large lithosphere thickness and the long-term stability of the craton lithosphere appear to be related to much higher viscosities at depth relative to the adjacent backarc, due to the combination of cool temperatures, chemical depletion, and possibly anhydrous conditions (see **Section 3.8**).

To study the effects of thick-craton lithosphere, a rigid rectangular block was introduced to the Cascadia models. The seaward boundary of the block is located 800 km from the trench, consistent with the eastern limit of the northern Cascadia backarc. The block has a thickness of 250 km, similar to estimates of the North America craton lithosphere thickness from seismic tomography [*Grand*, 1994; *van der Lee and Nolet*, 1997; *Frederiksen et al.*, 2001], xenolith P-T data [*Russell and Kopylova*, 1999], and thermal arguments [*Jaupart et al.*, 1998; *Rudnick et al.*, 1998; *Jaupart and* Mareschal, 1999; *Artemieva and Mooney*, 2001]. This thickness also coincides with the transition from a conductive to adiabatic gradient for the cool geotherm (**Figure 7.2b**), making the velocity conditions along the boundary more compatible with the thermal conditions (i.e., inflow is limited to high temperature regions for an isoviscous wedge). In the models, the cool craton geotherm is used.

For an isoviscous mantle wedge, the presence of the thick-craton lithosphere has a significant effect on mantle flow (**Figure 7.7**). The rigid craton deflects material from beneath the craton into the mantle wedge, resulting in the upward flow of hot material and producing a significant heating of the wedge. Surface heat flow increases from ~40 mW/m^2 at the craton to 50-60 mW/m^2 across the backarc. Mantle temperatures below the volcanic arc are ~500°C hotter than models without a craton, although still lower than inferred magma generation temperatures. In these models, the heating effect produced by the craton depends on the vertical distance between the top of the subducting plate and the base of the craton, given by the arc-craton distance, craton thickness, and subducting plate geometry. As the craton moves closer to the arc or as the craton thickness increases, the wedge temperatures are increased slightly (**Figure 7.8**). However, if this

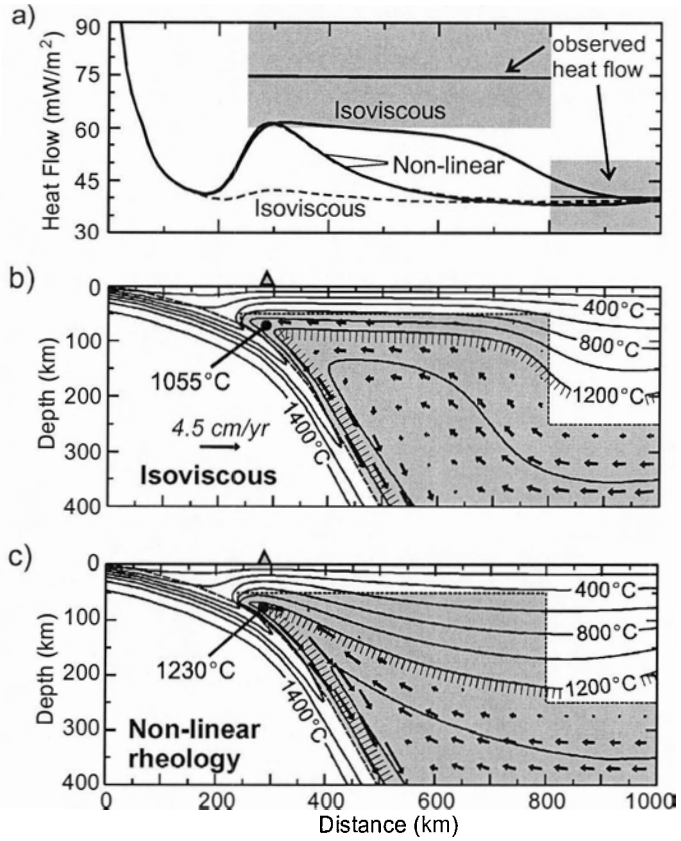

Figure 7.7. Cascadia thermal models with a rigid 250 km thick craton lithosphere located 800 km from the trench. a) Modelled surface heat flow for models with a craton (solid lines) and without a craton (dashed lines). The cool geotherm was prescribed to the landward boundary of all models. The observed heat flow (with standard deviation) is also shown. b) Thermal model for an isoviscous wedge (200°C contours). The shaded region indicates where viscous flow was allowed; arrows show flow direction. c) same as b, but for a non-linear wedge rheology.

space is too small to allow sufficient inflow of material, the cool down-going material on top of the plate is recirculated back into the wedge corner, instead of continuing downward with the slab and the heating effect of the craton is reduced (**Figure 7.9**).

For a non-linear wedge rheology, the presence of a craton has a negligible effect on the thermal structure of the wedge (**Figure 7.7**), as flow into the wedge has a large origin depth even without the craton, due to the strong temperature-dependence of viscosity. The presence of a craton is not sufficient to alleviate cooling of the backarc produced by the non-linear rheology. Variations in the thickness and location of the craton have little effect on the flow and thermal structure, unless the craton begins to

impinge on the region with high flow velocities. In this case, flow becomes deflected upward into the wedge, producing a slight heating **(Figure 7.8)**

The thermal structure of the wedge is sensitive to the temperatures prescribed to the backarc boundary below the base of the craton. At these depths, an adiabatic gradient is used, and thus, the wedge temperatures are directly related to the assumed mantle potential temperature. The temperatures below the volcanic arc can be increased by ~90°C by increasing the mantle potential temperature from 1295°C to 1400°C (**Figure**

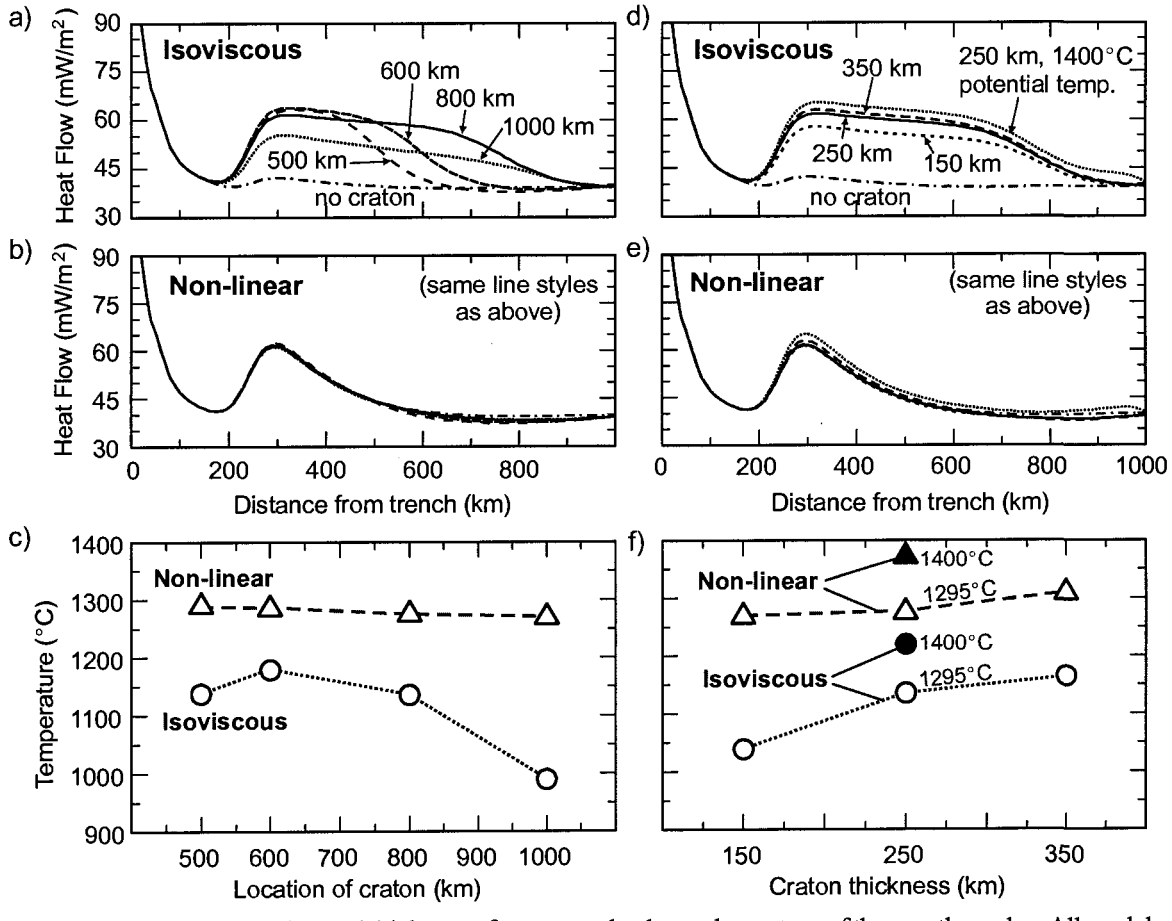

Figure 7.8. Effect of location and thickness of craton on the thermal structure of the mantle wedge. All models use a cool geotherm at the landward boundary of the model (x=1000 km). a) Surface heat flow for isoviscous models for various trench-craton distances. b) Same as a, but for a non-linear rheology. c) Maximum wedge temperature below the volcanic arc as a function of the trench-craton distance. Circles are an isoviscous rheology; triangles are a non-linear rheology. d) Surface heat flow for isoviscous models with various craton thickness (trench-craton distance is 800 km). Also shown is a model that uses a mantle potential temperature of 1400°C (craton thickness of 250 km). All other models use a 1295°C potential temperature. e) Same as d, but for a non-linear rheology. f) Maximum sub-arc wedge temperature as a function of craton thickness (circles are an isoviscous rheology; triangles are a non-linear rheology). Solid symbols are a model with a 1400°C mantle potential temperature.

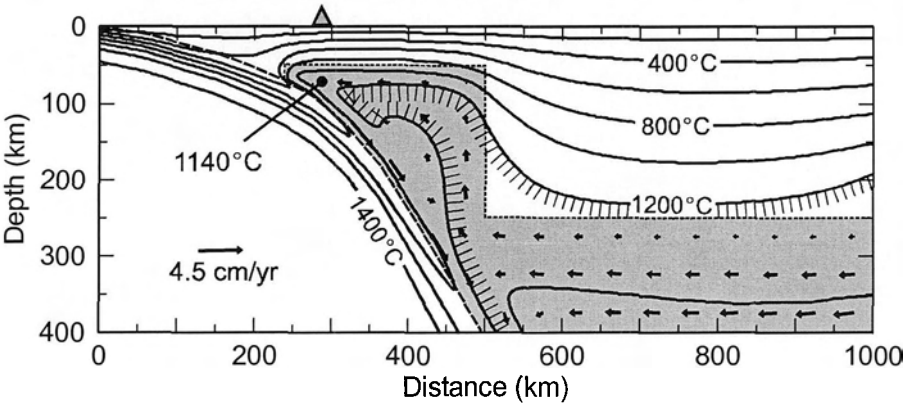

Figure 7.9. Cascadia thermal model with a rigid 250 km thick craton located 500 km from the trench. An isoviscous mantle wedge is used.

7.8f). Surface heat flow is increased by <5 mW/m^2 with the higher mantle potential temperature.

7.3.7 Lithosphere thickness and seaward extent of wedge flow

The above models use a 50 km thick lithosphere throughout the backarc, consisting of a 35 km continental crust and a 15 km mantle. This thickness marks the shallowest depth at which flow is allowed. In the case of an isoviscous wedge, flow extends up to the base of the lithosphere (e.g., **Figure 7.3a**). For a non-linear rheology, the strong temperature-dependence also controls the shallowest limit of flow. Although the shallow backarc regions have a viscous rheology, flow focusing into the corner leads to low temperatures, and therefore low viscosity and low strain rates in the uppermost backarc mantle, making this region effectively rigid.

In order to examine the sensitivity of the results to the prescribed thickness, models were developed with a lithosphere thickness of 35 km (corresponding to the base of the over-riding continental crust). For these tests, the Cascadia models with a craton are used, with the cool geotherm (1295°C potential temperature) prescribed to the backarc boundary. For an isoviscous rheology, the thinner lithosphere allows flow at shallower depths, resulting in a ~30°C increase in shallow backarc mantle temperatures. Surface heat flow is increased by 5-7 mW/m^2 throughout the backarc **(Figure 7.10).**

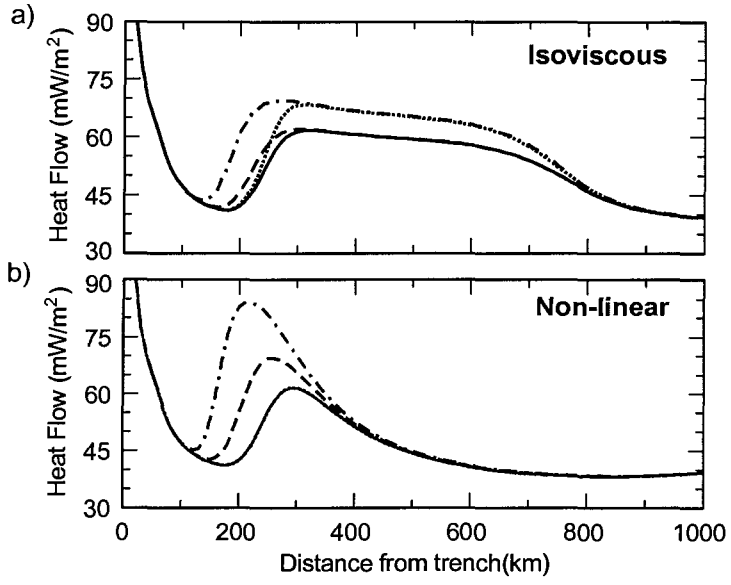

Figure 7.10. Effect of lithosphere thickness and seaward extent of wedge flow on surface heat flow for a) an isoviscous rheology and b) a non-linear rheology. Solid lines are a 50 km lithosphere thickness with a seaward limit of flow at x = 240 km. Dashed lines are a 50 km lithosphere, with flow into the wedge tip (x=190 km). Dotted lines are a 35 km lithosphere with a flow limit at x=240km. Dot-dashed lines are a 35 km lithosphere with flow into the wedge tip (x=153 km).

For a non-linear rheology, little change in surface heat flow or sub-arc mantle temperatures are observed for different lithosphere thicknesses. With this rheology, temperatures and heat flow in the vicinity in the volcanic arc are extremely sensitive to the seaward limit of mantle wedge flow. In the models, flow was prohibited from entering the forearc mantle wedge corner. Thus, the rigid corner is cooled by the subducting plate. Both the cool wedge corner and cooling to the Earth's surface result in a cooling of the viscous mantle near the wedge corner. Due to the cool temperatures and strongly temperature-dependent rheology, flow is limited to depths of ~50 km or greater, regardless of the prescribed lithosphere thickness. Thus, the surface heat flow and wedge temperatures at the volcanic arc are relatively insensitive to variations in lithosphere thickness.

The thermal structure of the forearc changes significantly if flow is allowed to extend all the way into the wedge tip, assuming that the lithosphere thickness remains constant to the intersection with the subducting plate. For both an isoviscous and a non-linear rheology, the transition from low forearc heat flow to high backarc heat flow

occurs approximately over the seaward limit of flow (150 km from the trench for a 35 km thick lithosphere; 190 km for a 50 km thick lithosphere) (**Figure 7.10**). For an isoviscous wedge, temperatures of the forearc are increased, but there is little change (<5°C) in the mantle temperature below the volcanic arc.

For a nonlinear rheology, there is a significant increase in the forearc/arc heat flow and wedge temperatures when flow is allowed to extend into the wedge corner. The flow focussing produced by the non-linear rheology means that high-velocity, high temperature flow "ablates" the wedge corner region, as first noted by *Andrews and Sleep* [1974]. The cool slab is inefficient at cooling the material in the wedge corner, and thus the shallowest depth of flow is determined by the prescribed thickness of the over-riding lithosphere. As the over-riding lithosphere thickness decreases, the heat flow maximum shifts seaward and increases. Mantle wedge temperatures below the arc are increased by 15°C for a 50 km lithosphere and 25°C for a 35 km lithosphere. If the entire over-riding plate were assumed to be viscous, flow would extend nearly to the Earth's surface at the trench, producing extremely high heat flow and high temperatures throughout the forearc region.

For many subduction zones, including Cascadia and NE Japan, surface heat flow observations indicate that the forearc regions are fairly cool; the transition to high mantle wedge temperatures and high heat flow occurs near the volcanic arc [*Lewis et al.*, 1988, 1992; *Furukawa*, 1993b]. These observations suggest that the seaward extent of wedge flow is mechanically-limited. In the models above, this was accomplished kinematically by assuming a rigid wedge tip. *Rowland and Davies* [1999] suggest that buoyancy of the over-riding crust prevents it from being ablated by wedge flow, and thus it is the crustal thickness that provides the seaward limit for flow. Based on the above models, it appears that a cool, rigid forearc mantle wedge is also required. A possible mechanism for prohibiting flow from entering the forearc tip is decoupling of the slab and wedge at shallow depths. For NE Japan, *Furukawa* [1993b] proposed that the slab and wedge are decoupled to depths of ~70 km by high pore pressure along the slab surface, due to dehydration of the slab. Alternatively, hydration and serpentinization of the forearc

mantle wedge may provide a mechanism for isolating the corner from wedge flow, due to its weak rheology and low density [*Bostock et al.*, 2002; *Hyndman and Peacock*, 2003].

The seaward extent of wedge flow is a critical parameter for modelling the thermal structure of the forearc and the shallow subducting slab. Temperatures in this region will significantly affect metamorphism and dehydration of the subducting slab, with implications for arc magma generation and the occurrence of in-slab earthquakes.

7.4 Comparison to NE Japan

To determine the sensitivity of the models to variations in the subduction geometry, plate age, and subduction rate, models were developed for the contrasting NE Japan subduction zone, using the finite element mesh shown in **Figure 7.1b.** The deep (>70 km) plate dip for NE Japan is 30°, whereas the dip for Cascadia is 60°. The NE Japan subduction zone has a much older subducting plate (130 Ma), resulting in a cooler incoming plate compared to Cascadia. The subduction rate is 9.1 cm/yr, approximately twice that of Cascadia.

The behaviour of the models is similar to that observed for the Cascadia models for both an isoviscous and a non-linear wedge rheology (**Figure 7.11**). For an isovisous wedge with a warm or hot prescribed backarc geotherm, temperatures below the volcanic arc are generally >50°C higher for the NE Japan models (relative to Cascadia), due to the higher subduction rate and thus wedge flow rate. For a non-linear wedge rheology, the thermal effects of an increased subduction rate are partially balanced by the shallower plate dip for NE Japan, which limits the maximum depth of inflow, and hence maximum inflow temperatures. In the backarc, the stagnant lid is slightly thinner, and backarc heat flow and temperatures are slightly higher than for Cascadia, due to the shallower plate dip for NE Japan. The modelled backarc heat flow for the non-linear rheology models is significantly lower than observed (~90 mW/m^2). It should be noted that the thermal structure of this region has been complicated by backarc spreading and extension (see **Chapter 4**).

Using different combinations of the deep plate geometry, subducting plate age

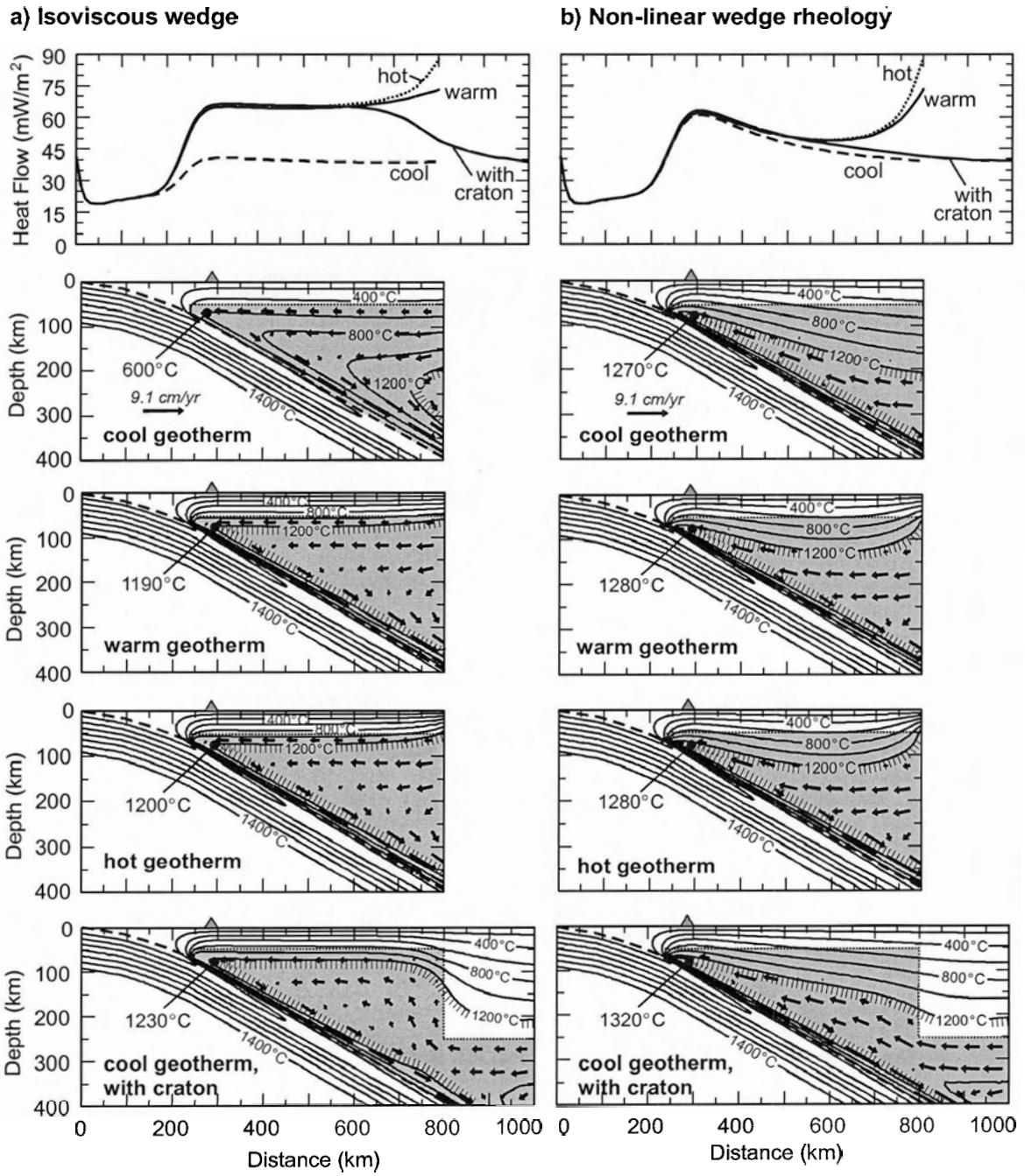

Figure 7.11. Surface heat flow (top) and thermal structure (lower four plots) for NE Japan subduction zone models that use a) an isoviscous mantle wedge and b) a non-linear mantle wedge rheology. The shaded region on each contour plot shows the viscous part of the wedge; arrows indicate flow direction. Temperature contours are 200°C. Three different geotherms for the backarc model boundary were investigated for an 800 km wide model (upper three contour plots). The lowermost plot is a model with a 250 km thick rigid craton located 800 km from the trench. The cool geotherm was prescribed to the backarc boundary for this model.

and subduction rate, it is found that these three parameters have only a small effect (<75°C) on wedge temperatures below the arc for a given landward geotherm and wedge rheology (**Figure 7.12**). *Furukawa* [1993b] reached a similar conclusion for models with a straight (constant dip) subducting plate.

7.5 Local Heat Sources

Some of the high temperatures in the mantle wedge and backarc may be due to local sources of heat. There are numerous local heat sources at a subduction zone, but all appear to be insufficient to significantly heat the wedge.

7.5.1 Frictional heating

Frictional heating along the top of the slab will primarily affect the forearc region where the subducting slab is in contact with the rigid over-riding lithosphere (see **Section 2.3.8**). Low values of heat flow over the forearc of most subduction zones, including Cascadia and NE Japan, suggest little frictional heating, with estimated shear stresses along the top of the subducting plate of 10-30 MPa [e.g., *Wang et al.*, 1995b; *Peacock*,

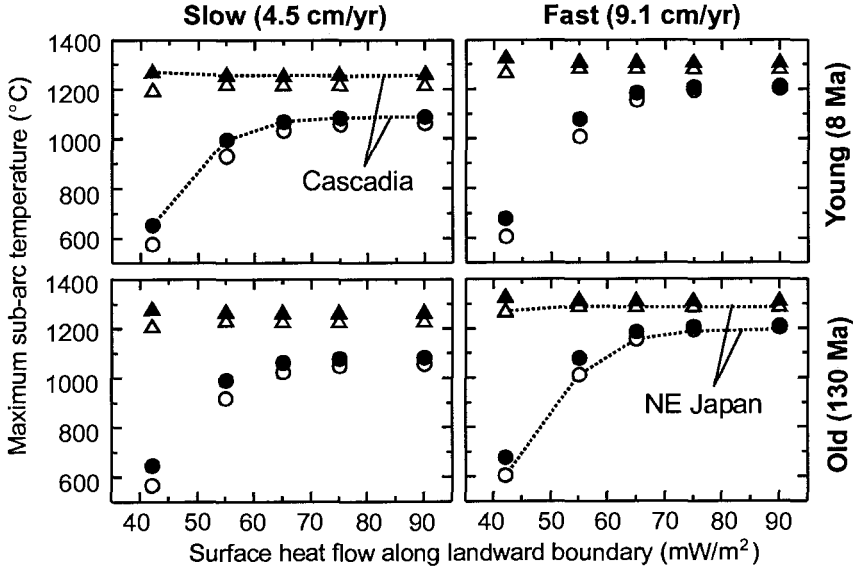

Figure 7.12. The maximum mantle wedge temperature beneath the volcanic arc as a function of the prescribed landward geotherm (given by the surface heat flow) for different combinations of subduction rate, subducting plate age, and subducting plate dip (Cascadia geometry: solid symbols; NE Japan geometry: open symbols) for both an isoviscous (circles) and a non-linear (triangles) mantle rheology.

1996]. Although even a small amount of frictional heating may increase the temperature along the top of the subducting plate by a few 10's of degrees, the effect on mantle wedge temperatures is small. At large depths (and high temperatures), relative motion between the subducting and over-riding plate is accommodated by ductile shear, where the amount of heat generated decreases with increasing temperature. In addition, any frictional heating is limited to depths less than 70 km, as the slab-driven wedge flow models assume full coupling between the subducting slab and mantle wedge at greater depths.

7.5.2 Viscous dissipation

Heat may also be produced through viscous dissipation within the wedge as it deforms. The amount of viscous dissipation depends on both the strain rate and wedge viscosity (i.e., **Equation 6.17**). For an isoviscous wedge, the flow field is independent of the absolute value of viscosity, and thus the amount of heat generated is determined by the viscosity of the mantle wedge. Strain rates in the wedge are on the order of 10^{-14} s^{-1} for isoviscous flow, with the largest values near the wedge corner. With these strain rates, viscous dissipation becomes significant for a mantle viscosity of 10^{21} Pa s or more, as illustrated in **Figure 7.13a**.

Figure 7.13b shows the results for a power law (non-linear) wedge rheology, using the parameters for dislocation creep of wet olivine [*Karato and Wu*, 1993]. With this rheology, viscous dissipation becomes a self-defeating mechanism for heat generation. Significant dissipation requires both a large strain rate and large effective viscosity. However, as a region is heated by viscous dissipation, the effective viscosity will sharply decrease, resulting in a decreased amount of heat generation. This feedback is further aided by the negative effect of large strain rates on the effective viscosity for the power law rheology. The strain rate dependence is particularly important for reducing the amount of dissipation near the wedge tip, where strain rates are fairly large ($\sim 10^{-13}$ s^{-1}). As a result, the inclusion of viscous dissipation has a negligible effect on wedge temperatures.

With a Newtonian rheology, the viscosity only depends on temperature. In this case, there may be significant heat production in the corner (>10 $\mu W/m^3$) if the viscosity

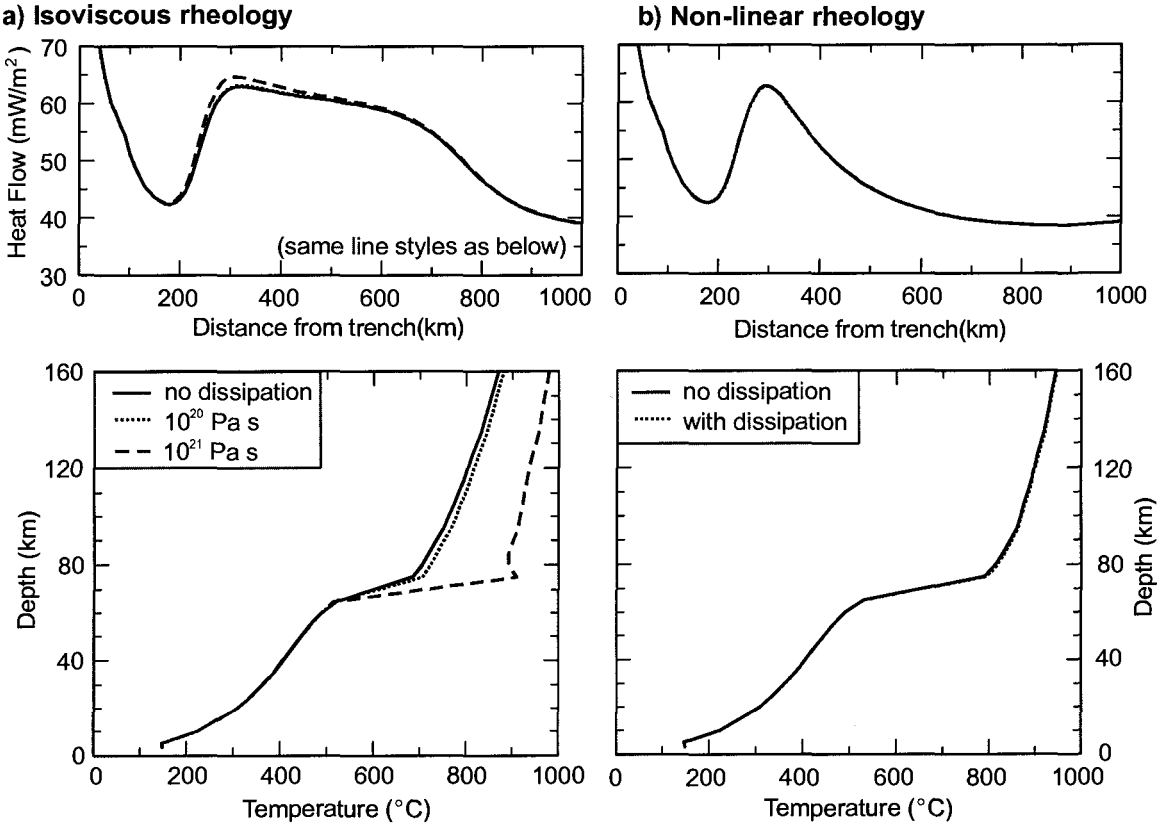

Figure 7.13. Effect of viscous dissipation on the surface heat flow (top) and the temperature along the top of the subducting crust (bottom) for Cascadia models (with a craton) that use a) an isoviscous rheology and b) a power law rheology, corresponding to dislocation creep of wet olivine [*Karato and Wu*, 1993].

is greater than 10^{21} Pa s. Because temperatures in the wedge corner are high (>1100°C) even without dissipation, this effect is only important for diffusion creep of dry mantle minerals, where viscosities are fairly large at high temperatures (**Figure 6.2**). In this case, the inclusion of viscous dissipation will locally increase temperatures in the wedge corner by 50-100°C. Temperatures in the rest of the wedge will be unaffected by viscous dissipation, due to lower strain rates. The mantle wedge is expected to be fairly wet, especially in the corner, due to hydration from the subducting slab. With a wet mantle rheology, viscous dissipation is self-defeating and has a negligible effect on the wedge thermal structure.

7.5.3 Radiogenic heat production

Another local heat source may be radiogenic heating in the mantle, through the decay of Th, U, and K isotopes. The mantle wedge may be enriched in radiogenic elements, due to the addition of these elements to the wedge from subducting slab dehydration [*Iwamori*, 1997], or through subduction erosion that carries crustal material, high in Th, U, and K, down with the subducting slab [*Scholl and von Huene*, 2003]. However, mantle xenolith studies suggest that this is a fairly minor heat source in the mantle (<0.1 $\mu W/m^3$) [*Iwamori*, 1997, *Rudnick et al.*, 1998]. The low concentration of radiogenic elements in arc magmas that appear to be derived from partial melting in the wedge also argues for low asthenosphere wedge concentrations [*Iwamori*, 1997]. In order to have a significant effect on the wedge temperatures, a concentration of radiogenic elements greater than 0.2 $\mu W/m^3$ is required. Although no studies have identified such high values in the backarc mantle, the magnitude of radiogenic heating within the mantle wedge remains an important uncertainty.

Figure 7.14 compares the modelled thermal structure of the wedge for models that use the standard mantle value of 0.02 $\mu W/m^3$ [e.g. *Rudnick et al.*, 1998], with an enriched wedge that has a heat production of 0.2 $\mu W/m^3$. For isoviscous flow, the enhanced heat production increases the maximum mantle temperature below the arc by over 200°C (1270°C vs. 1055°C). However, the surface heat flow is only increased by ~7 mW/m^2 and is still slightly less than that observed. For non-linear wedge flow, the sub-arc mantle temperature is 1430°C with the enhanced heat production (compared to 1230°C for the standard model). The focussing of flow into the corner results in increased heat flow near the arc. Heat flow in the backarc is larger than in the standard model, but is ~20 mW/m^2 lower than observed. Thus, even with the increased heat production, it is not possible to generate uniformly high backarc heat flow with a realistic wedge rheology.

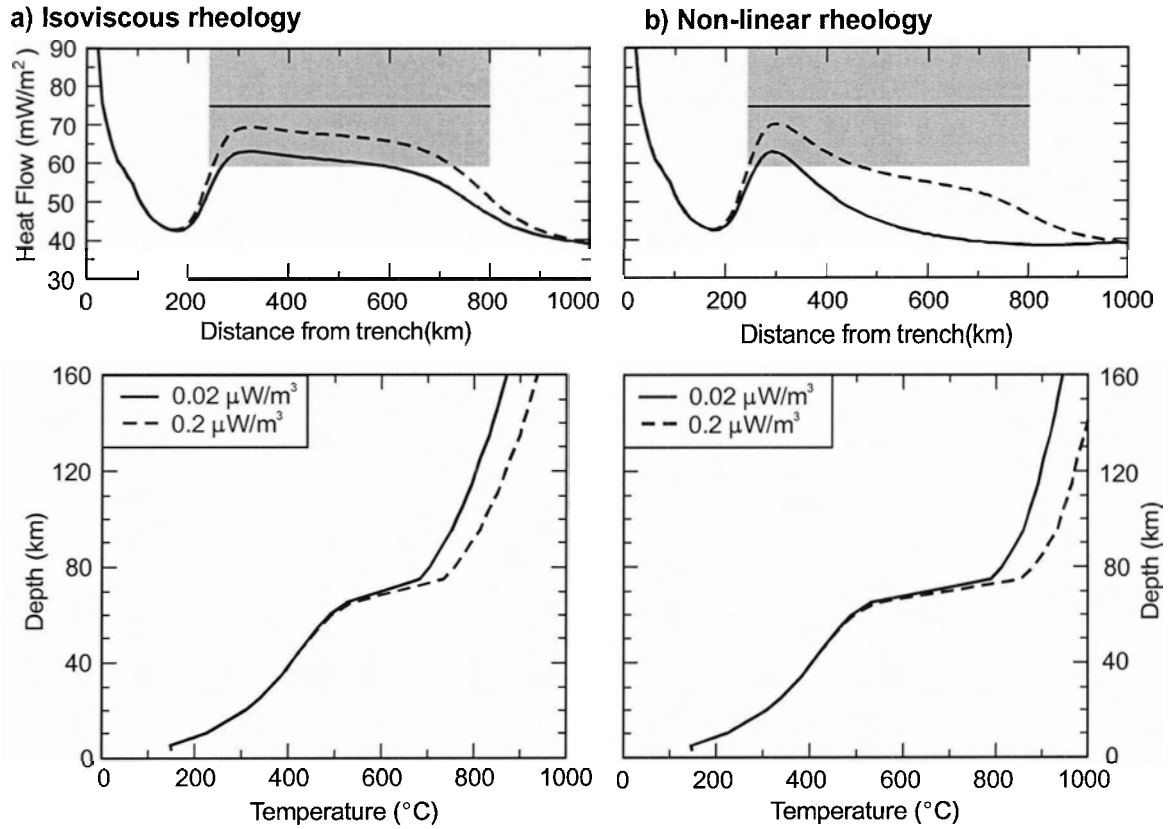

Figure 7.14. Effect of radiogenic heat production in the mantle wedge on the surface heat flow (top) and the temperature along the top of the subducting crust (bottom) for Cascadia models (with a craton) that use a) an isoviscous rheology and b) a power law rheology, corresponding to dislocation creep of wet olivine [*Karato and Wu*, 1993].

7.6 Assessment of Slab-Driven Mantle Wedge Flow

7.6.1 Summary of observations

Assuming that local heat sources contribute only a small amount to the heat budget, it is necessary to transport heat upward into the wedge by mantle flow. From the above models of mantle wedge flow driven by the subducting plate, the thermal structure of the wedge is primarily controlled by the assumed boundary conditions along the backarc boundary, as well as the location of this boundary. For an isoviscous wedge, flow enters the wedge across the backarc boundary at shallow depths, and wedge temperatures are most sensitive to the shallow (<200 km) boundary temperatures. Flow is too slow to transport enough heat into the wedge corner to satisfy constraints on magma generation temperatures, even if unrealistically high temperatures are prescribed

to the boundary. By introducing a thick craton lithosphere to the boundary, flow is forced to originate from depth, elevating temperatures within the wedge, although the temperatures below the arc are still too low for magma generation.

With a non-linear wedge viscosity, flow from depth is focussed into the wedge corner, significantly enhancing temperatures below the arc. In this case, wedge temperatures are determined by the prescribed deep (>150 km) temperatures along the backarc boundary. While this flow transports enough heat into the wedge corner for magma generation, extremely low backarc temperatures and backarc heat flow are produced. This is clearly inconsistent with the well-constrained thermal structure for the Cascadia backarc and the backarcs of other subduction zones.

7.6.2 Maximum thermal effects of slab-driven flow

The maximum thermal effects of slab-driven wedge flow can be evaluated by considering the maximum wedge flow velocity that can be obtained in a slab-driven flow model. An extreme, although physically unrealistic, model would be to completely decouple the viscous wedge from the stationary over-riding lithosphere. For the Cascadia craton model with an isoviscous wedge, decoupling leads to a stronger upflow along the seaward craton boundary and higher flow velocities in the upper backarc mantle. More heat is transported into the wedge, leading to a temperature increase of ~100°C in the shallow backarc, and an increase in heat flow of ~10 mW/m^2, barely sufficient to match the observations (**Figure 7.15**). Beneath the arc, the temperatures are increased by less than 50°C. For a non-linear viscosity, decoupling of the lithosphere and asthenosphere only affects the corner region of the wedge. Below the arc, temperatures are increased by 100°C, and a slightly higher heat flow is produced. The backarc thermal structure is not affected.

7.6.3 Decoupling the slab and wedge

In the models, wedge flow was driven by full coupling between the subducting plate and mantle wedge at depths greater than 70 km. Dehydration of the slab as it subducts may produce a thin layer of hydrated mantle material above the slab.

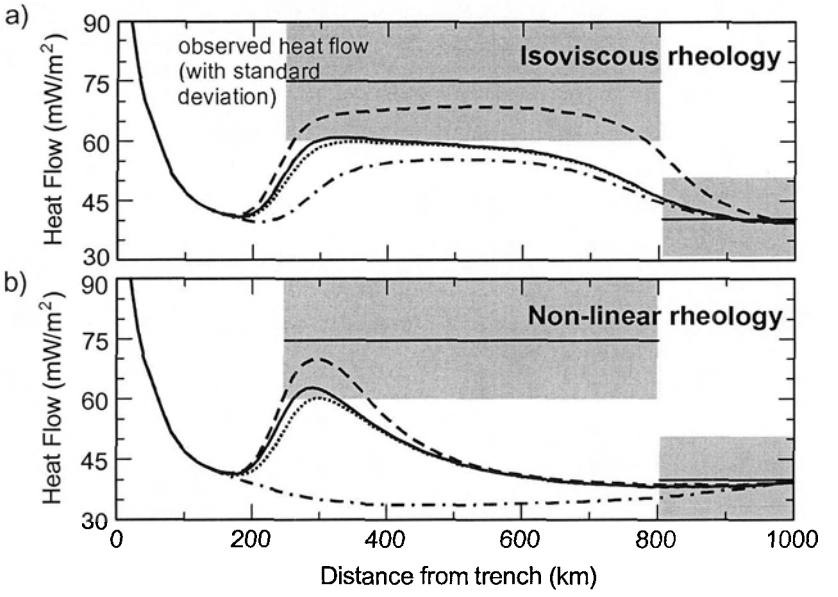

Figure 7.15. Effect of wedge velocity boundary conditions surface heat flow for an a) isoviscous wedge and b) a non-linear wedge rheology. The solid line is the standard model (full slab-wedge and wedge-lithosphere coupling). The dashed line is a model with a decoupled slab and over-riding lithosphere. The dotted and dash-dot lines are models with a 1 km thick low viscosity layer between the slab and wedge (dotted: layer viscosity is 10% of wedge viscosity; dot-dashed: layer viscosity is 1% of wedge viscosity).

Laboratory studies indicate that even a small amount of hydrous fluid can significantly reduce the mantle viscosity [*Hirth and Kohlstedt*, 1996; *Mei and Kohlstedt*, 2000a, b]. The low viscosity layer could, to some degree, decouple the slab and mantle wedge, leading to lower flow velocities in the wedge. The addition of hydrous fluids to the mantle may also result in the formation of weak hydrous minerals (e.g., serpentine), if temperatures are low enough (<700°C) [*Peacock*, 1990; *Ulmer and Trommsdorff*, 1995; *Peacock and Hyndman*, 1999; *Hyndman and Peacock*, 2003]. Both hydration and serpentinization of the mantle immediately above a subducting plate may result in a partial or full decoupling of the slab from the rest of the mantle wedge.

To examine this effect, a 1 km thick low viscosity layer was introduced along the top of the subducting plate. As the viscosity within this layer decreases (relative to the rest of the wedge), the shear induced by the subducting plate will become more localized within the layer, leading to lower flow velocities (and therefore lower temperatures) in the rest of the wedge.

For an isoviscous wedge, if the viscosity of this layer is an order of magnitude less than the rest of the wedge, only a slight decrease in surface heat flow and wedge temperatures is observed (**Figure 7.15a**). Temperatures below the volcanic arc are ~80°C less than models with full coupling. If the layer viscosity is two orders of magnitude less, the surface heat flow is significantly reduced and the wedge temperatures are decreased by 300-400°C.

For the non-linear wedge rheology, the rheology of the thin layer is assumed to have the same temperature- and stress-dependence as the rest of the wedge (i.e., parameters Q and n), but the value of the pre-exponential factor (A) is reduced, such that the absolute value of viscosity within the layer is decreased. As before, the parameters for dislocation creep of wet olivine are used [*Karato and Wu*, 1993]. For a pre-exponential factor of 0.1A, the wedge becomes partially decoupled from the slab, resulting in a slight decrease in surface heat flow and mantle wedge temperatures (<50°C) (**Figure 7.15b**). For a model with 0.01A, the wedge is almost completely decoupled from the slab. The already low viscosity within the layer is further decreased by high strain rates, and thus, nearly all the shear from the subducting slab is accommodated within the layer. The rest of the wedge is nearly stagnant and therefore cool.

7.6.4 Time-dependent models

These models show that it is not possible to simultaneously produce high temperatures beneath the volcanic arc and backarc using only slab-driven mantle wedge flow. Although the models in this study are steady-state models, they illustrate that subduction is primarily a cooling process. In a time-dependent model, the thermal structure at a given time will depend on the initial conditions prior to subduction, as well as the length of time since subduction started. Over time, the system will evolve toward the steady-state model. Regardless of the time scale, these models are not expected to yield a backarc hotter than the initial conditions.

7.7 Conclusions

This chapter provides an evaluation of subduction zone thermal models that include mantle wedge flow driven by a kinematic subducting plate. For these types of models, the location of the backarc model boundary and prescribed conditions along this boundary provide the primary controls on the thermal structure of the wedge. The subducting plate geometry, plate age, and subduction rate have a second-order effect. Given the significant effect that the backarc boundary has on model results, it is important to address the choice of backarc boundary conditions in these models and understand the implications.

The temperatures prescribed to the backarc boundary determine the amount of heat carried into the wedge by flow. The wedge rheology determines the flow pattern and thus the distribution of heat. For an isoviscous wedge, the flow field is fairly diffuse, and flow is too slow to carry a significant amount of heat into the wedge corner for arc magma generation, regardless of the prescribed thermal conditions along the backarc boundary. If thick-craton lithosphere is introduced at the boundary to focus flow from greater depths, temperatures in the backarc are increased, but the arc corner is still too cold for magma generation.

With a temperature- (and stress-) dependent wedge rheology, the entrained material and return flow are confined to a relatively narrow channel above the subducting plate. Flow rapidly carries heat from depth into the wedge corner, significantly enhancing temperatures below the arc. However, if the backarc boundary is located more than 200 km from the arc, a thick, stagnant lid develops in the backarc, resulting in low backarc temperatures and heat flow.

A hot backarc appears to be a characteristic of nearly all subduction zones; the only clear evidence that any backarc is cool is in regions with a flat slab (see **Chapter 4**). The models presented above examine a wide range of reasonable model parameters to look at the thermal consequences of slab-driven flow. None of these models are able to simultaneously produce high temperatures beneath the volcanic arc and throughout the backarc. One of the major conclusions of this study is that simple slab-driven flow is insufficient to carry the required amount of heat into the subduction zone; an additional

component of mantle flow is required. In the next chapter, the effects of buoyancy-driven thermal convection in the backarc mantle are considered.

CHAPTER 8
Thermal Convection In the Backarc Mantle

8.1 Introduction

Observations of high heat flow and inferred hot, thin lithosphere for 100's of kilometres into backarcs provide an important and very restrictive constraint for models of mantle wedge dynamics that has not been widely recognized. Given that local heat sources appear to be insufficient to generate the observed uniform high mantle wedge temperatures, mantle wedge flow is required to carry heat into the mantle wedge and backarc from outside the subduction zone.

The source of heat must be located at depth in the backarc regions. A shallow heat source landward of the backarc is not plausible, especially for backarcs that are adjacent to cold, stable cratons, such as Cascadia and South America. In the numerical models in this study, this heat source is approximated by prescribing high temperatures to the deeper part of the backarc boundary of the models. The implicit assumption is that there is a larger scale mantle convective process outside the subduction zone that maintains high temperatures in this region. Flow in the backarc taps this large mantle-wide ("infinite") heat source and carries the heat upward into the mantle wedge.

The models in the previous chapter examine mantle flow driven by viscous coupling with the subducting slab. This flow pattern consists of a single 2D "convection" cell, where flow velocity is limited by the rate of subduction (i.e., a few centimetres per year). For a reasonable range of boundary conditions and model parameters, it was not possible to efficiently advect a sufficient amount of heat into the wedge using slab-driven flow to produce the inferred high wedge temperatures. To maintain high temperatures throughout the mantle wedge and backarc, flow velocities much faster than plate rates are required. Thermal buoyancy was not included as a driving force for flow in the above

models. As in previous studies, it was assumed that viscous coupling with the slab is the dominant driving mechanism for backarc mantle flow.

The relative importance of forced (slab-driven) convection and free (thermal) convection is dependent primarily on the viscosity of the mantle [e.g., *Ida,* 1983]. At high viscosities, viscous drag from the subducting plate will dominate, as thermal buoyancy forces are insufficient to overcome the viscous resistance to flow and coupling to the subducting slab is strong. At lower viscosities, thermal buoyancy forces will become more important for driving flow and coupling to the slab is weak.

In this chapter, it is argued that mantle wedge flow driven by thermal buoyancy is much more significant than previously assumed. Thermal buoyancy forces in the mantle wedge arise from lateral and vertical temperature gradients, due to both cooling from the subducting slab and heating of the lowermost backarc wedge from below. As the mantle material immediately above the slab is cooled, its density will increase and it may sink, causing an influx of material from the backarc toward the wedge corner. The flow regime may be similar to slab-driven corner flow. In the case of heating from below, the positive thermal buoyancy of the hot material at depth will act as a driving force for flow, and the convective pattern may be more complex. It is likely that both forms of thermal convection occur in the mantle wedge.

A detailed analysis of the dynamics of backarc thermal convection is beyond the scope of the current study. The primary goal of this chapter is to address the thermal effects of free convection in general. First, simple models are developed to investigate the effects of thermal convection on mantle wedge temperatures. Two approaches are used: 1) parameterized convection models, and 2) numerical models with thermal buoyancy. Then, constraints on the mantle wedge viscosity are summarized. A wide range of data indicate that the viscosity of the backarc mantle is surprisingly low, and thus significant thermal convection is concluded to be likely. The chapter ends with a short discussion of a conceptual model for mantle wedge dynamics.

8.2 Thermal Effects of Free Convection

8.2.1 Proxy model for convection

Rapid heat transfer due to free convection is simulated using a simple conductive proxy model, following the approach of *Sharpe and Peltier* [1979] and *Davis et al.* [1997]. In this model, free convection is parameterized by assigning a very high thermal conductivity to the viscous mantle wedge. The ratio of the effective conductivity to the true mantle conductivity is equal to the Nusselt number (*Nu*) of the system. This number represents the ratio of the total heat transport to the heat transferred by conduction alone and is therefore a measure of the efficiency of convective heat transfer. Higher *Nu* values indicate more vigourous convection. Using this approach, it is possible to examine the time-averaged thermal effects of vigourous flow, without requiring that the full thermal-mechanical equations be solved [e.g., *Nyblade and Pollack*, 1993]. This method is particularly advantageous for understanding the thermal effects of extremely vigourous (and possibly chaotic) flow, where the flow pattern may be time-dependent and the numerical computation becomes complex and time-consuming.

The proxy models presented use the Cascadia geometry that includes a 250 km thick craton located 800 km from the trench (e.g., **Section 7.3.6**). The "cool" geotherm is assigned to the landward boundary of the model, to approximate the thermal structure of the adjacent craton. Mantle wedge flow is assumed to be driven by both thermal buoyancy and viscous coupling between the slab and wedge. To approximate the effects of free convection, the viscous mantle wedge has a thermal conductivity of 31 W m^{-1} K^{-1}, which is 10 times the conductivity value used in the models in **Chapter 7**. Slab-driven flow is included assuming full coupling along the slab-wedge interface, and, for computational simplicity, an isoviscous rheology for the wedge. Results are similar if a non-linear wedge rheology is used, as the thermal structure is primarily controlled by the enhanced conductive heat transfer.

Figure 8.1 shows the thermal structure and surface heat flow for this model. For comparison, a model with only slab-driven flow and the standard wedge conductivity of 3.1 W m^{-1} K^{-1} is also shown. The enhanced conductivity represents rapid mixing of the mantle wedge, and thus, the thermal field in the wedge becomes much smoother (i.e.,

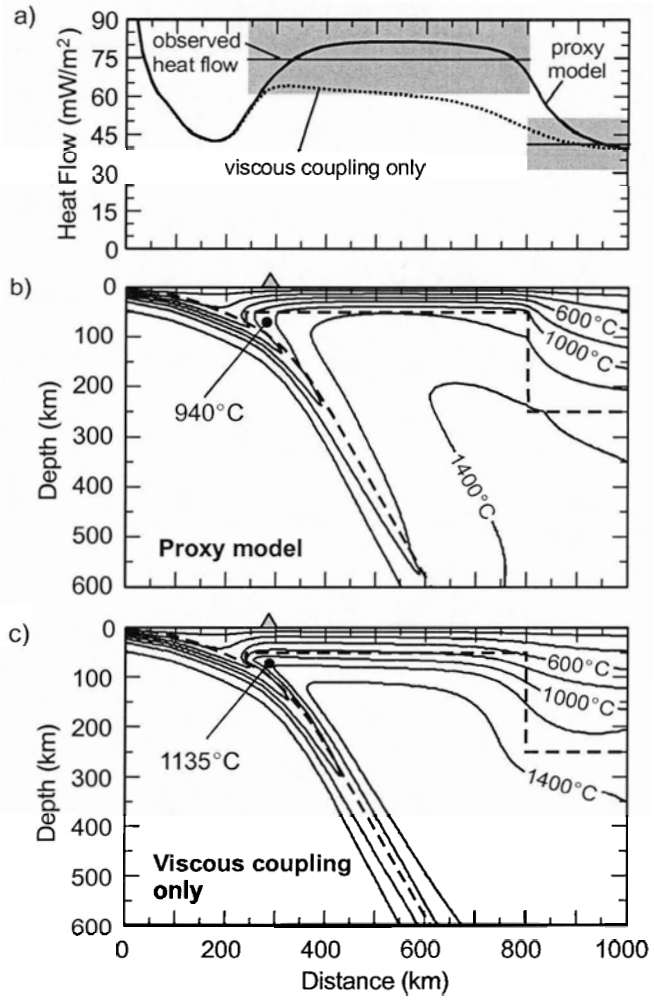

Figure 8.1. The effect of vigourous convection (approximated using an enhanced mantle wedge thermal conductivity) on the thermal structure. The Cascadia geometry (with a craton) and subduction parameters are used. a) Surface heat flow for the proxy model and a model with isoviscous slab-driven flow only. The observed heat flow (with standard deviation) is also shown. b) Proxy thermal model with an enhanced thermal conductivity and isoviscous slab-driven flow. Temperature contours are 200°C. c) Standard model with isoviscous slab-driven flow only.

thermal gradients are reduced). In the backarc regions, this results in much higher temperatures at shallow depth and higher surface heat flow, as heat is more efficiently transferred from depth to the base of the lithosphere. Over the backarc, the temperature at the Moho (35 km depth) is ~850°C for the proxy model, compared to ~600°C with slab-driven flow alone. The surface heat flow for the proxy model (70-80 mW/m^2) is approximately 20 mW/m^2 larger than the slab-driven flow model. Note that the surface

heat flow in the proxy model varies inversely with the assumed lithosphere thickness, and thus the model surface heat flow can be varied by simply changing this thickness.

Overall, the simple proxy model demonstrates that vigourous convection in the mantle wedge can carry a significant amount of heat into the whole backarc region. Note that mantle temperatures below the arc are decreased. As vigourous convection tends to homogenize mantle wedge temperatures, the temperatures in the wedge corner represent an average between those of the over-riding lithosphere and subducting plate, which are both cool. For the models above with an effective conductivity of 31 W m^{-1} K^{-1}, horizontal heat transport from the backarc regions due to slab-driven flow is insufficient to elevate mantle temperatures in this area. Temperatures in the wedge corner can be increased by assuming an even larger effective conductivity, which allows more heat to be focussed into the wedge corner. This requires even more vigourous convection.

8.2.2 Preliminary numerical models

The final model uses a more direct representation of free convection to determine if this type of convection is significant at reasonable viscosities in the backarc. Thermal buoyancy is included as a driving force for flow in the conservation of momentum equation (**Equation 6.9**) by calculating density variations caused by changes in temperature (**Equation 6.10**). A reference density of 3300 kg/m^3 at an arbitrary reference temperature of 1200°C is assumed, but the results are insensitive to this choice. The coefficient of thermal expansion for the mantle is 3.0×10^{5} K^{-1} [e.g., *Nyblade and Pollack*, 1993; *Turcotte and Schubert*, 2002].

The Cascadia geometry and subduction parameters are used, but the boundary conditions are slightly different from previous models, due to computational limitations. The landward boundary of the model is at 1000 km from the trench. The basal boundary of the mantle wedge is a horizontal boundary at a depth of 600 km (as in **Appendix C**). For simplicity, there is no thick craton lithosphere. Another key difference is that the landward and basal boundaries of the viscous wedge are closed, such that there is no mass flux through them; the rigid subducting slab is the only material that passes through the basal boundary. The landward and basal boundaries of the viscous wedge are

assumed to have no shear stress (i.e., free slip). All other wedge boundaries use a no slip boundary condition, such that the wedge is fully coupled to the over-riding lithosphere and subducting plate. The "cool" geotherm appropriate for the craton (**Figure 7.2b**) is prescribed to the landward boundary of the model. Along the basal boundary, a constant temperature of 1475°C is assigned between x=800 km and 1000 km; temperatures are free for the part of the basal boundary between the top of the subducting plate and x=800 km. The mantle wedge is assumed to have a constant viscosity.

The steady-state model is designed to illustrate the behaviour of mantle wedge flow when thermal buoyancy is included as a driving force and does not accurately represent the detailed thermal structure for the Cascadia wedge and backarc. A full study of thermal convection, including realistic models for Cascadia, requires careful consideration of model size, boundary conditions, and time-dependence.

The importance of thermal buoyancy depends strongly on the wedge viscosity. At high viscosities ($>10^{22}$ Pa s for the above boundary conditions), flow in the mantle wedge is driven primarily by the subducting slab, i.e., corner flow. As the viscosity is decreased, buoyancy forces become more significant. **Figure 8.2** shows the results for a model that uses a viscosity of 5×10^{20} Pa s, which is still higher than most estimates for backarcs (10^{18}-10^{19} Pa s, see below). This is the lowest viscosity for which a steady-state solution could be obtained. The results for flow driven only by viscous coupling with the slab are also shown. Due to the closed boundaries, the temperatures in the mantle wedge are lower than in previous models, because the cool material carried downward with the slab is forced to circulate back into the wedge. A comparison between the two models shows that thermal buoyancy has a significant effect on wedge temperatures. With the inclusion of thermal buoyancy, the upflow velocities of material near the landward boundary of the wedge become larger, and thus more heat is carried into the shallow backarc from depth, increasing backarc lithosphere temperatures and surface heat flow. The hotter material is then transported into the wedge corner by slab-driven flow, leading to higher temperatures below the arc.

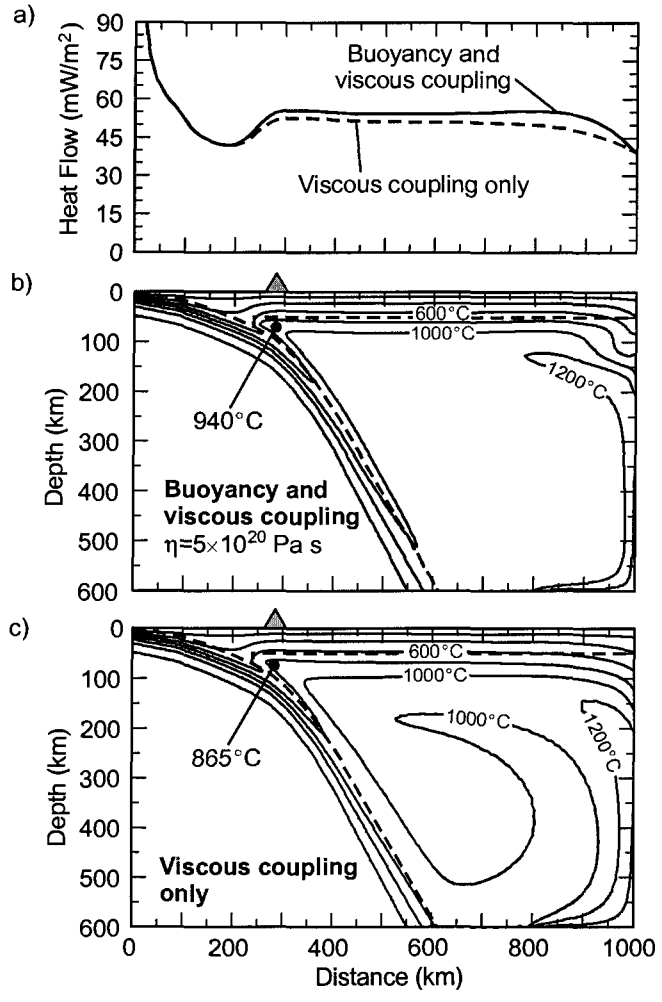

Figure 8.2. Cascadia models with and without thermal buoyancy. See text for a description of the boundary conditions. a) Surface heat flow. b) Thermal model with flow driven by viscous coupling and thermal buoyancy. The contour interval is 200°C. c) Thermal model with flow driven only by viscous coupling. For each model, the wedge has a constant wedge viscosity of 5×10^{20} Pa s.

These results illustrate that even with a relatively high backarc asthenosphere viscosity of 5×10^{20} Pa s, thermal buoyancy can have a large effect on the flow pattern and thermal structure of the mantle wedge. As the viscosity is decreased further, the effects of thermal convection should become larger, further increasing temperatures throughout the shallow backarc and beneath the arc. The above model shows the steady-state flow and thermal structure. At a viscosity of ~5×10^{20} Pa s or greater, thermal convection in the wedge occurs as stable convection cells, and a steady-state solution can be obtained.

At lower viscosities, thermal convection may become periodic and possibly chaotic [e.g., *Jarvis*, 1984; *Travis and Olson*, 1994]. Under these conditions, a steady-state solution is no longer possible, and time-dependent models must be used.

8.3 Constraints on Mantle Wedge Viscosity

For thermal convection to be a significant driving force for mantle wedge flow, the viscosity of the wedge must be fairly low. Using a simple model of convection in a narrow channel above a subducting plate, *Ida* [1983] suggests that thermal buoyancy will be the dominant driving force for flow when the mantle wedge viscosity is less than 10^{20} Pa s. As shown above, even at higher viscosities, the inclusion of thermal buoyancy in the flow calculations can affect wedge temperatures.

The backarc mantle at nearly all subduction zones is extremely hot (>1200°C) (see **Chapter 4**). At such high temperatures, it is expected that the mantle viscosity should be fairly low (e.g., **Figure 6.2**). For dislocation creep at strain rates of 10^{-13} s^{-1}, laboratory studies predict an effective viscosity of 10^{18}-10^{19} Pa s for both wet and dry conditions; for diffusion creep, the viscosity is ~10^{20} Pa s for wet conditions (10^{22} Pa s for dry conditions). In this section, observational constraints on the backarc mantle viscosity are examined.

8.3.1 Observational constraints

Observational constraints on the viscosity of the mantle come from studying the response of the Earth's surface to a variety of loading or unloading conditions. One of the key observations is post-glacial rebound, where the rate at which the surface uplifts after deglaciation is used to constrain the viscosity of the underlying mantle asthenosphere. Most studies of post-glacial rebound have focussed on Hudson's Bay (northern Canada), Scandinavia, and the British Isles. There, viscosities are inferred to be 10^{20}-10^{21} Pa s at depths of 100-200 km [e.g., *Mitrovica and Peltier*, 1995; *Peltier*, 1998, *Kaufmann and Lambeck*, 2002]. These estimates, while often considered to represent the average global viscosity structure, come from observations made mainly in cold cratonic regions.

There is increasing evidence that the viscosity of the upper mantle of backarcs is significantly lower than that below cratons. Viscosity in the backarc has been inferred using four main types of observations, all representing different time scales: 1) post-glacial rebound (1000's of yrs), 2) lacustrine loading/unloading (10's-1000's of yrs), 3) post-seismic relaxation (hours-100's of years), and 4) dynamic topography (1000's-millions of yrs). In these studies, geodetic and geological observations (GPS, shoreline tilting, etc.) of surface deformation are used to constrain rheological models. The mantle asthenosphere is usually modelled as a Maxwell viscoelastic body, where a constant viscosity is assigned to the mantle below some depth to approximate its behaviour over long time scales [e.g., *Ranalli*, 1995]. The mantle viscosity in these models is adjusted to fit the observed deformation rate and geometry.

Post-glacial rebound at a subduction zone has been examined at northern Cascadia and southern Chile (South America). Models of post-glacial rebound for northern Cascadia (47-48°N), constrained by data from lake shoreline tilting and relative sea level observations, used a mantle viscosity to be 5×10^{18} to 5×10^{19} Pa s [*James et al.*, 2000]. Note that the data for this study is in the vicinity of the forearc adjacent to the volcanic arc, and thus, the modelled viscosity reflects the average viscosity of the mantle wedge in the forearc and for a short distance into the backarc (probably no more than 100 km landward of the arc). The data may also be sensitive to the viscosity of the mantle below the subducting plate. These viscosities are similar to those inferred from post-glacial rebound of the arc/backarc region of the subduction zone in southern South America (south of 45°S) [*Ivins and James*, 1999].

Another constraint on backarc mantle wedge viscosity comes from observations of surface deformation associated with significant changes in the water level in large late Pleistocene and Holocene lakes. A classic example is Lake Bonneville, near the Basin and Range province in the southern Cascadia backarc. Here, drying of the lake over thousands of years has resulted in surface uplift. Based on the uplift rate, *Bills et al.* [1994 and references therein] infer a mantle viscosity of 4×10^{17} to 10^{20} Pa s at 40-150 km depth. Similar viscosity estimates are derived for the upper mantle from deformation due

to filling of lakes by glacial meltwater in the backarc regions of Kyushu, Japan (33°N, 130°E) [*Okuno and Nakada*, 1998], and due to water level increases in Lake Mead, Nevada (36°N, 115°W) after construction of the Hoover Dam [*Kaufmann and Amelung*, 2000]. Although Lake Mead is south of the present-day Cascadia subduction zone, this area was in the backarc of Farallon Plate subduction until subduction ceased at 20-30 Ma and is still hot [e.g., *Dixon et al.*, 2004].

The mantle viscosity can also be constrained using geodetic observations of shorter-term time-dependent deformation of the Earth's surface following a large earthquake, e.g., megathrust earthquakes at a subduction zone [e.g., *Wang*, in press, 2004]. Fault slip during the earthquake induces a large stress in the mantle, which is slowly relaxed over 10's to 100's of years. Most models of post-seismic relaxation for Cascadia, Alaska/Aleutian, Chile, SW Japan and NE Japan use mantle wedge viscosities of 4×10^{18} to 10^{20} Pa s to fit geodetic observations [*Wang*, in press, 2004 and references therein]. Note that these models represent an average viscosity of primarily the forearc mantle wedge and of the backarc wedge closest to the volcanic arc. Surface deformation following large crustal earthquakes in western Mongolia was modelled using a mantle viscosity of $1\text{-}4\times10^{18}$ Pa s [*Vergnolle et al.*, 2003]. This region is north of the Himalaya mountains and is in the backarc of the former subduction zone associated with India-Asia plate convergence.

Most of the above studies provide estimates of mantle viscosity for a small part of the mantle wedge. One important indicator of low viscosities throughout the mantle wedge comes from studies of dynamic topography over backarcs. Mass movement within the Earth's interior can affect surface topography. Over a subduction zone, models that use high viscosities (e.g., craton values of 10^{20}-10^{21} Pa s) predict that the backarc regions should experience up to 4 km of subsidence over a broad region (~500 km), due to the combined effects of a descending dense oceanic plate and slab-induced corner flow within the mantle wedge [e.g., *Billen and Gurnis*, 2001 and references therein]. This is much greater than the observed surface topography, as well as the dynamic topography inferred from measurements of the geoid and gravity [*Billen and*

Gurnis, 2001; *Wheeler and White*, 2002]. Instead, the seafloor depth, gravity and geoid data observations suggest that the subducting slab has little effect on surface topography. One interpretation is that the slab is decoupled from the over-riding plate by a low viscosity mantle wedge. *Billen and Gurnis* [2001] showed that if the viscosity of the mantle wedge is at least a factor of 10 less than the surrounding asthenosphere, the effect of the subducting slab on surface topography is significantly reduced, in good agreement with observations.

Taken together, the above observations indicate that the viscosity of the mantle wedge at many subduction zones is much lower than that inferred for cratonic regions. Most studies give a wedge viscosity of 10^{18}-10^{19} Pa s. Note that these viscosity estimates were derived assuming a Newtonian rheology for the mantle (i.e., linear stress-strain rate relationship) and using observations of deformation on short time scales (years to thousands of years). There is some question above the validity of the extrapolation of these results to mantle wedge flow, especially if the wedge rheology is strain-rate dependent. *Dixon et al.* [2004] argue that although variations in strain rate may affect mantle viscosity, the consistency of viscosity estimates from different types of observations with different time scales suggests that the conclusion of a low viscosity mantle wedge and backarc, relative to the craton regions, is robust.

Such low viscosities are consistent with the inferred very high temperatures in the backarc mantle (**Figure 6.2**). The viscosities may also be further decreased due to the presence of water [e.g., *Billen and Gurnis*, 2001 and references therein; *Dixon et al.*, 2004]. Laboratory data show that even a small amount of water significantly reduces the effective viscosity of olivine and other upper mantle minerals [e.g., *Karato et al.*, 1986; *Karato and Wu*, 1993; *Hirth and Kohlstedt*, 1996; *Mei et al.*, 2002, see also **Figure 6.2**]. Dehydration reactions in the subducting slab as it descends release significant amounts of water to the overlying mantle [e.g., *Peacock*, 1993; *Schmidt and Poli*, 1998]. It is expected that the mantle above the slab should be partially or fully saturated with water, and thus much weaker than dry mantle. Convection within the mantle wedge and backarc may provide a mechanism for carrying the water well landward of the subduction zone, resulting in low viscosities throughout backarc.

The backarc viscosities of 10^{18}-10^{19} Pa s inferred from surface deformation data and laboratory studies are well below the value for which thermal buoyancy becomes an important driving force for mantle flow [*Ida*, 1983], suggesting that thermal buoyancy should not be neglected in backarc thermal/flow models.

8.3.2 Rayleigh number considerations

The onset and vigour of thermal convection in the mantle is determined by the Rayleigh number for the system, which represents the ratio of forces that promote free convection (i.e., heating from below) to those that hinder it (e.g., mantle viscosity). For a simple box where the upper and lower boundaries are maintained at constant temperatures (with the lower boundary being hotter), the Rayleigh number (Ra) is defined as [e.g., *Turcotte and Schubert*, 2002]:

$$\mathrm{Ra} = \frac{\rho_0 g \alpha_V (\Delta T) b^3}{\eta \kappa} \tag{8.1}$$

where ρ_0 is the density, g is the gravitational acceleration, α_V is the thermal expansion co-efficient, ΔT is the temperature difference between the upper and lower boundaries, b is the height of the box, η is the (dynamic) viscosity, and κ is the thermal diffusivity. The critical Rayleigh number (Ra_{cr}) for this system is 657.5 if both boundaries are free slip (1707.8 if both are no-slip). If $Ra > Ra_{cr}$, free convection will occur in the box. As the Ra number increases above Ra_{cr}, the convective flow regime will progress from steady to periodic to chaotic.

As an example, assume that the backarc regions of the Cascadia subduction zone (well landward of the subducting plate) can be represented as a simple isoviscous box, with its top boundary at the base of the crust (35 km depth) at a temperature of ~900°C (see **Chapter 3**) and its bottom boundary at the base of the upper mantle (410-660 km) at a temperature of 1400-1600°C [e.g., *Ito and Katsura*, 1989]. Using the values for ρ_0, α_V, and κ from the numerical models, and the boundary conditions given above, the Rayleigh number can be expressed in terms of the backarc mantle viscosity as: $Ra \sim 10^{25\text{-}26}/\eta$. If the viscosity of the backarc mantle is as low as inferred (10^{18}-10^{19} Pa s), the Rayleigh

number is ~10^6-10^8, which is more than 1000 times the critical value, and thus thermal convection is expected. At high Rayleigh numbers (>10^6), convection in the backarc mantle is in the turbulent, time-dependent flow regime [e.g., *Travis and Olson*, 1994]. In this case, thermal convection should efficiently carry a significant amount of heat upward, as seen in the proxy model with enhanced thermal conductivity (**Figure 8.1**).

This simple analysis shows that conditions in the Cascadia backarc mantle likely allow for vigourous thermal convection. The subduction geometry and cooling effects of the subducting slab will increase the complexity of the system, and determination of the Rayleigh number is not straightforward. Further numerical modelling work is necessary to better understand the dynamics of backarc thermal convection.

8.4 Conceptual Model for Backarc Mantle Dynamics

Figure 8.3 shows a conceptual model of mantle dynamics that can satisfy the heat budget at a subduction zone. In the model, flow in the mantle wedge is driven by both slab-wedge coupling and thermal buoyancy, but the relative importance of each varies within the wedge. In the backarc, it is proposed that flow is dominated by vigourous small-scale thermal convection in a low viscosity mantle below 50-60 km. Convection is likely driven primarily by the positive buoyancy of hot material at depth in the backarc, where high temperatures are maintained by global mantle dynamics. The cooling effects of the subducting slab on the adjacent wedge may enhance convection. In this model, backarcs provide a "short circuit" for efficient heat transfer from the deep earth convective system to the surface.

For vigourous convection to occur, the viscosity of the backarc mantle must be fairly low, as expected from the combined effects of high temperatures and hydration of the wedge by water released from the subducting plate [see also *Dixon et al.*, 2004; *Hyndman et al.*, submitted manuscript, 2004]. Water released from the slab may be efficiently mixed throughout the mantle wedge and backarc by convective flow. With vigourous convection, heat from depth is rapidly carried upward, elevating shallow backarc mantle temperatures and surface heat flow. The flow pattern, and to some degree the thermal structure, of the backarc are likely time-dependent. If flow is extremely

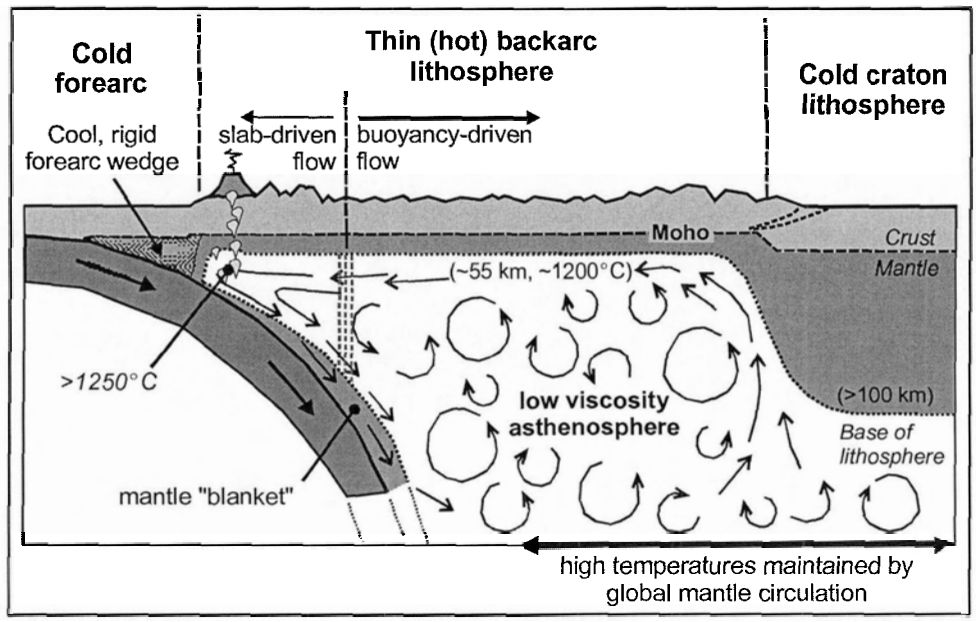

Figure 8.3. Schematic diagram of backarc mantle dynamics. The dashed grey lines show the approximate location of the transition from mantle flow dominated by thermal convection in the backarc to dominantly slab-induced flow near the wedge corner.

vigourous, asthenosphere temperatures should be fairly uniform across the entire backarc. Observations of nearly constant lateral heat flow across the backarc for Cascadia and other regions (see **Chapter 3 and 4**) suggest that convection must be rapid enough to maintain nearly constant temperatures in the uppermost backarc mantle on time scales similar to the thermal time constant of the over-riding lithosphere (<100 my). The landward limit of vigourous flow may be a thick craton lithosphere, which is isolated from the convective system by compositional differences that result in a higher viscosity [e.g., *Jordan*, 1975; *Forte and Perry*, 2000, *Hyndman et al.*, submitted manuscript, 2004].

Closer to the arc, it is proposed that viscous coupling with the slab will become the dominant driving force for mantle wedge flow. As seen in the proxy model (**Figure 8.1**), small-scale convection may result in temperatures in the wedge corner that are too low for volcanism, unless convection is extremely vigourous. Such vigourous convection is unlikely in this region, due to the combined effects of the decreased vertical temperature difference across the viscous wedge and the decreased height of viscous region (i.e., the local Rayleigh number is smaller). In the wedge corner region, flow is

probably driven mostly by viscous coupling between the mantle and subducting slab, although sinking of cool, dense mantle material immediately above the slab may also occur. Both processes should result in a corner-flow type convection cell, with shallow flow toward the wedge corner and deeper flow parallel to the dip of the subducting plate. The upper flow limb would carry heat into the wedge corner from the shallow, hot part of the vigourously convecting backarc.

In this model, there is a transition between flow dominated by thermal convection in the backarc to flow dominated by forced convection near the wedge corner, although both types of flow are super-imposed throughout the entire wedge. For the wedge corner region, the thermal effects of this flow pattern can be approximated using a slab-driven flow model (as in **Chapter 7**) with high temperatures prescribed to the backarc boundary of the model (which is in the backarc), under the assumption that vigourous convection maintains high temperatures at shallow depth. As seen in the models of slab-driven flow, the location of this boundary significantly affects the thermal structure (**Section 7.3.5**). On the basis of these models, the backarc boundary must be located fairly close to the volcanic arc (<200 km), so that the high temperatures can be efficiently carried into the wedge corner without cooling and with little effect on surface heat flow, especially for a realistic temperature- (and stress-) dependent mantle rheology. These arguments suggest that slab-driven mantle flow is dominant only in a small part of the wedge corner region close to the volcanic arc. With increasing distance from the arc, slab-driven flow becomes less important (but may not disappear completely), and the dynamics of the mantle wedge are dominated by vigourous thermal convection.

The conceptual model proposed here may explain, to first order, several key backarc observations. Of most importance to this study is the heat budget at a subduction zone. The model provides a mechanism for the efficient transport of heat into the shallow backarc regions as well as into the wedge corner, to satisfy the observational constraints of high temperatures throughout the mantle wedge and backarc from surface heat flow, seismic velocities, mantle xenoliths, etc. (**Chapters 3 and 4**). This model is consistent with observations of little dynamic topography over western Pacific backarcs [e.g., *Wheeler and White*, 2002]; the over-riding plate in the backarc is essentially

decoupled from the subducting slab due to vigourous convection in the low viscosity mantle. Vigourous convection may also explain why seismic anisotropy in the backarc does not conform to the standard corner-flow model at most subduction zones and appears to be less well-developed than in other tectonic settings (**Chapter 5**). This model is also consistent with recent three-dimensional models of mantle dynamics for NE Japan that suggest small-scale convection must occur to explain along-margin variations in volcanism [*Honda et al.*, 2002; *Honda and Saito*, 2003].

8.5 Consequences of a Vigourously Convecting Backarc Mantle

The conceptual model presented above has significant implications for many subduction zone processes. Below, three important issues are outlined.

8.5.1 Thermal structure of the subducting slab

This study has primarily focussed on the thermal structure of the mantle wedge. However, temperatures of the wedge may have a dramatic effect on the temperatures within the subducting slab and over-riding plate. In particular, if the wedge is as uniformly hot as suggested in this study, the deeper parts of the subducting slab may be much hotter than previously thought. This has implications for slab metamorphism, the occurrence of in-slab earthquakes, and the amount of water released from the slab, which in turn affects the amount of water in the wedge, wedge rheology, and the generation of arc magma. To address the thermal structure of the subducting plate, two key questions are: 1) why is the forearc mantle wedge corner cool?, and 2) is there a viscous mantle "blanket" on top of the subducting plate?

Surface heat flow and other geophysical observations suggest a rapid change in thermal structure that occurs just seaward of the volcanic arc. The forearc regions are inferred to be cool because mantle flow is mechanically prohibited from entering the thin corner of the forearc mantle wedge (see **Section 7.3.7**). The cause of this sharp contrast in wedge behaviour is not understood. Both serpentinization of the forearc mantle wedge and slab-wedge decoupling due to high pore fluid pressures have been proposed [e.g., *Furukawa*, 1993b; *Hyndman and Peacock*, 2003]. Future studies should examine this

region in greater detail. The greatest increase in the temperatures in the upper part of the subducting slab occurs near the seaward limit of mantle wedge flow, and thus, it is important to constrain this limit.

Slab temperatures will also be affected by the development of a viscous mantle "blanket" (i.e., boundary layer) on the top of the slab, due to the strong effect of temperature on mantle viscosity. The thickness of this boundary layer is very important; it will partially insulate the slab from the high wedge temperatures. In addition, if the viscous mantle layer is viscously coupled to the subducting plate, water released from the subducting plate may become trapped within the blanket (e.g., dissolved in olivine and other nominally anhydrous mantle minerals) and carried to great depths in the mantle. This may provide a mechanism for carrying water to the backarc.

8.5.2 Decay in backarc temperatures with time

The proposed model predicts that the uniformly high surface heat flow over backarcs is the result of rapid transport of heat from depth by vigourous convection. Such high backarc temperatures may persist for a long time after subduction has ceased, as suggested by the high surface heat flow for regions in former backarcs (e.g., northern Canadian Cordillera and SW US Cordillera, see **Chapter 4**).

In the conceptual model, the decline in backarc wedge temperatures with time after the termination of subduction is related to how quickly vigourous convection decays, which likely depends on how long slab dehydration continues, how quickly water is lost from the backarc mantle, and the dynamics of the former subducting slab (i.e., is it frozen in the mantle, or does it break off and sink?) [*Hyndman et al.*, submitted manuscript, 2004]. Although these processes may persist for a few 10's of Ma after subduction stops, the first-order approximation is that the backarc lithosphere cools and thickens fairly rapidly. This cooling can be approximated using a simple one-dimensional conductive cooling model. The initial thermal structure is assumed to be that of a hot backarc (e.g., Cascadia), with a surface heat flow of 80 mW/m^2, a fixed temperature of 1200°C at 50 km depth (taken to be the base of the lithosphere prior to cooling), and a linear, approximately adiabatic, temperature increase to 1400°C at 250

km depth. The model is allowed to cool conductively, keeping the upper and lower boundaries of the model fixed at 0°C and 1400°C, respectively. **Figure 8.4a** shows the decline in backarc temperatures over time. The time since the onset of conductive cooling is taken to define the "tectonic age". The most rapid cooling occurs in the first 50-100 my, as shown by the sharp decay in surface heat flow (**Figure 8.4b**). After ~300 my, the change in surface heat flow with time is very small.

The model results can be compared with the observed decay in heat flow for former backarcs (the examples of the Northern Canadian Cordillera and Appalachians are shown in **Figure 8.4b**), as well as compilations of heat flow vs thermo-tectonic age for mobile belts [e.g., *Chapman and Pollack*, 1975; *Pavlenkova*, 1996; *Artemieva and Mooney*, 2001]. *Hyndman et al.* [submitted manuscript, 2004] propose that mobile belts are hot and weak because they are in present or former backarcs. As noted above, there is some uncertainty in the length of time between subduction termination and the start of conductive cooling. In addition, the thermo-tectonic age for mobile belts is usually determined from orogenic metamorphism and plutonism; this may be a few 10's of Ma after subduction termination.

To first order, the modelled decay in heat flow fits the observed decay. This suggests that the relative timing of subduction termination, cessation of vigourous

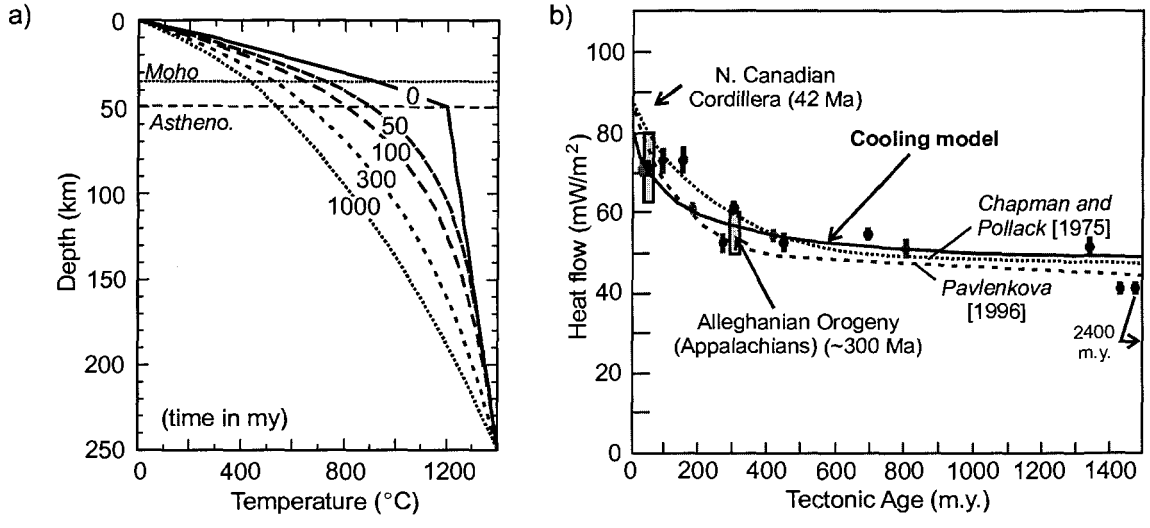

Figure 8.4. a) Geotherms for models of backarc cooling. The zero time corresponds to the termination of vigourous backarc convection and onset of conductive cooling. b) Heat flow vs. tectonic age for the cooling model (solid line) [after *Hyndman et al.*, submitted manuscript, 2004]. Also shown is the proposed cooling trend from studies of the decay in heat flow with thermo-tectonic age for different orogenies (dotted and dashed lines). The circles are the data used in these studies (bars show the uncertainty range).

convection, and thermo-tectonic age is similar (i.e., within a few 10's of Ma). Future work should examine backarc/mobile belt cooling in greater detail. In particular, thermal data for backarc regions with subduction termination and thermo-tectonic ages less than 200 my would aid in better constraining this process.

8.5.3 Global heat budget

The existence of a vigourously convecting backarc provides a pathway for heat to rapidly escape from the Earth's interior, resulting in high surface heat flow over present-day backarcs and enhanced heat flow over regions in former backarcs (<300 Ma) and mobile belts. *Ballard and Pollack* [1987] suggest that cratons have low surface heat flow and low mantle heat flow, relative to surrounding mobile belts and active tectonic regions, because conductive transport of heat through the thick lithosphere is relatively inefficient. Instead, deep mantle heat is diverted to adjacent regions with much thinner lithosphere, i.e., a thermal short-circuit. Although a significant amount of heat may escape through the backarc, the overall effect on the global heat budget is estimated to be small. The mantle heat flow for the northern Cascadia backarc is inferred to be a factor of ~3 larger than that for the North America craton (see **Chapter 3**). Assuming that present and former backarcs make up ~20% of the land areas on Earth [e.g., *Stein and Freymueller*, 2002], the amount of mantle heat escaping through these areas is probably less than that through the remainder of the continents, and is still much less than the mantle heat that escapes through the ocean basins. Thus, the high heat loss to backarcs can readily be provided by the global convective system.

8.6 Discussion

Rapid upward transport of heat from depth into the shallow backarc is necessary to maintain the inferred uniformly high temperatures in the backarc of nearly all subduction zones. Simple slab-driven corner flow has been shown to be too inefficient to provide enough heat to all parts of the backarc, as required by the inferred high temperatures. This conclusion, plus the observational constraints that indicate that the

many backarcs have low mantle viscosities (10^{18}-10^{19} Pa s), suggests that flow driven by thermal buoyancy may be significant in the backarc mantle.

To satisfy the heat budget at a subduction zone, it is proposed that backarc mantle flow is dominated by vigourous small-scale convection. As shown above, vigourous convection, driven by thermal buoyancy in a low-viscosity mantle, is an effective mechanism to efficiently transport heat to shallow depths in the backarc. Very close to the arc, slab-driven mantle flow may become significant. This flow could carry heat from the hot backarc into the thin wedge corner to enhance temperatures below the arc, as required for arc volcanism.

Future studies should focus on evaluating and refining this convective model. Of most importance is the development of time-dependent thermal-mechanical numerical models to determine if free convection at wedge viscosities of 10^{18}-10^{19} Pa s is a viable mechanism for carrying the required amount of heat into the subduction zone. Initial models may use an isoviscous wedge and kinematic subducting slab. From these, models of increasing complexity could be developed, including those with a temperature- (and stress-) dependent mantle rheology, three-dimensional models, models that include slab-normal motion of the subducting plate (e.g., slab rollback), and those with heterogeneities in mantle wedge composition, water content and melt content.

The flow models must be reconciled with a wide range geophysical and geochemical constraints on mantle dynamics. As argued in this study, the thermal structure is one critical constraint on wedge flow. There are numerous other types of constraints that have not been considered in detail here. For example, the free convection model predicts that the mantle wedge is generally well-mixed. Are there any geochemical observations that support this (e.g., variations in magma composition from the backarc to the arc)? In addition, are there any constraints on the degree of hydration of present-day backarc asthenosphere from seismology or backarc volcanism?

CHAPTER 9

Conclusions

9.1 The Thermal Structure of Subduction Zones

In this thesis study, the thermal structure of a number of subduction zones has been examined using two complementary approaches: 1) geophysical, geological, and geochemical observations, and 2) numerical models that investigate the thermal effects of geodynamic processes associated with subduction. The integration of these two approaches is critical for accurately constraining the thermal structure of a subduction zone and the key processes that govern it. The geodynamic models can then be used predictively to examine thermal controls on different subduction processes, including earthquake occurrence, the generation of volcanic magmas, and deformation of the over-riding plate.

Thermally, the forearc and backarc are distinct regions for most subduction zones. The forearc regions are generally cool; the backarc regions are extremely hot for 100's of kilometres landward of the volcanic arc. The main conclusions of this study are summarized below.

1. Factors affecting temperatures in the forearc and shallow (<50 km) subducting plate. Observations of low surface heat flow (generally 30-50 mW/m^2) over most forearcs are consistent with cooling of the over-riding plate by the subducting oceanic plate. The primary factors controlling the forearc temperatures are the subduction rate, the thermal structure of the incoming oceanic plate (given by its age and sediment cover), and the geometry of the subducting plate. Two other potentially significant factors for some subduction zones are frictional heating along the thrust fault and hydrothermal circulation within the upper crust of the incoming oceanic plate. The thermal structure of the forearc region is insensitive to backarc mantle processes. For subduction zones where

the structural and subduction parameters are well-constrained, numerical models can be used to obtain temperatures of the shallow part of the subducting slab (<50 km depth) to within 50-100°C. Some key applications of these forearc models are: thermal controls on megathrust earthquakes, metamorphism within the subducting plate and its implications for slab dehydration and in-slab earthquakes, and the nature of the forearc mantle wedge (e.g., the stability of serpentine and other hydrous mantle minerals).

2. Thermal structure of the Mexico subduction zone and the megathrust seismogenic zone. Two-dimensional thermal models for the Mexico subduction zone forearc show that although the subducting Rivera and Cocos Plates are young (11.5 to 15.5 Ma), they are much cooler than other subducting plates of similar age (e.g., the Juan de Fuca Plate at the Cascadia subduction zone), due to only a thin layer of insulating sediments on the incoming plate (~200 m for Mexico compared to >3 km for Cascadia). With the thin sediment cover, the upper part of the subducting crust may be further cooled by hydrothermal circulation. Because the subducting plates below Mexico are cool, the brittle part of the subduction thrust fault extends to depths of 30-40 km. At these depths, even a small amount of frictional heating can increase the deep (30-40 km) thrust fault temperatures by over 100°C. Megathrust earthquake rupture areas for Mexico are generally limited to depths between 5 and 30 km. The updip limit of rupture is consistent with the proposed thermal limit of about 100°C along most of the margin. The deep limit of rupture is updip of the intersection of the thrust fault with the continental Moho. If the downdip rupture limit is controlled by a temperature of 350°C, a small amount of friction, corresponding to an average shear stress of 15 MPa along the fault, must be included in the models. This shear stress is well within the estimates for other subduction thrust faults and is consistent with past conclusions that, although there is some friction, the thrust fault is generally weak.

3. Observational constraints on the thermal structure of backarcs. A remarkable feature of subduction zones is that the arc and backarc regions are extremely hot, despite

of the cooling effects of a subducting plate. Most studies have recognized that high mantle wedge temperatures (>1200°C) are required for arc volcanism, but the spatial extent of these high temperatures (100's to 1000's of km behind the arc) has not been widely appreciated. Several independent types of observations can be used as indicators of high temperatures in the upper backarc mantle:

- surface heat flow > 70 mW/m^2 for continental crust with average radiogenic heat production (> 60 mW/m^2 for oceanic crust with little heat production) and reduced heat flow for both > 50 mW/m^2
- upper mantle seismic velocities >2% lower than average mantle velocities
- P_n velocity < 7.9 km/s
- effective elastic thickness < 30 km
- maximum earthquake depths in the over-riding plate < 20 km
- high surface elevations in spite of a thin crust
- lithosphere thickness << 100 km
- upper mantle viscosities < 10^{20} Pa s
- estimates of high in-situ temperatures in backarc upper mantle from xenoliths
- widespread sporadic basaltic volcanism in the backarc
- pervasive "thick-skinned" deformation in the backarc crust

The main study area is the northern Cascadia subduction zone, where there has been no significant recent backarc extension. This region exhibits all of the above characteristics. Together, the observations are consistent with temperatures of 800-1000°C at the Moho (~35 km depth) and a lithosphere thickness of 50-60 km, with no significant variation in thermal structure for ~500 km east of the arc. A compilation of data from five other non-extensional backarcs shows that the thermal structure of these regions is similar to Cascadia, with uniformly high backarc temperatures that extend from 400 to >1000 km behind the arc. For the Cascadia and Central Andean subduction zones, the hot backarc is limited on its landward edge by thick, cool craton lithosphere, making the high backarc temperatures even more surprising. The heat source for the high backarc temperatures must come from great depth, > ~250 km. Many subduction zones exhibit current or

recent (<50 Ma) backarc extension and spreading. These backarcs often appear to have temperatures similar to non-extensional backarcs. Some appear to be hotter, but it is difficult to separate the thermal effects of extension/spreading from underlying processes and determine if an additional heat source is required. Overall, the only clear evidence that any backarc is cool comes from a few regions where the subducting slab flattens to near horizontal in the uppermost mantle (50-100 km depth), e.g., Peru region of South America. A flat slab may exclude a backarc mantle wedge and limit the convection required for high backarc temperatures.

4. Backarc heat source. An active volcanic arc and high temperatures throughout the shallow backarc mantle appear to be characteristic features of nearly all subduction zones, suggesting that there is a common subduction-related mechanism. Local sources of heat are insufficient to produce the observed high temperatures. Frictional heating on the thrust fault, heat associated with metamorphism, and radiogenic heat production do not appear to be significant heat sources. The strong temperature-dependence of mantle viscosity suggests that viscous dissipation is a self-defeating mechanism for generating heat. The main source of heat appears to be located at depth in the backarc regions, where high temperatures are inferred to be maintained by general mantle circulation not associated with the subduction zone. This heat is carried into the subduction zone by convective flow in the backarc mantle.

5. Seismic anisotropy constraints on backarc mantle flow. A teleseismic shear wave splitting study for the Cascadia subduction zone backarc yields a fast direction for anisotropy parallel to the subduction direction (~N70°E) and fairly small delay times of ~1.3s. These observations are consistent with the 2D corner flow in the mantle wedge. However, at most other subduction zone, the fast direction of backarc mantle anisotropy does not conform to the corner flow model, suggesting that slab-wedge coupling does not exert a strong control on the backarc mantle flow. In addition, for many subduction zones, anisotropy in the mantle wedge seems to be 1-2%, much less than that in other

tectonic environments. These results are consistent with a more complex pattern of thermal convection than the simple corner flow model.

6. Slab-driven mantle wedge flow. Flow driven by viscous coupling between the subducting slab and mantle wedge results in a single 2D "convection" cell, with flow velocities limited by the subduction rate (a few cm/yr). For realistic temperature- (and stress-) dependent mantle rheologies for the viscous wedge, flow is focussed upward into the wedge corner, resulting in the rapid transport of heat from depth into the corner and enhanced temperatures below the arc, compatible with temperatures required for arc magma generation. However, this strong flow focussing produces a nearly stagnant shallow backarc mantle, where model temperatures and heat flow are much lower than observed. For a reasonable range of boundary conditions, it is not possible to simultaneously produce high temperatures below the arc and throughout the backarc using slab-driven flow alone, suggesting that simple slab-driven flow alone is insufficient to carry the required amount of heat into the subduction zone.

7. Vigourous thermal convection in the backarc. Thermal convection in the backarc mantle is induced by heating from below (near the landward boundary of the backarc) and cooling by the subducting slab. Constraints from post-glacial rebound, post-seismic relaxation, dynamic topography, etc. suggest that the backarc mantle viscosity is very low (10^{18}-10^{19} Pa s) for most subduction zones. The low viscosities are likely due to the combined effects of high temperature and hydration of the backarc mantle by dewatering of the subducting slab. At these viscosities, it is expected that thermal buoyancy is a significant driving force for flow and should be included in all thermal-mechanical models of mantle wedge dynamics. To satisfy the heat budget at a subduction zone, it is proposed that backarc mantle flow is dominated by vigourous thermal convection that rapidly carries heat from depth upward into the shallow backarc. Close to the volcanic arc (< 200 km), the slab-driven flow may become more important, providing a mechanism to efficiently carry hot backarc mantle material into the wedge corner.

9.2 Recommendations for Future Research

This research has highlighted the importance of combining numerical models with observational constraints and laboratory studies to develop a better understanding of geodynamic processes and their thermal consequences at a subduction zone. Three important directions for future research are:

*1. **Numerical models of backarc mantle flow with thermal buoyancy.*** Numerical models are required to investigate thermal convection in the backarc at low mantle viscosities (10^{18}-10^{19} Pa s). At these viscosities, thermal convection is likely time-dependent. This work will require a careful study of the model boundary locations and the prescribed thermal and flow conditions along these boundaries. To ensure the physical validity of the models, observational constraints on mantle dynamics provided by a range of geophysical, geological and geochemical observations must be considered when constructing and interpreting the models. Several key observational constraints come from surface heat flow, seismic velocities, lithosphere thickness and strength (deformation) and petrology of arc and backarc magmas.

*2. **Forearc-backarc transition.*** Subduction zone forearcs appear to be cool because flow does not extend into the forearc mantle wedge. The transition from a cool forearc to a hot arc/backarc seems to occur 20-30 km seaward of the volcanic arc, on the basis of surface heat flow for many subduction zones (e.g., Cascadia, NE Japan, Mexico). This suggests the maximum seaward extent of wedge flow approximately coincides with this transition. The nature of the rapid change in wedge behaviour is not understood. Both serpentinization of the forearc mantle wedge and slab-wedge decoupling have been proposed as mechanisms for isolating the forearc mantle wedge from flow. Each of these should be investigated further.

*3. **The thermal structure of the subducting plate.*** Temperatures in the subducting plate at depths > 50 km are strongly affected by the thermal structure of the overlying wedge. Likewise, the dynamics and thermal structure of the overlying wedge are strongly

influenced by water released from the subducting slab (which is controlled by temperature-dependent metamorphism within the slab), as well as possible cooling from the slab. Future modelling efforts should focus on developing a more complete description of slab temperatures at depths > 50 km. Two important parameters are: 1) the seaward limit of wedge flow, as the location of the greatest increase in slab temperatures approximately coincides with this limit, and 2) the possible development of a thermal boundary layer on top of the slab, which partially insulates the slab from the hot wedge.

REFERENCES

Akinin, V.V., M.F. Roden, D. Francis, J. Apt, and E. Moll-Stalcup, Compositional and thermal state of the upper mantle beneath the Bering Sea basalt province: Evidence from the Chukchi Peninsula of Russia, *Canadian Journal of Earth Sciences, 34*, 789-800, 1997.

Allmendinger, R.W. and T. Gubbels, Pure and simple shear plateau uplift, Altiplano-Puna, Argentina and Bolivia, *Tectonophysics, 259*, 1-13, 1996.

Allmendinger, R.W., R.E. Jordan, S.M. Kay, and B.L. Isacks, The evolution of the Alitplano-Puna Plateau of the Central Andes, *Annual Review of Earth and Planetary Sciences, 25*, 139-174, 1997.

ANCORP Working Group, Seismic imaging of a convergent continental margin and plateau in the central Andes (Andean Continental Research Project 1996 (ANCORP'96)), *Journal of Geophysical Research, 108*(B7), 2328, doi: 10.1029/2002JB001771, 2003.

Anderson, R.N., 1980 update of heat flow in the East and Southeast Asian Seas, *In:* D.E. Hayes (Ed.), *The tectonic and geologic evolution of Southeast Asian Seas and Islands, Geophysical Monograph 23*, American Geophysical Union, Washington DC, pp. 319-326, 1980.

Ando, M., Y. Ishikawa, and F. Yamazaki, Shear wave polarization anisotropy in the upper mantle beneath Honshu, Japan, *Journal of Geophysical Research, 88*, 5850-5864, 1983.

Andrews, D.J. and N.H. Sleep, Numerical modelling of tectonic flow behind island arcs, *Geophysical Journal of the Royal Astronomical Society, 38*, 237-251, 1974.

Artemieva, I.M. and W.D. Mooney, Thermal thickness and evolution of Precambrian lithosphere: A global study, *Journal of Geophysical Research, 106*, 16,387-16,414, 2001.

Arzate, J.A., M. Mareschal, and J. Urrutia-Fucugauchi, A preliminary crustal model of the Oaxaca continental margin and subduction zone from magnetotelluric and gravity measurements, *Geofisica Internacional, 32*, 441-452, 1993.

Atwater, T., Plate tectonic history of the northeast Pacific and western North America, *In*, E.L. Winterer, D.M. Hussong, and R.W. Decker (Eds.), *The Eastern Pacific Ocean and Hawaii, The Geology of North America, vol. N.*, Geological Society of America, Boulder, Colorado, pp. 21- 72, 1989.

Audoine, E., M.K. Savage, and K. Gledhill, Seismic anisotropy from local earthquakes in the transition region from a subduction to a strike-slip plate boundary, New Zealand, *Journal of Geophysical Research, 105*, 8013-8033, 2000.

Babeyko, A.Y., V.V. Sobolev, R.B. Trumbull, O. Oncken, and L.L. Lavier, Numerical models of crustal scale convection and partial melting beneath the Altiplano-Puna plateau, *Earth and Planetary Science Letters, 199*, 373-388, 2002.

Ballard, S. and H.N. Pollack, Diversion of heat by Archean cratons: A model for southern Africa, *Earth and Planetary Science Letters,* 85, 253-264, 1987.

Bandy, W.L., V. Kostoglodov, and C.A. Mortera-Gutierrez, Southwest migration of the instantaneous Rivera-Pacific Euler pole since 0.78 Ma, *Geofisica Internacional, 37*, 153-169, 1998.

Bandy, W., V. Kostoglodov, A. Hurtado-Diaz, and M. Mena, Structure of the southern Jalisco subduction zone, Mexico, as inferred from gravity and seismicity, *Geofisica Internacional, 38*, 127-136, 1999.

Baranov, B, H.K. Wong, K. Dozorova, B. Karp, T. Ludmann, and V. Karnaukh, Opening geometry of the Kurile Basin (Okhotsk Sea) as inferred from structural data, *The Island Arc, 11*, 206-219, 2002.

Bardoux, M., and J. Mareschal, Extension in south-central British Columbia: mechanical and thermal controls, *Tectonophysics, 238,* 451-470, 1994.

Batchelor, G.K., *An Introduction to Fluid Dynamics*, Cambridge University Press, New York, 615 pp, 1967.

Baumont, D., A. Paul, G. Zandt, and S.L. Beck, Inversion of Pn travel times for lateral variations of Moho geometry beneath the Central Andes and comparison with the receiver functions, *Geophysical Research Letters, 28*, 1663-1666, 2001.

Baumont, D., A. Paul, G. Zandt, S.L. Beck, and H. Pedersen, Lithospheric structure of the central Andes based on surface wave dispersion, *Journal of Geophysical Research, 107*(B12), 2371, doi: 10.1029/2001JB000345, 2002.

Beck, S.L., G. Zandt, S.C. Myeres, T.C. Wallace, P.G. Silver, and L. Drake, Crustal thickness variations in the central Andes, *Geology, 24*, 407-410, 1996.

Billen, M.I. and M. Gurnis, A low viscosity wedge in subduction zones, *Earth and Planetary Science Letters, 193*, 227-236, 2001.

Bills, B.G., D.R. Currey, and G.A. Marshall, Viscosity estimates for the crust and upper mantle from patterns of lacustrine shoreline deformation in the Eastern Great Basin, *Journal of Geophysical Research, 99,* 22,059-22,086, 1994.

Black, P.R. and L.W. Braile, P_n velocity and cooling of the continental lithosphere, *Journal of Geophysical Research, 87*, 10,557-10,568, 1982.

Blackwell, D.D., J.L. Steele, M.K. Frohme, C.F. Murphey, G.R. Priest, and G.L. Black, Heat flow in the Oregon Cascade Range and its correlation with regional gravity, Curie point depths and geology, *Journal of Geophysical Research, 95*, 19,475-19,493, 1990a.

Blackwell, D.D., J.L. Steele, S. Kelley, and M.A. Korosec, Heat flow in the state of Washington and thermal conditions in the Cascade Range, *Journal of Geophysical Research, 95,* 19,495-19,516, 1990b.

Blanpied, M.L., D.A. Lockner, and J.D. Byerlee, Frictional slip of granite at hydrothermal conditions, *Journal of Geophysical Research, 100,* 13,045-13,064, 1995.

Blenkinsop, T., *Deformation Microstructures and Mechanisms in Minerals and Rocks*, Kluwer Academic Publishers, London, 150 pp., 2000.

Bodri, L. and B. Bodri, Numerical investigations of tectonic flow in island-arc areas, *Tectonophysics, 50*, 163-175, 1978.

Bostock, M.G. and J.C. van Decar, Upper mantle structure of the northern Cascadia subduction zone, *Canadian Journal of Earth Sciences, 32*, 1-12, 1995.

Bostock, M.G. and J.F. Cassidy, Variations in SKS splitting across western Canada, *Geophysical Research Letters, 22*, 5-8, 1995.

Bostock, M.G., R.D. Hyndman, S. Rondenay, and S.M. Peacock, An inverted continental Moho and serpentinization of the forearc mantle, *Nature, 417*, 536-538, 2002.

Bowman, J.R. and Ando, M., Shear-wave splitting in the upper mantle wedge above the Tonga subduction zone, *Geophysical Journal of the Royal Astronomical Society, 88*, 25-41, 1987.

Brace, W.F. and J.D. Byerlee, California earthquakes: Why only shallow focus?, *Science, 168*, 1573-1575, 1970.

Brocher, T.M., R. Parsons, A.M. Trehu, C.M. Snelson, and M.A. Fisher, Seismic evidence for widespread serpentinized forearc upper mantle along the Cascadia margin, *Geology, 31*, 267-270, 2003.

Burianyk, M.J.A. and E.R. Kanasewich, Crustal structure of the Omineca and Intermontane Belts, southeastern Canadian Cordillera, *Journal of Geophysical Research, 100,* 15,303-15,316, 1995.

Burianyk, M.J.A., E.R. Kanasewich, and N. Udey, Broadside wide-angle seismic studies and three-dimensional structure of the crust in the southeast Canadian Cordillera, *Canadian Journal of Earth Sciences, 34*, 1156-1166, 1997.

Buttles, J. and P. Olson, A laboratory model of subduction zone anisotropy, *Earth and Planetary Science Letters, 164*, 245-262, 1998.

Byerlee, J.D., Friction of rocks, *Pure and Applied Geophysics, 116*, 615-626, 1978.

Byrne, D.E., D.M. Davis, and L.R. Sykes, Loci and maximum size of thrust earthquakes and the mechanics of the shallow region of subduction zones, *Tectonics, 7*, 833-857, 1988.

Cahill, T. and B.L. Isacks, Seismicity and shape of the subducted Nazca Plate, *Journal of Geophysical Research, 97*, 17,503-17,529, 1992.

Caristan, Y., The transition from high temperature creep to fracture in Maryland diabase, *Journal of Geophysical Research, 87*, 6781-6790, 1982.

Cassidy, J.F. and M.G. Bostock, Shear-wave splitting above the subducting Juan de Fuca plate, *Geophysical Research Letters, 23*, 941-944, 1996.

Cermak, V. Lithosphere thermal regimes in Europe, *Physics of the Earth and Planetary Interiors, 79*, 179-1993, 1993.

Cermak, V. and L. Ryback (Eds.), *Terrestrial Heat Flow in Europe*, Springer-Verlag, New York, 328 pp., 1979.

Chapman, D.S., Thermal gradients in the continental crust, *In:* J.B. Dawson, D.A. Carswell, J. Hall and K.H. Wedephol (Eds), *The nature of the lower continental crust*, Geological Society of America Special Publication No. 24, pp. 63-70, 1986.

Chapman, D.S. and H.N. Pollack, Global heat flow: A new look, *Earth and Planetary Science Letters,* 28, 23-32, 1975.

Chen, W. and P. Molnar, Focal depth of intracontinental and interplate earthquakes and its implications for the thermal and mechanical properties of the lithosphere, *Journal of Geophysical Research, 88*, 4183-4214, 1983.

Chen, Y. and W.J. Morgan, A nonlinear rheology model for mid-ocean ridge axis topography, *Journal of Geophysical Research, 95*, 17,583-17,604, 1990.

Chopra, P.N. and M.S. Paterson, The experimental deformation of dunite, *Tectonophysics, 78*, 453-473, 1981.

Chopra, P.N. and M.S. Paterson, The role of water in the deformation of dunite, *Journal of Geophysical Research, 89*, 7861-7876, 1984.

Christensen, N.I., Compressional wave velocities in rocks at high temperature and pressures, critical thermal gradients, and crustal low velocity layers, *Journal of Geophysical Research, 84*, 6849-6857, 1979.

Clauser, C. and E. Huenges, Thermal conductivity of rocks and minerals, *In:* T. Ahrens (Ed.), *Rock physics and phase relations: A handbook of physical constants*, American Geophysical Union, Washington DC, pp. 105-126, 1995.

Clowes, R.M., C.A. Zelt, J.R. Amor, and R.M. Ellis, Lithospheric structure in the southern Canadian Cordillera from a network of seismic refraction lines, *Canadian Journal of Earth Sciences, 32*, 1485-1513, 1995.

Cooper, A.K., M.S. Marlow, D.W. Scholl, and A.J. Stevenson, Evidence for Cenozoic crustal extension in the Bering Sea region, *Tectonics, 11*, 719-731, 1992.

Conder, J.A., D.A. Wiens, and J. Morris, On the decompression melting structure at volcanic arcs and backarc spreading centers, *Geophysical Research Letters, 29*(15), doi: 10.1029/2002GL015390, 2002.

Couch, R. and S. Woodcock, Gravity and structure of the continental margins of southwestern Mexico and northwestern Guatemala, *Journal of Geophysical Research, 86*, 1829-1840, 1981.

Currie, C.A., J.F. Cassidy, and R.D. Hyndman, A regional study of shear wave splitting above the Cascadia subduction zone: Margin-parallel crustal stress, *Geophysical Research Letters, 28*, 659-662, 2001.

Currie, C.A., J.F. Cassidy, R.D. Hyndman, and M.G. Bostock, Shear wave anisotropy beneath the Cascadia subduction zone and western North American craton, *Geophysical Journal International, 157*, 341-353, 2004a.

Currie, C.A., K. Wang, R.D. Hyndman, and J. He, The thermal effects of steady-state slab-driven mantle flow above a subducting plate: The Cascadia subduction zone and backarc, *Earth and Planetary Science Letters, 223*, 35-48, 2004b.

Davies, J.H. and D.J. Stevenson, Physical model of source region of subduction volcanics, *Journal of Geophysical Research, 97*, 2037-2070, 1992.

Davis, E.E. and T.J. Lewis, Heat flow in a back-arc environment: Intermontane and Omineca Crystalline Belts, southern Canadian Cordillera, *Canadian Journal of Earth Sciences, 21*, 715-726, 1984.

Davis, E.E., K. Wang, J. He, D.S. Chapman, H. Villinger, and A. Rosenberger, An unequivocal case for high Nusselt number hydrothermal convection in sediment-buried igneous oceanic crust, *Earth and Planetary Science Letters, 146*, 137-150, 1997.

Defant, M.J. and M.S. Drummond, Derivation of some modern arc magmas by melting of young subducted lithosphere, *Nature, 347*, 662-665, 1990.

DeMets, C. and D.S. Wilson, Relative motions of the Pacific, Rivera, North American, and Cocos Plates since 0.78 Ma, *Journal of Geophysical Research, 102*, 2789-2806, 1997.

DeMets, C. and S. Traylen, Motion of the Rivera plate since 10 Ma relative to the Pacific and North American Plates and the mantle, *Tectonophysics, 318*, 119-159, 2000.

Dimitru, T.A., Effect of subduction parameters on geothermal gradients in forearcs, with an application to Franciscan subduction in California, *Journal of Geophysical Research, 96*, 621-641, 1991.

Dixon, J.E., T.H. Dixon, D.R. Bell, and R. Malservisi, Lateral variation in upper mantle viscosity: Role of water, *Earth and Planetary Science Letters, 222*, 451-467, 2004.

Dragert., H., R.D. Hyndman, G.C. Rogers, and K. Wang, Current deformation and the width of the seismogenic zone of the northern Cascadia subduction thrust, *Journal of Geophysical Research, 99*, 653-668, 1994.

Engebretson, D.C., A. Cox, and R.G. Gordon, Relative motions between oceanic and continental plates in the Pacific basin, *Special Paper of the Geological Society of America 206*, 59 pp. 1985.

Elkins Tanton, L.T., T.L. Grove, and J. Donnelly-Nolan, Hot, shallow mantle melting under the Cascades volcanic arc, *Geology, 29,* 631-634, 2001.

Epp, D., P.J. Grim, and M.G. Langseth, Heat flow in the Caribbean and Gulf of Mexico, *Journal of Geophysical Research, 75*, 5655-5669, 1970.

Fischer, K.M. and D.A. Wiens, The depth distribution of mantle anisotropy beneath the Tonga subduction zone, *Earth and Planetary Science Letters, 142*, 253-260, 1996.

Fischer, K.M. and X. Yang, Anisotropy in Kuril-Kamchatka subduction zone structure, *Geophysical Research Letters, 21*, 5-8, 1994.

Fischer, K.M., M.J. Fouch, D.A. Wiens, and M.S. Boettcher, Anisotropy and flow in Pacific subduction zones backarcs, *Pure and Applied Geophysics, 151*, 463-475, 1998.

Fischer, K.M., E.M. Parmentier, A.R. Stine, and E.R. Wolf, Modeling anisotropy and plate-driven flow in the Tonga subduction zone backarc, *Journal of Geophysical Research, 105*, 16,181-16,191, 2000.

Flanagan, M.P. and D.A. Wiens, Radial upper mantle attenuation structure of inactive back arc basins from differential shear wave measurements, *Journal of Geophysical Research, 99*, 15,469-15,485, 1995.

Fliedner, M.M. and S.L. Klemperer, Crustal structure transition from oceanic arc to continental arc, eastern Aleutian Islands and Alaska Peninsula, *Earth and Planetary Science Letters, 179*, 567-579, 2000.

Flück, P., Contributions to the geodynamics of western Canada, Ph.D. thesis, University of Victoria, 326 pp., 2003.

Flück, P., R.D. Hyndman, and C. Lowe, Effective elastic thickness T_e of the lithosphere in western Canada, *Journal of Geophysical Research, 108*(B9), 2430, doi: 10.1029/2002JB002201, 2003.

Flück, P., R.D. Hyndman, and K. Wang, 3-D dislocation model for great earthquakes of the Cascadia subduction zone, *Journal of Geophysical Research, 102*, 20,539-20,550, 1997.

Forte, A.M. and H.K.C. Perry, Geodynamic evidence for a chemically depleted continental tectosphere, *Science, 290*, 1940-1944, 2000.

Fouch, M.J. and Fischer, K.M., Mantle anisotropy beneath northwest Pacific subduction zones, *Journal of Geophysical Research, 101*, 15,987-16,002, 1996.

Fouch, M.J. and Fischer, K.M., Shear wave anisotropy in the Mariana subduction zone, *Geophysical Research Letters, 25*, 1221-1224, 1998.

Frederiksen, A.W., M.G. Bostock, and J.F. Cassidy, S-wave velocity structure of the Canadian upper mantle, *Physics of the Earth and Planetary Interiors, 124*, 175-191, 2001.

Frederiksen, A.W., M.G. Bostock, J.C. van Decar, and J.F. Cassidy, Seismic structure of the upper mantle beneath the northern Canadian Cordillera from teleseismic travel-time inversion, *Tectonophysics, 294*, 43-44, 1998.

Furukawa, Y., Magmatic processes under arcs and formation of the volcanic front, *Journal of Geophysical Research, 98*, 8309-8319, 1993a.

Furukawa, Y., Depth of the decoupling plate interface and thermal structure under arcs, *Journal of Geophysical Research, 98*, 20,005-20,013, 1993b.

Gabrielse, H. (Comp.), Structural styles, *In:* H. Gabrielse and C.J. Yorath (eds.), *The Geology of North America, vol. G-2, Geology of the Cordilleran Orogen in Canada*, Geological Society of America, Boulder CO, pp. 571-675, 1992.

Gabrielse, H. and C.J. Yorath (Eds.), *The Geology of North America, vol. G-2, Geology of the Cordilleran Orogen in Canada*, Geological Society of America, Boulder CO, 844 pp., 1992.

Gasparon, M. and R. Varne, Sumatran granitoids and their relationship to Southeast Asian terranes, *Tectonophysics, 251*, 277-299, 1995.

Gill, J., Orogenic andesites and plate tectonics, Springer Verlag, Berlin, 390 pp., 1981.

Global Heat Flow Data Base, International Heat Flow Commission (see also *Pollack et al.*, 1993), http://www.heatflow.und.edu, last accessed, May 2004.

Gorbatov, A., J. Dominguez, G. Suarez, V. Kostoglodov, D. Zhao, and E. Gordeev, Tomographic imaging of the P-wave velocity structure beneath the Kamchatka peninsula, *Geophysical Journal International, 137*, 269-279, 1999.

Goes, S. and S. van der Lee, Thermal structure of the North American uppermost mantle inferred from seismic tomography, *Journal of Geophysical Research, 107*(B3), doi: 10.1029/2000JB000049, 2002.

Goes, S., R. Govers, and P. Vacher, Shallow mantle temperatures under Europe from P and S wave tomography, *Journal of Geophysical Research, 105*, 11,153-11,169, 2000.

Gomberg, J.S., K.F. Priestly, T.G. Masters, and J.N. Brune, The structure of the crust and upper mantle of northern Mexico, *Geophysical Journal, 94*, 1-20, 1988.

Gomberg, J., K. Priestley, and J. Brune, The compressional velocity structure of the crust and upper mantle of northern Mexico and the border region, *Bulletin of the Seismological Society of America, 79*, 1496-1519, 1989.

Gough, D.I., Mantle upflow tectonics in the Canadian Cordillera, *Journal of Geophysical Research, 91*, 1909-1919, 1986.

Grand, S.P., Mantle shear structure beneath the Americas and surrounding oceans, *Journal of Geophysical Research, 99*, 11,591-11,621, 1994.

Gripp, A.E. and R.G. Gordon, Young tracks of hotspots and current plate velocities, *Geophysical Journal International, 150*, 321-361, 2002.

Haberland, C. and A. Rietbrock, Attenuation tomography in the western central Andes: A detailed insight into the structure of a magmatic arc, *Journal of Geophysical Research, 106*, 11,151-11,167, 2001.

Hall, C.E., K.M. Fischer, E.M. Parmentier, and D.K. Blackman, The influence of plate motions on three-dimensional backarc mantle flow and shear wave splitting, *Journal of Geophysical Research, 105*, 28,009-28,033, 2000.

Hamza, V.M. and M. Munoz, Heat flow map of South America, *Geothermics, 25*, 599-646, 1996.

Harder, M. and J.K. Russell, Thermal state of the mantle lithosphere beneath the Northern Cordilleran Volcanic Province, British Columbia, manuscript submitted to *Lithos*, July 2004.

Harris, R.N. and K. Wang, A thermal model of the Middle America Trench at the Nicoya Peninsula, Costa Rica, *Geophysical Research Letters, 29*(21), 2010, 10.1029/2002GL015406, 2002.

Hasebe, K., N. Fujhi, and S. Uyeda, Thermal processes under island arcs, *Tectonophysics, 10*, 335-355, 1970.

Hatcher, R.D., Jr., Tectonic synthesis of the U.S. Appalachians, *In:* R.D. Hatcher, Jr., W.A. Thomas, and G.W. Viele (Eds.), *The Geology of North America, Vol. F-2, The Appalachian-Ouachit Orogen in the United States*, Geological Society of America, Boulder CO, pp. 511-535, 1989.

Helsley C.E., J.B. Nation, and R.P. Meyer, Seismic refraction observations in southern Mexico, *EOS Transactions of the American Geophysical Union, 56*, 452, 1975.

Hiramatsu, Y., M. Ando, and Y. Ishikawa, ScS splitting of deep earthquakes around Japan, *Geophysical Journal International, 128*, 409-424, 1997.

Hirth, G. and D.L. Kohlstedt, Experimental constraints on the dynamics of the partially molten upper mantle: Deformation in the diffusion creep regime, *Journal of Geophysical Research, 100*, 1981-2001, 1995a.

Hirth, G. and D.L. Kohlstedt, Experimental constraints on the dynamics of the partially molten upper mantle 2. Deformation in the dislocation creep regime, *Journal of Geophysical Research, 100*, 15,441-15,499, 1995b.

Hirth, G. and D.L. Kohlstedt, Water in the oceanic upper mantle: Implications for rheology, melt extraction and the evolution of the lithosphere, *Earth and Planetary Science Letters, 144*, 93-108, 1996.

Hirth, G., R.L. Evans, A.D. Chave, Comparison of continental and oceanic mantle electrical conductivity: Is the Archean lithosphere dry? *Geochemisty, Geophysics, Geosystems, 1*, doi: 2000GC000048, 2000.

Hochstaeder, A.G., J.B. Gill, B. Taylor, O. Ishizuka, M. Yuasa, and S. Morita, Across-arc geochemical trends in the Izu-Bonin arc: Constraints on source composition and mantle melting, *Journal of Geophysical Research, 105*, 495-512, 2000.

Honda, S., Thermal structure beneath Tohoku, Northeast Japan – A case study for understanding the detailed thermal structure of the subduction zone, *Tectonophysics, 112*, 69-102, 1985.

Honda, S. and M. Saito, Small-scale convection under the back-arc occurring in the low viscosity wedge, *Earth and Planetary Science Letters,* 216, 703-715, 2003.

Honda, S., M. Saito, and T. Nakakuki, Possible existence of small-scale convection under the back-arc, *Geophysical Research Letters, 29*(21), 2043, doi: 10.1029/2002GL015853, 2002.

Hsui, A.T. and M.N. Toksoz, The evolution of thermal structures beneath a subduction zone, *Tectonophysics, 60*, 43-60, 1979.

Hsui, A.T., B.D. Marsh, and M.N. Toksoz, On melting of the subducted oceanic crust: Effects of subduction induced mantle flow, *Tectonophysics, 99*, 207-220, 1983.

Hughes, T.J.R., L.P. Franca, G.M. Hulbert, A new finite element formulation for computational fluid dynamics: VIII. The Galerkin-Least-Squares method for advective-diffusive equations, *Computational Methods for Applied Mechanical Engineering, 73*, 173-189, 1989.

Hutchison, I., The effects of sedimentation and compaction on oceanic heat flow, *Geophysical Journal of the Royal Astronomical Society, 82*, 439-459, 1985.

Hutton, W., C. DeMets, O. Sanchez, G. Suarez, and J. Stock, Slip kinematics and dynamics during and after the 1995 October 9 M_W=8.0 Colima-Jalisco earthquake, Mexico, from GPS constraints, *Geophysical Journal International, 146*, 637-658, 2001.

Hyndman, R.D. and T.J. Lewis, Review: The thermal regime along the southern Canadian Cordillera Lithoprobe corridor, *Canadian Journal of Earth Sciences, 32*, 1611-1617, 1995.

Hyndman, R.D. and T.J. Lewis, Geophysical consequences of the Cordillera-Craton thermal transition in southwestern Canada, *Tectonophysics, 306*, 397-422, 1999.

Hyndman, R.D. and S.M Peacock, Serpentinization of the forearc mantle, *Earth and Planetary Science Letters,* 212, 417-432, 2003.

Hyndman, R.D. and K. Wang, Thermal constraints on the zone of major thrust earthquake failure: The Cascadia subduction zone, *J. Geophys. Res., 98*, 2039-2060, 1993.

Hyndman R.D. and K. Wang, The rupture zone of Cascadia great earthquakes and the thermal regime, *Journal of Geophysical Research, 100*, 22,133-22,154, 1995.

Hyndman, R.D., C.A. Currie, and S. Mazzotti, Subduction zone backarcs, continental mobile belts, and orogenic heat, manuscript submitted to *GSA Today*, June 2004.

Hyndman, R.D., K. Wang, and M. Yamano, Thermal constraints on the seismogenic portion of the southwestern Japan subduction thrust, *Journal of Geophysical Research, 100*, 15,373-15,392, 1995.

Hyndman, R.D., M. Yamano, and D.A. Oleskevich, The seismogenic zone of subduction thrust faults, *Island Arc, 6*, 244-260, 1997.

Ida, Y., Convection in the mantle wedge above the slab and tectonic processes in subduction zones, *Journal of Geophysical Research, 88*, 7449-7456, 1983.

Iidaka, T. and K. Obara, Shear-wave polarization anisotropy in the mantle wedge above the subducting Pacific Plate, *Tectonophysics, 249*, 53-68, 1995.

Ito, E. and T. Katsura, A temperature profile of the mantle transition zone, *Geophysical Research Letters, 16*, 425-428, 1989.

Ivins, ER. and T.S. James, Simple models for late Holocene and present-day Patagonian glacier fluctuations and predications of a geodetically detectable isostatic response, *Geophysical Journal International, 138*, 601-624, 1999.

Iwamori, H., Heat sources and melting in subduction zones, *Journal of Geophysical Research, 102*, 14,803-14,820, 1997.

Iwamori, H., Transportation of H_2O and melting in subduction zones, *Earth and Planetary Science Letters, 160*, 65-80, 1998.

James, T.S., J.J. Clague, K. Wang, and I. Hutchinson, Postglacial rebound at the northern Cascadia subduction zone, *Quaternary Science Reviews, 19*, 1527-1541, 2000.

Jarvis, G.T., Time-dependent convection in the Earth's mantle, *Physics of the Earth and Planetary Interiors, 36*, 305-327, 1984.

Jaupart, C. and J.C. Marechal, The thermal structure and thickness of continental roots, *Lithos, 48*, 93-114, 1999.

Jaupart, C., J.R. Mann, and G. Simmons, A detailed study of the distribution of heat flow and radioactivity in New Hampshire (U.S.A.), *Earth and Planetary Science Letters, 59*, 267-287, 1982.

Jaupart, C., J.C. Mareschal, L. Guillou-Frottier, and A. Davaille, Heat flow and thickness of the lithosphere in the Canadian Shield, *Journal of Geophysical Research, 103*, 15,269-15,289, 1998.

Ji, S. and B. Xia, *Rheology of Polyphase Earth Materials*, Polytechnic International Press, Montreal, 259 pp., 2002.

Johnston, S.T. and D.J. Thorkelson, Cocos-Nazca slab window beneath Central America, *Earth and Planetary Science Letters, 146*, 465-474, 1997.

Jolivet, L., K.Tamaki, and M. Fournier, Japan Sea, opening history and mechanism: A synthesis, *Journal of Geophysical Research, 99*, 22,237-22,259, 1994.

Jordan, T.H., The continental tectosphere, *Reviews of Geophysics and Space Physics, 13*, 1-13, 1975.

Jung, H. and S. Karato, Water-induced fabric transitions in olivine, *Science, 293*, 1460-1463, 2001.

Kaila, K.L. and V.G. Krishna, Upper mantle velocity structure in the Kurile Islands, Kamchatka, and the Sea of Okhotsk regions, *Bulletin of the Seismological Society of America, 74*, 2269-2296, 1984.

Kamiya, S. and Y. Kobayashi, Seismological evidence for the existence of serpentinized wedge mantle, *Geophysical Research Letters, 27*, 819-822, 2000.

Kaneshima, S. and P.G. Silver, Anisotropic loci in the mantle beneath central Peru, *Physics of the Earth and Planetary Interiors, 88*, 257-272, 1995.

Karato, S., Does partial melting reduce the creep strength of the upper mantle?, *Nature, 319*, 309-310, 1986.

Karato, S., Seismic anisotropy due to lattice preferred orientation of minerals: Kinematic or dynamic?, *In:* M.H. Manghnani and Y. Syono (Eds.), *High Pressure Research in Mineral Physics, Geophysical Monograph Series 39*, AGU, Washington, DC, pp. 455-471, 1987.

Karato, S., On the Lehmann discontinuity, *Geophysical Research Letters, 19*, 2255-2258, 1992.

Karato, S. and P. Wu, Rheology of the upper mantle: A synthesis, *Science, 260*, 771-778, 1993.

Karato, S., M.S. Paterson, and JD. Fitzgerald, Rheology of synthetic olivine aggregates: Influence of grain size and water, *Journal of Geophysical Research, 91*, 8151-8176, 1986.

Kaufmann, G. and F. Amelung, Reservoir-induced deformation and continental rheology in the vicinity of Lake Mead, Nevada, *Journal of Geophysical Research, 105*, 16,341-16,358, 2000.

Kaufmann, G. and K. Lambeck, Glacial isostatic adjustment and the radial viscosity profile from inverse modelling, *Journal of Geophysical Research, 107*, doi: 10.1029/2001JB000941, 2002.

Kelemen, P.B., J.L. Rilling, E.M Parmentier, L. Mehl, and B.R. Hacker, Thermal structure due to solid-state flow in the mantle wedge beneath arcs, *In:* J. Eiler (Ed.), *Inside the Subduction Factory, AGU Monograph 138*, American Geophysical Union, Washington DC, pp. 293-311, 2003.

Keller, G.R., and R.D. Hatcher, Jr., Some comparisons of the structure and evolution of the southern Appalachian-Ouachita orogen and portions of the Trans-European Suture Zone region, *Tectonophysics, 314*, 43-68, 1999.

Kendall, J.-M. Teleseismic arrivals at a mid-ocean ridge: Effects of mantle melt and anisotropy, *Geophysical Research Letters, 21*, 301-304, 1994.

Kennett, B.L.N., E.R. Engdahl, and R. Buland, Constraints on seismic velocities in the Earth from traveltimes, *Geophysical Journal International, 122*, 108-124, 1995.

Kincaid, C. and I.S. Sacks, Thermal and dynamical evolution of the upper mantle in subduction zones, *Journal of Geophysical Research, 102*, 12,295-12,315, 1997.

Kirby, S.H., Rheology of the lithosphere, *Reviews of Geophysics and Space Physics, 21*, 1458-1487, 1983.

Klitgord, K. and J. Mammerickx, Northern East Pacific Rise: Magnetic anomaly and bathymetric framework, *Journal of Geophysical Research., 87*, 6725-6750, 1982.

Kogan, M.G., Gravity field of the Kuril-Kamchatka Arc and its relation to the thermal regime of the lithosphere, *Journal of Geophysical Research, 80*, 1381-1390, 1975.

Kohlstedt, D.L. and M.E. Zimmerman, Rheology of partially molten mantle rocks, *Annual Review of Earth and Planetary Sciences, 24*, 41-62, 1996.

Kostantinovskaia, E.A., Arc-continent collision and subduction reversal in the Cenozoic evolution of the Northwest Pacific: An example from Kamchatka (NE Russia), *Tectonophysics, 333*, 75-94, 2001.

Kostoglodov, V. and W. Bandy, Seismotectonic constraints on the convergence rate between the Rivera and North American Plates, *Journal of Geophysical Research., 100*, 17.977-17,989, 1995.

Kostoglodov, V. and J.F. Pacheco, One hundred years of seismicity in Mexico (map), Instituto de Geofisica, UNAM, 1999.

Kostoglogdov, V., W. Bandy, J. Cominguez, and M. Mena, Gravity and seismicity over the Guerrero seismic gap, Mexico, *Geophysical Research Letters, 23*, 3385-3388, 1996.

Lachenbruch, A.H., Preliminary geothermal model of the Sierra Nevada, *Journal of Geophysical Research, 73*, 6977-6989, 1968.

Lachenbruch, A.H., Crustal temperature and heat production: Implications of the linear heat-flow relation, *Journal of Geophysical Research, 75*, 3291-3300, 1970.

Langseth, M.G. and E.A. Silver, The Nicoya convergent margin - a region of exceptionally low heat flow, *Geophysical Research Letters, 23*, 891-894, 1996.

Langseth, M.G., M.A. Hobart, and K. Horai, Heat flow in the Bering Sea, *Journal of Geophysical Research, 85*, 3740-3750, 1980.

Lee, T. and L.A. Lawver, Cenozoic plate reconstruction of Southeast Asia, *Tectonophysics, 251*, 85-138, 1995.

Lee, Y. and D. Deming, Evaluation of thermal conductivity temperature coreections applied in terrestrial heat flow studies, *Journal of Geophysical Research, 103*, 2447-2454, 1998.

Leeman, W.P., Boron and other fluid-mobile elements in volcanic arc lavas: Implications for subduction processes, *In:* G.E. Bebout, D.W. Scholl, S.H. Kirby, and J.P. Platt (Eds.), *Subduction: Top to bottom, AGU Monograph 96,* American Geophysical Union, Washington DC, pp. 269-276, 1996.

Levshin, A.L., M.H. Ritzwoller, M.P. Barmin, A. Villasenor, and C.A. Padgett, New constraints on the Arctic crust and uppermost mantle: surface wave group velocities, P_n and S_n, *Physics of the Earth and Planetary Interiors, 123*, 185-204, 2001.

Lewis, T.J., W.H. Bentkowski, and R.D. Hyndman, Crustal temperatures near the Lithoprobe Southern Canadian Cordillera transect, *Canadian Journal of Earth Sciences, 29*, 1197-1214, 1992.

Lewis, T.J., C. Lowe, and T.S. Hamilton, Continental signature of a ridge-trench-triple junction: northern Vancouver Island, *Journal of Geophysical Research, 102*, 7767-7781, 1997.

Lewis, T.J., R.D. Hyndman, and P. Flück, Heat flow, heat generation, and crustal temperatures in the northern Canadian Cordillera: Thermal control of tectonics, *Journal of Geophysical Research, 108*(B6), 2316, doi: 10.1029/2002JB002090, 2003.

Lewis, T.J., W.H. Bentkowski, E.E. Davis, R.D. Hyndman, J.G. Souther, and J.A. Wright, Subduction of the Juan de Fuca Plate: Thermal consequences, *Journal of Geophysical Research, 93*, 15,207-15,225, 1988.

Liu, M. and K.P. Furlong, Crustal shortening and Eocene extension in the southeastern Canadian Cordillera: Some thermal and rheological considerations, *Tectonics, 12*, 776-786, 1993.

Lowe, C. and G. Ranalli, Density, temperature, and rheological models for the southeastern Canadian Cordillera: Implications for its geodynamic evolution, *Canadian Journal of Earth Sciences, 30*, 77-93, 1993.

Lowry, A.R. and R.B. Smith, Flexural rigidity of the Basin and Range-Colorado Plateau-Rocky Montain transition from coherence analysis of gravity and topography, *Journal of Geophysical Research*, 99, 20,123-20,140, 1994.

Lucassen, F., S. Lewerenz, G. Franz, J. Viramonte, and K. Mezger, Metamorphism, isotopic ages and composition of lower crustal granulite xenoliths from the Cretaceous Salta Rift, Argentina, *Contributions to Mineralogy and Petrology, 134*, 325-341, 1999.

Lucassen, F.L., R. Becchio, R. Harmon, S. Kasemann, G. Franz, R. Trumbull, H-G. Wilke, R.L. Romer, and P. Dulski, Composition and density model of the continental crust at an active continental margin – the Central Andes between 20° and 27°S, *Tectonophysics, 341*, 195-223, 2001.

MacKenzie, J.M. and D. Canil, Composition and thermal evolution of cratonic mantle beneath the central Archean Slave Province, NWT, Canada, *Contributions to Mineralogy and Petrology, 134*, 313-324, 1999.

Majorowicz, J.A. and D.I. Gough, Crustal structure from MT soundings in the Canadian Cordillera, *Earth and Planetary Science Letters, 102*, 444-454, 1991.

Majorowicz, J.A. and A.M. Jessop, Regional heat flow patterns in the western Canadian Sedimentary Basin, *Tectonophysics, 74*, 209-238, 1981.

Majorowicz, J.A., D.I. Gough, and T.J. Lewis, Electrial conductivity and temperature in the Canadian Cordilleran crust, *Earth and Planetary Science Letters, 115*, 57-64, 1993.

Mantovani, E., M. Viti, D. Babbucci, C. Tamburelli, and D. Albarello, Back arc extension: Which driving mechanism?, *Journal of the Virtual Explorer, 3,* 17-45, 2001.

Marone, C., D.M. Saffer, K.M. Frye, and S. Mazzoni, Laboratory results indicating intrinsically stable frictional behaviour of illite clay, *EOS Transactions of the AGU, 82(47)*, Fall Meeting Supplement, Abstract T51G-06, 2001.

Matcham, I., M.K. Savage, and K.R. Gledhill, Distribution of seismic anisotropy in the subduction zone beneath the Wellington region, New Zealand, *Geophysical Journal International, 140,* 1-10, 2000.

Mazzotti, S., H. Dragert, J. Henton, M. Schmidt, R. Hyndman, T. James, Y. Lu, and M. Craymer, Current tectonics of northern Cascadia from a decade of GPS measurements, *Journal of Geophysical Research, 108*(B12), 2554, doi: 10.1029/2003JB002653, 2003.

McCulloch, M.T. and J.A. Gamble, Geochemical and geodynamical constraints on subduction zone magmatism, *Earth and Planetary Science Letters, 102*, 358-374, 1991.

McKenzie, D.P., Speculations on the consequences and causes of plate motions, *Geophysical Journal of the Royal Astronomical Society, 18,* 1-32, 1969.

McKenzie, D.P., Finite deformation during fluid flow, *Geophysical Journal of the Royal Astronomical Society, 58*, 689-715, 1979.

McKenzie, D.P. and M.J. Bickle, The volume and composition of melt generated by extension of the lithosphere, *Journal of Petrology, 29*, 625-679, 1988.

McKenzie, D.P. and J.G. Sclater, Heat flow inside the island arcs of the Northwestern Pacific, *Journal of Geophysical Research, 73*, 3173-3179, 1968.

McNamara, D.E. and M.E. Pasyanos, Seismological evidence for a sub-volcanic arc mantle wedge beneath the Denali volcanic gap, Alaska, *Geophysical Research Letters, 29*(16), doi: 10.1029/2001GL014088, 2002.

Mei, S. and D.L. Kohlstedt, Influence of water on plastic deformation of olivine aggregates 1. Diffusion creep regime, *Journal of Geophysical Research, 105*, 21,457-21,469, 2000a.

Mei, S. and D.L. Kohlstedt, Influence of water on plastic deformation of olivine aggregates 2. Dislocation creep regime, *Journal of Geophysical Research, 105*, 21,471-21,481, 2000.

Mei, S., W. Bai, T. Hiraga, and D.L. Kohlstedt, Influence of melt on the creep behaviour of olivine-basalt aggregates under hydrous conditions, *Earth and Planetary Science Letters, 201*, 491-507, 2002.

Meissnar, R.O., E.R. Flueh, R. Stibane, and E. Burg, Dynamics of the active plate boundary in southwest Columbia according to recent geophysical measurements, *Tectonophysics, 35*, 115-136, 1976.

Melbourne, T., I. Carmichael, C. DeMets, K. Hudnut, O. Sanchez, J. Stock, G. Suarez, and F. Webb, The geodetic signature of the M8.0 Oct. 9, 1995, Jalisco subduction earthquake, *Geophysical Research Letters, 24*, 6715-6718, 1997.

Mendoza, C. and S.H Hartzell, Slip distribution of the 19 September 1985 Michoacan, Mexico, earthquake: Near-source and teleseismic constraints, *Bulletin of the Seismological Society of America, 79*, 655-669, 1989.

Mendoza, C. and S. Hartzell, Fault-slip distribution of the 1995 Colima-Jalisco, Mexico, earthquake, *Bulletin of the Seismological Society of America, 89*, 1338-1344, 1999.

Meschede, M. and W. Frisch, A plate-tectonic model for the Mesozoic and Early Cenozoic history of the Caribbean plate, *Tectonophysics, 296*, 269-291, 1998.

Michaud, F., J.J. Danobeitia, R. Carbonell, R. Bartolome, D. Cordoba, L. Delgado, F. Nunez-Cornu, and T. Monfret, New insights into the subducting oceanic crust in the Middle American Trench of western Mexico (17-19°N), *Tectonophysics, 318*, 187-200, 2000.

Minear, J.W. and M.N. Toksoz, Thermal regime of a downgoing slab and new global tectonics, *Journal of Geophysical Research, 75*, 1397-1419, 1970.

Mitrovica, J.X. and W.R. Peltier, Constraints on mantle viscosity based upon the inversion of post-glacial uplift data from the Hudson Bay region, *Geophysical Journal International, 122*, 353-377, 1995.

Molnar, P., and P. England, Temperatures, heat flux and frictional stress near major thrust faults, *Journal of Geophysical Research, 95*, 4833-4856, 1990.

Monger, J.W.H. and R.A. Price, The Canadian Cordillera: Geology and tectonic evolution, *CSEG Recorder*, 17-36, February, 2002.

Mooney, W.D. and T.M. Brocher, Coincident seismic relection/refraction studies of the continental lithosphere, *Reviews of Geophysics, 25*, 723-742, 1987.

Moore, J.C., J.S. Watkins, T.H. Shipley, K.J. McMillen, S.B. Bachman, and N. Lundberg, Geology and tectonic evolution of a juvenile accretionary terrane along a truncated convergent margin: Synthesis of results from Leg 66 of the Deep Sea Drilling Project, southern Mexico, *Geological Society of America Bulletin, 93*, 847-861, 1982.

Moore, J.C. and D. Saffer, Updip limit of the seismogenic zone beneath the accretionary prism of Southwest Japan: An effect of diagenetic to low-grade metamorphic processes and increasing effective stress, *Geology, 29*, 183-186, 2001.

Morris, J.D., W.P. Leeman, and F. Tera, The subducted component in island arc lavas: Constraints from Be isotopes, and B-Be systematics, *Nature, 344*, 31-36, 1990.

Nakajima, J. and A. Hasegawa, Estimation of thermal structure in the mantle wedge of northeastern Japan from seismic attenuation data, *Geophysical Research Letters, 30*(14), 1760, doi: 10.1029/2003GL017185, 2003.

Nava, F., F. Nunez-Cornu, D. Cordoba, M. Mena, J. Ansorge, J. Gonzalez, M. Rodriguez, E. Banda, S. Mueller, A. Udias, M. Garcia-Garcia, G. Calderon, and the Mexican working group for Deep Seismic Profiling, Structure of the Middle America Trench in Oaxaca, Mexico, *Tectonophysics, 154*, 241-251, 1988.

Nicolas, A. and N.I. Christensen, Formation of anisotropy in upper mantle peridotites: A review, *In:* K. Fuchs and C. Froidevaux (Eds.), *Composition, Structure and Dynamics of the Lithosphere-Asthenosphere System, Geodynamics Series 16*, American Geophysical Union, Washington, DC, pp. 111-123, 1987

Nyblade, A.A. and H.N. Pollack, A comparative study of parameterized and full thermal-convection models in the interpretation of heat flow from cratons and mobile belts, *Geophysical Journal International, 113*, 747-751, 1993.

Oda, H. and H. Shimizu, S wave splitting observed in southwest Japan, *Tectonophysics, 270*, 73-82, 1997.

Okada, T., T. Matsuzawa, and A. Hasegawa, Shear-wave polarization anisotropy beneath the north-eastern part of Honshu, Japan, *Geophysical Journal International, 123*, 781-797, 1995.

Okuno, J. and M. Nakada, Rheological structure of the upper mantle inferred from the Holocene sea-level change along the west coast of Kyushu, Japan, *In:* P. Wu (Ed.), *Dynamics of the Ice Age Earth: A Modern Perspective*, GeoResearch Forum Series, Trans Tech Publications, Zurich, pp. 443-458, 1998.

Oleskevich, D.A., R.D. Hyndman, and K. Wang, The updip and downdip limits to great subduction earthquakes: Thermal and structural models of Cascadia, south Alaska, SW Japan, and Chile, *Journal of Geophysical Research, 104*, 14,965-14,991, 1999.

Ortiz, M., S.K. Singh, V. Kostoglodov, and J. Pacheco, Source areas of the Acapulco-San Marcos, Mexico earthquakes of 1962 (M 7.1; 7.0) and 1957 (M 7.7), as constrained by tsunami and uplift records, *Geofisica Internacional, 39*, 337-348, 2000a.

Ortiz, M., V. Kostoglodov , S.K. Singh, and J. Pacheco, New constraints on the uplift of October 9, 1995 Jalisco-Colima earthquake (M_W 8) based on the analysis of tsunami records at Manzanillo and Navidad, Mexico, *Geofisica Internacional, 39*, 349-357, 2000b.

Oxburgh, E.R. and D.L Turcotte, Problem of high heat flow and volcanism associated with zones of descending mantle convective flow, *Nature, 218*, 1041-1043, 1968.

Oxburgh, E.R. and D.L. Turcotte, Thermal structure of island arcs, *Geological Society of America Bulletin, 81*, 1665-1688, 1970.

Pacheco, J., S.K. Singh, J. Dominguez, A. Hurtado, L. Quintanar, Z. Jimenez, J. Yamamoto, C. Gutierrez, M. Santoyo, W. Bandy, M. Guzman, V. Kostoglodov, G. Reyes, and C. Ramirez, The October 9, 1995 Colima-Jalisco, Mexico earthquake (M_W 8): An aftershock study and a comparison of this earthquake with those of 1932, *Geophysical Research Letters, 24*, 2223-2226, 1997.

Pardo, M. and G. Suarez, Steep subduction geometry of the Rivera Plate beneath the Jalisco block in western Mexico, *Geophysical Research Letters, 20,* 2391-2394, 1993.

Pardo, M. and G. Suarez, Shape of the subducted Rivera and Cocos Plates in southern Mexico: Seismic and tectonic implications, *Journal of Geophysical Research, 100*, 12,357-12,373, 1995.

Park, C-H., K. Tamaki, and K. Kobayashi, Age-depth correlation of the Philippine Sea back-arc basins and other marginal basins in the world, *Tectonophysics, 181*, 351-371, 1990.

Parsons, B. and J.G. Sclater, An analysis of the variation of oceanic floor bathymetry and heat flow with age, *Journal of Geophysical Research, 82*, 803-827, 1977.

Pavlenkova, N.I., Crust and upper mantle structure in northern Eurasia from seismic data, *Advances in Geophysics, 37*, 1-133, 1996.

Peacock, S.M., Thermal effects of metamorphic fluids in subduction zones, *Geology, 15*, 1057-1060, 1987.

Peacock, S.M., Fluid processes in subduction zones, *Science, 248*, 329-337, 1990.

Peacock, S.M., Large-scale hydration of the lithosphere above subducting slabs, *Chemical Geology, 108*, 49-59, 1993.

Peacock, S.M., Thermal and petrologic structure of subduction zones, *In:* G.E. Bebout, D.W. Scholl, S.H. Kirby, J.P. Platt (Eds.), *Subduction: Top to Bottom, AGU Monograph 96,* American Geophysical Union, Washington, DC, pp. 119-133, 1996.

Peacock, S.M. and R.D. Hyndman, Hydrous minerals in the mantle wedge and the maximum depth of subduction thrust earthquakes, *Geophysical Research Letters, 26*, 2517-2520, 1999.

Peacock, S.M. and K. Wang, Seismic consequences of warm versus cool subduction metamorphism: Examples from southwest and northeast Japan, *Science, 286*, 937-939, 1999.

Peacock, S.M, T. Ruchmer, and A.B. Thompson, Partial melting of subducting oceanic crust, *Earth and Planetary Science Letters, 121*, 227-244, 1994.

Peltier, W.R., Post-glacial variations in the level of the sea: Implications for climate dynamics and solid earth geophysics, *Reviews of Geophysics, 36*, 603-689, 1998.

Peyton, V., V. Levin, J. Park, M. Brandon, J. Lees, E. Gordeev, and A. Ozerov, Mantle flow at a slab edge: Seismic anisotropy in the Kamchatka region, *Geophysical Research Letters, 28*, 379-382, 2001.

Polet, J., P.G. Silver, S. Beck, T. Wallace, G. Zandt, S. Ruppert, R. Kind, and A. Pudloff, Shear wave anisotropy beneath the Andes from the BANJO, SEDA, and PISCO experiments, *Journal of Geophysical Research, 105*, 6287-6304, 2000.

Pollack, H.N., S.J. Hurter, and J.R. Johnson, Heat flow from the earth's interior: Analysis of the global data set, *Reviews of Geophysics, 31*, 267-280, 1993.

Prol-Ledesma, R.M., Terrestrial heat flow in Mexico, *In:* V. Cermak and L. Rybach (Eds.), *Terrestrial heat flow and the lithosphere structure*, Springer-Verlag, New York, pp. 475-485, 1991.

Prol-Ledesma, R.M., V.M. Sugrobov, E.L. Flores, G. Juarez, Y.B. Smirnov, A.P. Gorshkov, V.G. Bondarenko, V.A. Rashidov, L.N. Nedopekin, and V.A. Gavrilov, Heat flow variations along the Middle America Trench, *Marine Geophysical Researches, 11*, 69-76, 1989.

Puspito, N.T. and K. Shimazaki, Mantle structure and seismotectonics of the Sunda and Banda arcs, *Tectonophysics, 251*, 215-228, 1995.

Ranalli, G., *Rheology of the Earth, second edition*, Chapman and Hall, New York, 413 pp., 1995.

Reinen, L.A., Seismic and aseismic slip indicators in serpentinite gouge, *Geology, 28*, 135-138, 2000.

Ribe, N.M., Seismic anisotropy and mantle flow, *Journal of Geophysical Research, 94*, 4213-4223, 1989.

Ribe, N.M., On the relation between seismic anisotropy and finite strain, *Journal of Geophysical Research,* 97, 8737-8747, 1992.

Riddihough, R.P., A model for recent plate interactions off Canada's west coast, *Canadian Journal of Earth Sciences, 14,* 384-396, 1977.

Ristau J., G. Rogers, and J. Cassidy, Relative plate motions and stress orientation in western Canada from regional moment-tensor analysis, *Seismological Research Letters, 73*, 261, 2002.

Ritzwoller, M.H. and A.L. Levshin, Eurasian surface wave tomography: Group velocities, *Journal of Geophysical Research, 103*, 4839-4878, 1998.

Ritzwoller, M.H., M.P. Barmin, A. Villasenor, A.L. Levshin, and E.R. Engdahl, Pn and Sn tomography across Eurasia to improve regional seismic event locations, *Tectonophysics, 358,* 39-55, 2002.

Robertson Maurice, S.D., D.A. Wiens, K.D. Koper, and E. Vera, Crustal and upper mantle structure of southernmost South America inferred from regional waveform inversion, *Journal of Geophysical Research, 108*(B1), doi: 10.1029/1002JB001828, 2003.

Ross, J.V., The nature and rheology of the Cordilleran upper mantle of British Columbia: Inferences from peridotite xenoliths, *Tectonophysics, 100*, 321-357, 1983.

Rowland, A. and J.H. Davies, Buoyancy rather than rheology controls the thickness of the overriding mechanical lithosphere at subduction zones, *Geophysical Research Letters, 26*, 3037-3040, 1999.

Roy, R.F., D.D. Blackwell, and F. Birch, Heat generation of plutonic rocks and continental heat flow provinces, *Earth and Planetary Science Letters, 5*, 1-12, 1968.

Rudnick, R.L. and D.M. Fountain, Nature and composition of the continental crust: A lower crustal perspective, *Reviews of Geophysics, 33*, 267-309, 1995.

Rudnick, R.L., W.F. McDonough, and R.J. O'Connell, Thermal structure, thickness and composition of continental lithosphere, *Chemical Geology 145*, 395-411, 1998.

Ruff, L.J. and R.W. Tichelaar, What controls the seismogenic plate interface in subduction zones?, *In:* G.E. Bebout, D.W. Scholl, S.H. Kirby, and J.P. Platt (Eds.), *Subduction: Top to Bottom, AGU Monograph 96,* American Geophysical Union, Washington DC, pp. 105-111, 1996.

Russell, J.K. and M.G. Kopylova, A steady state conductive geotherm for the north central Slave, Canada: Inversion of petrological data from the Jericho Kimberlite pipe, *Journal of Geophysical Research, 104*, 7089-7101, 1999.

Russo, R.M. and P.G. Silver, Trench-parallel flow beneath the Nazca Plate from seismic anisotropy, *Science, 263*, 1105-1111, 1994.

Saffer, D.M., K.M. Frye, C. Marone, and K. Mair, Laboratory results indicating complex and potentially unstable frictional behavior of smectite clay, *Geophysical Research Letters, 28*, 2297-2300, 2001.

Saruwatari, K., S. Ji, C. Long, and M.H. Salisbury, Seismic anisotropy of mantle xenoliths and constraints on upper mantle structure beneath the southern Canadian Cordillera, *Tectonophysics, 339*, 403-426, 2001.

Sass, J.H., A.H. Lachenbruch, R.H. Moses Jr., and P. Morgan, Heat flow from a scientific research well at Cajon Pass, California, *Journal of Geophysical Research, 97*, 5017-5030, 1992.

Savage, M.K., Seismic anisotropy and mantle deformation: What have we learned from shear wave splitting?, *Reviews of Geophysics,* 37, 65-106, 1999.

Scholl, D.W. and R. von Huene, Evidence for, and amounts of, continental crustal material recycled to the mantle at Cenozoic subduction zones, Abstracts with Program, 2003 Annual Meeting of the Geological Society of America, Geological Society of America, Boulder CO, 2003.

Schmidt, M.W. and S. Poli, Experimentally based water budgets for dehydrating slabs and consequences for arc magma generation, *Earth and Planetary Science Letters, 163*, 361-379, 1998.

Schmitz, M., W.-D. Heinsohn, and F.R. Schilling, Seismic, gravity and petrological evidence for partial melt beneath the thicknened Central Andean crust (21-23°S), *Tectonophysics, 270*, 1997, 313-326, 1997.

Scholz, C.H., *The Mechanics of Earthquakes and Faulting*, Cambridge University Press, New York, 439 pp., 1990.

Sclater, J.G., Heat flow and elevation of the marginal basins of the western Pacific, *Journal of Geophysical Research, 77*, 5705-5719, 1972.

Sclater, J.G., D. Karig, L.A. Lawver, and K. Louden, Heat flow, depth, and crustal thickness of the marginal basins of the South Philippine Sea, *Journal of Geophysical Research, 81*, 309-318, 1976.

Seno, T, T. Sakurai, and S. Stein, Can the Okhotsk Plate be discriminated from the North American Plate?, *Journal of Geophysical Research, 101,* 11,305-11,315, 1996.

Shapiro, N.M, A.V. Gorbatov, E. Gordeev, and J. Dominguez, Average shear-wave velocity structure of the Kamchatka peninsula from dispersion of surface waves, *Earth Planets Space, 52*, 573-577, 2000.

Sharpe, H.N. and W.R. Peltier, A thermal history model for the Earth with parameterized convection, *Geophysical Journal of the Royal Astronomical Society, 59*, 171-205, 1979.

Sheppard, L.E., and K.J. McMillen, Sedimentation rates of the southern Mexico continental margin, Deep Sea Drilling Project Leg 66, *Initial Reports of the Deep Sea Drilling Project, 66*, pp. 445-452, 1981.

Shih, X.R., R.P. Meyer, and J.F. Schneider, Seismic anisotropy above a subducting plate, *Geology, 19*, 807-810, 1991.

Silver, P.G., Seismic anisotropy beneath the continents: Probing the depths of geology, *Annual Review of Earth and Planetary Sciences, 24*, 385-432, 1996.

Silver, P.G. and W.W. Chan, Shear wave splitting and subcontinental mantle deformation, *Journal of Geophysical Research, 96*, 16,429-16,454, 1991.

Silver, P.G. and M.K. Savage, The interpretation of shear-wave splitting parameters in the presence of two anisotropic layers, *Geophysical Journal International, 119*, 949-963, 1994.

Singh, S.K., J. Havskov, K.C. McNally, L. Ponce, T. Hearn, and M. Vassiliou, The Oaxaca, Mexico earthquake of 29 November 1978: A preliminary report on aftershocks, *Science, 207*, 1211-1213, 1980.

Singh, S.K., L. Ponce, and S.P. Nishenko, The great Jalisco, Mexico, earthquake of 1932: Subduction of the Rivera Plate, *Bulletin of the Seismological Society of America, 75*, 1301-1313, 1985.

Singh, S.K., M. Ordaz, L. Alcantara, N. Shapiro, V. Kostoglodov, J.F. Pacheco, S. Alcocer, C. Gutierrez, R. Quaas, T. Mikumo, and E. Ovando, The Oaxaca earthquake of 30 September 1999 (M_W=7.5): A normal-faulting event in the subducted Cocos Plate, *Seismological Research Letters, 71*, 67-78, 2000.

Sleep, N. and M.N. Toksoz, Evolution of marginal basins, *Nature, 233*, 548-550, 1971.

Smith, D.L., C.E. Nuckels, R.L. Jones, and G.A. Cook, Distribution of heat flow and radioactive heat generation in northern Mexico, *Journal of Geophysical Research, 84*, 2371-2379, 1979.

Smith, G.P., D.A. Wiens, K.M. Fischer, L.M. Dorman, S.C. Webb, J.A. Hildebrand, A complex pattern of mantle flow in the Lau backarc, *Science, 292*, 713-716, 2001.

Southeast Asia Heat Flow Database, www.gl.rhbnc.ac.uk/seasia/Research/Heatflow/body_heatflow.html, last accessed May 2004.

Springer, M., Interpretation of heat-flow density in the Central Andes, *Tectonophysics, 306*, 377-395, 1999.

Springer, M. and A. Forster, Heat-flow density across the central Andean subduction zone, *Tectonophysics, 291*, 123-139, 1998.

Stein, C.A. and S. Stein, A model for the global variation in oceanic depth and heat flow with lithospheric age, *Nature, 359*, 123-129, 1992.

Stein, S. and J.T. Freymueller (Eds.), *Plate Boundary Zones, AGU Monograph 30*, American Geophysical Union, Washington DC, 425 pp., 2002.

Stern, C.R., R. Kilian, B. Olker, E.H. Hauri, and T.K. Kyser, Evidence from mantle xenoliths for relatively thin (<100 km) continental lithosphere below the Phanerozoic crust of southernmost South America, *Lithos, 48*, 217-235, 1999.

Stern, C.R., F.A. Frey, K. Futa, R.E. Zartman, Z. Peng, and T.K. Kyser, Trace-element and Sr, Nd, Pb, and O isotopic composition of Plicence and Quaternary alkali basalts of the Patagonian Plateau lavas of southernmost South America, *Contributions to Mineralogy and Petrology, 104*, 294-308, 1990.

Stern, R.J., Subduction zones, *Reviews of Geophysics, 40*(4), 1012, doi: 10.1029/2001RG000108, 2002.

Stewart G.S., E.P. Chael, and K.C. McNally, The November 29, 1978, Oaxaca, Mexico, earthquake: A large simple event, *Journal of Geophysical Research, 86*, 5053-5060, 1981.

Stolte, C., K.C. McNally, J. Gonzalez-Ruiz, G.W. Simila, A. Reyes, C. Rebollar, L. Munguia, and L. Mendoza, Fine structure of a post-failure Wadati-Benioff zone, *Geophysical Research Letters, 13*, 577-580, 1986.

Stone, D.B., J.N. Stihler, and C.H. Estabrook, Basement (Pn) velocities in Interior Alaska and the Yukon Flats, *EOS Transactions of the American Geophysical Union, 68*, 1458, 1987.

Suarez, G., T. Monfret, G. Wittlinger, and C. David, Geometry of subduction and depth of the seismogenic zone in the Guerrero gap, Mexico, *Nature, 345*, 336-338, 1990.

Sugrobov, V.M and F.A. Yanovsky, Terrestrial heat flow, estimation of deep temperature and seismicity of the Kamchatka region, *Tectonophysics, 217*, 43-53, 1993.

Suyehiro, K., N. Takahashi, Y. Ariie, Y. Yokoi, R. Hino, M. Shinohara, T. Kanazawa, N. Hirata, H. Tokuyama, and A. Taira, Continental crust, crustal underplating, and low-Q upper mantle beneath an oceanic island arc, *Science, 272*, 390-392, 1996.

Tatsumi, Y., Formation of the volcanic front in subduction zones, *Geophysical Research Letters, 13*, 717-720, 1986.

Tatsumi, Y., M. Sakuyama, H. Fukuyami, and I. Kushiro, Generation of arc basalt magmas and thermal structure of the mantle wedge in subduction zones, *Journal of Geophysical Research, 88*, 5815-5825, 1983.

Thamrin, M., An investigation of the relationship between the geology of Indonesian sedimentary basins and heat flow density, *Tectonophysics, 121*, 45-62, 1985.

Tichelaar, B.W. and L.J. Ruff, Depth of seismic coupling along subduction zones, *Journal of Geophysical Research, 98*, 2017-2037, 1993.

Toksoz, M.N. and A.T. Hsui, Numerical studies of back-arc convection and the formation of marginal basins, *Tectonophysics, 50*, 177-196, 1978.

Toksoz, M.N., J.W. Minear, and B.R. Julian, Temperature field and geophysical effects of a downgoing slab, *Journal of Geophysical Research, 76*, 1113-1138, 1971.

Travis, B. and P. Olson, Convection with internal heat sources and thermal turbulence in the Earth's mantle, *Geophysical Journal International, 118*, 1-19, 1994.

Tse, S.T. and J.R. Rice, Crustal earthquake instability in relation to the depth variation of frictional slip properties, *Journal of Geophysical Research, 91*, 9452-9472, 1986.

Tsenn, M.C. and N.L. Carter, Upper limits of power law creep of rocks, *Tectonophysics, 136*, 1-26, 1987.

Turcotte, D.L. and G. Schubert, *Geodynamics, second edition*, Cambridge University Press, Cambridge UK, 456 pp., 2002.

Turner, S. and C. Hawkesworth, Using geochemistry to map mantle flow beneath the Lau Basin, *Geology, 26*, 1019-1022, 1998.

UNAM Seismology Group, The September 1985 Michoacan earthquakes: Aftershock distribution and history of rupture, *Geophysical Research Letters, 13*, 573-576, 1986.

Ulmer, P., Partial melting in the mantle wedge - the role of H_2O in the genesis of mantle-derived "arc-related" magmas, *Physics of the Earth and Planetary Interiors, 127*, 215-232, 2001.

Ulmer, P. and V. Trommsdorff, Serpentine stability to mantle depths and subduction-related magmatism, *Science, 268*, 858-861, 1995.

Vacquier, V., J.G., Sclater, and C.E. Corry, Studies of the thermal state of the Earth. The 21st paper: Heat-flow, eastern Pacific, *Bulletin of the Earthquake Research Institute, University of Tokyo, 45*, 375-393, 1967.

Vacquier, V., S. Uyeda, M. Yasui, J. Sclater, C. Corry, and T. Watanabe, Heat flow measurements in the Northwestern Pacific, *Bulletin of the Earthquake Research Institute, University of Tokyo, 44*, 1519-1535, 1966.

Valdes, C.M., W.D. Mooney, S.K. Singh, R.P. Meyer, C. Lomnitz, J.H. Luetgert, C.E. Helsley, B.T.R. Lewis, and M. Mena, Crustal structure of Oaxaca, Mexico, from seismic refraction measurements, *Bulletin of the Seismological Society of America, 76*, 547-563, 1986.

van den Beukel, J. and R. Wortel, Temperatures and shear stresses in the upper part of a subduction zone, *Geophysical Research Letters, 14*, 1057-1060, 1987.

van der Lee, S. and G. Nolet, Upper mantle S velocity structure of North America, *Journal of Geophysical Research, 102*, 22,815-22,838, 1997.

van der Lee, S., D. James, and P. Silver, Upper mantle S velocity structure of central and western South America, *Journal of Geophysical Research, 106*, 30,821-30,834, 2001.

van Keken, P.E., B. Kiefer, and S.M. Peacock, High-resolution models of subduction zones: Implications for mineral dehydration reactions and the transport of water into the deep mantle, *Geochemistry Geophysics Geosystems, 3*(10), 1056, doi: 10.1029/2001GC000256, 2002.

Vergnolle, M., F. Pollitz, and E. Calais, Constraints on the viscosity of the continental crust and mantle from GPS measurements and postseismic deformation models in western Mongolia, *Journal of Geophysical Research, 108*(10), 2502, doi: 10.1029/2002JB002374, 2003.

Vinnik, L.P., L.I. Makeyeva, A. Milev, and A.Y. Usenko, Global patterns of azimuthal anisotropy and deformation in the continental mantle, *Geophysical Journal International, 111*, 433-447, 1992.

von Herzen, R., C. Ruppel, P. Molnar, M. Nettles, S. Nagihara, and G. Ekstrom, A constraint on the shear stress at the Pacific-Australian plate boundary from heat flow and seismicity at the Kermadec forearc, *Journal of Geophysical Research,* 106, 6817-6833, 2001.

Vrolijk, P., On the mechanical role of smectite in subduction zones, *Geology, 18*, 703-707, 1990.

Wang, C.Y., Sediment subduction and frictional sliding in a subduction zone, *Geology, 8*, 530-533, 1980.

Wang, K., Elastic and viscoelastic models of crustal deformation in subduction earthquake cycles, *In:* T. Dixon (Ed.), *Subduction zone seismogenic zones*, Columbia University Press, New York, manuscript in press, September 2004.

Wang, K. and E.E. Davis, Thermal effect of marine sedimentation in hydrothermally active areas, *Geophysical Journal International, 110*, 70-78, 1992.

Wang, K. and J. He, Mechanics of low-stress forearcs: Nankai and Cascadia, *Journal of Geophysical Research, 104*, 15,191-15,205, 1999.

Wang, K., R.D. Hyndman, and M. Yamano, Thermal regime of the southwest Japan subduction zone: Effects of age history of the subducting plate, *Tectonophysics, 248*, 53-69, 1995a.

Wang, K., T. Mulder, G.C. Rogers, and R.D. Hyndman, Case for very low coupling stress on the Cascadia subduction fault, *Journal of Geophysical Research, 100*, 12,907-12,918, 1995b.

Wang, K., R. Wells, S. Mazzotti, R.D. Hyndman, and T. Sagiya, A revised dislocation model of interseismic deformation of the Cascadia subduction zone, *Journal of Geophysical Research, 108*(1), 2009, doi:10.1029/2001JB001227, 2003.

Watanabe, T., M.G. Langseth, and R.N. Anderson, Heat flow in back-arc basins of the western Pacific, *In:* , M. Talwani and W.C. Pittman III (Eds.), *Island arcs, deep sea trenches and back-arc basins, Maurice Ewing Series 1*, American Geophysical Union, Washington DC, pp. 137-161, 1977.

Wheeler, J.O. and P. McFeely (Comp.), Tectonic assemblage map of the Canadian Cordillera and adjacent parts of the United States of America, Geological Survey of Canada, Map 1712A, scale: 1:2000000, 1991.

Wheeler, P. and N. White, Measuring dynamic topography: An analysis of Southeast Asia, *Tectonics, 21*(5), 1040, doi: 10.1029/2001TC900023, 2002.

Widiyantoro, S. and R. van der Hilst, Mantle structure beneath Indonesia inferred from high-resolution tomographic imaging, *Geophysical Journal International, 130*, 167-182, 1997.

Wiemer, S., G. Tytgat, M. Wyss, and U. Duenkel, Evidence for shear-wave anisotropy in the mantle wedge beneath south central Alaska, *Bulletin of the Seismological Society of America, 89*, 1313-1322, 1999.

Wiens, D.A. and G.P. Smith, Seismological constraints on structure and flow patterns within the mantle wedge, *In:* J. Eiler (Ed.), *Inside the Subduction Factory, AGU Monograph 138*, American Geophysical Union, Washington DC, pp. 59-81, 2003.

Wickens, A.J., The upper mantle of southern British Columbia, *Canadian Journal of Earth Sciences, 14*, 1100-1115, 1977.

Wolfe, C. and P.G. Silver, Seismic anisotropy of oceanic upper mantle: Shear wave splitting methodologies and observations, *Journal of Geophysical Research, 103*, 749-771, 1998.

Xie, J., Shear-wave splitting near Guam, *Physics of the Earth and Planetary Interiors, 72*, 211-219, 1992.

Xu, Y., M.E. Zimmerman, and D.L. Kohstedt, Deformation behaviour of partially molten mantle rocks, *In:* G.D. Karner, B. Taylor, N.W. Driscoll, and D.L. Kohlstedt (Eds.), *Rheology and deformation of the lithosphere and continental margins*, Columbia University Press, New York, pp. 284-310, 2004.

Yamano, M., Recent heat flow studies in and around Japan, *In:* M.L. Gupta and M. Yamano (Eds.), *Terrestrial heat flow and geothermal energy in Asia*, Oxford and IBH Publishing Co. Pvt. Ltd., Bombay, pp. 173-201, 1995.

Yang, X., K.M. Fischer, and G.A. Abers, Seismic anisotropy beneath the Shumagin Islands segment of the Aleutian-Alaska subduction zone, *Journal of Geophysical Research, 100*, 18,165-18,177, 1995.

Yuan, X., SV. Sobolev, and R. Kind, Moho topography in the central Andes and its geodynamic implications, *Earth and Planetary Science Letters, 199*, 389-402, 2002.

Yuen, D.A., L. Fleitout, G. Schubert, and C. Froidevaux, Shear deformation zones along major transform faults and subducting slabs, *Geophysical Journal of the Royal Astronomical Society, 54*, 93-119, 1978.

Zelt, C.A. and D.J. White, Crustal structure and tectonics of the southeastern Canadian Cordillera, *Journal of Geophysical Research, 100*, 24,255-24,273, 1995.

Zhang, S. and S. Karato, Lattice preferred orientation of olivine aggregates deformed in simple shear, *Nature, 375*, 774-777, 1995.

Zhang, Z. and S.Y. Schwartz, Depth distribution of moment release in underthrusting earthquakes at subduction zones, *Journal of Geophysical Research, 97*, 537-544, 1992.

Zhao, D., Seismological structure of subduction zones and its implications for arc magmatism and dynamics, *Physics of the Earth and Planetary Interiors, 127*, 197-214, 2001.

Zhao, D., D. Christensen, and H. Pulpan, Tomographic imaging of the Alaska subduction zone, *Journal of Geophysical Research, 100*, 6487-6504, 1995.

Ziagos, J.P., D.D. Blackwell, and F. Mooser, Heat flow in southern Mexico and the thermal effects of subduction, *Journal of Geophysical Research, 90*, 5410-5420, 1985.

Zimmerman, M.E. and D.L. Kohlstedt, Rheological properties of partially molten lherzolite, *Journal of Petrology, 45*, 275-298, 2004.

Zoth, G. and R. Haenel, Appendix: Thermal Conductivity, *In:* R. Haenel, L. Rybach, and L. Stegena (Eds.), *Handbook of Terrestrial Heat-flow Density Determination*, Kluwer, Dordrecht, pp. 449-466, 1988.

APPENDIX A

Benchmark Models for a Sheared Box

A.1 Model Description

The first set of benchmarks examines flow in a viscous rectangular box, driven by horizontal movement of the upper boundary. These models are used to examine the velocity boundary conditions along the vertical boundaries of the box and to understand the effects of variations in rheology and viscous dissipation on the velocity and thermal fields.

The finite element mesh and boundary conditions are shown in **Figure A.1**. The box has a width of 200 km and a height of 100 km. The lower boundary of the box is stationary, while the upper boundary moves at a constant horizontal velocity of 10 cm/yr to the right. This induces flow within the interior of the box. Material is allowed to enter the box through the left-hand boundary and exit at the right-hand boundary. A pressure of 0 GPa is assigned at the upper right-hand corner of the box. The upper and lower boundaries are prescribed temperatures of 300°C and 1300°C, respectively. These temperatures were chosen because the effective viscosity of upper mantle minerals varies most rapidly over this temperature range (e.g., **Figure 6.2**) and these temperatures are similar to those in the upper part of the mantle wedge in the subduction zone models. Temperatures along the inflow (left) boundary are assigned temperatures corresponding to a geotherm that has a temperature of 300°C at the top of the box and a linear thermal gradient of 10°C/km. The right-hand boundary uses the outflow thermal boundary condition:

$$\nabla T \cdot \mathbf{v} = 0 \qquad \text{(A.1)}$$

where T is the temperature and **v** is the velocity field. The entire model domain has a thermal conductivity of 3.0 W m^{-1} K^{-1}, a density of 3300 kg/m^3, and a heat capacity of 1250 J kg^{-1} K^{-1}. There are no internal heat sources except viscous dissipation.

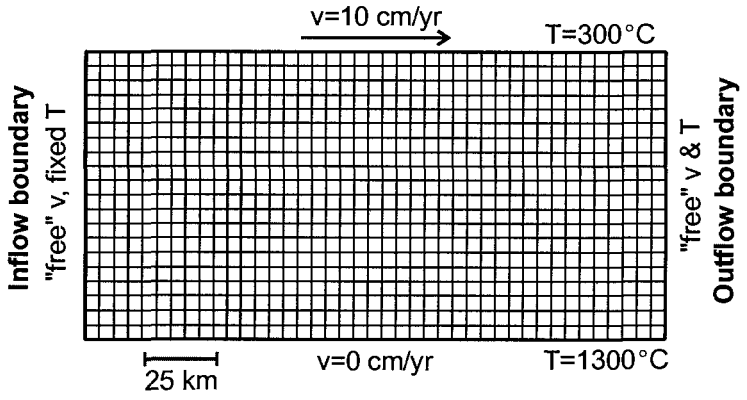

Figure A.1. The finite element mesh used for the sheared viscous box models. The model domain is 200 km wide and 100 km high. The velocity and temperature boundary conditions used on each boundary are indicated.

A.2 Velocity boundary conditions

The first tests study the effect of velocity boundary conditions along the left and right vertical boundaries of the box. In the models, the velocity along the vertical boundaries is "free". Two options for a free velocity boundary are to assume: 1) no velocity gradient across the boundary, or 2) no stress on the boundary. For this test, the box has a constant viscosity ($\eta=10^{21}$ Pa s). With a constant viscosity, flow is independent of the temperature field.

The first boundary condition assumes no velocity gradient perpendicular to the vertical boundaries:

$$\frac{\partial v_x}{\partial x} = 0 \quad \text{and} \quad \frac{\partial v_z}{\partial x} = 0 \tag{A.2}$$

With this boundary condition, flow lines within the box are everywhere parallel to the upper and lower boundaries of the box (**Figure A.2a**). Velocity vectors are horizontal, with magnitudes that linearly decrease from 10 cm/yr at the top of the box to 0 cm/yr at the base. Although this is a two-dimensional model, the flow field in the box is one-dimensional (varies only in the vertical direction), and the location of the vertical boundaries does not affect the flow field at any point in the box. This flow pattern is also called Couette flow. Note that with this boundary condition, there is a velocity gradient *along* the two vertical boundaries $(\partial v_x/\partial z \neq 0)$, indicating that the shear stress along these boundaries is not zero.

The other option for a "free" velocity boundary is a stress-free boundary condition:

$$\boldsymbol{\sigma}' - \mathbf{PI} = \mathbf{0} \tag{A.3}$$

where $\boldsymbol{\sigma}'$ is the deviatoric stress tensor and P is the dynamic pressure. For a vertical boundary, this can be rewritten in terms of the effective viscosity and velocity gradients (using **Equations 6.12 and 6.13**) as:

$$2\eta\frac{\partial v_x}{\partial x} - P = 0 \tag{A.4a}$$

and

$$\eta\left(\frac{\partial v_x}{\partial z} + \frac{\partial v_z}{\partial x}\right) = 0 \tag{A.4b}$$

where the first equation is the normal stress and the second equation is the shear stress on the vertical boundary.

Figure A.2b shows the resulting velocity field in the viscous box. The flow vectors near the inflow and outflow boundaries have a vertical component. This is due to the requirement that there be no stress on the vertical boundary; flow near the boundaries

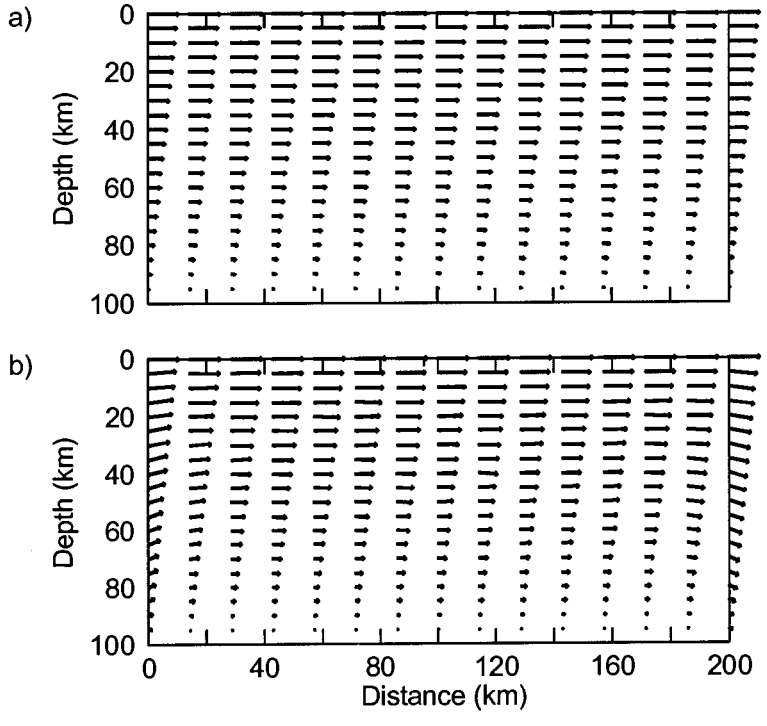

Figure A.2. The effect of the vertical boundary conditions on the velocity within the sheared box. a) No velocity gradient across the vertical boundaries. b) Stress-free boundaries. The vectors at the top of the box are 10 cm/yr.

must have a vertical component to compensate for the horizontal shearing induced by movement of the upper boundary. The effects of the boundary conditions are confined to within ~30 km of the boundaries. In the middle of the box, the flow field is approximately that of 1-D Couette flow. Due to the strong effects of the "no stress" condition on the velocity field near the boundaries, the preferred boundary condition for the viscous box models is "no velocity gradient". This boundary condition is used in the models below.

A.3 Rheology

The next series of tests examines the effect of rheology on viscous flow within the sheared box. Viscous dissipation is not included in the temperature calculations for these models. First, three models with a constant viscosity of 10^{20}, 10^{21} and 3×10^{21} Pa s are used. These viscosities span the range over which viscous dissipation becomes important (see next section). **Figure A.3a** shows the velocity, strain rate, effective viscosity, viscous dissipation and temperature as a function of depth (arbitrarily taken at x=100 km). In all cases, the flow field is identical to that in **Figure A.2a**. The velocity linearly decreases from 10 cm/yr at the upper boundary to 0 cm/yr at the lower boundary, producing a constant strain rate of 1.58×10^{-14} s^{-1} throughout the box. The amount of viscous dissipation depends on the strain rate and the effective viscosity (**Equation 6.17**), and thus models with the higher viscosity have a higher dissipation. Since viscous dissipation was not included as a heat source in the thermal calculations, the temperature profile shows a linear increase from 300°C at top of the box to 1300°C at the base for all three models.

The second group of models uses the hypothetical Newtonian rheologies in **Table 6.1**. With this rheology, the effective viscosity decreases with increasing temperature. This affects the flow pattern because shear will be concentrated in regions with a low effective viscosity. For the viscous box, deformation becomes localized near the base of the box, due to the high temperatures here (**Figure A.3b**). This is illustrated by the large vertical strain rates in the lower 20 km of the box. Note that the total (integrated) strain

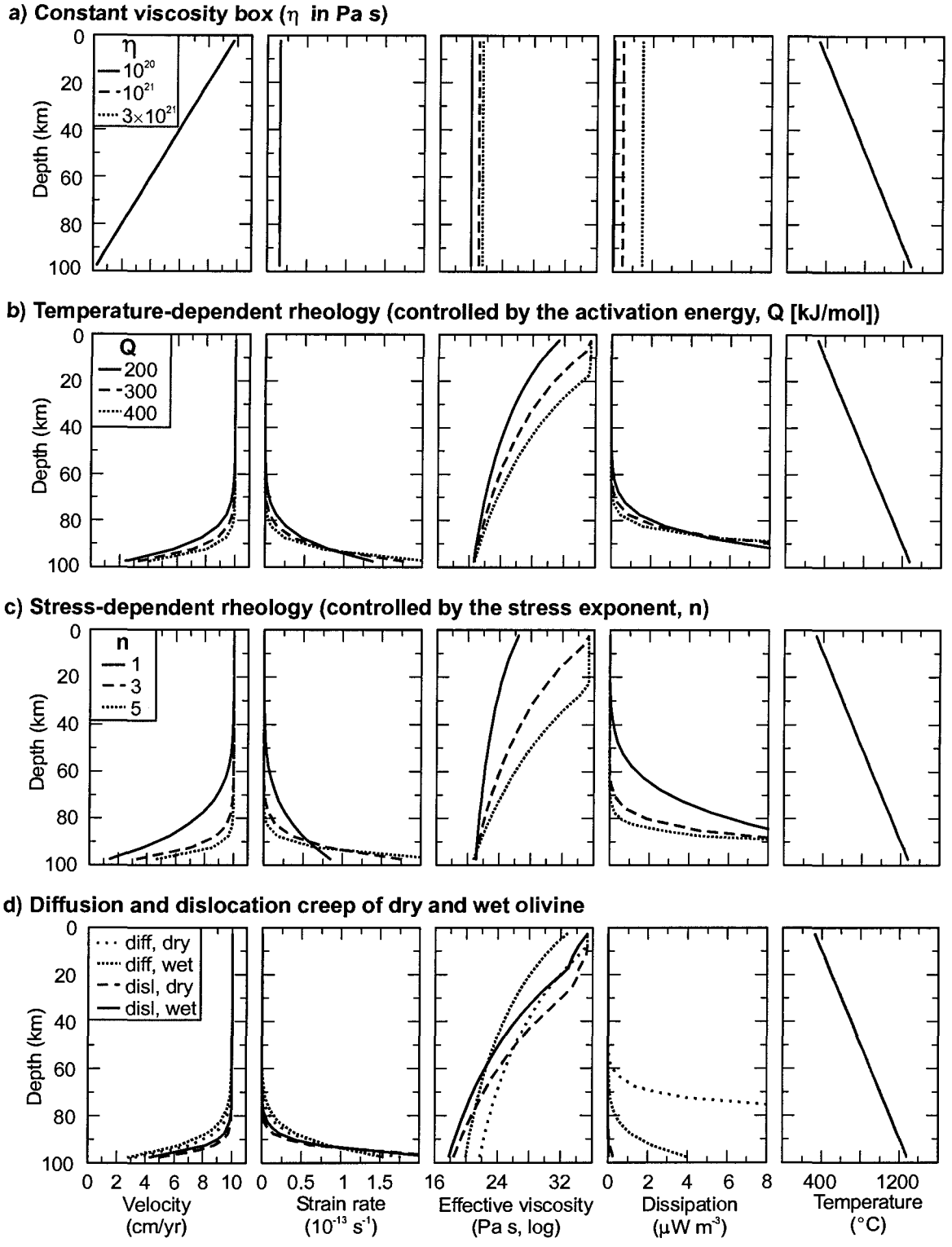

Figure A.3. Sheared box models with a) isoviscous, b) temperature-dependent, and c) stress-dependent rheology (with a weak temperature-dependence). d) Models with diffusion (diff) and dislocation (disl) creep of dry and wet olivine from laboratory data [*Karato and Wu*, 1993]. For each rheology, the velocity, strain rate, effective viscosity, viscous dissipation and temperature as a function of depth at x=100 km are shown. Viscous dissipation is not included as a heat source, and thus the temperature field is identical for all models.

rate is equal to that of the isoviscous box. The strain localization is stronger for rheologies with a larger temperature-dependence (higher Q). The high strain rates in the lower part of the box, as well as the high effective viscosity, result in significant viscous dissipation at depths greater than 80 km.

Next, the effect of a stress-dependent rheology was examined, using a hypothetical power law rheology with only a small temperature-dependence (**Table 6.1**). With no temperature-dependence (Q=0 J/mol), the entire box would experience a strain rate of 1.58×10^{-14} s^{-1}, resulting in a constant effective viscosity for the whole box, and the flow field would be that of Couette flow. Thus, a weak temperature-dependence was included , corresponding to a Q/n ratio of 100000 J/mol for the hypothetical rheologies (with n = 1, 3 and 5). With this small temperature-dependence, flow is localized in the high temperature regions near the base of the box. As the stress-dependence increases (higher n), the strain localization becomes stronger (**Figure A.3c**). Note that for n=1, the strain localization is much less than that for the Newtonian rheologies in **Figure A.3b**, due to the weaker temperature-dependence (Q=100000 J/mol). The high strain rates, combined with high effective viscosities, result in large amounts of viscous dissipation in the lower part of the box.

In the fourth test, realistic rheologies for the upper mantle are investigated, using the rheological parameters from laboratory experiments of *Karato and Wu* [1993] (**Table 6.1**). These parameters represent diffusion and dislocation creep of dry and water-saturated (wet) olivine. The strong temperature-dependence of all four rheologies results in a localization of strain near the base of the box (**Figure A.3d**). The dislocation creep rheologies show slightly more localization, due to the combined effects of temperature and stress. The effective viscosity of the diffusion creep rheologies is larger than that of dislocation creep, resulting in greater viscous dissipation, especially for diffusion creep of dry olivine. The other upper mantle rheologies given in **Table 6.1** give similar results (not shown), due to the similarities in the rheological parameters (e.g., **Figure 6.2**).

A.4 Viscous Dissipation

As a final test, viscous dissipation was included as a heat source in the models described in the previous section. For the isoviscous models, the entire box experiences a strain rate of 1.58×10^{-14} s^{-1} and thus, the amount of viscous dissipation is directly proportional to the viscosity of the box. With viscous dissipation, the temperatures within the box are elevated, particularly for models with a higher viscosity, but the flow field is unchanged (**Figure A.4a**). For the above strain rate, viscous dissipation has a negligible effect on the thermal field for a viscosity of 10^{20} Pa s (or less). However, for viscosities greater than 10^{21} Pa s, viscous dissipation results in significantly increased temperatures in the box.

For a Newtonian or power law rheology, the effective viscosity is strongly dependent on temperature, leading to a localization of strain near the base of the box. The high strain rates result in significant viscous dissipation, increasing the temperatures in the lower part of the box. As the temperature increases, the effective viscosity decreases, further localizing the strain but decreasing the amount of viscous dissipation. Thus, viscous dissipation becomes a self-defeating mechanism for generating a substantial amount of heat. This feedback effect is illustrated for models that use the hypothetical Newtonian rheologies (**Figure A.4b**). Strain is localized in a slightly narrower region than in the models with no dissipation. In addition, the region with greatest strain is ~10 km above the base of the box, corresponding to the region of highest temperature. As the temperature-dependence of the rheology increases, the width of the shear zone becomes narrower. In all three cases, the amount of viscous dissipation is fairly small (<4 $\mu W\ m^{-3}$) and is concentrated within the narrow shear zone. There is only a minor increase in temperature within the box compared to models with no dissipation.

For the hypothetical power law rheologies, the inclusion of viscous dissipation produces a stronger strain localization, due to the combined effects of the high strain rates and temperature on the effective viscosity (**Figure A.4c**). As the stress-dependence increases, strain localization is enhanced, and the shear zone is further from the

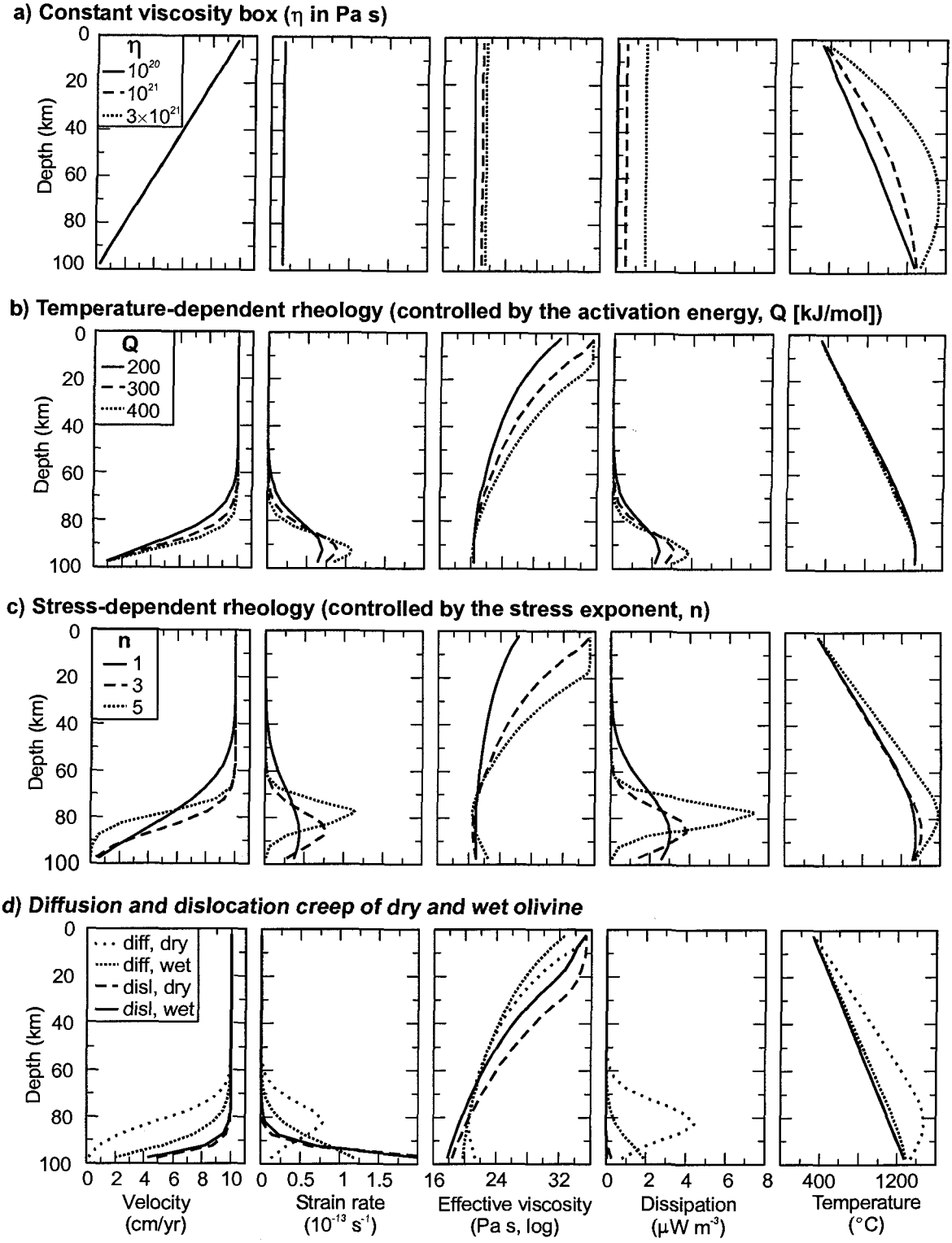

Figure A.4. Sheared box models with a) isoviscous, b) temperature-dependent, and c) stress-dependent rheology (with a weak temperature-dependence). d) Models with diffusion (diff) and dislocation (disl) creep of dry and wet olivine from laboratory data [*Karato and Wu*, 1993]. For each rheology, the velocity, strain rate, effective viscosity, viscous dissipation and temperature as a function of depth at x=100 km are shown. Viscous dissipation is included in the models.

base of the box. The amount of viscous dissipation is increases as the stress-dependence increases. With the largest stress-dependence (n=5), temperatures in the lower part of the box are increased by up to 300°C relative to those no dissipation.

For diffusion creep of dry olivine, the effective viscosity is fairly large, even at high temperatures (e.g., **Figure 6.2**). Thus, the inclusion of viscous dissipation results in a stronger strain localization, and higher temperatures in the lower part of the box (**Figure A.4d**). Viscous dissipation has little effect on diffusion creep of wet olivine, or dislocation creep of wet or dry olivine, as all have a low effective viscosity ($<10^{20}$ Pa) over the range of strain rates and temperatures in the model (**Figure A.4d**). For the majority of laboratory-derived upper mantle rheologies (e.g., **Table 6.1**), the inclusion of viscous dissipation leads to a slightly stronger strain localization, but does not have a large effect on the temperature field. In general, for the expected strain rates for asthenosphere processes (10^{-14} to 10^{-13} s^{-1}), viscous dissipation becomes a significant heat source (>0.1 $\mu W\ m^{-3}$) if the effective viscosity is greater than 10^{20} Pa.

APPENDIX B
Benchmarks for Subduction Zone Models

B.1 Model Description

The second set of benchmark models uses a subduction geometry to examine the numerical modelling approach used in subduction zone models that include viscous flow in the mantle wedge. In these types of models, the geometry and plate motions of the subducting and over-riding plate are prescribed, and viscous flow in the mantle wedge is calculated numerically. The benchmark models were developed after the MARGINS workshop on subduction zone thermal modelling (University of Michigan, October 2002). A more detailed description of the benchmarks can be found at www.geo.lsa.umich.edu/~keken~subduction02.html. These models are part of a benchmarking exercise involving modelling groups from the University of Michigan, Pacific Geoscience Centre/University of Victoria, Purdue Universty, Brown University, and the California Institute of Technology [*van Keken et al.*, manuscript in preparation, 2004].

The model geometry is shown in **Figure B.1**. The computational domain is 660 km wide and 600 km high. In the models, a straight plate with a constant dip of 45° subducts at 5 cm/yr below a 50 km thick rigid over-riding plate. Velocities are prescribed to both the subducting slab (5 cm/yr in the subduction direction) and over-riding plate (0 cm/yr). Flow within the viscous wedge (i.e., the region between the slab and over-riding plate) is driven by viscous coupling with the subducting plate. Thermal buoyancy forces are not included in the models.

With this geometry, there is a numerical singularity that occurs at the point where the subducting slab, stationary over-riding plate, and mantle wedge intersect (the tip of the mantle wedge). At this point, the pressure approaches infinity, due to the discontinuity in the velocity boundary conditions. One of the objectives of the

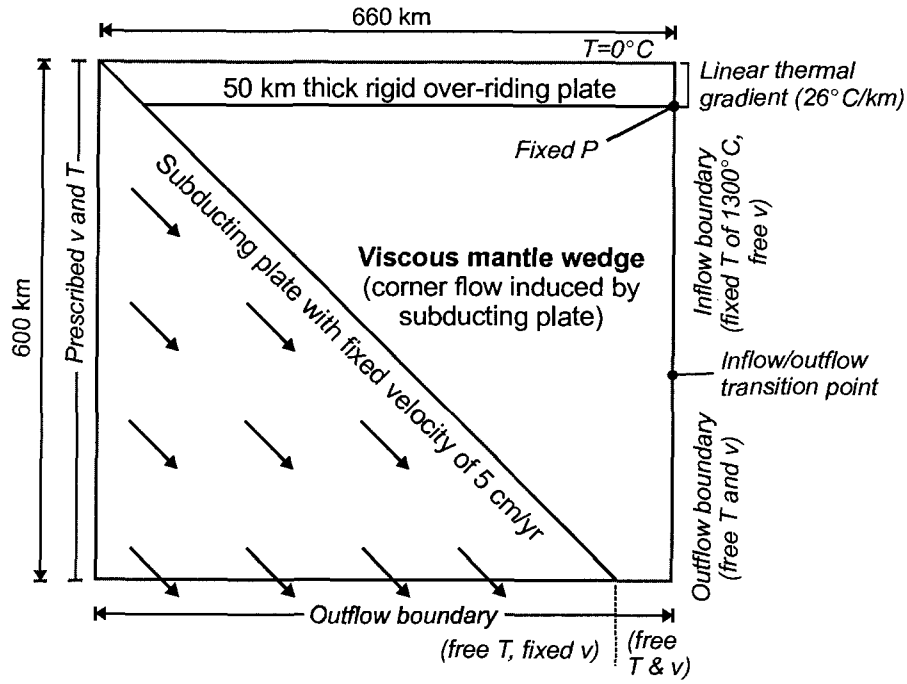

Figure B.1. Geometry and boundary conditions for the subduction zone benchmark models. Viscous flow in the mantle wedge is driven by traction along the top of a slab that is subducting at a rate of 5 cm/yr. See text for details of the thermal and velocity boundary conditions.

benchmarking exercise is to examine how the numerical modelling code handles the near-singularity behaviour of the flow field.

The finite element mesh is shown in **Figure B.2**. There are a total of 10100 elements (40805 temperature/velocity nodes) in the model, with 4880 elements (19845 temperature/velocity nodes and 5043 pressure nodes) in the viscous wedge. A variable element spacing is used, with element sizes from 0.001 m to 40 km. The highest node density is in areas with large thermal and pressure gradients, e.g., near the top of the subducting slab and at the tip of the mantle wedge. To deal with the numerical singularity at the wedge tip and to aid in grid construction, an artificial vertical boundary in the mantle wedge is placed 1 m landward of the tip, resulting in a 1 m long "seaward boundary" for the wedge. Viscous flow is only calculated in the area landward (to the right) of this boundary. Even 1 m away from the wedge tip, the pressure gradients are extremely large. In addition, the velocity discontinuity in boundary conditions on the top of the slab remains. In the numerical model, the boundary conditions along the top of the

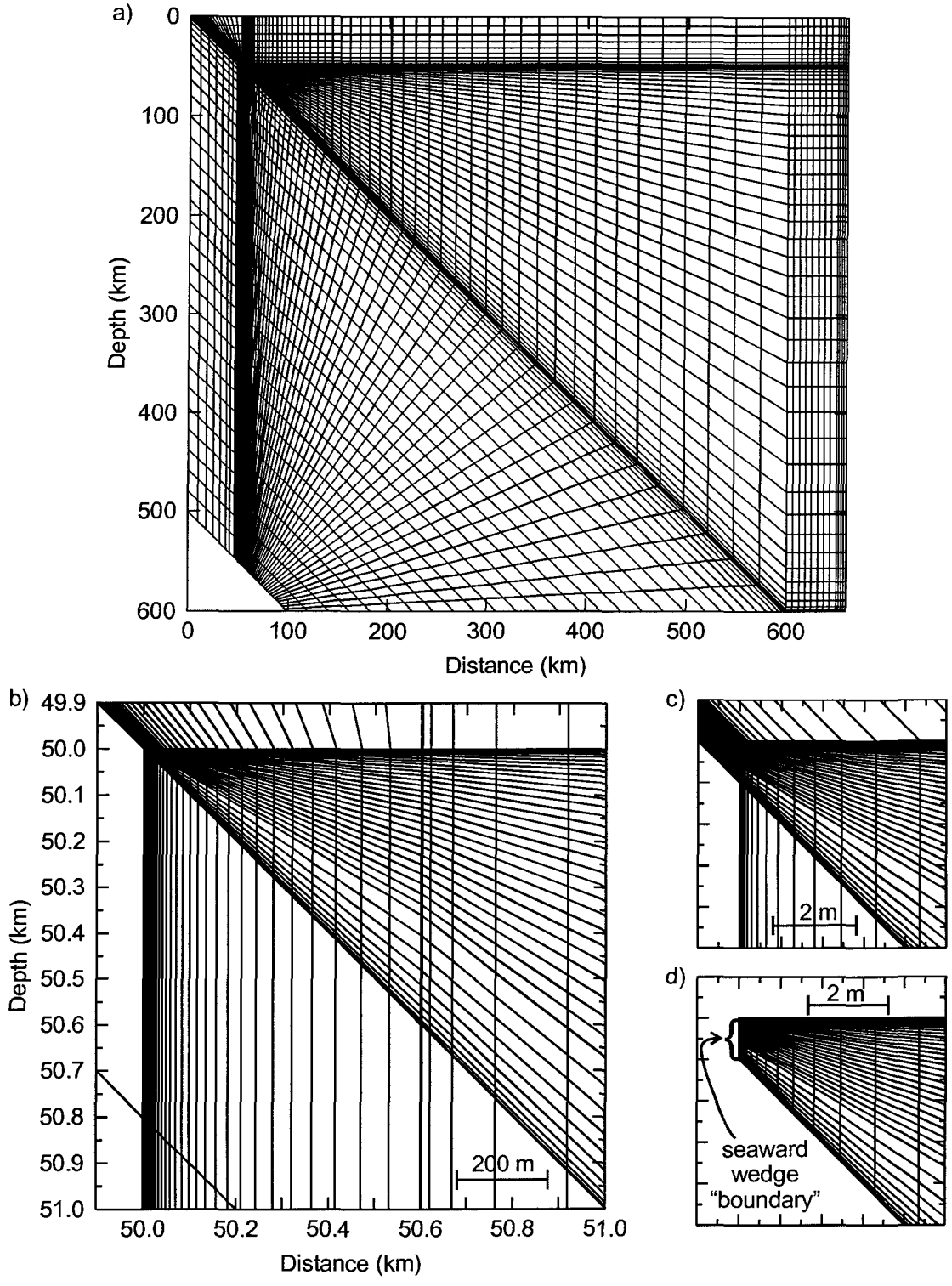

Figure B.2. Finite element mesh for subduction zone benchmark models: a) full mesh, b) close-up of the wedge corner region, c) mesh used for temperature calculation, d) mesh used for flow calculation. The seaward wedge "boundary" is an artificial vertical boundary located 1 m landward of the wedge tip.

slab are applied so that the velocity increases from 0 cm/yr at the artificial vertical boundary to the full subduction rate (5 cm/yr) over the width of one element. To accurately model the near-singularity behaviour, a very high node density is used in this area, with element sizes of ~0.001 m.

The entire model space has a density of 3300 kg/m^3, thermal conductivity of 3.0 W m^{-1} K^{-1}, and heat capacity of 1250 J kg^{-1} K^{-1}. The upper boundary of the model has a constant temperature of 0°C. At the slab inflow boundary (x=0 km), the temperature (T) as a function of depth (z) is calculated using the standard half-space (error function) cooling model for 50 my old lithosphere [e.g., *Turcotte and Schubert*, 2002]:

$$T(z) = T_S + (T_M - T_S) \times \mathrm{erf}\left(\frac{z}{2\sqrt{\kappa t}}\right) \qquad \text{(B.1)}$$

where T_S is the surface temperature (273 K), T_M is the mantle temperature (1573 K), κ is the thermal diffusivity (0.73×10^{-6} m^2/s using the values for density, thermal conductivity and heat capacity given above), and t is the age of the lithosphere in seconds (1.58×10^{15} s for 50 my lithosphere). Note that the absolute temperature is used in this equation.

The temperature of the over-riding plate along the right boundary (x=660 km) increases linearly from 0°C at the surface to 1300°C at 50 km depth. Below this, the inflow boundary of the wedge has a constant temperature of 1300°C. The position of the inflow-outflow transition is determined within the modelling code. For the outflow boundaries, there is assumed to be no conductive heat flow across the boundary parallel to flow lines (i.e., **Equation A.1**). Neither radiogenic heat sources nor viscous dissipation are included in the models.

It is necessary to specify a pressure at one point in the wedge. The point is arbitrarily chosen along the wedge inflow boundary, at the interface between the over-riding plate and wedge (i.e., x=660 km, z=50 km). In the models below, a fixed pressure of 0 GPa is used, unless otherwise stated. The right-hand and bottom boundaries of the wedge are open such that material can flow through them.

B.2 Constant viscosity wedge

For subduction zone models that have a subducting slab with a constant plate dip and a constant mantle viscosity, there is an analytic solution for the pressure and velocity field in the mantle wedge [*Batchelor*, 1967; see also *McKenzie*, 1969 and *Turcotte and Schubert*, 2002]. **Figure B.3** shows the analytic solution for the isoviscous subduction benchmark models. Also shown are the temperature field and surface heat flow, calculated using the analytic flow velocities for the wedge. This model is used for comparison with isoviscous models where wedge flow is calculated numerically.

The first numerical isoviscous model is designed to reproduce the analytic solution. For this purpose, velocities are prescribed on all boundaries of the viscous

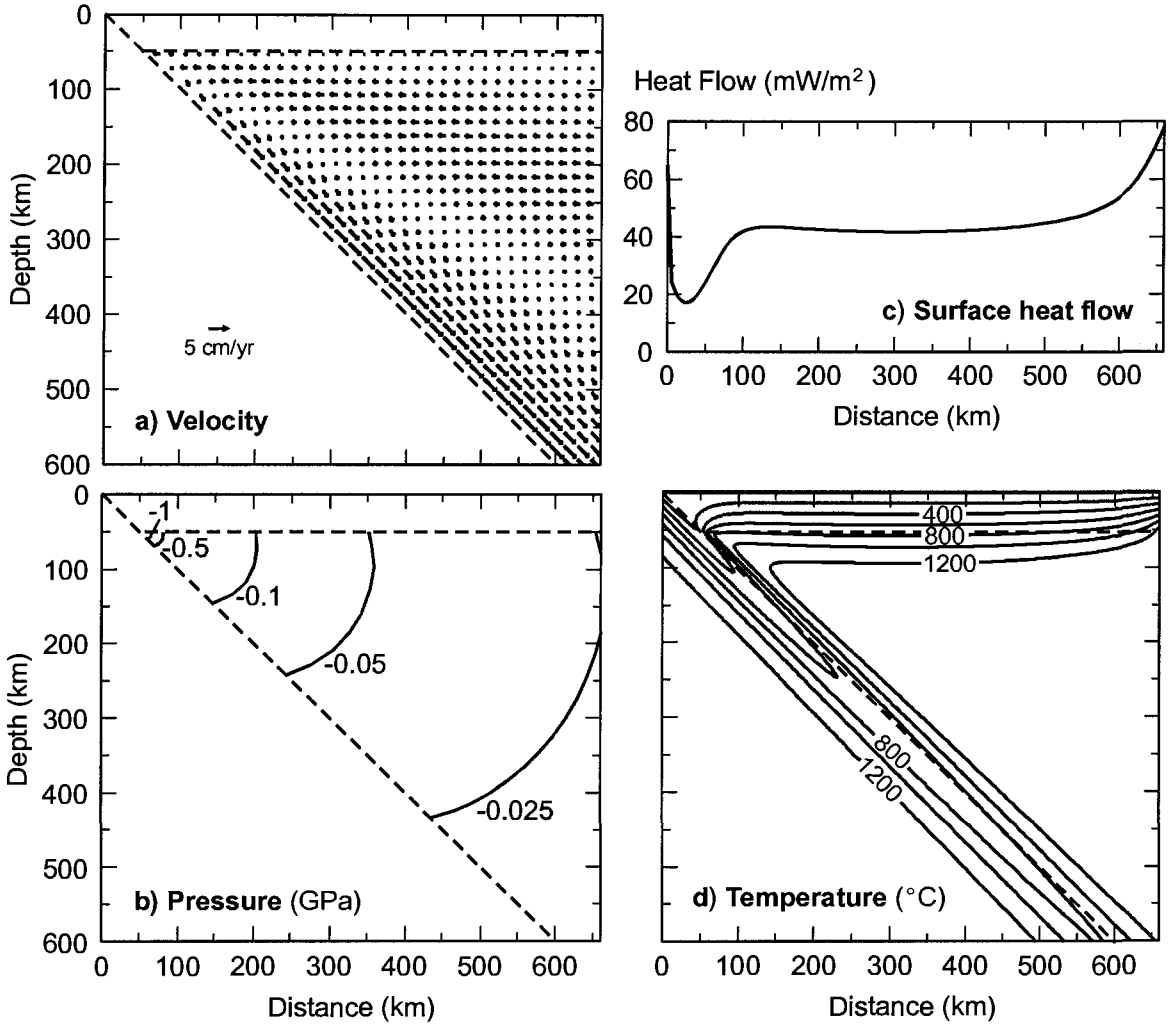

Figure B.3. Analytic corner flow solution for a) velocity and b) pressure for an isoviscous mantle wedge. c) Surface heat flow and d) thermal structure (200°C temperature contours) calculated from the analytic velocity field and prescribed thermal boundary conditions.

wedge. The top boundary has a velocity of 0 cm/yr, the slab-wedge boundary has a velocity of 5 cm/yr (the subduction velocity), and the inflow/outflow and "seaward" wedge boundaries are prescribed the velocities given by the analytic solution. The prescribed pressure at (660, 50) is -0.0247 GPa (the analytic value for pressure at this point). Given these boundary conditions, the velocity field in the interior of the wedge is calculated numerically. **Figure B.4** shows the difference in velocity and pressure between the numerical solution and analytic model. The pressure differences are shown as percentages due to the large range in pressure values (e.g., **Figure B.3b**). The average difference in velocity is 1.3×10^{-4} cm/yr, with a maximum difference of 2.58×10^{-3} cm/yr near the tip of the wedge. The largest differences are near the wedge tip due to the large pressure gradient in this region. The velocity differences at x=600 km result from a slight numerical instability from a sharp change in element size. The numerical solution has matched the analytic pressure gradient extremely well, including the very large pressure gradient near the tip of the wedge. The absolute value of pressure depends on the prescribed pressure at (660, 50). With the analytic value of –0.0247 GPa, the average pressure difference between the numerical and analytic solutions is 0.31%, with a maximum difference of 1.18% near the tip of the wedge. If instead a pressure of 0 GPa is used, the numerical model pressures are 0.0247 GPa larger than the analytic values, but

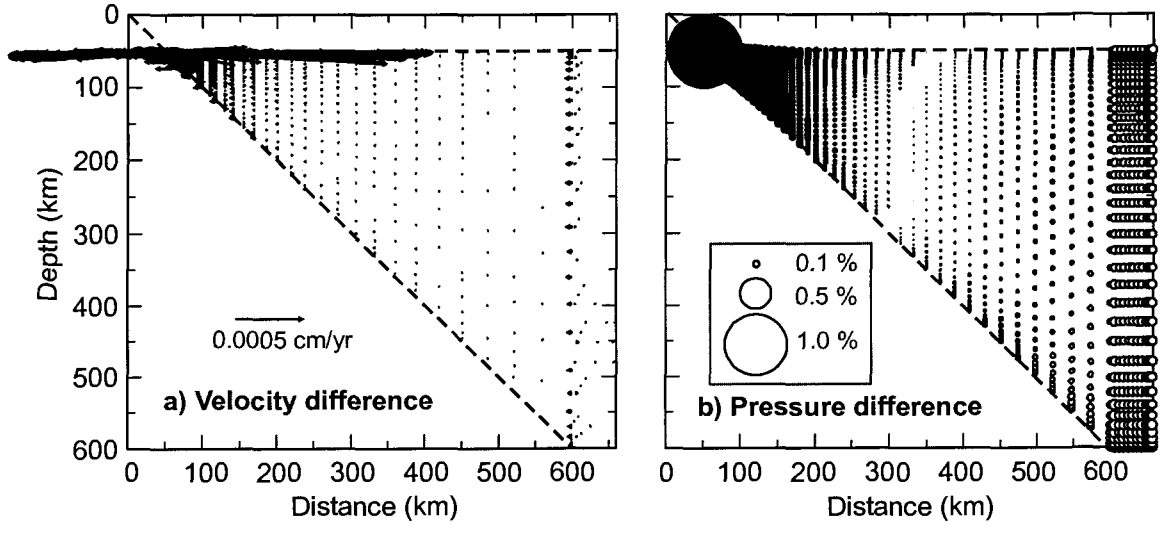

Figure B.4. Difference between the first numerical model (see text for description) and the analytic solution for isoviscous corner flow. a) Velocity differences in cm/yr. b) Percentage difference in pressure. Open symbols indicate that the absolute value of pressure for the numerical model is larger than the analytic pressure; solid symbols indicate the absolute value of the analytic pressure is larger.

the pressure gradient (and velocity field) is not affected. The small velocity and pressure differences between the numerical and analytic models have a negligible effect on the resulting thermal structure. The average temperature difference between the two models is 5.8×10^{-5} °C, with a maximum difference of 9.8×10^{-4} °C.

In the next numerical isoviscous model, the velocities on the inflow/outflow boundaries of the wedge are "free". Two different boundary conditions are tested: 1) a "no velocity gradient" condition, and 2) a "stress-free" condition (see **Appendix A** for details). In these models, a velocity of 0 cm/yr is prescribed along the "seaward boundary" of the wedge, and a pressure of 0 GPa is assigned at the point (660, 50).

Figure B.5 shows the results for models with a "no velocity gradient" boundary condition. Fairly large velocity differences between the analytic solution and numerical model are found near the inflow/outflow boundary, where the numerical solution gives larger velocities. These differences arise due to the combined effects of the velocity boundary conditions and edge effects from the subducting slab. The analytic solution assumes an infinitely long slab. In the numerical model, traction on the wedge is only applied along the finite length of the slab, and thus the distribution of forces on the wedge is slightly different. There are also large velocity and pressure differences near the wedge tip, because of the prescribed velocity of 0 cm/yr along the "seaward" wedge boundary in the dynamic model. These are confined to within 5 m of the wedge corner (and are not shown on **Figure B.5** where only the velocity and pressure differences more than 5 m from the corner are given). The average difference between the numerical and analytic model is 0.10 cm/yr for velocity (maximum of 4.89 cm/yr in wedge tip), 4.0% for pressure (maximum of ~3550% in wedge tip), and 0.9°C for temperature (maximum of 28.6°C near the point (600,50). Note that to calculate the pressure differences, a pressure of 0.0247 GPa is subtracted from the numerical model, so that the absolute value of pressure at the point (660, 50) is the same as that of the analytic model. The flow field in the wedge depends only on the pressure gradient, not the absolute value of pressure.

Figure B.6 shows the results for models with "stress free" boundary conditions. With these boundary conditions, flow toward the bottom boundary of the model becomes

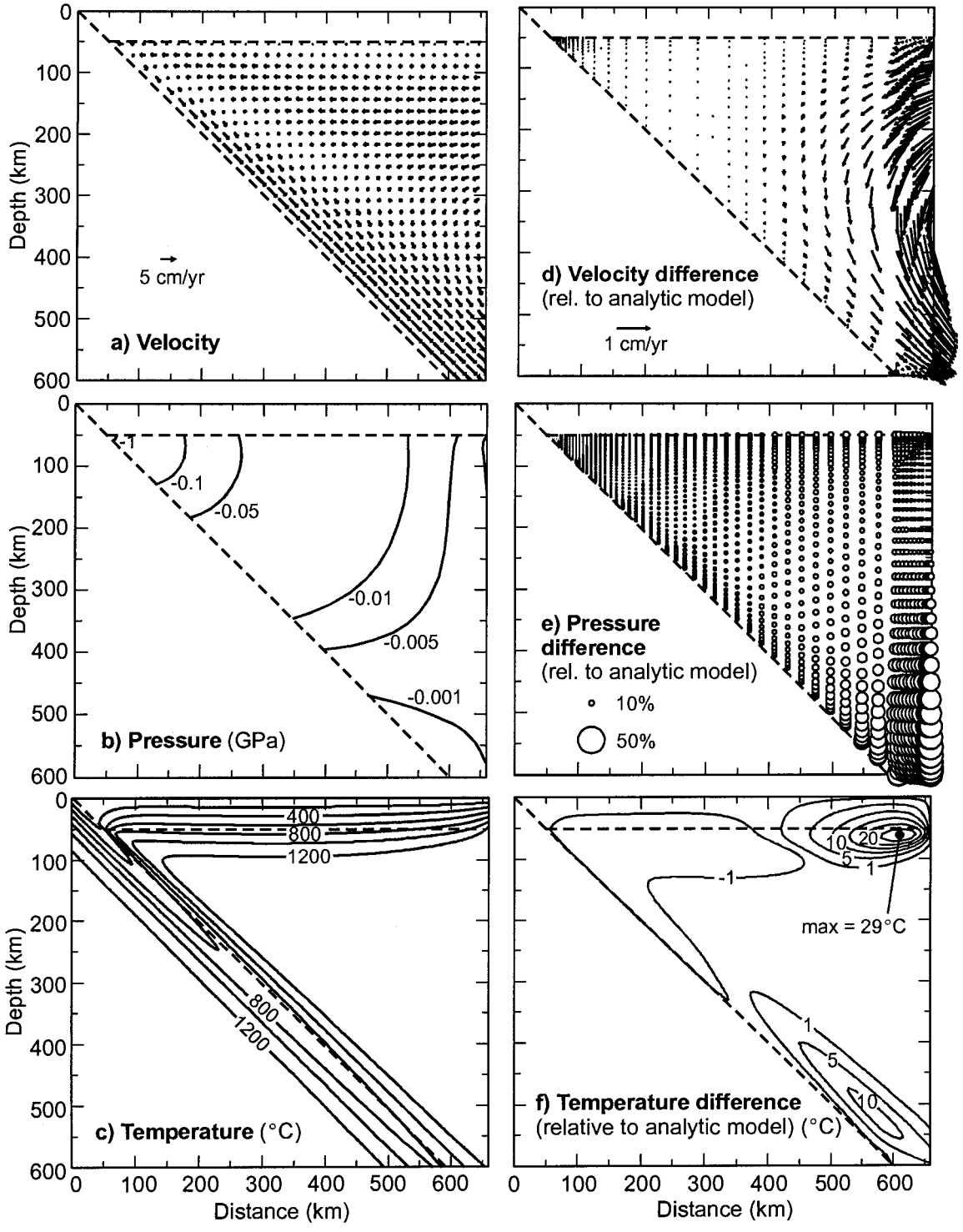

Figure B.5. Benchmark model for an isoviscous mantle wedge with a "no velocity gradient" boundary condition along the open wedge boundary: a) velocity, b) pressure, and c) temperature. These results are compared to the analytic corner flow model (Figure B.3). d) Velocity difference - only vectors more than 5 m from the wedge tip are shown (maximum difference in wedge tip is 4.89 cm/yr). e) Pressure difference (symbols as in Figure B.4). Only values more than 5 m from the wedge tip are shown (maximum difference in the wedge tip is ~3550%). f) Temperature difference.

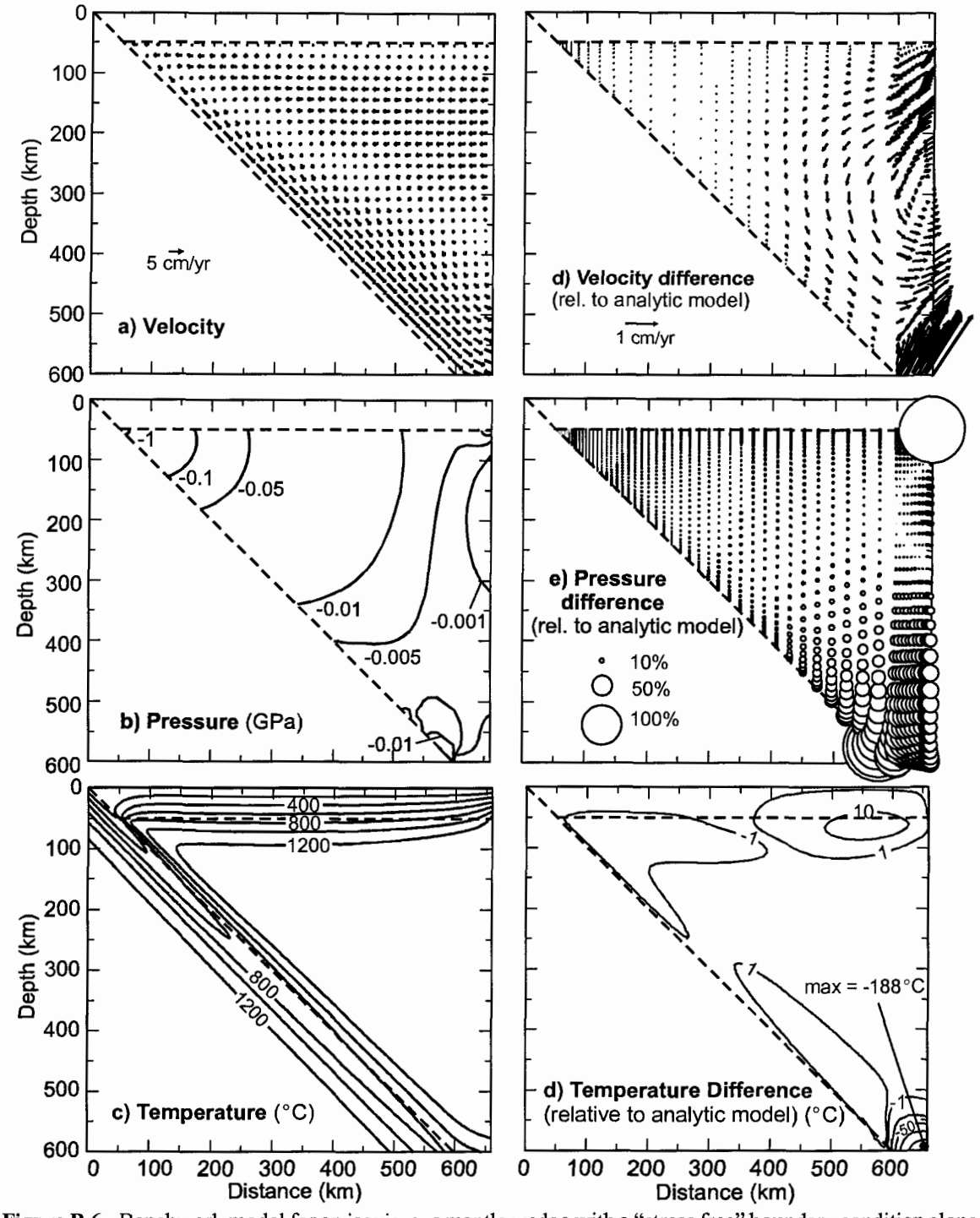

Figure B.6. Benchmark model for an isoviscous mantle wedge with a "stress free" boundary condition along the open wedge boundary: a) velocity, b) pressure, and c) temperature. These results are compared to the analytic corner flow model (Figure B.3). d) Velocity difference - only vectors more than 5 m from the wedge tip are shown (maximum difference in wedge tip is 4.80 cm/yr). e) Pressure difference (symbols as in Figure B.4). Only values more than 5 m from the wedge tip are shown (maximum difference in the wedge tip is ~3600%). f) Temperature difference.

sub-horizontal as it nears the boundary and a large negative pressure is generated at the point where the slab exits the bottom boundary. This results in cooler temperatures in the bottom righthand part of the wedge. The average difference between this model and the analytic solution is 0.09 cm/yr for velocity (maximum of 4.80 cm/yr in the wedge tip), 4.6% for pressure (maximum of ~3600% in the wedge tip; note that 0.0247 GPa is subtracted from the numerical model for the difference calculations, as above), and -0.6°C for temperature (maximum of -187.8°C in the lower right-hand corner of the wedge). With these boundary conditions, the wedge is slightly cooler than the analytic solution. Additional tests show that if the model width is increased (without increasing the depth of the model), an eddy develops in the wedge, where flow lines from near the slab surface follow a sub-horizontal trajectory along the bottom boundary and are then deflected upward and turn toward the wedge corner, without exiting the model domain. This causes the wedge to become even cooler than the analytic solution.

Overall, the numerical solution for isoviscous mantle wedge flow obtained using the PGC modelling code is in excellent agreement with the analytic corner flow solution. Of key importance is the accuracy to which the PGC modelling code can reproduce the analytic pressure gradient, especially near the theoretical singularity at the wedge tip.

B.3 Variable Mantle Rheology

The second group of subduction zone benchmarks investigates the effects of a variable mantle wedge viscosity, using Newtonian and power law rheologies. For both rheologies, the mantle viscosity is temperature-dependent, and thus, the flow field is coupled to the thermal field, making the problem highly non-linear. For a power law rheology, the viscosity also depends on stress (or strain rate).

Due to the non-linearity of the problem, benchmark exercises are critical to ensure accuracy and stability of the numerical modelling code. For non-linear (i.e., temperature-dependent) mantle rheologies, there is no analytic solution for corner flow with which to compare the numerical results. Thus, two approaches for testing the numerical modelling code are: 1) compare the output for finite element meshes with a different node density, using the same numerical modelling program, and 2) compare the output from different

numerical modelling programs. For the benchmark tests, the second approach is used, where the results from the PGC modelling code are compared with those obtained by other modelling groups.

In the benchmark models, the velocity at the top of the wedge is 0 cm/yr and the velocity at the slab/wedge interface is 5 cm/yr. Along the "seaward wedge boundary" a velocity of 0 cm/yr is prescribed. Along the inflow/outflow boundaries, velocities are free and a "no stress" condition is assumed. A pressure of 0 GPa is assigned at the point (660, 50). **Table B.1** gives the rheological parameters for each model (as defined for **Equations 6.5** and **6.6**). For the Newtonian rheology, the pre-exponential factor (A) was chosen to give an arbitrary viscosity of 10^{21} Pa s at a temperature of 1200°C. The parameters for the power law rheology are the dislocation creep parameters of dry olivine from *Karato and Wu* [1993].

Figure B.7 shows the model results for the Newtonian rheology using the PGC modelling code. These results were obtained with residuals of both velocity and temperature of less than 10^{-6} (see **Chapter 6** for details of the convergence criteria). For this residual, a total of 15 iterations were required for convergence. In the mantle wedge, flow is concentrated in a narrow channel near the top of the subducting plate. There is no significant flow in the shallow (<150 km) part of the backarc mantle. The large upward flow velocities in the channel above the plate mean that heat is efficiently transported toward the wedge tip, leading to higher temperatures and heat flow here. However, this flow pattern produces low temperatures and heat flow in the upper part of the backarc. This flow pattern is characteristic for corner flow with a temperature-dependent mantle rheology (see **Chapter 7**).

Figure B.8 shows the PGC model results for the power law rheology. These results were obtained in 19 iterations, with a residual of 10^{-6} for velocity and temperature. This rheology produces a similar flow pattern and thermal structure to those for the

Table B.1. Rheological parameters for subduction zone benchmark models.

Rheology	A ($Pa^{-n} s^{-1}$)	n	Q (J/mol)	B ($Pa\ s^{1/n}$)
Newtonian	2.5244×10^{-10}	1.0	335000	1.32043×10^{-9}
Power Law	2.8483×10^{-17}	3.5	540000	14484.3

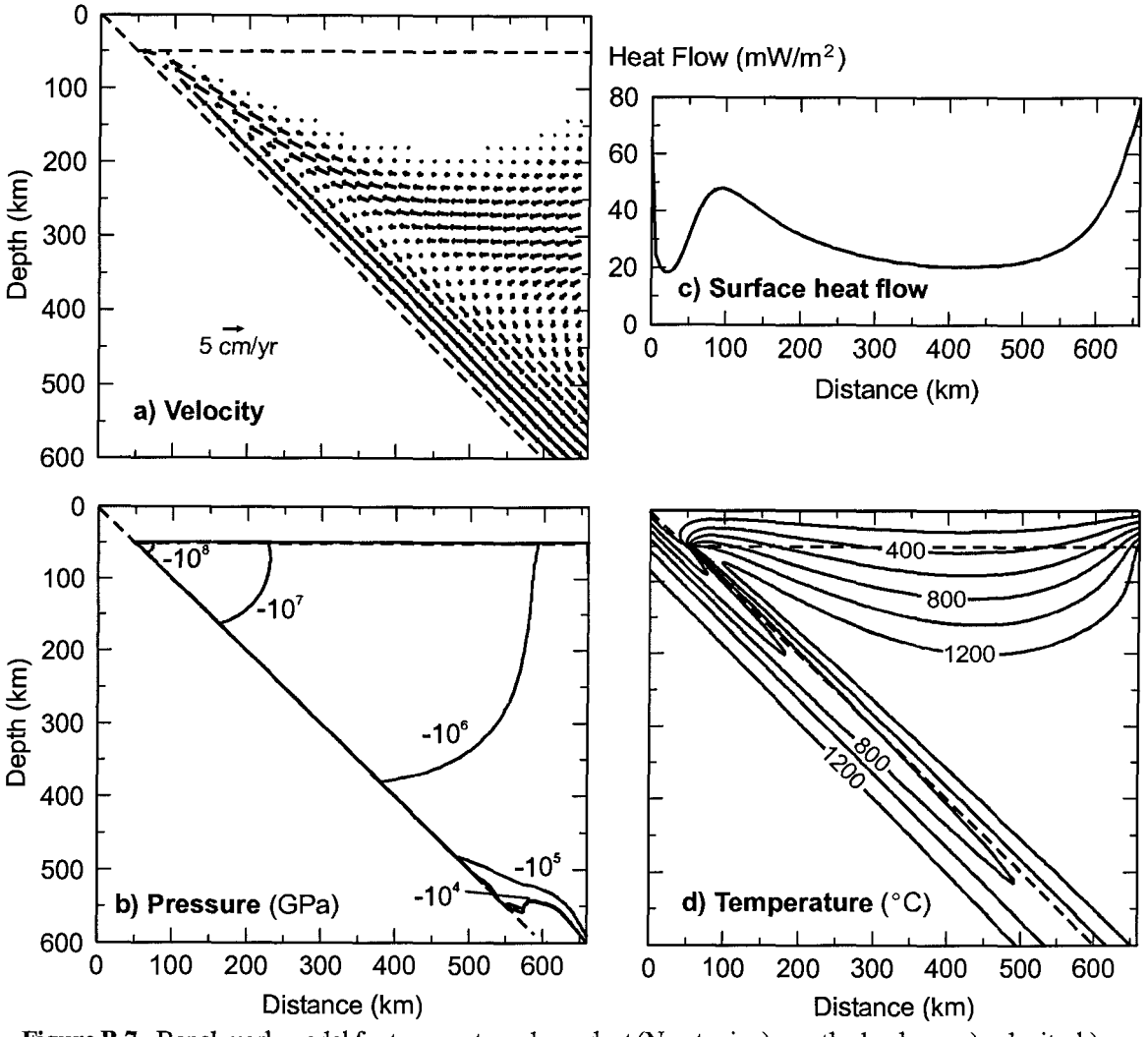

Figure B.7. Benchmark model for temperature-dependent (Newtonian) mantle rheology: a) velocity, b) pressure, c) surface heat flow, and d) temperature contours (200°C).

Newtonian rheology above. Flow is focused towards the wedge corner, significantly enhancing temperatures and heat flow in this region, but the shallow backarc mantle is nearly stagnant and cool.

For the non-linear models, it is critical to ensure that the solution has fully converged to the steady-state solution. To examine this, a model was run using stricter convergence criteria. In this model, convergence is obtained with residuals for velocity and temperature of 10^{-8}, which is a factor of 100 smaller than the models above. **Figure B.9** shows the difference in the model results for the two convergence criteria, using the

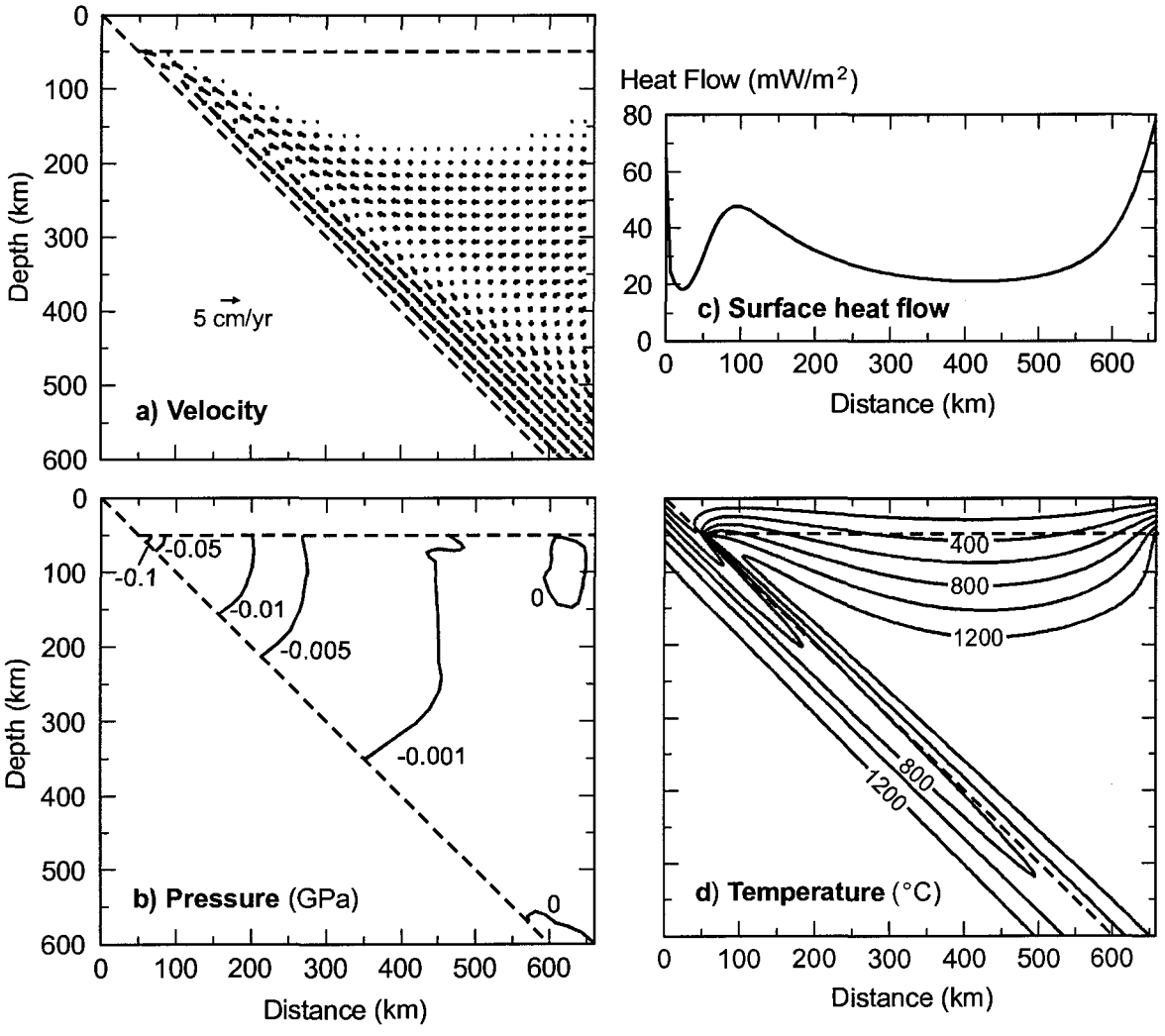

Figure B.8. Benchmark model for temperature- and stress-dependent (power law) mantle rheology, using the dislocation creep parameters for dry olivine [*Karato and Wu*, 1993]. a) velocity, b) pressure, c) surface heat flow, and d) temperature contours (200 °C).

power law rheology for the mantle wedge; the results of the models with convergence to 10^{-6} (the standard model) are subtracted from those for the model with convergence to 10^{-8}. Due to the large range in pressure within the models, the pressure differences are reported as percentages of the pressure in the standard model at each node (e.g., **Figure B.8**). Only the region where the absolute value of the pressure is larger than 0.001 GPa in the standard model is used for the comparison because as the pressures approach zero, the percentage differences become extremely large. The average difference in pressure

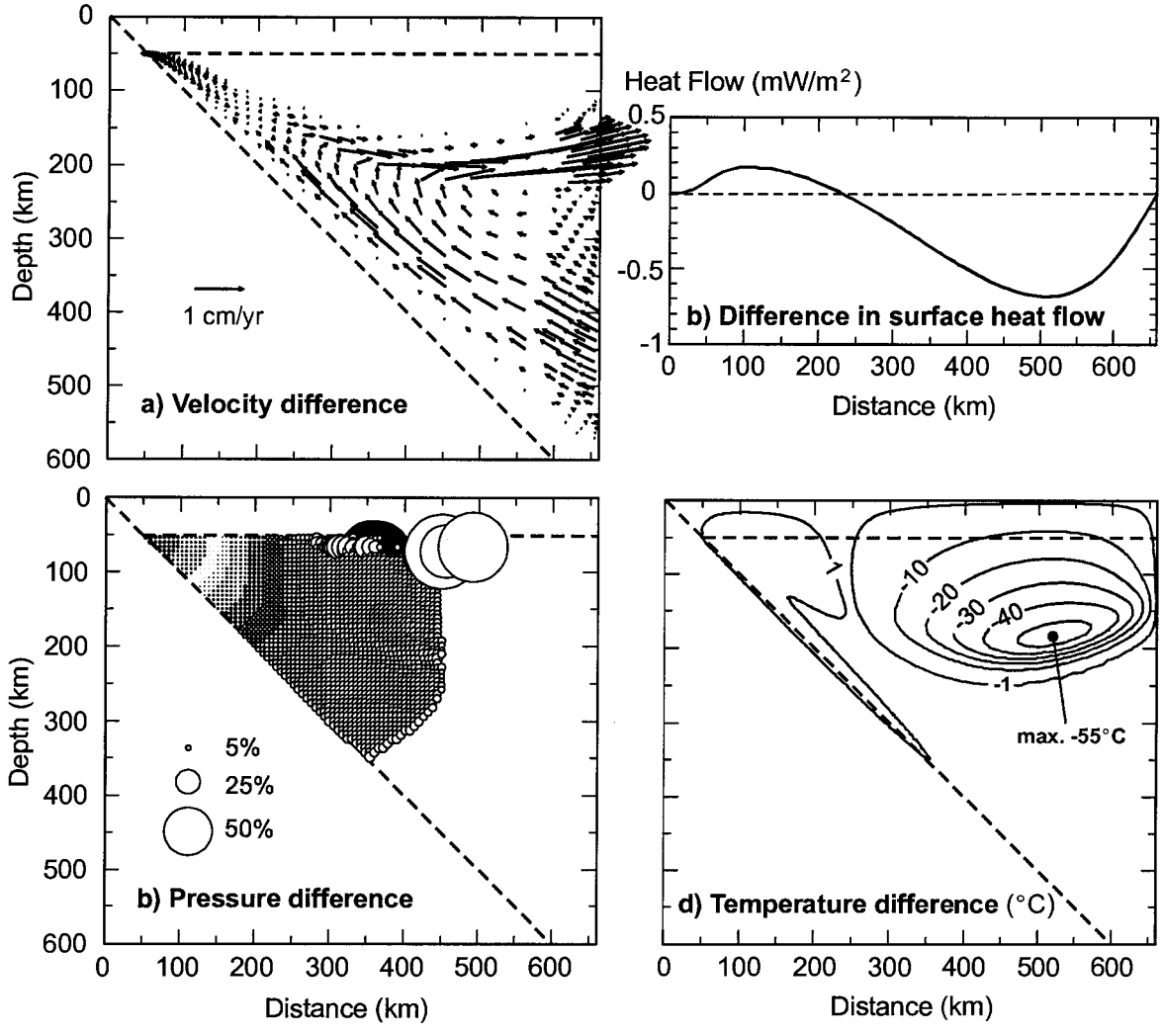

Figure B.9. Test of the convergence criteria for the non-linear models. Difference between a model with convergence to a residual of 10^{-8} and a model with convergence to 10^{-6} (the standard model). The mantle wedge has a power law rheology, using the dislocation creep parameters for dry olivine [*Karato and Wu*, 1993]. a) velocity, b) pressure (symbols as in Figure B.5), c) surface heat flow, and d) temperature. For the pressure differences, only the area with a dynamic pressure less then 0.001 GPa for the standard model is considered.

between the two models is 7.0%, with a maximum of 78.9% in the upper part of the backarc mantle. The largest velocity differences are found in the central part of the largest velocity differences are found in the central part of the backarc mantle wedge. These differences indicate that flow is focussed more strongly into the wedge corner with the stricter convergence criteria, resulting in a slightly narrower high velocity channel in the mantle wedge. The effect on the temperature field is fairly small (<1°C) for most of the wedge. The stronger flow focussing in the model with stricter convergence criteria

results in slightly higher temperatures in the wedge corner and lower temperatures in the upper part of the backarc mantle, with a maximum difference of –54.5°C. The low temperatures arise due to the thicker near-stagnant mantle "lid" relative to the standard model. These temperature differences are reflected in the very small differences (<1 mW/m^2) in heat flow between the two models.

Overall, better numerical solutions for the flow and thermal fields for a non-linear rheology are obtained using stricter convergence criteria, at the expense of greatly increasing the computing time. The standard model required 19 iterations (~68 minutes using one processor on a Sparc-60 workstation), compared to 86 iterations for convergence to 10^{-8} (~5.1 hrs). The slight improvement in the numerical results with the stricter convergence criteria does not seem to warrant the significantly longer computing time, and thus models with convergence to 10^{-6} appear to be satisfactory.

Another factor that must be considered is the adequacy of the node spacing, especially in the tip of the mantle wedge. For the isoviscous models, excellent agreement with the analytic solution for pressure was obtained using the finite element mesh in **Figure B.2**. However with the non-linear wedge rheology, the pressure and thermal gradients in the tip become larger and a smaller node spacing may result in better resolution of the gradients. No detailed tests were carried out using smaller elements for the benchmark models. As shown in **Appendix C**, as the element size is decreased, a better resolution of the flow and thermal fields, especially the effects flow focussing, is obtained. However, the computation time greatly increases due to the larger number of nodal points.

The models with the non-linear rheology are part of ongoing work to establish benchmarks for numerical modelling of subduction zone thermal structure with a non-linear (stress/temperature dependent mantle wedge rheology. Early comparisons with models developed by Peter van Keken at the University of Michigan (UM) show that the thermal fields between the PGC and UM models are in very good agreement, with the temperature differences less than 2°C for most of the model domain. The largest differences occur near the wedge tip, where differences of over 200°C are found. These appear to result from the modelling approach used to handle the numerical singularity, as

well as the type and size of elements used in the models. The PGC models use a rigid vertical boundary 1 m from the wedge tip and an increase from 0 to 5 cm/yr along the slab-wedge interface over the width of the element closest to the boundary (~0.001 m). The UM models use a smeared velocity boundary, where the prescribed velocity along the slab-wedge boundary increases from 0 cm/yr at the tip to the full subduction rate over a distance of a few kilometres (see *van Keken et al.* [2002] for details). In addition, the PGC code uses extremely small quadratic elements, as opposed to the larger triangular elements in the UM model. Fortunately, the largest differences (>10°C) between the models are confined to within 40 km of the wedge tip. The very good agreement observed for the rest of the model suggests that there are no numerical artifacts that affect the solution for the non-linear problems in either modelling code.

APPENDIX C

Numerical Tests for the NE Japan and Cascadia Meshes

C.1 Introduction

This appendix discusses numerical tests that were carried out using the finite element meshes of the NE Japan and Cascadia subduction zones shown in **Figure 7.1**. It is important to verify that these finite element meshes are adequate to produce accurate results and to understand the effects of different model assumptions on the thermal and flow fields.

C.2 Isoviscous Mantle Wedge

The first set of tests focusses on isoviscous corner flow using the NE Japan mesh. The seaward extent of wedge flow is 240 km from the trench, where the subducting plate is at a depth of 70 km. At greater depths, the subducting plate has a constant dip of 30°. Thus, for an isoviscous wedge, it is possible to use the analytic solution for corner flow [*Batchelor*, 1967] to verify the numerical calculations. Of particular importance is the region near x=240 km, where a vertical boundary separates the rigid wedge tip from the viscous wedge. This boundary marks a transition from no coupling to full coupling between the slab and wedge. Such a sharp transition causes mathematical difficulties. Thus, it is important to ensure the numerical accuracy of the model calculations in this region. A secondary objective of the tests is to understand the effect of the prescribed velocity boundary conditions along the landward boundary of the wedge.

In the models, the upper and lower boundaries of the model have fixed temperatures of 0°C and 1450°C. The oceanic boundary is assigned a geotherm corresponding to a 130 Ma oceanic plate. Prescribed temperatures along the landward boundary are given by the "warm" continental geotherm, which gives a surface heat flow of 75 mW/m^2 (see **Chapter 7**). The upper boundary of the wedge has a velocity of 0

cm/yr, and the lower boundary (slab/wedge interface) is assigned the subduction velocity (9.1 cm/yr) tangential to the slab surface.

Figure C.1a shows the analytic velocity field for an isoviscous wedge. **Figure C.1b** gives the temperature field that results from the analytic flow velocities and thermal boundary conditions. In the following, the boundary conditions along the landward boundary and the boundary that defines the seaward limit of flow are varied. The results of each test are compared to those of the analytic solution.

First, the analytic velocity values for corner flow are prescribed to the two vertical wedge boundaries, and flow in the interior of the wedge is calculated numerically. This test is designed to examine the numerical accuracy of the flow calculations, especially near the seaward limit of flow. **Figure C.2a** shows the difference in velocity between the numerical model and the analytic solution. Overall, the agreement between the numerical and analytic flow fields is excellent. The average velocity difference is 5.5×10^{-4} cm/yr, with a maximum difference of 3.78×10^{-3} cm/yr. The largest velocity differences are

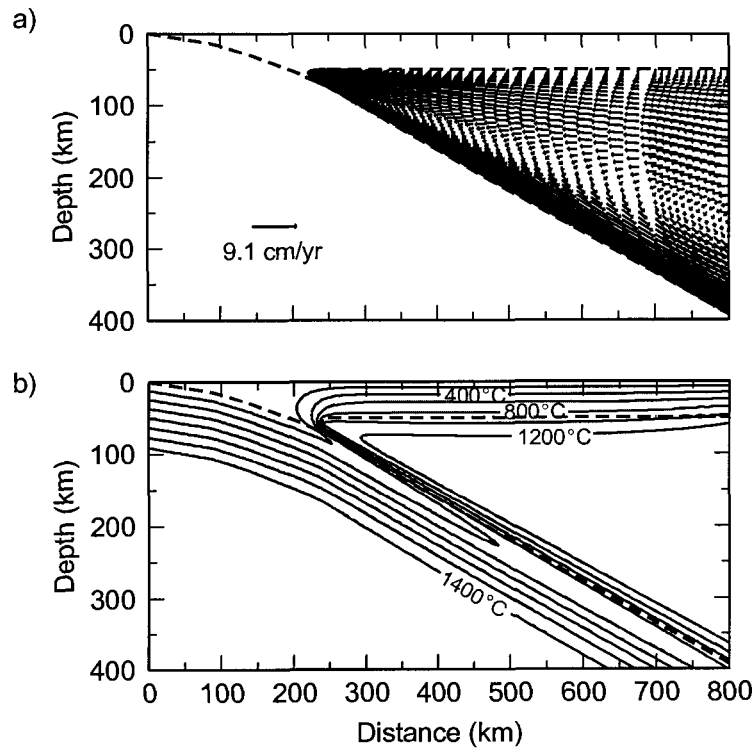

Figure C.1. Isoviscous corner flow models for NE Japan. a) Analytic solution for the corner flow velocity field for an isoviscous mantle wedge. b) The thermal field calculated using the analytic velocities and the thermal boundary conditions described in the text.

found near the seaward limit of flow (x=240 km), due to the large pressure gradients here. The element size in this region is ~0.3 km. An even better agreement to the analytic solution can be obtained by using even smaller elements, at the expense of increasing computing time due the larger number of elements in the mesh. The small

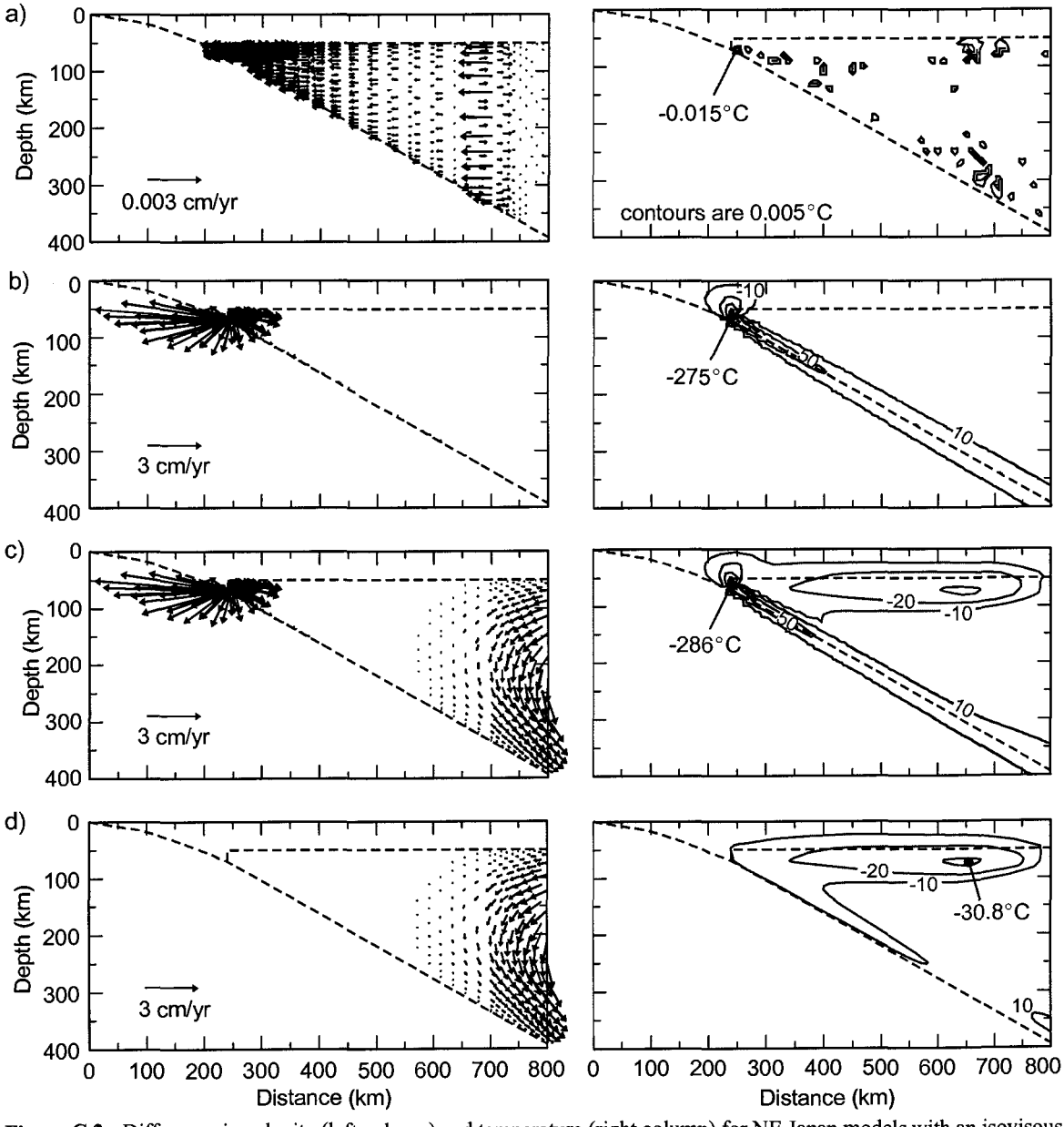

Figure C.2. Difference in velocity (left column) and temperature (right column) for NE Japan models with an isovisous mantle wedge. a) Difference relative to the analytic solution for a model with analytic velocities prescribed to wedge boundaries. b) Difference relative to the analytic solution for a model with analytic velocities on landward wedge boundary (x=800 km) and a velocity of 0 cm/yr on seaward wedge boundary (x=240 km). c) Difference relative to analytic solution for a model with a "free" (no velocity gradient) landward wedge boundary and a velocity of 0 cm/yr on seaward wedge boundary. d) Difference between a model with a "free" (no velocity gradient) landward wedge boundary and a model with the analytic velocities on this boundary. The seaward wedge boundary has a velocity of 0 cm/yr for both models.

velocity differences between the numerical and analytic velocity fields have only a minor effect on the thermal field, where the average temperature difference is 3.9×10^{-4} °C, with a maximum difference of 1.5×10^{-2} °C.

For the second model, the seaward boundary of the wedge (at x=240 km) is assigned a velocity of 0 cm/yr (i.e., the boundary is rigid). The analytic velocities are prescribed to the landward boundary. This test examines the effects of assuming a rigid seaward boundary. The largest velocity differences relative to the analytic solution occur near the seaward limit of flow due to the prescribed no-velocity condition along the seaward wedge boundary (**Figure C.2b**). The maximum velocity difference is 7.77 cm/yr. Large velocity differences (>0.05 cm/yr) are confined to within 35 km of the seaward wedge boundary. More than 35 km from the boundary, the average velocity difference is 2.0×10^{-4} cm/yr. With these velocity differences, there are fairly large temperature differences near the seaward wedge boundary. Away from the boundary, higher temperatures (10-50°C) are found along the slab surface for the numerical solution. These differences are due to the rigid seaward wedge boundary in the numerical model; the downward flow velocities near the boundary are slightly less than the analytic model, and thus, cool temperatures from forearc are less efficiently advected downward. Overall, the average temperature difference is 3.0°C for the entire model domain.

In the third model, the velocities along the landward wedge boundary (at x=800 km) are free, and a "no velocity gradient" boundary condition is assumed. The seaward wedge boundary is rigid. Relative to the analytic model, there are small velocity differences near the landward boundary **(Figure C.2c)**, similar to those seen in the models in **Appendix B**. These velocity differences result in slightly lower temperatures in the upper part of the wedge for the numerical model. The velocity and temperature differences in the wedge tip arise from the assumed rigid seaward wedge boundary in the numerical model, as noted for model 2. The combined effects of the two boundaries lead to an average temperature difference of –3.2°C between the numerical and analytic models.

The final comparison looks at the difference between a model with analytic velocities on the landward boundary and one with a "no velocity gradient" boundary condition (i.e., the difference between model 2 and model 3). In both cases, the seaward boundary of the wedge has a velocity of 0 cm/yr. The velocity differences near the landward wedge boundary are identical to those seen in the previous comparison (**Figure C.2d**). This test illustrates that the "free" velocity boundary condition produces slightly lower temperatures in the mantle wedge. The numerical model is an average of 6.3°C cooler than the fully analytic model.

In summary, these tests have shown that the node spacing in the finite element mesh is adequate to accurately reproduce the analytic solution, including the large pressure gradients near the wedge corner. The boundary conditions on the vertical wedge boundaries have only a small effect on the results.

C.3 Non-linear Mantle Wedge Rheology

The second set of tests investigates slab-driven flow in a mantle wedge with a stress- and temperature-dependent (power law) rheology, using the NE Japan mesh. The purpose is to examine the adequacy of the node spacing in the finite element mesh and the convergence criteria. Since there is no analytic solution with which to compare the results, models were run with a greater node density and using stricter convergence criteria. For these tests, the dislocation creep parameters for wet olivine are used [*Karato and Wu*, 1993]. These models use the thermal boundary conditions described above. The wedge boundary at x=240 km is assumed to be rigid (v=0 cm/yr) and the landward wedge boundary is free (no velocity gradient). The variations in node spacing and convergence criteria are compared to the "warm geotherm" model shown in **Figure 7.11b**, which uses the mesh shown in **Figure 7.1b** and has converged to a residual in velocity and temperature of 10^{-6}.

First, the adequacy of the finite element mesh was examined by comparing the results for a model using the mesh shown in **Figure 7.1b** with a model that contains twice as many elements (i.e., node spacing is approximately half of the standard model). As shown in **Figure C.3a**, variations in node spacing lead to only small differences in

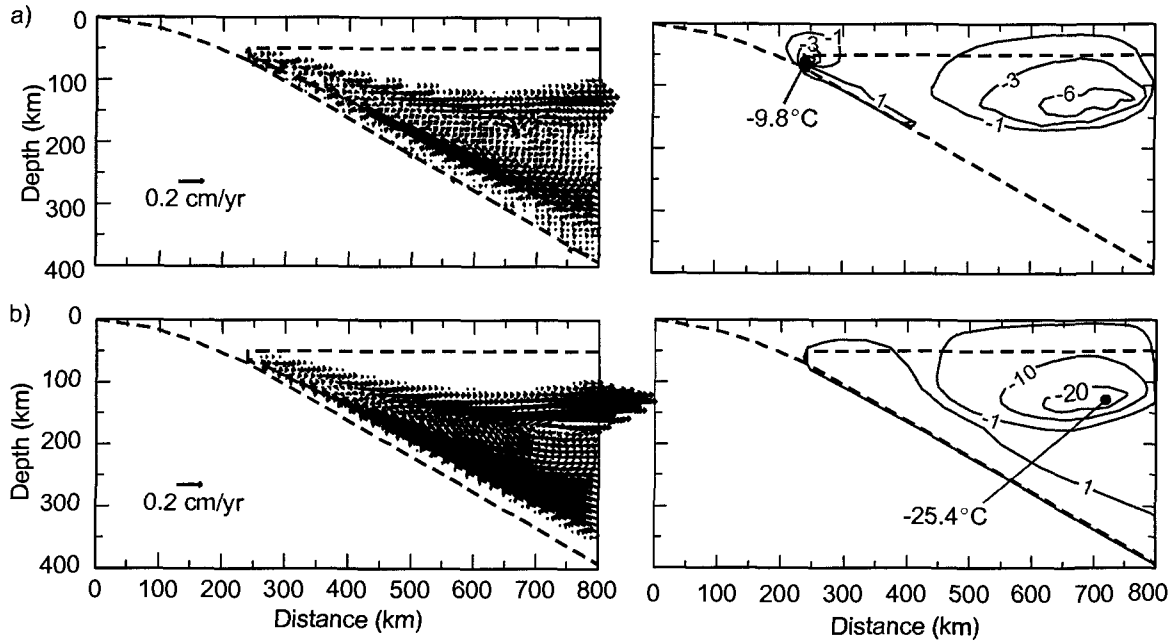

Figure C.3. Difference in velocity (left column) and temperature (right column) for NE Japan models that use a stress- and temperature-dependent wedge rheology (dislocation creep of wet olivine). a) Grid resolution. The difference between a "high resolution" model (twice as many elements in the mantle wedge) and a model that uses the standard NE Japan mesh. b) Convergence criteria. The difference between a model that converged to a residual of 10^{-8} and that to 10^{-6}.

velocity. The average difference is less than 0.01 cm/yr, with a maximum difference of 0.27 cm/yr. The effect on the thermal field is also small. The high resolution model is an average of 0.85°C cooler than the standard model, with a maximum difference of –9.8°C near the wedge corner. These differences arise from the slightly better resolution of the flow focussing effect obtained using a higher density mesh.

Next, the convergence criteria were examined by comparing results for convergence to a residual to 10^{-6} for both temperature and velocity (i.e., **Figure 7.11b**), to those with convergence to 10^{-8}. For these tests, the mesh in **Figure 7.1** is used. For convergence to 10^{-6}, 20 iterations are required, as opposed to 49 iterations for convergence to 10^{-8}. **Figure C.3b** shows the difference in the velocity and thermal fields between the two models. With the smaller residual, the amount of flow focusing is slightly increased, as illustrated by the velocity differences. For example, the model with greater convergence has smaller velocities in the shallow backarc. The maximum difference in velocity is 0.82 cm/yr. With the greater flow focussing, the temperatures in

the upper part of the backarc mantle are slightly lower. On average, the model with stricter convergence criteria is 2.3 °C cooler.

For a non-linear wedge rheology, the above tests show that satisfactory results can be obtained using the mesh in **Figure 7.1b** and convergence to a residual of 10^{-6} for temperature and velocity. Although slightly better results can be obtained by increasing the node density and using stricter convergence criteria, the computing time required for convergence increases because 1) more time is required for each iteration due to the increased number of nodes, and 2) the total number of iterations is much larger.

C.4 Lower Boundary of Wedge

As noted in **Chapter 7**, the base of the viscous mantle wedge is the top of the subducting plate. For the NE Japan and Cascadia models, the subducting plate exits through the landward (backarc) boundary of the model. Thus, the depth of the plate at the backarc boundary gives the maximum depth of the mantle wedge flow. For NE Jpan, the maximum depth of flow is ~400 km. For Cascadia, the steep dip of the subducting plate and the 800 km model width mean that wedge flow extends to 900 km depth. Thus, the mantle wedge in the model reaches into the lower mantle. Phase transitions in the mantle transition zone (410-660 km depth) are proposed to have a strong effect on mantle convection patterns, as they involve a change in density and may result in an increase in viscosity of several orders of magnitude between the transition zone and lower mantle [e.g., *Turcotte and Schubert*, 2002]. This may lead to layered mantle convection, where there is little transfer of material between the upper and lower mantle. It is important to ensure that possible effects from the mantle transition zone do not significantly change the shallow backarc thermal structure for the Cascadia models.

A second finite element mesh was developed for the Cascadia subduction zone (**Figure C.4**). In the new mesh, the base of the model is a horizontal boundary at a depth of 600 km. Thus, the subducting plate exits the model domain through the basal boundary, and this boundary forms the base of the mantle wedge between x=620 and 800 km. Two different boundary conditions were tested for this boundary: 1) an open boundary, such that flow is allowed through it using a no velocity gradient boundary

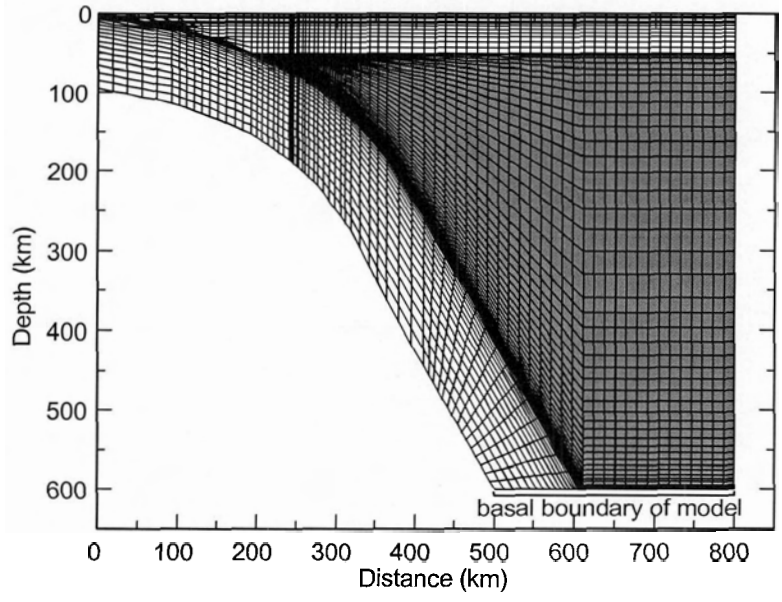

Figure C.4. Finite element mesh for Cascadia models with a horizontal basal boundary at a depth of 600 km. The shaded region is the viscous mantle wedge. Note that the basal boundary of the model forms the base of the viscous wedge between x=620 and 800 km.

condition, and 2) a no-flow boundary, where there is no vertical flow through the boundary.

Figure C.5 shows the model results for each case for both an isoviscous and non-linear wedge rheology. For comparison, the results obtained using the original model geometry are also shown. With an open basal boundary, the modelled thermal structure of the wedge is very similar to that in the original model. The largest differences are less than 50°C and are confined to the depths greater than 300 km. These differences occur because the length of the subducting slab varies between the two models, resulting in differing amounts of total traction on the viscous wedge.

The second condition for the basal boundary is a no-flow boundary. This condition approximates a very large viscosity increase at the base of the mantle transition zone which prohibits flow from entering the lower mantle. With this boundary condition, temperatures in the mantle wedge are somewhat larger than in the original models, and surface heat flow is very slightly higher (<1 mW/m^2). This is because there are slightly larger inflow velocities through the landward boundary of the model with the closed

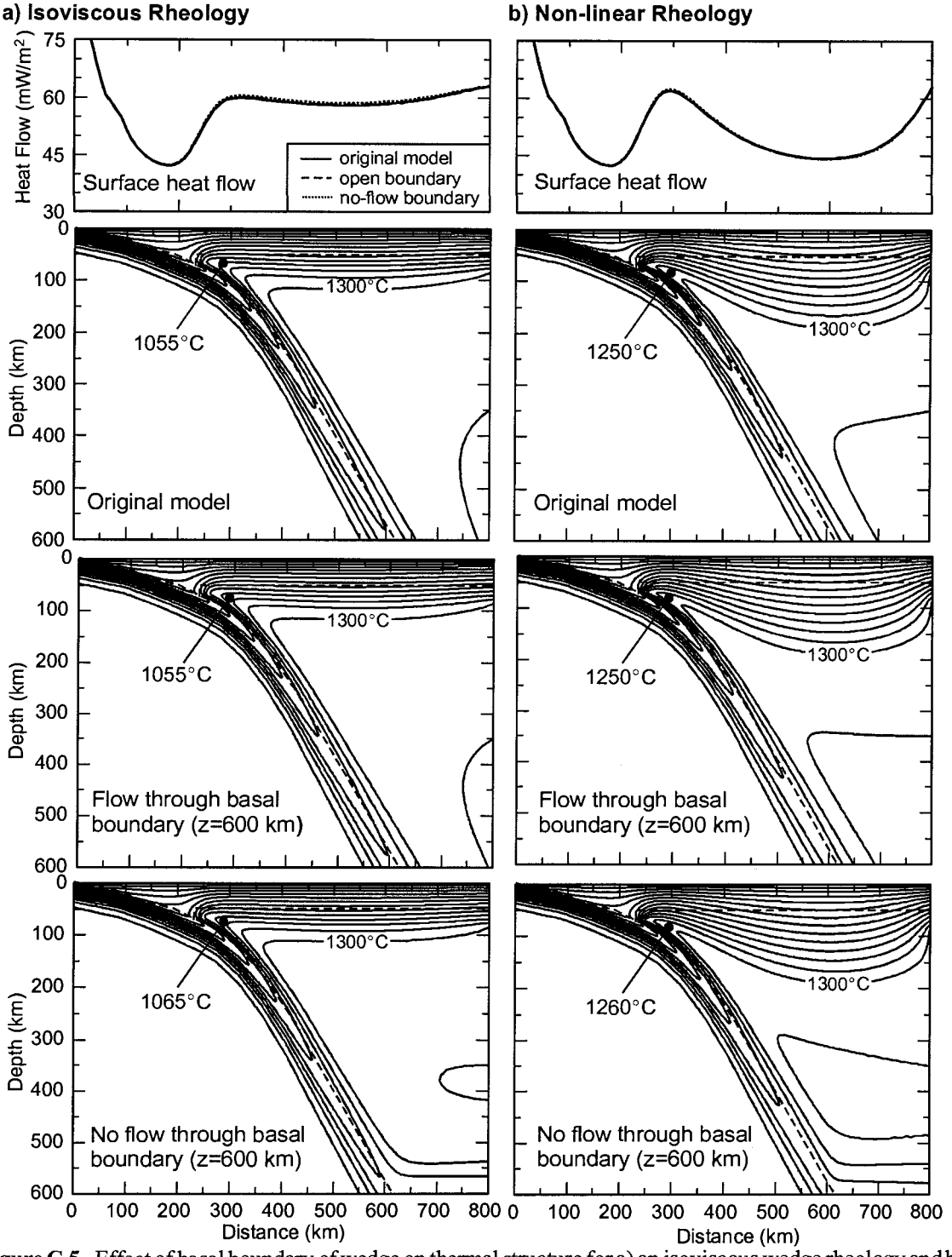

Figure C.5. Effect of basal boundary of wedge on thermal structure for a) an isoviscous wedge rheology and b) a non-linear (power law) wedge rheology (dislocation creep of wet olivine [*Karato and Wu*, 1993]). The top plot is the surface heat flow for each model. The three lower plots show the modelled thermal structure (100° C contours): (top) The original model with the slab exiting at the landward model boundary (x=800 km), as in the models in Chapter 7. (middle) Model with a horizontal basal boundary at z=600 km (slab exits through this boundary); flow is allowed through the boundary. (bottom) Model with a horizontal basal boundary (z=600 km); no vertical flow is allowed through the boundary.

boundary, due to the shorter length of the inflow/outflow boundary. The effect on the thermal structure is relatively small, with differences less than 15°C at shallow depths (<200 km).

Overall, the effect of the assumed geometry of the base of the viscous mantle wedge does not have a large effect on the modelled thermal structure at shallow depths (<300 km) for slab-driven mantle flow.

C.5 Real versus Potential Temperatures

This test examines the effects of using real temperatures during model calculations, as opposed to potential temperatures. The potential temperature of the mantle is the temperature at a pressure of 0 GPa. With increasing pressure (depth), temperatures should increase due to compression of the material, following an adiabatic temperature gradient. In this study, the potential temperature and adiabatic gradient were taken to be 1295°C and 0.3°C/km [*Ito and Katsura*, 1989; *Turcotte and Schubert*, 2002].

In the models in this study, real temperatures were used throughout the model calculations, with the effects of adiabatic compression approximated by using an adiabatic thermal gradient along the backarc boundary. This boundary condition is not completely compatible with the equations used in the model calculations, because the effects of adiabatic heating are not included as a pressure-dependent heat source term in the heat equation (**Equation 6.16**). Ideally, the modelling should be carried out using real temperatures and the adiabatic heating source term. However, this can become time-consuming and thus approximate methods (like the one above) are used to account for the effects of adiabatic heating. Another common approximate method is to use potential temperatures (T_P) during model calculations and then convert the final results to real temperatures (T_R) [e.g., *van Keken et al.*, 2002]:

$$T_R = T_P + \phi z \qquad \text{(C.1)}$$

where ϕ is the adiabatic gradient (0.3°C/km in this study) and z is the depth (in km). This method is more compatible with the heat equation (with no adiabatic heat source term) used in this study.

To assess the effect of the "potential temperature" approach used by *van Keken et al.* [2002] and others, a Cascadia model was developed, using an isoviscous wedge and the "warm" landward geotherm (see **Chapter 7** for more details). The prescribed temperatures on the two vertical model boundaries and the base of the slab were modified from the "real temperature" boundary conditions by subtracting the adiabatic temperature at each node (i.e., depth × 0.3°C/km). The model calculations were then performed using the potential temperature boundary conditions, and the final thermal structure was converted to real temperatures by adding the adiabatic gradient (**Equation C.1**). This model can be compared to the model in **Figure 7.3** (warm geotherm), where the "real temperature" approach is used.

Figure C.6 shows the difference in temperature between the two models (taken as the potential temperature model minus the real temperature model). At shallow depths (<250 km), the two approaches are in good agreement, with differences less than 50°C in the wedge. At greater depths, there are significant differences between the two models, where the model with potential temperatures is hotter than that with real temperatures in the upper part of the slab and lowermost wedge. The shallow (<250 km) thermal structure is of most importance to this study. Thus, it is concluded that the use of real temperatures in model calculations yields satisfactory results in the shallow wedge. However, this approach should not be used in modelling studies of the deep mantle thermal structure.

C.6 Temperature-dependent Conductivity

The thermal models presented in **Chapter 7** assume a constant thermal conductivity of 2.5 W m^{-1} K^{-1} for the over-riding continental crust and 3.1 W m^{-1} K^{-1} for the mantle wedge and subducting plate. The thermal conductivity of most rocks decreases with increasing temperature, although at temperatures greater than 800-900°C, radiative heat transfer may act to increase the conductivity of some rocks [e.g., *Clauser and Huenges,* 1995; see also **Chapter 3**].

In order to examine the effect of varying conductivity on the thermal structure, models of the Cascadia subduction zone were developed using a temperature-dependent

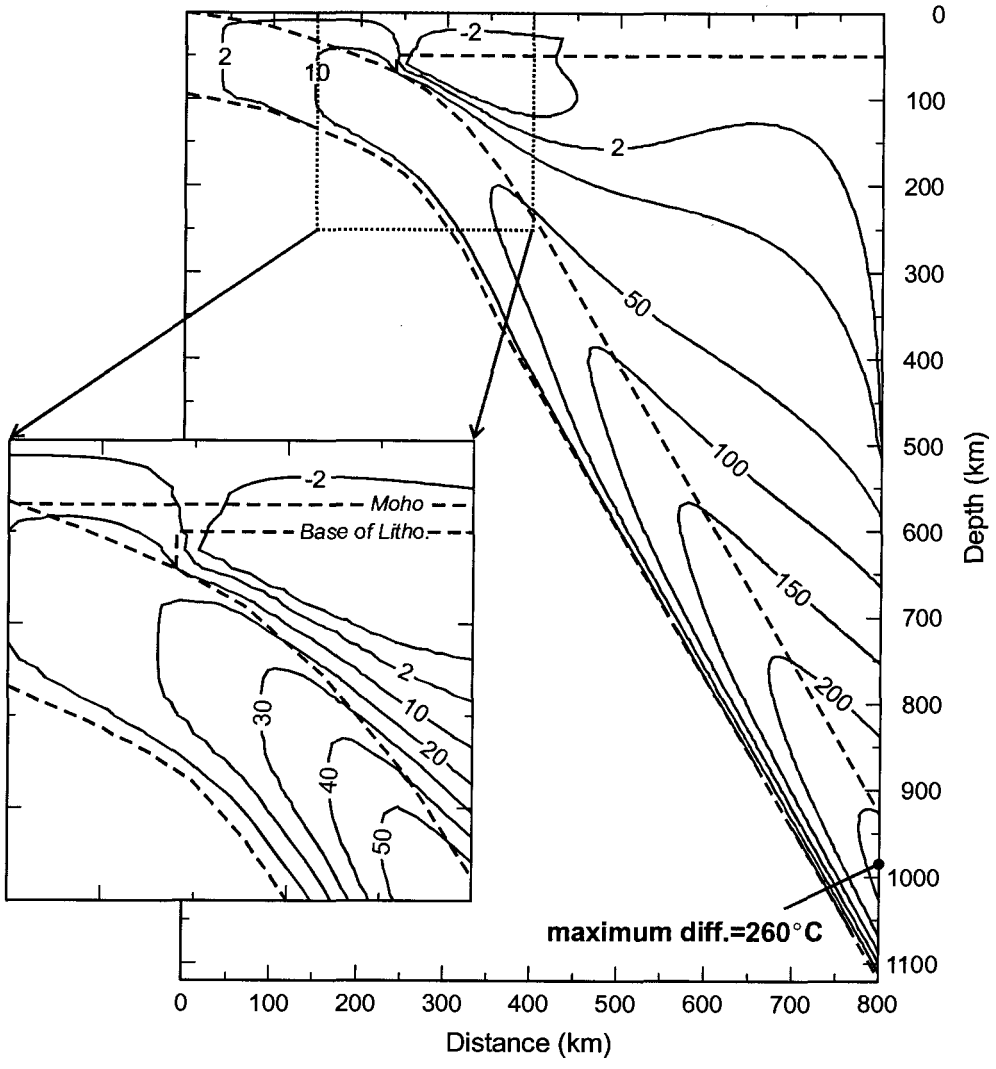

Figure C.6. Difference in temperature between using potential temperatures during model calculations and real temperatures. For the model with potential temperatures, the calculated thermal field is converted to real temperatures by adding an adiabatic gradient of 0.3 °C/km (Equation C.1).

conductivity. For these tests, the conductivity as a function of temperature is determined using the *Sass et al.* [1992] relation (**Equation 3.6**), with 0°C conductivity and temperature coefficients from *Lewis et al.* [2003] and *Flück* [2003] (see **Chapter 3**). The effects of radiative heat transfer are not included explicitly, but as discussed in **Section 3.6.3**, the *Sass et al.* relation may be a good approximation for radiative transfer by giving higher conductivities at high temperatures than the *Zoth and Haenel* [1988] relation. All other models parameters are identical to those used in the Cascadia models above, and the "warm" geotherm is prescribed to the backarc boundary. Both an

isoviscous rheology and non-linear wedge rheology (using the dislocation creep parameters of wet olivine [*Karato and Wu*, 1993]) are tested.

Figure C.7 shows the difference in temperature between the variable and constant thermal conductivity models for each rheology (the constant conductivity models are shown in **Figure 7.3**). For an isoviscous rheology, the temperature-dependent conductivity model results in a slightly hotter mantle wedge (<10°C) and slightly cooler over-riding plate (<30°C). The average difference between the models is +0.1°C, with a maximum (absolute value) difference of –31.9°C in the over-riding plate. With the non-linear rheology, both the mantle wedge and over-riding plate are slightly cooler (<30°C) with a temperature-dependent conductivity. The average difference is –4.0°C, with a

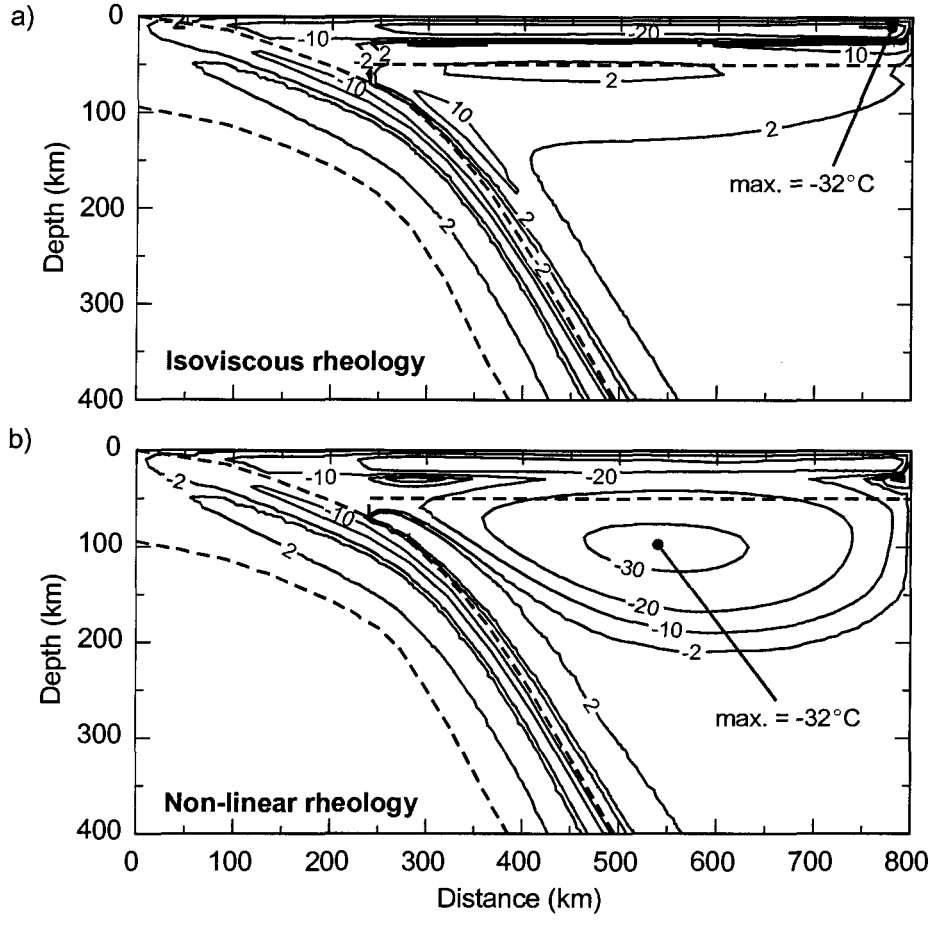

Figure C.7. Difference in temperature between using a temperature-dependent conductivity (following *Sass et al.* [1992]) and a constant thermal conductivity for each model unit for the Cascadia subduction zone models with a) an isoviscous mantle wedge rheology and b) a non-linear wedge rheology with the dislocation creep parameters of wet olivine [*Karato and Wu*, 1993].

maximum of –31.9°C in the shallow backarc mantle wedge. Overall, for either rheology, the difference between using a constant and temperature-dependent conductivity for the thermal models is quite small (<30°C).

C.7 Comparison with Published Models

As a final test, models were developed based on published subduction zone thermal modelling studies. *Peacock and Wang* [1999] and *van Keken et al.* [2002] have developed finite element models for the thermal structure of NE Japan. *van Keken et al.* [2002] also present models for Cascadia.

The model geometry used in these studies is similar to that in **Figure 7.1**, except that the model width is 500 km. Thus, the Cascadia and NE Japan meshes were modified to have a backarc boundary 500 km from the trench. The thermal parameters and subduction rates for each published model are identical to those in this study, except that the heat generation in the lower crust of the over-riding plate is 0.27 $\mu W/m^3$ (instead of 0.4 $\mu W/m^3$). The upper and lower boundaries of the model are assigned temperatures of 0°C and 1450°C, respectively. The prescribed geotherm for the oceanic boundary is a geotherm for 130 Ma lithosphere for NE Japan, as used in this study. For Cascadia, a geotherm for 10 Ma lithosphere covered with 3 km sediments is used, following *van Keken et al.* [2002]. Note that this plate is 2 my older than that used in the model in **Chapter 7**. The prescribed backarc geotherm of *Peacock and Wang* [1999] and *van Keken et al.* [2002] is also different. These studies use a geotherm that gives a surface heat flow of 65 mW/m^2 at the surface. Using **Equation 3.3**, a backarc geotherm was calculated using this heat flow and the thermal properties of the crust and mantle. The transition from a conductive to an adiabatic gradient is taken to occur at a depth of 95 km, where the temperature is 1450°C. Below this, an adiabatic gradient of 0.3°C/km is used.

The first comparison is for models of isoviscous flow for NE Japan. **Figure C.8a** shows the thermal structure calculated using the PGC modelling code, with the 500 km model width and the backarc geotherm described above. The calculated temperatures on the top of the subducting slab, as well as those at the base of the subducting crust (7 km

into the slab), are shown in **Figure C.8b**. These are compared to the isoviscous models of *Peacock and Wang* [1999] and *van Keken et al.* [2002]. *Peacock and Wang* [1999] incorporate flow into their models using the analytic solution [*Batchelor*, 1967]. On the other hand, *van Keken et al.* [2002] numerically calculate flow in the isoviscous wedge, as in the current study.

At depths greater than 60 km, the *van Keken et al.* results agree very well with those obtained using the PGC modelling code. The *Peacock and Wang* model gives

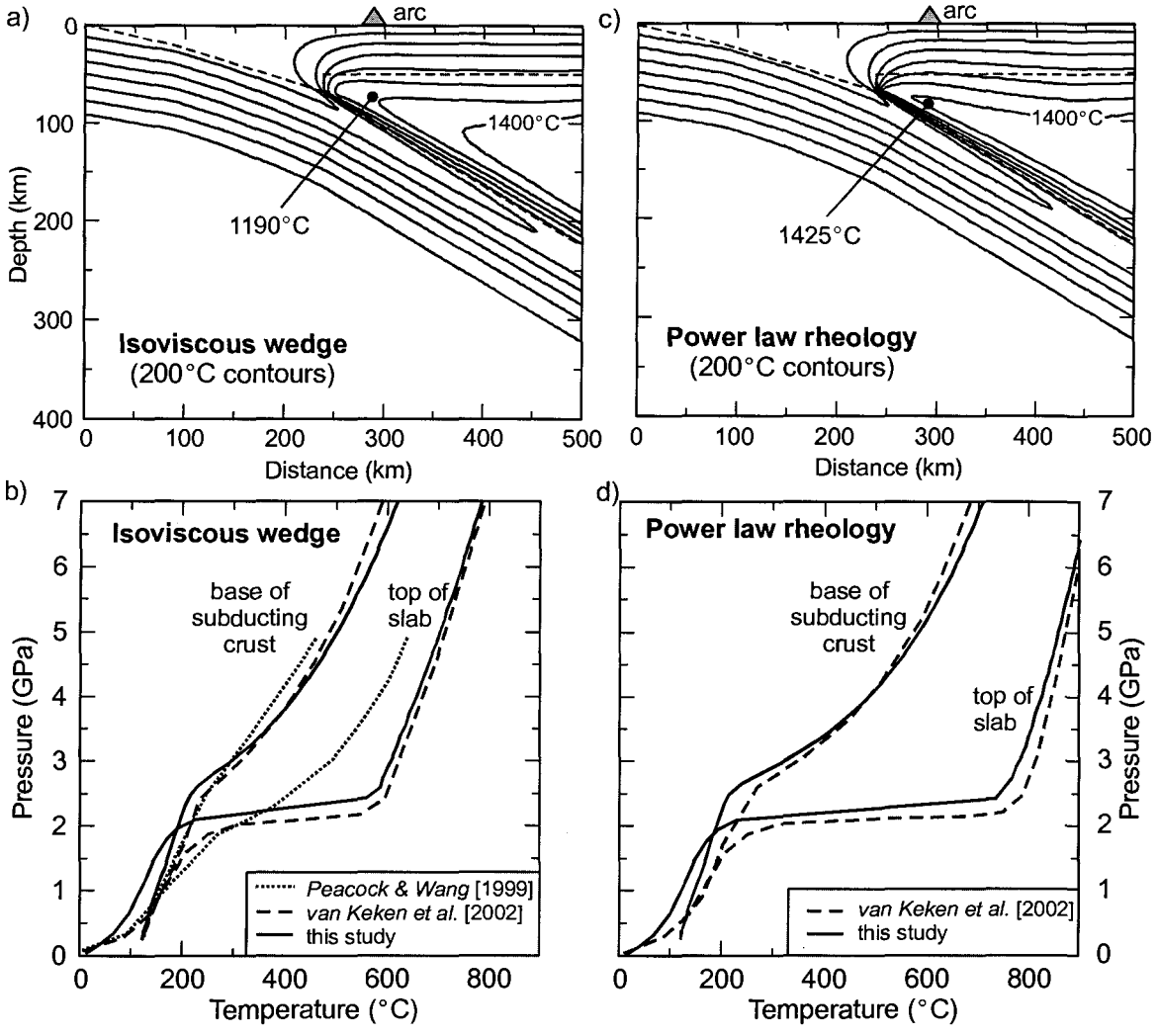

Figure C.8. Thermal models for NE Japan calculated with a 500 km wide mesh and the landward geotherm used by *Peacock and Wang* [1999] and *van Keken et al.* [2002] (see text). a) Thermal model for an isoviscous wedge. b) Temperatures on top of subducting slab and at the base of the subducting crust (7 km depth into the slab) for the isoviscous model in (a). Also shown are the slab temperatures in the models of *Peacock and Wang* [1999] and *van Keken et al.* [2002]. c) Thermal model for a power law rheology (dislocation creep of dry olivine [*Karato and Wu*, 1993]). d) Comparison of the slab temperatures in (c) with those of *van Keken et al.* [2002]. Note that 1 GPa≈30 km.

slightly lower temperatures along the top of the subducting slab at these depths. Note that the slab surface temperatures at shallow depths (<60 km) are slightly cooler for the PGC model because frictional heating was not included. *Peacock and Wang* [1999] and *van Keken et al.* [2002] incorporated a small amount of frictional heating in their models to a depth of 70 km (corresponding to a shear heating rate of 29 mW/m^2).

Next, corner flow models were developed for NE Japan using a non-linear wedge rheology. In this case, the dislocation creep parameters for dry olivine [*Karato and Wu*, 1993] were used, following *van Keken et al.* [2002]. **Figure C.8c** shows the thermal model calculated using the PGC modelling code and **Figure C.8d** shows the temperatures at the top and bottom of the subducting crust. These results agree very well with those of *van Keken et al.* [2002]. As above, the differences in slab surface temperatures at shallow depth arise due to the inclusion of frictional heating by *van Keken et al.* [2002].

As a final test, a model for the Cascadia subduction zone was developed using the dislocation creep rheology for dry olivine (**Figure C.9a**). The temperatures along the top and bottom of the subducting crust are shown in **Figure C.9b**. These temperatures are

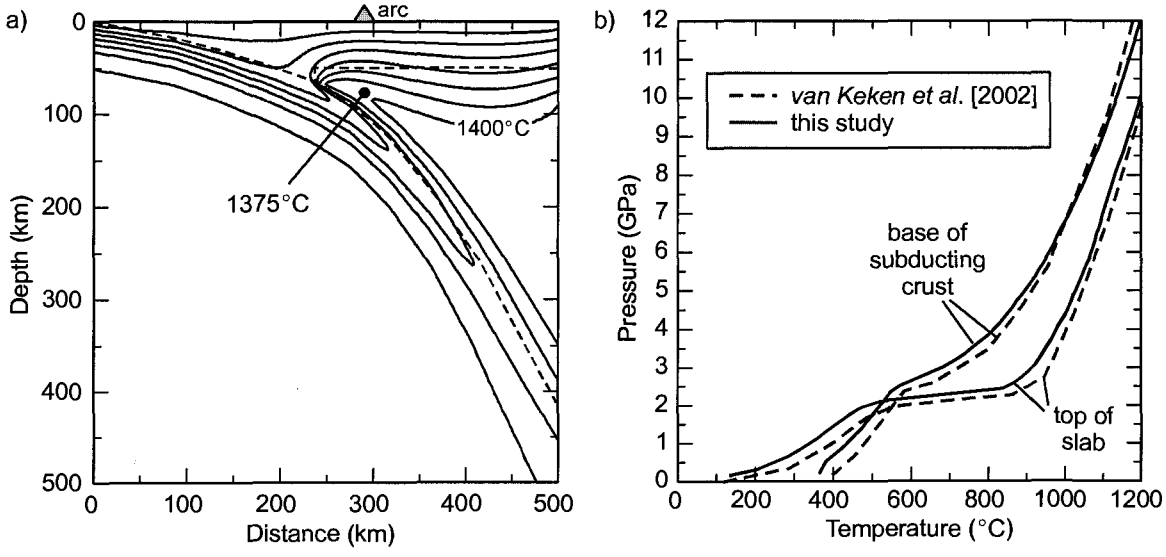

Figure C.9. a) Thermal model for the Cascadia subduction zone, with a 500 km wide mesh and the landward geotherm used by *van Keken et al.* [2002]. The dislocation creep parameters for dry olivine are used for the viscous wedge [*Karato and Wu*, 1993]. b) The temperature along the top of the subducting slab and at the base of the subducting crust (7 km depth into the slab) for the PGC model (solid lines) and the *van Keken et al.* [2002] model (dashed lines).

consistent with those obtained by *van Keken et al.* [2002]. Differences in the shallow temperatures are likely due to slight differences in the geometry of the subducting plate.

These tests have shown that the thermal models for Cascadia and NE Japan calculated using the PGC modelling code are in good agreement with those presented by *Peacock and Wang* [1999] and *van Keken et al.* [2002] for both isoviscous and non-linear wedge rheologies.